Application of a 3D Model to Simulate Water Quality in a Stormwater Pond

by

Mahyar Mehdizadeh

A thesis submitted in partial fulfillment of the requirements for the degree of

Doctor of Philosophy

in

Water Resources Engineering

Department of Civil and Environmental Engineering

University of Alberta

ABSTRACT

The coupled three-dimensional hydrodynamic and water quality ELCOM-CAEDYM model was used to investigate the factors impacting the abundance of algae as a key indicator of water quality in a stormwater pond in the city of Edmonton, Canada. Field measurements collected from May to October of 2014 and 2015 were used to set up the model and to calibrate the model. The inflow time series, as an important boundary condition, was estimated using the reverse level pool routing method with low-pass filtering of the observed water level time series. Both analytical and Monte Carlo simulations showed that errors in the estimated inflows are directly related to the area of the pond and inversely related to the numerical time step.

ELCOM was calibrated and validated for water temperature. The model accurately simulated the thermal structure of the pond including mixing and stratification. Sensitivity analysis of ELCOM showed that the model is most sensitive to albedo. Sensitivity analysis showed that the most influential CAEDYM model parameters were, the *maximum potential growth rate*, *algal respiration*, *mortality and excretion rate*, *minimal internal phosphorous concentration*, and *light half saturation constant for algae limitation*. Total chlorophyll-a (TCHLA) was found to be the most sensitive model variable and as a result CAEDYM was calibrated and validated, primarily focusing on TCHLA, while also considering other state variables such as dissolved oxygen, total phosphorous, and total nitrogen.

Furthermore, the sensitivity of ELCOM-CAEDYM to the boundary conditions and depth was comprehensively assessed. For this, different scenarios were defined by altering flow rates, nutrient loads, air temperature, wind speed, and depth, and their corresponding impacts on different biogeochemical and hydrodynamic processes were evaluated. The trophic state of the pond under these scenarios was also assessed. Given that ELCOM-CAEDYM effectively simulated algae dynamics, as demonstrated through calibration and validation, and considering its responsiveness to changes in boundary conditions, it can be used as a tool to predict water quality under future climate and management plans.

KEYWORDS: ELCOM-CAEDYM, sensitivity, reverse level pool routing, water quality, stormwater pond.

ACKNOWLEDGMENTS

I would like to express my sincere appreciation to my supervisor, Dr. Mark Loewen, for his exceptional understanding, patience, professionalism, and invaluable guidance throughout the completion of this thesis. His support and mentorship made all the difference.

I am grateful to my co-supervisor, Dr. Leon Boegman, for his help, support, and the generous sharing of his experience.

I also extend my gratitude to my other examining committee members: Dr. Evan Davies, Dr. Samuel Li, and Dr. Maricor Arlos, for their detailed reading of this thesis and for their insightful comments.

I also appreciate the help and support of Dr. Nader Nakhaei. Thank you for sharing your expertise honestly.

I had the chance to work in the field with many responsible people. Field work would have been so difficult without the competency and management of my colleague Jeff Kemp. Thank you, Jeff, for all the dedicated and organized work you have done. I am also thankful to Dr. Vincent McFarlane, Dr. Evan Davies, Dr. Yuntong She, Dr. Rocio Luz Fernandez, Dr. Mohamed Gaafar, Kissinger Lo, Jenna Pearse, Paul Stark, Stefan Emmer, Laurel Richards, Briley Lewis, Brent Majcher from the University of Alberta; as well as the engineers and technicians from the City of Edmonton who were involved in this project.

Special thanks to Dr. Edyta Jasinska for her time and effort in analysing the algae samples.

This research was funded through the Natural Sciences and Engineering Research Council of Canada (NSERC), and the City of Edmonton (Collaborative Research and Development Grant (CRDPJ 451210-13)) whose support is gratefully acknowledged.

Great thanks are also owed to Arlene Figley, the invaluable graduate program advisor of our department. Her welcoming smile and kind heart made my difficult moments tolerable.

Thanks to Perry Fedun for his exceptional help in the hydraulics lab and technical support. His knowledge and gentle attitude are greatly appreciated.

My heartfelt thanks to Dr. Faye Hicks. Without her unwavering belief in me during tough times, pursuing my dream would have been impossible.

I would like to thank Dr. Peter Steffler for the great and insightful conversations we had.

I am also very grateful for the friendship, conversations and unconditional support of two incredible friends Dr. Jennifer Nafziger and Dr. Shaghayegh Abtahi. I was so lucky to have them by my side.

Thank you so much for the precious support and friendship of Daee Yousef, Mahmoud, Behrouz, Atsko, Agata, Somayyeh, Arezu, Akram, Hamidreza, Niloofar, Elnaz, Nima, Ali, Sara. Your companionship fills my heart with love and warmth.

My respect to the memory of my father, whose progressive mindset and belief in equity gave me the courage to choose my path. Warm hugs to my mother, whose unconditional support and best wishes for my success never let me give up.

My respect to the memory of my aunt Golestan. I will never forget the words she said: 'Be on the positive lineup, even if you are the last one.'

I would like to express my appreciation to my siblings and their families. They are invaluable gems in my life, always supporting me with love and attention. To my sisters: Mehrzad, my role model; Mehrnaz, my second mom; and Mahnaz, my understanding friend. Additionally, I want to extend my thanks to my brother Mehdi. His dedication and hard work have made a significant difference in my life.

I would also like to thank the moon of my life, Daniel, whose presence has brightened my life and shined my smile.

My dear husband, Massoud Shafieifar, no words seem sufficient to convey the immense appreciation I hold for you. Your unconditional love and support, endless sacrifices, and constant companionship fill my heart with boundless gratitude and respect that words alone cannot express. So, in simplicity, thank you, I owe you, and I love you more.

DEDICATION

To my parents, who gave me life,

To my sister, Mehrzad, who taught me to soar and illuminated the horizons,

And to my beloved husband, Massoud, who flew by my side, wing by wing, and tirelessly eased all difficulties.

TABLE OF CONTENTS

LIST OF TABLES

LIST OF FIGURES

Chapter 1. INTRODUCTION

Stormwater ponds are considered one of the most effective management practices for mitigating the adverse effects of excessive runoff on surrounding ecosystems (Siegel et al. 2011). They have been integrated into Canadian urban drainage systems since the 1960s. Originally, stormwater ponds were constructed to reduce drainage costs and mitigate flooding by storing storm runoff and releasing it gradually to a receiving water body (Watt et al. 2004). However, their functionality has expanded over time to protect receiving water bodies by improving the quality of released water through different physical, chemical, and biological processes (AEP 1999; Marsalek et al. 1992, 2002). Currently, many stormwater ponds are designed to include additional purposes such as irrigation, recreational, and aesthetics (He et al. 2015).

However, stormwater pond functionality can be compromised by factors such as stratification, increased nutrient and metal loading, eutrophication, and oxygen depletion (Oberts 2003; Song et al. 2015). Additionally, the excessive growth of undesirable aquatic plants can not only diminish pond aesthetics but also lead to the emission of unpleasant odors (e.g., Sallenave 2011). Nutrient loading can originate from both external and internal sources. Common sources of external loading include runoff and wastewater entering the pond (Thomann and Mueller 1987). Internal loading, however, refers to the release of nutrients from the sediment through diffusive fluxes or sediment resuspension (Søndergaard et al. 2001; Fisher et al. 2005; Kristensen et al. 1992). Increased nutrient loading can cause eutrophication, which is the excessive growth of autotrophs, including algae. Eutrophication adversely affects the functionality of stormwater ponds by accelerating the degradation of aquatic plants, depleting of dissolved oxygen (DO), and releasing minerals, thereby increasing internal loading (Mortimer 1941; Orihel et al. 2017).

Wakelin et al. (2003) investigated the water quality of 58 stormwater ponds in Winnipeg, Manitoba. Water samples collected during the growing season (May to September) showed an increase in chlorophyll concentrations and a decrease in DO near the bed in the second half of the season. These changes were attributed to algal growth and degradation of biomass in the study ponds. Olding (2000) analyzed the composition of algal communities in two stormwater ponds in Richmond Hill, Ontario, with different geometries and catchment land-use. The study found that the catchment land-use, determining the chemical composition of inflow, affected the biological communities within the ponds. Furthermore, Olding et al. (2000) studied 27 water bodies in the urbanized area of the Greater Toronto, Ontario, and found that the algal communities were affected by the hydrodynamics and residence time of the body of water. For instance, the dominance of cyanobacteria communities was attributed to longer residence times.

Analysis of water samples collected from nine urban stormwater ponds in southern Ontario revealed elevated levels of dissolved phosphorus in the outflows compared to the inflows (Song et al. 2015). The role of stormwater ponds in transforming phosphorus into its dissolved forms, thereby increasing the risk of eutrophication in the receiving water bodies downstream, was highlighted as a potential negative impact of stormwater ponds in urbanized areas. Field monitoring of four stormwater ponds in Calgary, Alberta, revealed prolonged and frequent stratification during the open-water season (Ahmed et al. 2022, 2023). Vertical thermal and chemical gradients were identified as the primary drivers of the observed stratification. The morphology and configurations of inlet and outlet structures were also found to impact the thermal structure of the ponds, influencing stratification. Furthermore, the presence of dense aquatic plants and local landscape features were identified as factors inhibiting wind-induced mixing.

Stormwater ponds in cold climates have their own challenges, as stratification and the physical and chemical processes are temperature-dependent. Road salt and de-icing solutions, commonly used in cold regions, can enter the ponds and enhance their chemical stratification. The stronger stratification, whether thermal or chemical, leads to reduced mixing, increased hypoxia and anoxia, particularly near the bed, and decreased residence time (Ahmed et al. 2022; Marsalek 2003). A shorter residence time, along with lower oxygen levels, can decrease the removal efficiency of ponds, posing a risk to the quality and biodiversity of downstream bodies of water (Ahmed et al. 2022; Ji and Jin 2016; Torres et al. 1997). Low oxygen levels can also trigger the release of metals previously deposited in the sediment (Oberts 2003). Additionally, the sediment removal efficiency of the ponds is reduced during snowmelt events, particularly when the pond is still ice-covered (Marsalek et al. 2000; Roseen et al. 2006; Semadeni-Davies 2006).

Algae biomass is commonly used as a key indicator of water quality in bodies of water. Algae dynamics are influenced by both biogeochemical and hydrodynamic processes (Qin and Shen 2017). These two processes interact with each other, making it challenging to isolate their individual effects. Biogeochemical processes, like light, temperature, nutrients, and settling, affect algae's net growth rate. Hydrodynamic processes, such as advective and diffusive transport, redistribute not only algae biomass but also other factors such as nutrients. Qin (2017) introduced the transport rate method to estimate each process's contribution separately. Their study in the Upper James River, the USA, showed that both local (e.g., photosynthesis, respiration and settling) and transport processes significantly influenced the local variability of phytoplankton biomass. However, the importance of each process varied across different timescales.

In order to improve the functionality of stormwater ponds to meet the current and future environmental concerns, several studies investigated different management strategies including modifying the depth, volume, residence time, configuration of inlets and outlets, and managing the nutrient and mineral loads (e.g., Marsalek et al. 1992; Nakhaei et al. 2021; Olding et al. 2000; Sutherland et al. 2014; Walker 1998). For example, (Nakhaei et al. 2021) concluded that a 50% reduction in nutrient load is needed to control algae blooms in two stormwater ponds.

1.1 Motivation

This study is part of a comprehensive research initiative driven by complaints from residents of certain residential areas in Edmonton, Alberta, regarding the abundance of algae, unpleasant odors, and concerns about ice safety in nearby stormwater ponds. Out of more than 100 stormwater ponds, four were selected for this comprehensive research. Other studies were conducted to examine ice cover variability (She et al. 2016), hydrodynamic (Nakhaei et al. 2018) and water quality (Nakhaei et al. 2021) in subsets of the selected ponds. Furthermore, the potential need for modifying existing ponds and evaluating hydrological, climatological, and biogeochemical factors for future designs became the motivation of current study.

Numerical modeling has become a valuable tool for simulating the complex interactions of physical, chemical, and biological processes in stormwater ponds, and evaluating the potential impacts of climate and management scenarios. (Jin et al. 2007, Oberts et al. 2000). While 1D and 2D models can simulate some fundamental hydrodynamic and biogeochemical processes (e.g., Boegman et al. 2008; Hamilton and Schladow 1997), they may not adequately capture more complex processes such as mixing, circulation patterns, and localized algal blooms (Lee et al. 2013; Leon et al. 2011). Therefore, because of the presence of water quality heterogeneity or complex morphology, and due to available computational power, the application of 3D models has been growing (e.g., German et al. 2003; Hodges et al. 2000; Lee et al. 2013; Nakhaei et al. 2021).

Shaw et al. (1997) used the 3D hydrodynamic software package PHOENICS (Rosten and Spalding 1987) to study the flow patterns in a stormwater pond in Kingston, Ontario. They found that flow patterns are influenced by wind stress, inflow momentum, and geometry. Bentzen et al. (2008) applied the 3D computational fluid dynamic (CFD) software MIKE3 to model the hydrodynamics of a stormwater pond in Denmark. They concluded that wind was the primary factor influencing the retention time and flow patterns within the pond. The Environmental Fluid

Dynamic Code, EFDC (Hamrick 1992), is another 3D model for simulation of flow, transport, and biogeochemical processes in surface water systems. This model has also been applied to a variety of aquatic systems, including rivers, lakes, estuaries, reservoirs, wetlands, and coastal regions (Ji et al. 2007). Based on the EFCD code, the Lake Okeechobee Environment Model (LEOM) was developed to simulate water quality processes in constructed wetlands (Ji 2017).

In this study, the coupled 3D ELCOM-CAEDYM model was employed. This model consists of the Estuary and Lake COmputer Model (ELCOM) (Hodges and Dallimore 2013a) and the Computational Aquatic Ecosystem Dynamic Model (CAEDYM) (Hipsey et al. 2013), both developed at the University of Western Australia. Detailed descriptions of the model can be found in Hodges et al. (2000), Romero et al. (2004), and Bruce and Imberger (2009).

Mooij et al. (2010) and Trolle et al. (2012) highlighted ELCOM-CAEDYM as one of the most frequently cited models, widely applied in various hydrodynamics and water quality studies. For instance, it has been used to investigate modeling challenges, such as mixing and energy transport, in a stratified lake in Israel (Hodges et al. 2000), as well as to identify the processes controlling nutrient fate in two reservoirs in Australia. The model has also been applied to simulate hydrodynamic and geochemical processes in morphologically complex lakes in the USA (Missaghi and Hondzo 2010., Missaghi et al. 2013., Missaghi and Hondzo 2011), to assess the water quality of a shallow coastal lagoon in Western Australia receiving wastewater effluent (Machado and Imberger 2012), and to identify the conditions that lead to the dominance of specific algae groups in a shallow estuary in Argentina (Silva et al. 2014). Additionally, Carraro et al. (2012) applied ELCOM-CAEDYM to a medium-sized lake in Italy to investigate the influence of nutrients and hydrodynamics on the temporal and spatial distribution of cyanobacteria.

Yajima and Choi (2013) used the ELCOM-CAEDYM model to evaluate the impact of an inflow bypass on water temperature, DO, nutrient load, and algae concentration in a reservoir in

Japan. The study concluded that the proper operation of the bypass could decrease nutrient and algae concentrations within the reservoir, as well as reduce transportation of biomass downstream. Furthermore, Chan et al. (2002) utilized ELCOM-CAEDYM to investigate the impacts of land use alterations and tributary regulation on algae dynamics in the Swan River, Western Australia. While these hydrological changes were associated with increased flushing and reduced residence times, increased nutrient loading was determined to be the primary cause of more frequent and larger algae blooms. Additionally, Linden et al. (2015) simulated the water quality of a reservoir in Australia to examine the ELCOM-CADEYM model's sensitivity to altered wind, air temperature, and inflow boundary conditions. Since the model was responsive to climatic drivers, it was concluded that it could be used for investigating the impact of climate change on water quality of bodies of water.

DYRESM-CAEDYM, which couples the 1D DYRESM hydrodynamic model (DYnamic REservoir Simulation Model) with CAEDYM, has also been used in water quality studies. For example, Cui et al. (2016) employed this model to evaluate the effect of reducing external nutrient loads on algae biomass in the Shahe Reservoir, China. Multiple scenarios with varying reductions in nitrogen (N) and phosphorus (P) in inflow boundary conditions were examined. It was found that simultaneous reductions in both N and P were more effective in controlling algae growth compared to reducing only one nutrient. Trolle (2011) also used DYRESM-CAEDYM to investigate the potential impacts of climate change on the trophic status of lakes. Three lakes in New Zealand with varying tropic status were selected. Future scenarios were defined by a temperature increase of approximately 2.6°C and changing nutrient loadings up to ±50% from the base scenario. The results indicated that the trophic levels of the three lakes would deteriorate under the projected temperatures, which was equivalent to the impact of a 25-50% increase in external nutrient loading.

The calibration and sensitivity analysis of ELCOM-CAEDYM have received relatively less attention in research compared to its application, likely due to the large number of model parameters in CAEDYM. While ELCOM has a limited number of model parameters, calibration of CAEDYM requires adjusting a large number of model parameters (Hipsey 2013; Missaghi and Hondzo 2010). Hence, in most studies, only a subset of model parameters has been considered important for calibration. For example, in a water quality study of Lake Minnetonka, the USA, Missaghi et al. (2014) identified 29 important CAEDYM parameters. Further, their sensitivity analysis indicated that the following model parameters had the most influence on the model outputs, including the mineralization of dissolved organic carbon, sediment phosphorus release rate, algal metabolic loss rate, internal phosphorus concentration, and phosphorus uptake rate. However, it should be noted that their finding for a relatively larger body of water, such as Lake Minnetonka, may not directly apply to smaller water bodies like the stormwater ponds.

In addition to model parameters, sensitivity analysis can be conducted based on boundary conditions. Since boundary conditions are often defined based on measurements, there is generally more confidence in their accuracy compared to the model parameters. However, boundary conditions such as inflows may not always be measured accurately or frequently enough (Linden et al. 2015; Missaghi et al. 2014). Additionally, understanding model sensitivity to the boundary conditions is crucial for future climate and management studies (e.g., Elliott et al. 2006; Linden et al. 2015; Mooij et al. 2007b; Nakhaei et al. 2021; Trolle et al. 2008a, 2011).

Mooij et al. (2007a) used the lake ecosystem model PCLake to examine the effects of changes in nutrient loadings and water temperature on the quality of a hypothetical shallow lake. Linden et al. (2015) explored the sensitivity of the ELCOM-CAEYDOM developed for the Happy Valley Reservoir, Australia, to boundary conditions, including air and inflowing water temperature, wind speed, and inflow and outflow. Trolle et al. (2008b) used the DYRESM-CAEDYM model to investigate the impact of external nutrient loading on Lake Ravn in Denmark. Based on the defined nutrient scenarios, it was found that up to 50% phosphorus reduction was necessary to meet the European Union Water Framework.

The depth and bathymetry of a body of water can also influence its quality. Conn and Fiedler (2006) examined the influence of bottom topographic features on residence times in a hypothetical wetland using a 2D hydrodynamic model, and Sabouri et al. (2016) used an Artificial Neural Network approach to investigate the impact of depth on the outflow temperature. Based on field observations, Olding et al. (2000) studied the relationship between depth and composition of algal communities while Wen et al. (2023) explored the relationship between depth and macrophyte biomass.

To the best of the authors' knowledge, the application of ELCOM-CAEDYM for modelling urban stormwater ponds' hydrodynamics and water quality is limited to the study conducted by Nakhaei et al. (2018, 2021). Nakhaei et al. (2018) employed ELCOM to simulate the hydrodynamics of three stormwater ponds in Edmonton. The study found that ELCOM was sensitive to atmospheric stability, albedo, and attenuation coefficient. Additionally, Nakhaei et al. (2021) calibrated the CAEDYM model for two stormwater ponds, providing a subset of calibrated parameters. They proposed these parameters could be used to model nutrient dynamics and trophic states in similar stormwater ponds without further calibration. However, the model's inability to accurately simulate total chlorophyll-a raises concerns about the applicability of the suggested parameters in other ponds.

1.2 **OBJECTIVES AND STRUCTURE OF THE THESIS**

The objectives of this study are as follows:

(i) To evaluate the ability of ELCOM-CAEDYM to model algae biomass in the South Terwillegar Towne2 (ST2) stormwater pond, by focusing on total chlorophyll-a (TCHLA). However, this evaluation also includes other state variables such as temperature, dissolved oxygen, and nutrients, which influence algae growth.

(ii) To perform a sensitivity analysis to examine the impact of model parameters on the simulated state variables, particularly TCHLA.

(iii) To analyze the sensitivity of the calibrated model to boundary conditions, including flow, nutrient, wind, and temperature, as well as to depth and bathymetry.

This study distinguishes itself from previous research due to its emphasis on the urban stormwater pond scale, rigorous calibration and validation based on extensive field measurements, as well as a thorough sensitivity analysis of the model to various parameters and input data.

The thesis is structured into six chapters. Following this introductory chapter, Chapter 2 provides a description of the South Terwillegar Towne2 (ST2), Terwillegar Towne2 (TT2), and Silverberry4 (SB4) stormwater ponds. It also outlines the fieldwork conducted and the data collected and processed for various aspects of the study. Chapter 3 focuses on the reverse level-pool routing method used to estimate inflow, a crucial boundary condition for ELCOM-CAEDYM modeling. This chapter quantifies the inherent error associated with the reverse level-pool routing and describes a filtering approach to mitigate its magnitude. The available inflow measurements from the SB4 and TT2 ponds are utilized to evaluate the effectiveness of the proposed approach for estimating inflow into the ST2 pond.

In Chapter 4, the ELCOM-CAEDYM is used to simulate the hydrodynamics and water quality of the ST2 pond. The chapter details the calibration and validation processes. Additionally, a sensitivity analysis of the ELCOM-CAEDYM model is conducted to identify the most influential model parameters. Following this, Chapter 5 defines multiple scenarios by altering boundary conditions of the ST2 model, including depth, inflow rates, nutrient loading, wind speed, and air temperature. The calibrated model is then used to assess the impact of each scenario on the state variables that determine the water quality of the pond. Special attention is given to total chlorophyll-a, as a key indicator of algae biomass and overall water quality. Finally, Chapter 6 summarizes the results of the study and provides conclusions.

Chapter 2. STUDY AREA, FIELD MEASUREMENTS AND DATA PROCESSING

This chapter describes the characteristics of the study stormwater ponds, the field measurements conducted to collect the required data, and the processing of collected data.

2.1. DESCRIPTION OF STUDY STORMWATER PONDS

Three stormwater ponds, namely Silverberry4 (SB4), Terwillegar Towne2 (TT2), and South Terwillegar2 (ST2), were selected for this study. All three ponds are located in residential areas of Edmonton. Figure 2-1 illustrates the schematic views of the ponds, along with the locations of their inlets and outlets. Each study pond has only one outlet and two to four inlets with varying inflows contributions. Table 2-1 presents the basic properties of the study ponds.

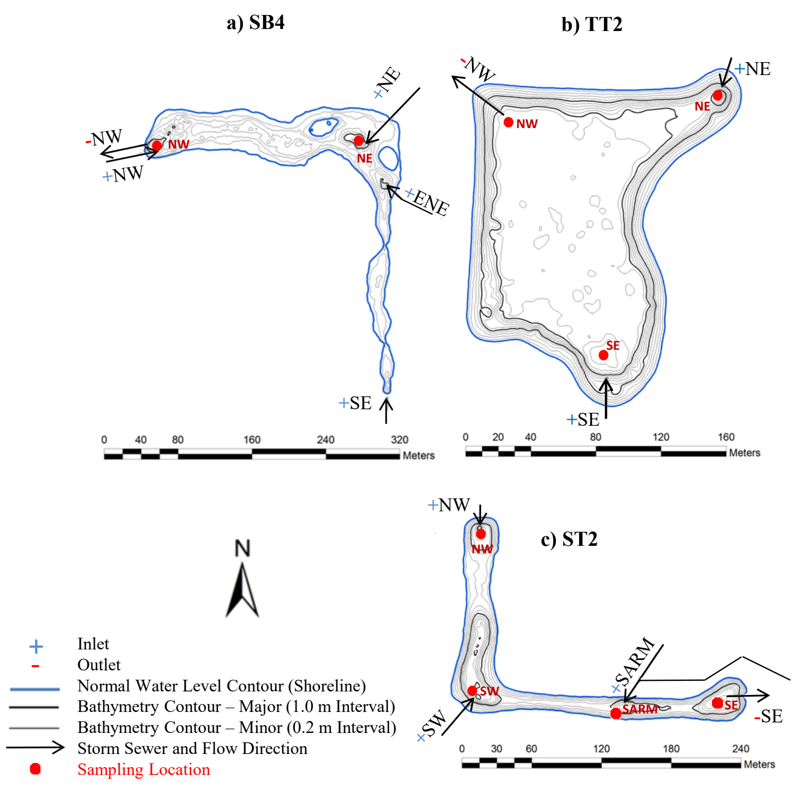

Figure 2-1: Schematic view of study stormwater ponds; a) Silverberry4 (SB4), b) Terwillegar Towne2 (TT2), and c) South Terwillegar2 (ST2).

Table 2-1: Basic properties of study ponds.

Study Pond	Average Depth (m)	Surface Area (ha)	Volume (m^3)	Basin Area (ha)	Location of Outlet	Location of Inlet	Inlet Flow Contribution (%)
SB4	0.44	1.82	8,100	92.9	North-West (NW)	South-East (SE)	60.0
						North-East (NE)	25.3
						East of the pond toward the North (ENE)	12.4
						North-West (NW)	2.3
TT2	1.78	2.18	39,000	91.4	North-West (NW)	North-East (NE)	78.5
						South-East (SE)	21.5
ST2	0.85	0.90	7,700	40.8	South-East (SE)	North-West (NW)	74.5
						South arm (SARM)	22.4
						South-West (SW)	3.1

2.2. FIELD MEASUREMENTS AND DATA PROCESSING

The fieldwork conducted from October 2013 to October 2015 was part of this current research project, which was undertaken through collaboration with other students and researchers. The fieldwork involved surveying, instrumentation installation, and data monitoring. Water quality and precipitation data were measured during the open-water seasons. Additionally, direct measurements of inflows and outflows were conducted from January to May 2015 at the SB4 and TT2 ponds. Subsets of collected data were used in this study as needed. Data collected at SB4 and TT2 were used to validate the reverse level pool method outlined in Chapter 3, while data collected at the ST2 pond were utilized for hydrodynamics and water quality modeling, as discussed in Chapters 4 and 5, respectively.

2.2.1. Bathymetry

To define the bathymetry of the study ponds, as well as documenting the position of the installed instruments, a Real Time Kinematic Global Positioning System (RTK-GPS) survey system [Trimble, USA] and SONARMITE-BT® depth sensor [Seafloor, CA] were used. First, area calibrations were created using five to six Alberta Surveying Control Markers (ASCM) located in the vicinity of the study ponds, in the Silverberry and Terwillegar areas. Then, without moving the RTK base station, and using the local calibration, at least four fixed accessible local benchmarks (e.g., top of manholes) were selected around each pond. Subsequently, the elevations and coordinates of all the surveyed points were referred to the ASCMs. Each pond's bathymetry was surveyed nearly up to the high-water level. For surveying the pond, the depth sounder was mounted on a boat. However, wading was required both for sounding the areas shallower than 0.35 cm, and verifying echo sound readings. Surveyed data was processed using ESRI ArcGIS® software [Environmental Systems Research Institute, USA] for model setup, and to develop the level-volume and level-area relationship. Figure 2-2 illustrates ST2 hypsometric curves (level-volume and level-area relationships). SB4 and TT2 hypsometric curves are presented in Appendix A, Figure A-1 and Figure A-2, respectively.

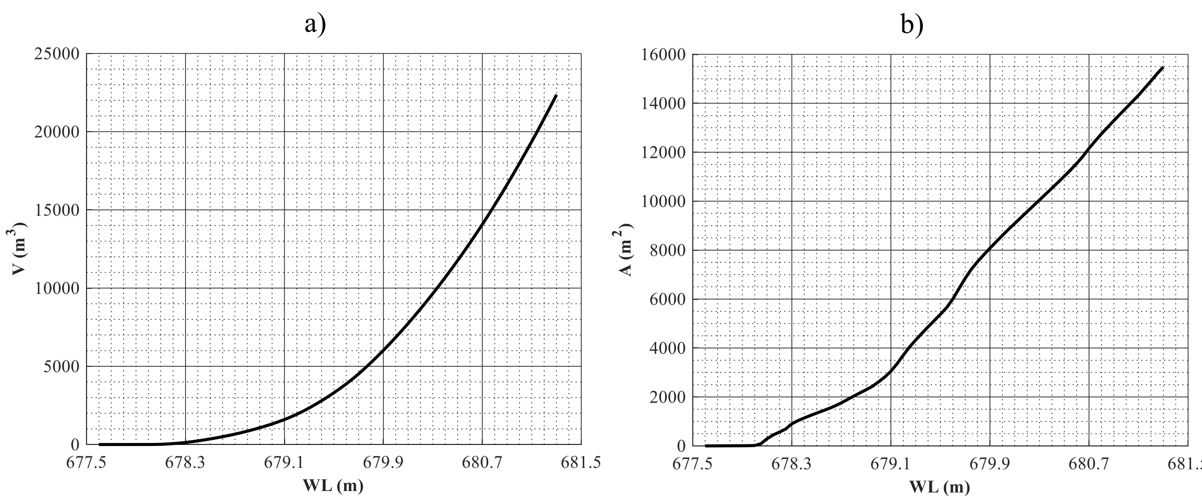

Figure 2-2: Hypsometric curves of ST2: a) Water level versus Volume b) Water level versus area.

2.2.2. **Meteorological Data**

In order to acquire meteorological data, at each study pond a weather station was installed at an elevation of approximately 10 m above the water surface on a hinged flagpole. The weather stations were equipped with HOBO U30 weather station data loggers [Model U30-NRC-000-10-S100-000, ONSET, USA] and the following sensors:

- Temperature and relative humidity [Model S-THB-M002], with accuracy of ±0.21°C for temperature range between 0° to 50°C, and ±2.5% from 10% to 90% RH typical to a maximum of ±3.5% including hysteresis at 25°C.
- Barometric pressure [Model S-BPB-CM50], ±3.0 mbar over full pressure range (i.e., 660 to 1070 mbar) at 25°C with maximum error of ±5.0 mbar over -40° to 70°C.
- Wind speed and wind direction [Model S- WSB-M003], with accuracy ±1.1m/s or ±4% of reading whichever is greater over measurement range of 0 to 76 m/s.
- Pyranometer [Model S-LIB-M003], with accuracy of ±10 W/m2 or ±5%, whichever is greater in sunlight.
- Rain Gauge Smart sensor [Model S-RGA-M002]. The data logger recorded data every 10 minutes from each sensor. Measures rainfall with intensity up to five inches per hour with a resolution of 0.01 inch, and 1% accuracy for rainfall rates up to 1"/hour.

The weather stations underwent routine inspections, with data retrieval both at the beginning and end of the open-water season, as well as one or two times during the open-water. Rainfall was measured only during the open-water seasons. Examples of the meteorological data measured at ST2 weather station are presented here: wind speed and direction in Figure 2-3, rainfall intensity in Figure 2-4, and air temperature in Figure 2-5. Additional examples are provided in Appendix A, Figure A-3 to Figure A-5.

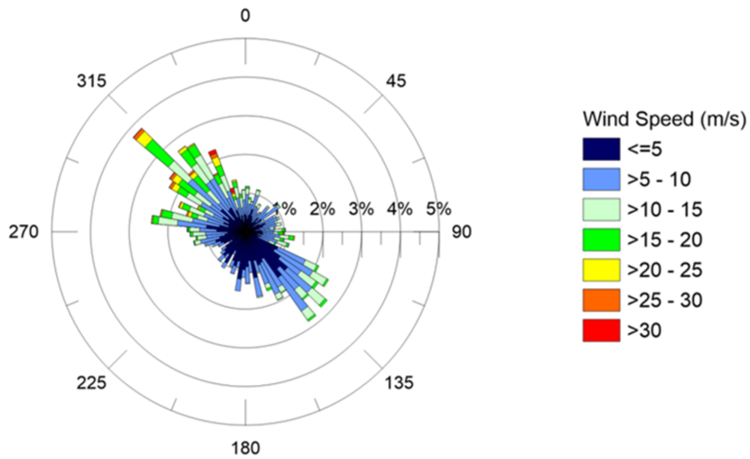

Figure 2-3: Wind speed and direction illustrated as a windrose, measured at ST2 from October 2013 to October 2015.

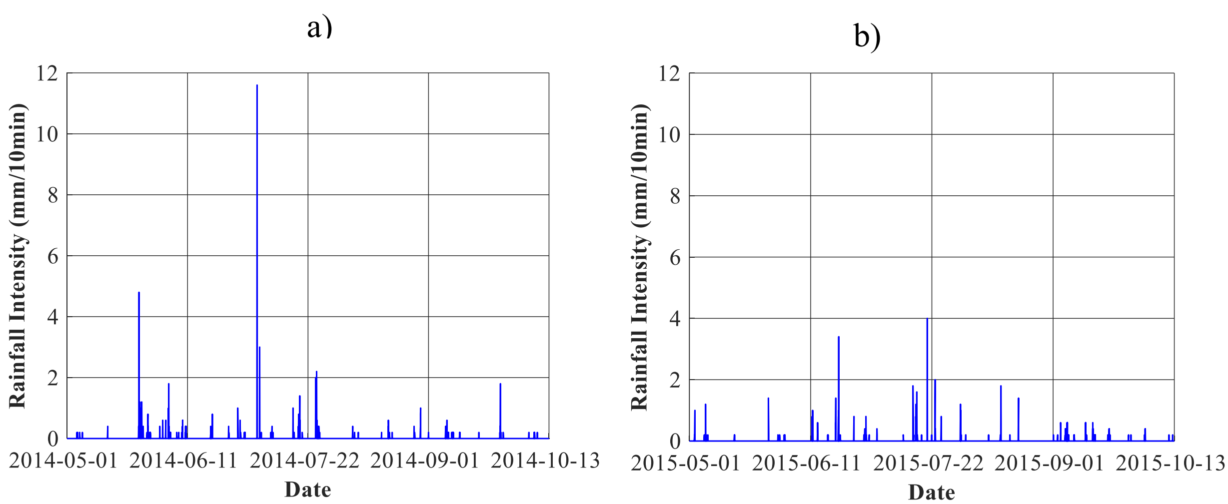

Figure 2-4: Rainfall intensity at ST2 measured during open-water season: a) 2014 and b) 2015.

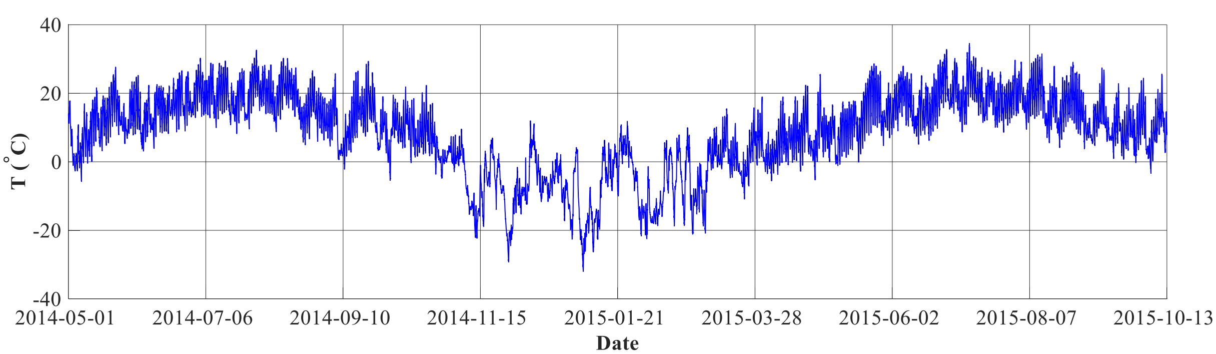

Figure 2-5: Air temperature measured at 10-minute intervals from the weather station installed at ST2.

2.2.3. **Biogeochemical Data Collection**

Biogeochemical data were collected from the study ponds to support the water quality modelling objectives of this study. Various datasets were collected through in-pond instrumentation, outlet structure instrumentation, profiling, and water quality sampling. As depicted in Figure 2-1, all the sampling locations are near the inlets and outlets of the study ponds.

2.2.3.1 In-Pond Instrumentation

From October 2013 to October 2015, in-pond instruments collected data water level (WL), water temperature (T), dissolved oxygen (DO), and total chlorophyll-a (TCHLA). Instruments were grouped into measurement stations and installed at the sampling locations. Each measurement station comprised a steel cable, fixed to a cinderblock anchor and a buoy to hold it vertically. Each station was equipped with different numbers and types of sensors as listed below:

- Divers (SWS-TD and SWD-CTD)(©Schlumburger) to measure water pressure with accuracy of 0.5 to 1.0 cm H2O and temperature with accuracy of 0.1°C,
- HOBO-Tidbit (©Onset) to measure temperature with accuracy of 0.2°C,
- RBR-Duo (©RBR) to measure temperature with accuracy of 0.002°C and dissolved oxygen with accuracy of 2% O_2 saturation, and
- EXO_2 [YSI Inc., a Xylem brand, U.S.A.] to measure temperature with accuracy of 0.01°C, dissolved oxygen with accuracy of 1% of reading, and chlorophyll-a with accuracy of 0.01 mcg/L.

The sensors were attached to the cable and suspended at various depths. Figure 2-6 illustrates three measurement stations before deployment and one after deployment. Figure 2-6a depicts a measurement station containing several HOBO-Tidbits at different elevations as well as an EXO2. On the top of the buoy a HOBO-Tidbit was installed to measure the water temperature close to the water surface. Figure 2-6b shows another measurement station equipped with two RBR-Duo and a diver. After attaching the sensors, the sensors height referenced to the bottom of cinder block was measured, as presented in Figure 2-6c. Figure 2-6d shows a measuring station after deployment in the pond. Details on installation and retrieval dates, types and elevations of all sensors installed at sampling locations in the study ponds are presented in Appendix A, Table A-1 to Table A-3.

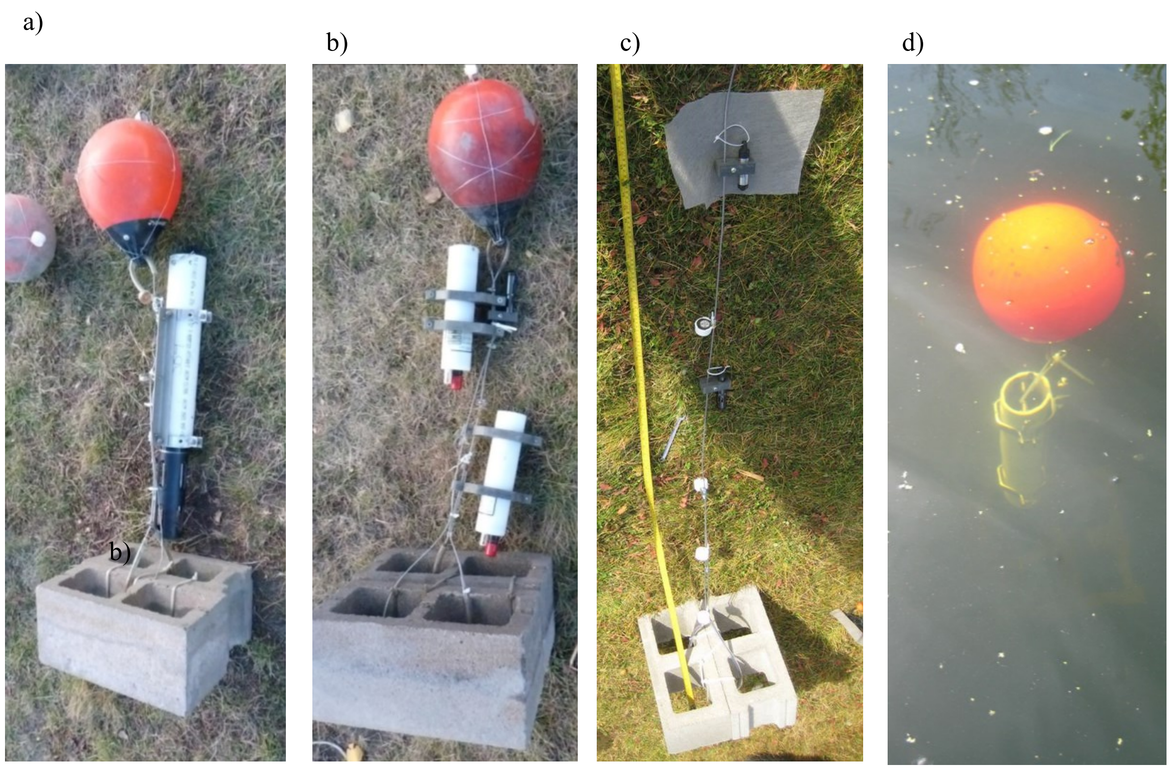

Figure 2-6: Example of measurement stations, before deployment (panels a, b and c) and after deployment (panel d).

2.2.3.1 Outlet Structure Instrumentation

Two divers were placed in the outlet structure of each study pond at different depths and programmed to measure the water level at intervals of 3 or 6 minutes. These data, along with those acquired from all in-pond divers and manual water surface elevation measurements, were then used to construct water level time series at each study pond.

2.2.3.1 Profiling

During the open-water season of 2015, in addition to the point measurements taken by the moored sensors, bi-weekly vertical profiles of temperature, dissolved oxygen and total chlorophyll-a were measured. During profiling, an EXO2 was slowly lowered from the surface to the bed of the ponds and then raised back up. Only the profiling data from ST2 that have been used in this study is presented here. In this pond, weekly profiling was conducted at all the measuring locations, i.e., NW, SW, SARM and SE.

2.2.3.1 Water Quality Sampling

Starting in October 2013, water samples were taken from sampling locations of all the study ponds, but only the ST2 data used in this study is presented here. During open-water seasons, water samples were collected bi-weekly using a Van Dorn sampler. Samples were typically collected near the surface and bed to capture vertical variations. In 2014, surface samples were taken at the sampling locations at depths of 0.5-1.0 m, while in 2015 samples were taken from both the surface (0.5-1.0 m deep) and the bottom (1.5-2.0 m deep). The water samples were stored in 1 L Nalgene© plastic bottles, either packed on ice or refrigerated, and transported to the Biogeochemical Analytical Service Laboratory (BASL) at the University of Alberta within 24 hours. The BASL holds ISO/IEC 17025 accreditation for specific tests from the Canadian Association for Laboratory Accreditation (CALA), a recognized accreditation body in Canada for ISO/IEC 17025 standards. The complete list of accreditations are presented in the BASL website: https://basl.biology.ualberta.ca/. Table A-4 in Appendix A presents some examples of confidence intervals for parameters analyzed at BASL. The .water samples were analysed for biochemical parameters such as Ammonia (NH3), nitrite+nitrate (NO2+NO3), total nitrogen (TN), total dissolved nitrogen (TDN), total kjeldahl nitrogen (TKN), soluble reactive phosphorous (SRP), total phosphorous (TP), total dissolved phosphorous (TDP), total particulate phosphorous (TPP), dissolved organic carbon (DOC), dissolved inorganic carbon (DIC), total chlorophyll-a (TCHLA). Additionally, water transparency was measured at each location using a Secchi disk. Information on the date, location, and results of analysed water quality samples for ST2 are presented in Appendix A, Table A-5 and Table A-6.

Figure 2-7 illustrates the measured data collected at the NW sampling location of ST2 during the open-water season of 2015. The data were collected using in-pond instruments (depicted as a sequence of horizontal dots), profiling (depicted as a sequence of vertical dots), or discrete water samples (depicted as single dots). Depths are referenced to the outline of the pond, which is 1.68 m above the normal water level (NWL). Additional plots of measured T, DO, TCHLA, TP and TN are presented in Appendix A, Figure A-13 to Figure A-21.

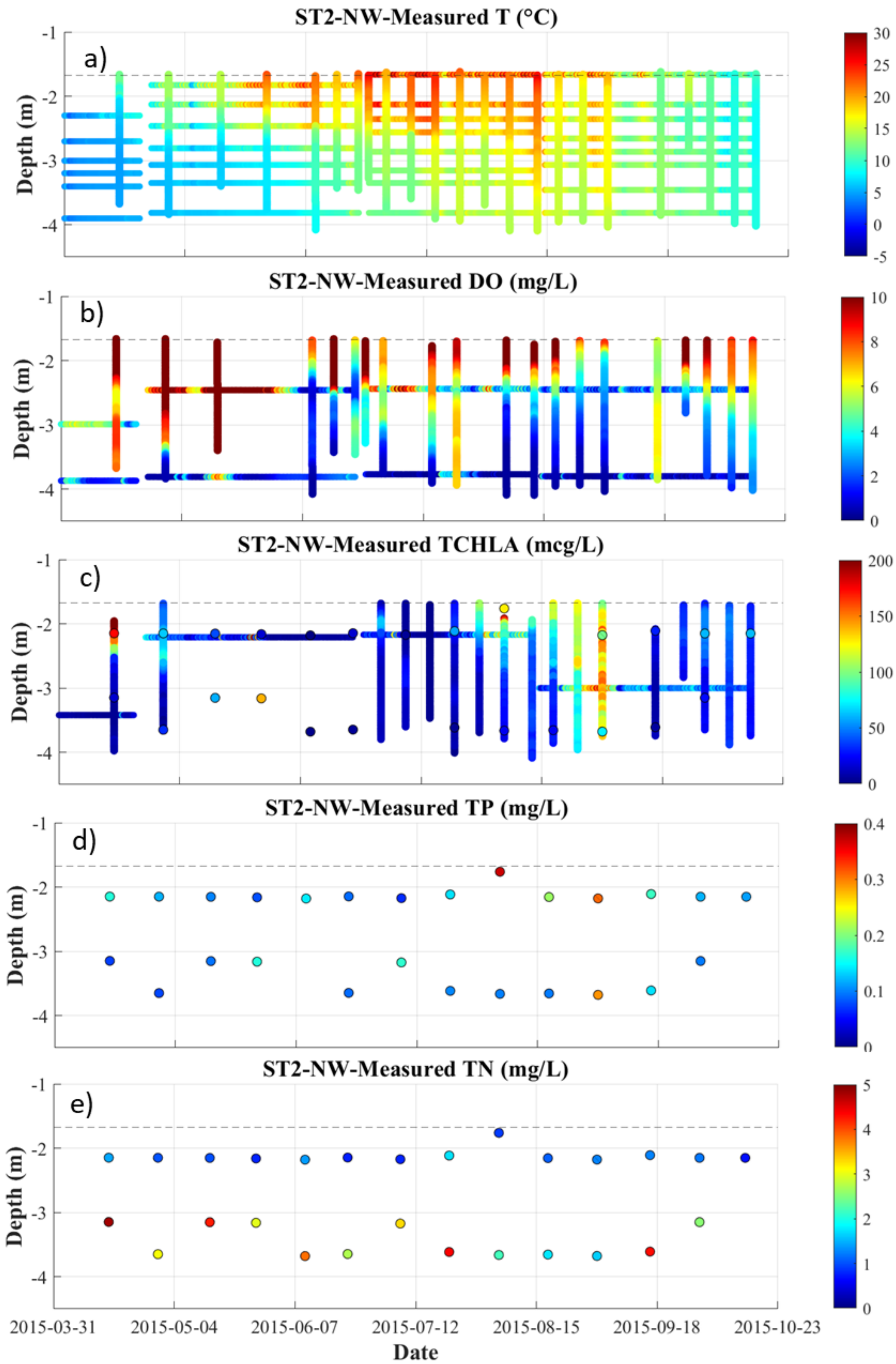

Figure 2-7: Measured water quality variables at the NW sampling location of ST2: a) water temperature, b) dissolved oxygen, c) total chlorophyll-a, d) total phosphorus, and e) total nitrogen. The dashed lines represent the normal water level at elevation 680.07m.

2.2.4. Algae Sampling and Taxonomic Analysis

In addition to water sampling, algae samples were collected during the open-water season to allow taxonomic analysis of phytoplankton in the study ponds. Depth-integrated water column samples were taken using a custom-made algae sampler depicted in Figure 2-8a and b. The sampler was a transparent plastic cylinder with a height of 1.8 m and diameter of 10 cm. The cylinder was clamped to an L-shaped bracket so that the lower end of the cylinder was kept 20 cm above the pond bottom.

At each sampling location, the algae sampler was slowly lowered into the pond to minimize mixing of the water column until either the sampler was completely submerged or the bracket foot reached the bottom of the pond. A stopper was then inserted into the top of the cylinder. Subsequently, the sampler was slowly lifted and a second stopper was inserted into the lower end of the cylinder. The depth of water inside the sampler was measured, and the captured water was transferred to sample bottles. If floating algae (scum) was present in the pond (e.g., Figure 2-8c), scum samples were also taken in a glass sampling jar. The samples were then preserved in the laboratory by adding formalin to the jars. Identification of algae species was conducted by Dr. Edyta Jasinska, an aquatic ecologist at the University of Alberta. Taxonomic results are presented in Appendix A, Table A-7.

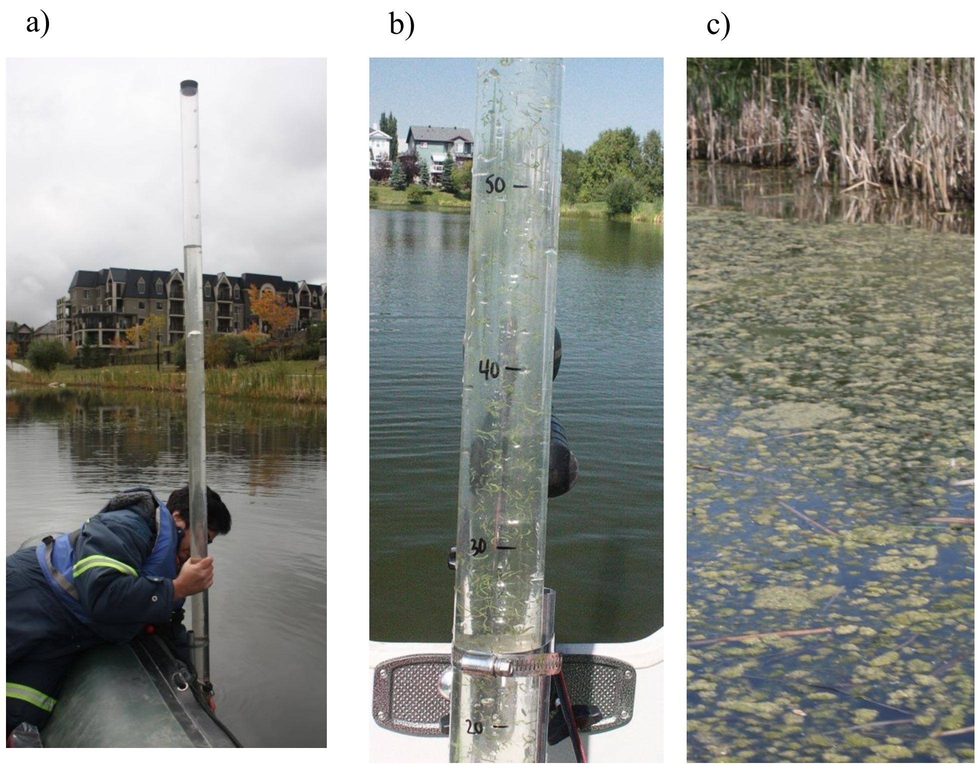

Figure 2-8: Algae sampling: a) lowering algae sampler into the pond, b) view of floating algae in an algae sampler, and c) floating scums on ST2.

2.2.5. **Outlet Structures and Rating Curves**

Outflows from the study ponds are controlled either by weirs or orifices in the outlet structures. The 'designed' dimensions of outlet structures, as documented in design reports, were supplied by the City of Edmonton. However, visual assessments and field measurements indicated some modifications and adjustments over time. Therefore, the 'as-built' dimensions of outlet structures were measured directly during fieldwork. Due to safety concerns and difficulties in accessing the outlet structure of SB4, this structure was surveyed in cooperation with a crew from the City of Edmonton.

Figure 2-9 to Figure 2-11 show the as-built outlet structures of TT2, SB4, and ST2, respectively. TT2 outlet is a contracted weir (i.e., the weir crest does not extend to the side walls) with a width of 1.041 m, and a circular orifice with a diameter of 0.292 m. The outlet structure at SB4 consists of a rectangular orifice with a width of 0.343 m and a height of 0.100 m, as well as a rectangular weir with a crest at the high water level. The outlet structure at ST2 includes a rectangular orifice with a width of 0.305 m and height of 0.145 m, along with a rectangular weir with a crest at the high water level.

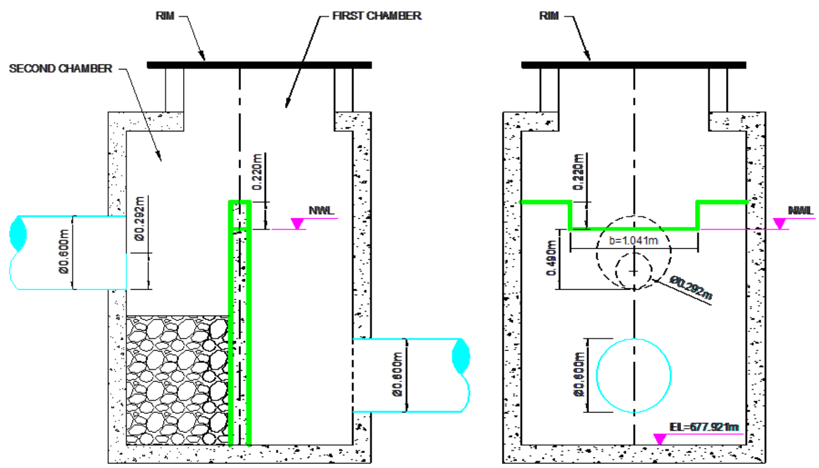

Figure 2-9: Outlet structure at TT2. Left: Side view, Right Front view

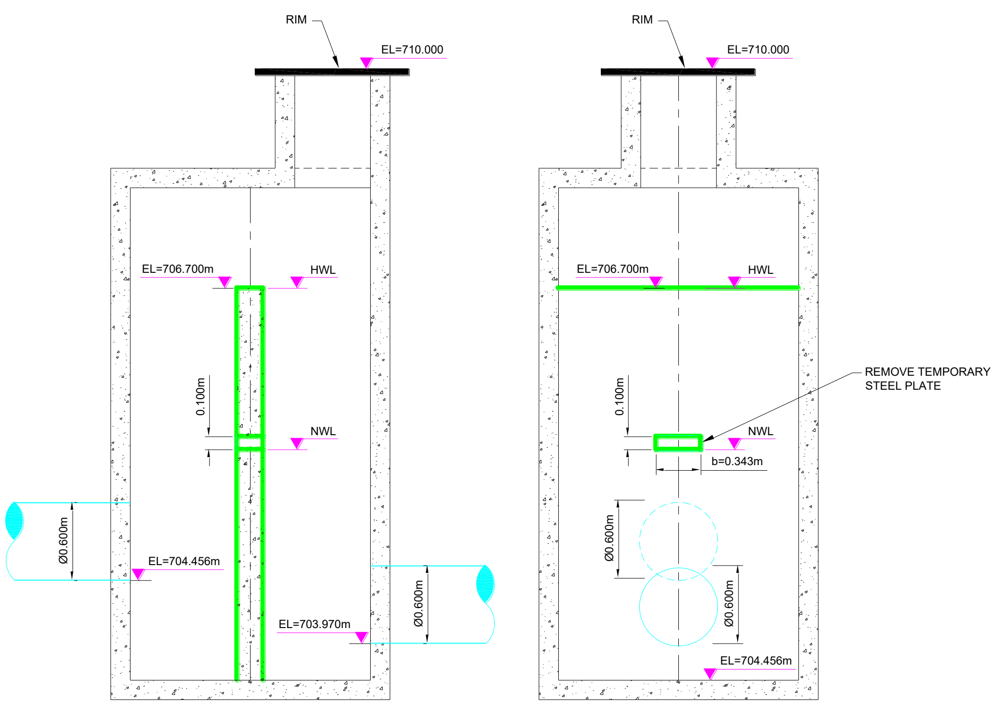

Figure 2-10: Outlet structure at SB4. Left: Side view, Right Front view.

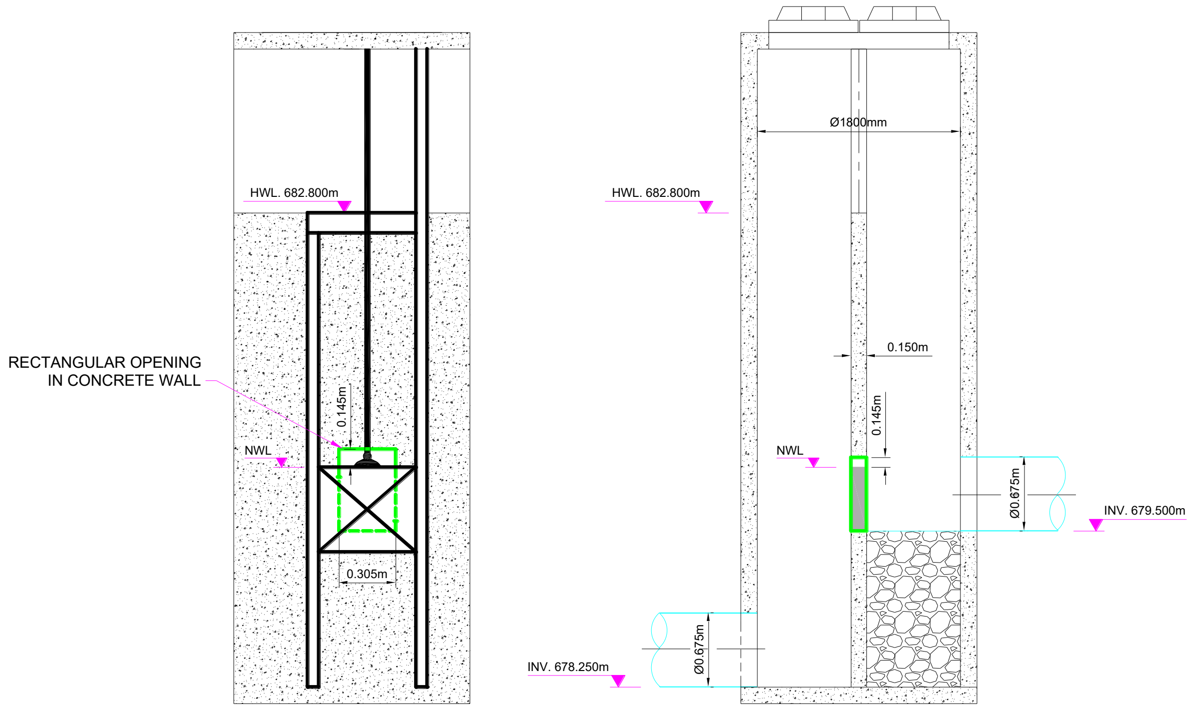

Figure 2-11: Outlet structure at ST2. Left: Side view, Right Front view.

The 'as-built' rating curves, presented in Figure 2-12 to Figure 2-14, were derived from the as-built dimensions (details in Appendix A). As expected, the as-built rating curves differ from those reported by the City of Edmonton.

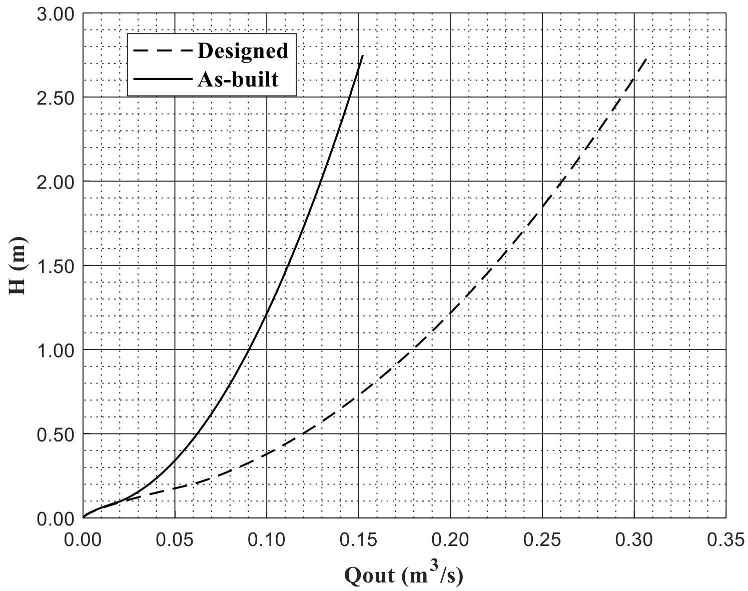

Figure 2-12: Designed and As-Built rating curves for SB4.

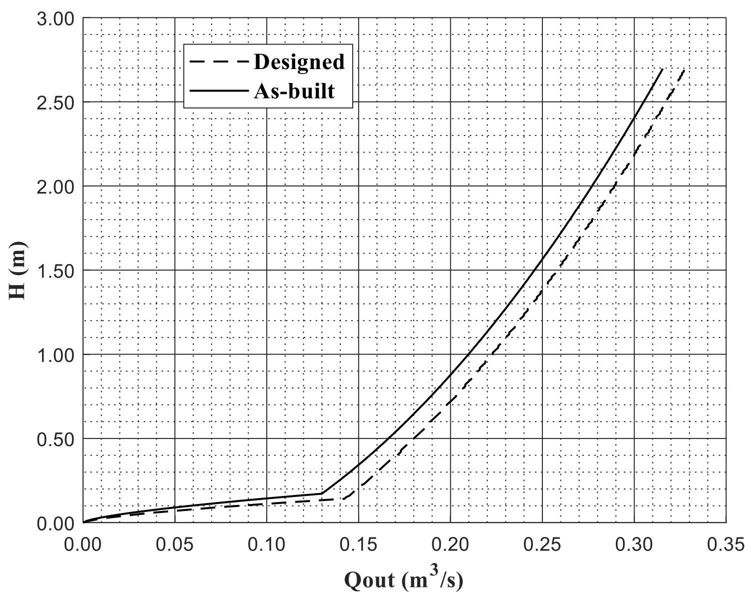

Figure 2-13: Designed, and As-Built rating curve for TT2.

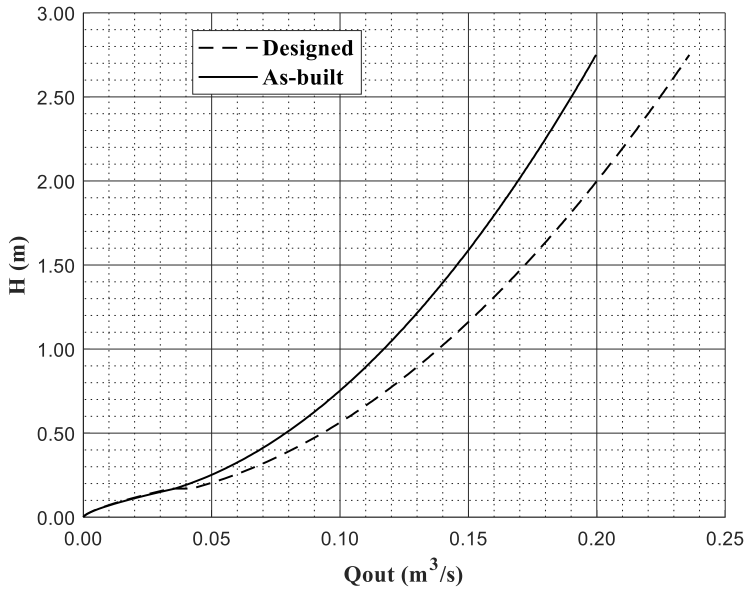

Figure 2-14: Designed and As-Built rating curve for ST2.

2.2.6. **Inflow and Outflow Measurements**

In the SB4 and TT2 ponds, between January 2015 and May 2015, inflows and outflows were directly measured by the City of Edmonton. The flow rates were measured at five-minute intervals using ISCO 2150® area-velocity flowmeters [TELEDYNE ISCO, USA] mounted in the inlet and outlet pipes. The flowmeter accuracy is ±0.003 m for water levels of 0.01 m to 3.05 m and ±0.03 m/s for velocities of -1.5 m/s to +1.5 m/s. Inflows were measured from early January to late May 2015, although the flowmeter at the SE inlet of TT2 stopped recording from late February to late April 2015. The normal ratio method (Chow et al. 1988) was used to fill this gap in the measured inflows data. Examination of measured inflow data showed that the total inflow at SE inlet were 45% of the NE inflow. Therefore, the inflow gap at SE inlet was estimated by multiplying the the measured inflows at the NE inlet by 0.45. The pond outflows were recorded from late March 2015 at SB4 and from late April 2015 at TT2 and continued to late May 2015. Figure A-6 to Figure A-9 in Appendix A illustrate the measured inflows and outflows at SB4 and TT2.

2.2.7. **Water Level Elevations**

The time series of water levels in each pond were determined by averaging the levels measured by all divers in that pond. Since the divers recorded the total pressure, barometric compensation was required to convert their readings to water levels. Details are outlined in Appendix A, Section A.5. Furthermore, during the open-water season, water level elevations were measured biweekly at a minimum of three locations in each pond using an AC 2s® automatic level [Nikon, Japan]. These measurements served to validate the accuracy of divers' readings.

2.2.8. **Normal Water Level**

The normal water level (NWL) is defined as the threshold above which outflows occur from the pond. This level corresponds to the elevation of the weir crest (e.g., at TT2) or the bottom of the rectangular orifice (e.g., at SB4). Therefore, accurate determination of NWL is essential for estimation of outflows. Attempts were made to directly measure NWL in the field; however, due to challenges in accessing the outlet structures and safety concerns, the measurements were not sufficiently accurate. Therefore, NWL was estimated indirectly through trial and error. Based on field measurement and observed water levels, a plausible range (conservatively set to be 10 cm) for NWL was established for each pond. NWL was then varied within this range in one-mm increments, and the corresponding outflows were calculated.

Due to lack of flow measurements at ST2, its NWL was estimated using hydrodynamic modeling, which is discussed in Chapter 4. For the SB4 and TT2 ponds, NWL was estimated by minimizing the difference between observed and estimated outflows based on the root mean square error (RMSE) defined as:

$$RMSE = \sqrt{\frac{1}{n}\sum_{i=1}^{n}\left(\varphi_i - \varphi_i^0\right)^2} \qquad (2\text{-}1)$$

where n is the number of observed data, φ represents the estimated variable (for example outflow), and φ_i and φ_i^0 are the ith observed and estimated variables, respectively. Using this approach the RMSE was minimized at SB4 and TT2 at NWL = 706.342 m and NWL = 681.443 m, respectively. Figure 2-15 and Figure 2-16 indicate that these normal water levels yield reasonable agreement between measured and estimated outflows at SB4 and TT2. It should be noted that due to the failure of the flowmeter installed at the outlet pipe of TT2, outflow measurement was limited to a single storm event in early May 2015. The dotted blue line in Figure 2-16 denotes erroneous readings, attributed to the malfunctioning of the flowmeter, which were not used in the estimation of NWL.

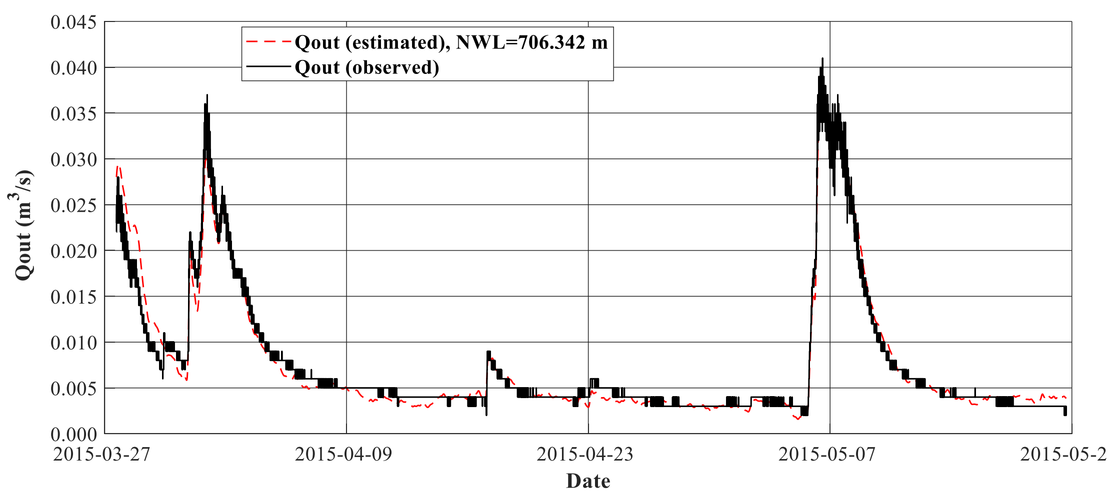

Figure 2-15: Comparison of measured and estimated outflows at SB4.

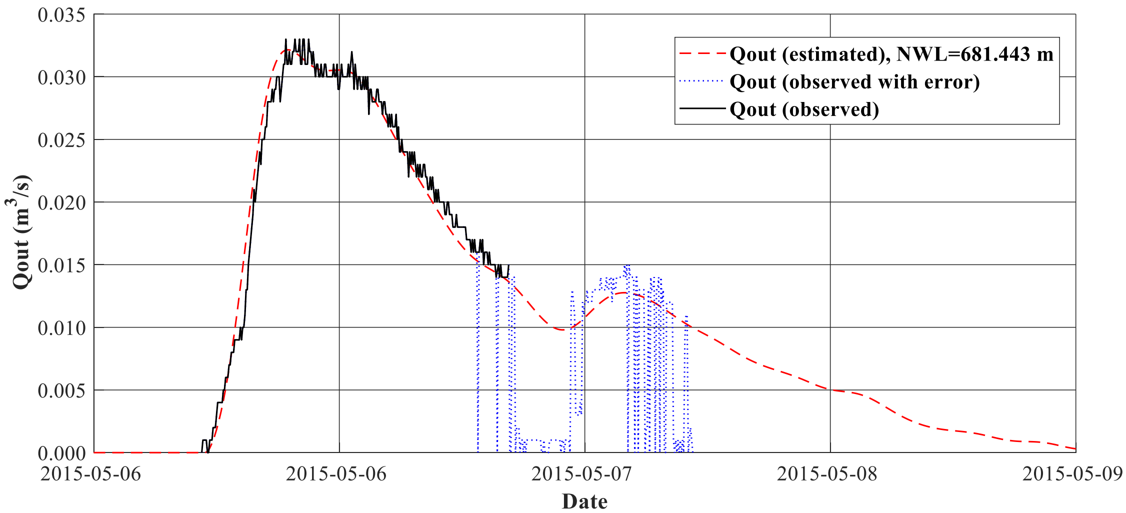

Figure 2-16: Comparison of measured and estimated outflows at TT2.

Chapter 3. EVALUATION OF THE PERFORMANCE OF REVERSE LEVEL POOL ROUTING IN ESTIMATION OF INFLOWS INTO STORMWATER PONDS IN THE CITY OF EDMONTON

3.1. INTRODUCTION

Knowing the rate and variability of flows entering and exiting stormwater ponds is essential for hydrodynamics and water quality modelling. Therefore, either direct measurement or indirect estimations of inflows and outflows are required. However, the installation, maintenance, and operation of flow measuring devices are costly and time-consuming (Perumal et al. 2010). Moreover, flowmeters may not be sufficiently accurate during low and high-flow conditions. Additionally, other factors such as sedimentation in the inlet structure impacts the accuracy of measured inflows. As a result, continuous flow measurement into and out of stormwater ponds is not commonly available. Furthermore, components such as overland runoff, seepage, and groundwater that do not pass through the inlet and outlet structures cannot be directly measured. Therefore, the net flux of water into the stormwater ponds may not be accurately quantified solely by flow measurements (Deng et al. 2015). Alternatively, some studies suggested that inflows can be estimated using the principle of mass balance (i.e., the continuity equation) (e.g., D'Oria and Tanda 2012; Leonhardt et al. 2014). This approach requires data such as time series of water levels and the level-volume relationship.

In reservoirs, changes in volume (storage) are determined by the difference between rates of all the inflows and outflows. Reservoir storage and outflows through the outlets are determined by water level, as prescribed by the level-volume relationship and characteristics of the outlet structures. Thus, in theory, if either inflows or outflows are measured, the other can be estimated using the principle of mass balance. When inflows are known, the outflow hydrograph can be predicted using the 'level pool routing' method. This 'hydrologic routing' is based on the continuity equation and the 'level pool' approximation, which assumes the water surface in the reservoir is horizontal (Chow 1959; Fenton 1992; Ponce 1989; Yevdjevich 1959).

Conversely, when water levels (and hence outflows) are known, the inflow hydrograph can be calculated using the 'reverse level pool routing' method (e.g., Deng et al. 2015; Leonhardt et al. 2014; Zoppou 1999). While both direct and reverse routings are developed based on the same governing equation and assumptions, the reverse method is an ill-posed problem, meaning it is highly sensitive to noise in the input data (Dooge and Bruen 2005; Koussis and Mazi 2015; Szymkiewicz 1993; Todaro et al. 2019). Noise in the water level measurements, whether due to measurement errors, electronic noise or water level fluctuations induced by environmental factors such as wind, lead to significantly larger oscillations in the estimated inflows by reverse level pool routing (i.e., back-routed inflows) (e.g., Deng et al. 2015; Koussis and Mazi 2015; Leonhardt et al. 2014; Zoppou 1999). Nevertheless, estimating inflows though reverse routing is necessary in many practical applications, such as reservoir operations (Bruen and Dooge 2007; D'Oria and Tanda 2012; Deng et al. 2015; Dooge and Bruen 2005; Fenton 1992), flood management (Badfar et al. 2021; Dooge and Bruen 2005; Tayfur and Moramarco 2022), and water quality modeling (Koussis and Mazi 2015; Pagendam and Percival 2015).

Depending on the magnitudes of the oscillations in the back-routed inflows compared to the true inflows, reverse routing may generate non-physical negative inflows. Most studies employing reverse routing have dealt with high-flow events or reservoirs with continuous inflows (e.g., D'Oria et al. 2012; Todaro et al. 2019; Zoppou 1999), where the relative significance of oscillations in the estimated inflows is less important. However, inflows into urban stormwater ponds, such as those considered in this study, are frequently zero or near zero. Hence, the spurious oscillations can lead to negative inflows more frequently.

Based on a hypothetical problem, Zoppou (1999) concluded that oscillations in the predicted inflows can be removed by employing the centred explicit scheme without filtering water levels.

However, implementing the same schemes in this study led to oscillatory inflows. Other studies have also noted that the centred explicit schemes alone cannot prevent spurious oscillations (e.g., Aldama and Aguilar 2007). Applying a filter to the measured water levels before employing the reverse level pool method has been suggested as a measure to reduce the magnitude of oscillations in the back-routed hydrograph (e.g., Aldama and Aguilar 2007; Deng et al. 2015; Koussis and Mazi 2015; Leonhardt et al. 2014; Wang et al. 2014). However, the smoothing effect of filtering also attenuates the peaks and distorts the shape of the inflow hydrograph, indicating a trade-off between noise reduction and preservation of inflow hydrograph characteristics. Since filtering water levels does not completely remove inflow noise and negative values, some studies (e.g., Koussis et al. 2012) have further post-processed the estimated inflows, either by additional filtering or by removing negative inflows and rescaling the positive inflows to maintain the mass balance.

The objective of this chapter is to evaluate the performance of the reverse level pool routing approach to estimate inflows. The chapter first quantifies the errors in the back-routed inflows and then explores the impact of filtering water levels on the estimated inflows. Limited inflow measurements at the Terwillegar Towne 2 (TT2) and Silverberry 4 (SB4) ponds provided confidence in this approach, so it was employed to estimate inflows into South Terwillegar 2 (ST2).

3.2. METHODOLOGY

3.2.1. Governing Equations and Numerical Schemes

The governing equation is the continuity equation, which states the change in volume is controlled by the net flux of water into the system:

$$\frac{dV}{dt} = I - O \tag{3-1}$$

where, V (m³) is the volume of water, t (s) indicates time, I (m³/s) represents flow entering the pond, including inflow through the inlets, overland flow, and direct precipitation over the pond, and O (m³/s) represents flow exiting the pond, including outflows through the outlets and evaporation. As discussed in Chapter 2, precipitation was directly measured at the weather stations, and depth of evaporation was obtained from published climatological values for shallow lakes in Edmonton (Alberta Government 2013). Equation (3-1) can be solved given an inflow hydrograph, an initial condition, and the level-volume and level-outflow relationships. This is known as (direct) routing which calculates water levels and outflows. A MATLAB® code utilizing the 'ode45' solver, a 5th-order accurate numerical scheme for solving initial-value differential equations (MathWorks. 2023), was developed for routing of given hydrographs into the study ponds. The water level resulting from routing a hydrograph, whether hypothetical or measured is considered the "exact" water level here.

Figure 3-1a illustrates a hypothetical inflow hydrograph with a peak and duration comparable with the observed values into the SB4 and TT2 ponds. This hydrograph has no base flow and its volume is sufficiently large to cause outflows out of the study ponds with an initial level of 5 cm below the normal water level (NWL). The hydrograph was routed through the study ponds, and the routed water levels at SB4 are shown in Figure 3-1b.

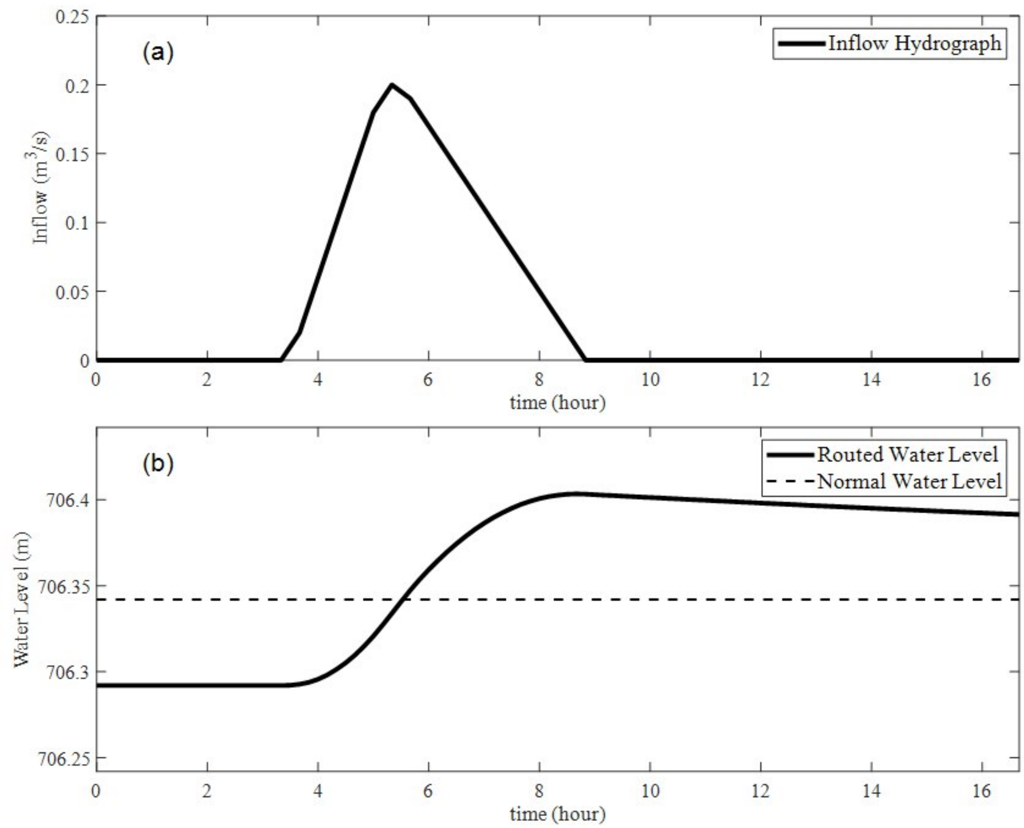

Figure 3-1: a) A realistic hypothetical inflow hydrograph and b) routed water level in the SB4 pond.

For reverse level pool routing, Equation (3-1) was discretized by the centered, forward, and trapezoidal finite difference schemes, as presented in Equations (3-2) to (3-4), respectively:

$$I^n = O^n + \frac{V^{n+1} - V^{n-1}}{2\Delta t} \tag{3-2}$$

$$I^n = O^n + \frac{V^{n+1} - V^n}{\Delta t} \tag{3-3}$$

$$I^n = O^{n-1} + O^n - I^{n-1} + 2\left(\frac{V^n - V^{n-1}}{\Delta t}\right) \tag{3-4}$$

Here the superscript (n) indicates values at time step n (e.g., $I^n = I(t = n\Delta t)$), and Δt is the numerical time step, set at 10 minutes to match the measurement frequency. In these equations, I encompasses the net influx as result of pipe inflows, evaporation, precipitation, groundwater interactions and surface runoff, since their combined influence is already reflected in the change of water level over each time step. The discretized equations were also implemented in the MATLAB programming environment.

To illustrate the noise amplification problem of the reverse level routing, the exact routed water level time series, displayed in Figure 3-1b, was perturbed by normal random noise (ϵ) with a mean of zero ($\mu = 0$) and standard deviation of one ($\sigma = 1$mm). Subsequently, the perturbed inflow time series was determined using the centred, forward, and trapezoidal schemes (Equations (3-2) to (3-4)). Figure 3-2b indicates that the centred scheme is the most accurate of the three, consistent with the findings of Zoppou (1999). Nonetheless, even this scheme suffers from noise amplification. The forward scheme yields more oscillatory inflows compared to the centred scheme, while the oscillations of the trapezoidal scheme are so large that inflows at multiple times exceed the limits of the vertical axis.

The noisy inflows presented in Figure 3-2b were back-routed from a single set of randomly perturbed water levels. To analyze the accuracy of each scheme, a Monte Carlo technique was employed, involving the generation of 10,000 randomly perturbed water level time series and the calculation of their corresponding back-routed inflow time series. Figure 3-3 illustrates the 95% confidence intervals of perturbed inflows at SB4, back-routed by the three discretization schemes. It is obvious that the centered scheme provides the most accurate results, and hence only this scheme was used in this study.

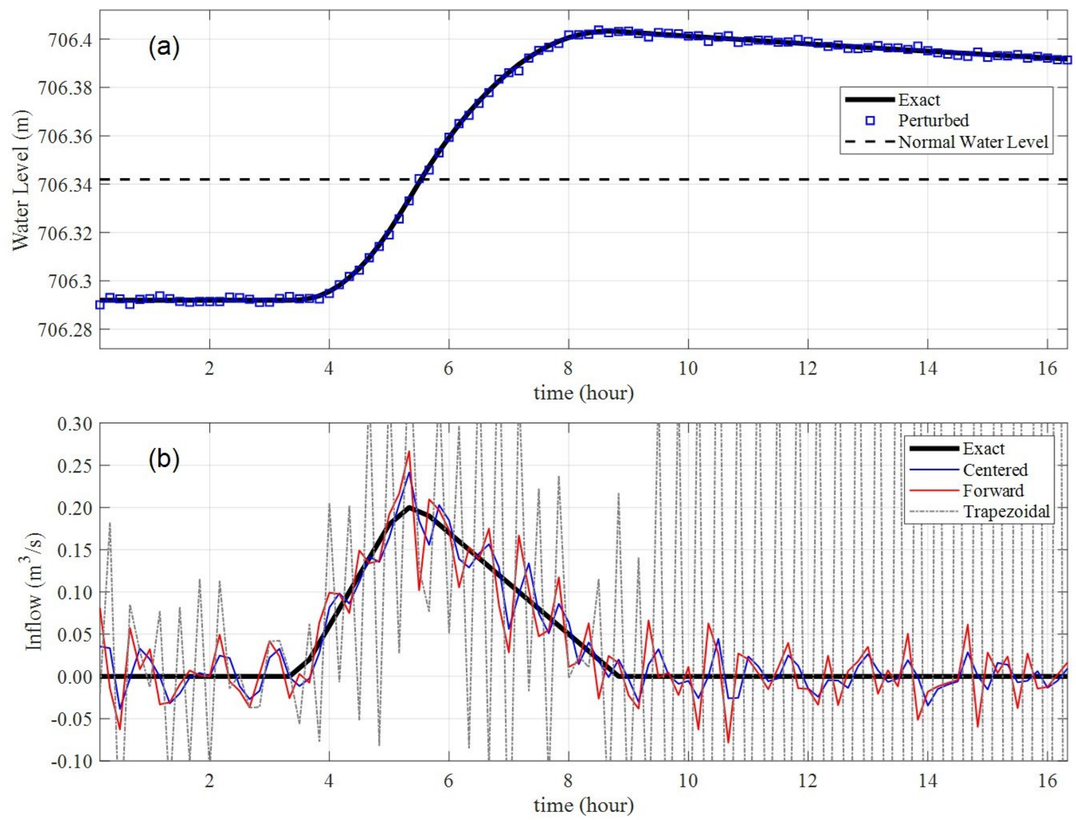

Figure 3-2: An example of noise amplification from water levels to inflows at the SB4 Pond. (a) Exact (routed) and perturbed water levels with σ=1mm; (b) Exact and back-routed inflows using centred, forward and trapezoidal schemes. $\Delta t = 600$ s.

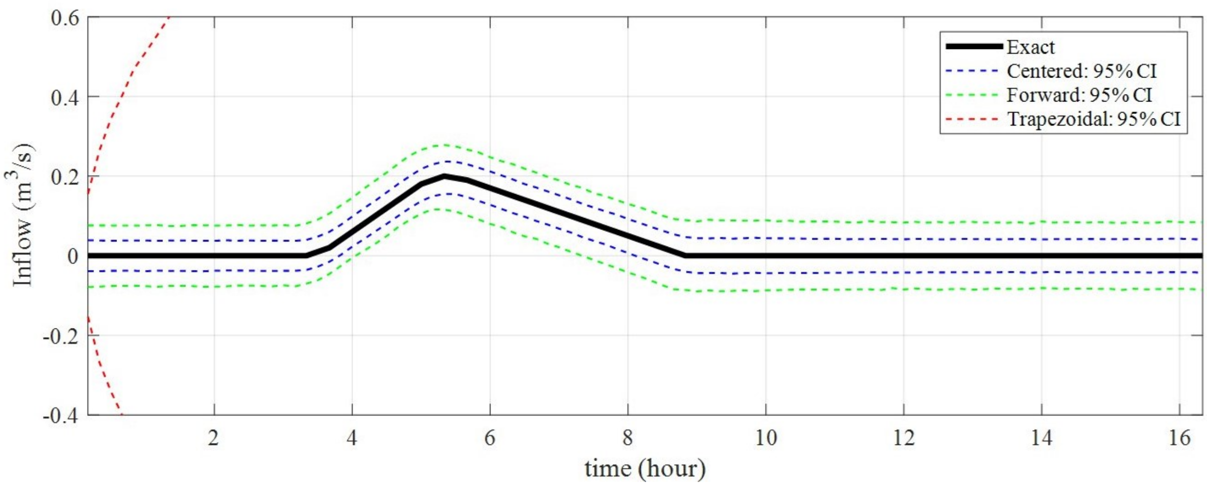

Figure 3-3: Performance of centred, forward, and trapezoidal schemes at SB4 based on 10,000 simulations. $\sigma = 1$ mm, $\Delta t = 600$ s.

3.2.2. **Analyzing the Impact of Water Level Noise on Back-routed Inflows**

In this section, how the properties of noise in the observed water levels were evaluated is described. Then, how the impact of noise in the water level time series on the back-routed inflow was quantified using three methods is explained. These methods included an analytical method based on the properties of random variables, Taylor Series expansion, and order-of-magnitude analysis. Subsequently, the procedure for validating this relationship through a Monte Carlo simulation is explained.

3.2.2.1 Water Level Noise Magnitude and Distribution

In order to predict error in the back-routed inflows, first the magnitude of noise in the observed water level time series was estimated. For this, MATLAB was used to apply the Butterworth low-pass filter (Butterworth 1930) to the measured water levels to remove high frequency noise. The noise at each time step was then calculated as the difference between the observed and filtered water levels. For instance, Figure 3-4 illustrates observed and filtered water levels at the study ponds during a period of relatively constant water levels. Next, the standard deviation of noise (σ) was calculated over a 72-hour time window (i.e., a sample size of 432). Figure 3-4 illustrates that over the 72 hours plotted, noise magnitudes at SB4, TT2 and ST2 were 1.0, 1.1, and 1.3 mm, respectively. Additionally, as shown in Figure 3-5, the distribution of noise is approximately normal. It should be noted that time window lengths, ranging from half a day to 30 days, were also tested, and very similar results were obtained. Figure 3-4 and Figure 3-5 display a 72-hour window from April 28 to May 01, 2015. This window was moved across the entire observation period (November 2013 to October 2015), and the calculated σ values are presented in Figure 3-6. The inter-quartile ranges of σ are 1.0-1.3 mm for SB4, 1.1-2.1 mm for TT2, and 1.0 to 1.5 mm for ST2. This indicates that noise in the observed water levels is generally between 1 and 2 mm, with the noise levels at SB4 and ST2 being slightly smaller than at TT2.

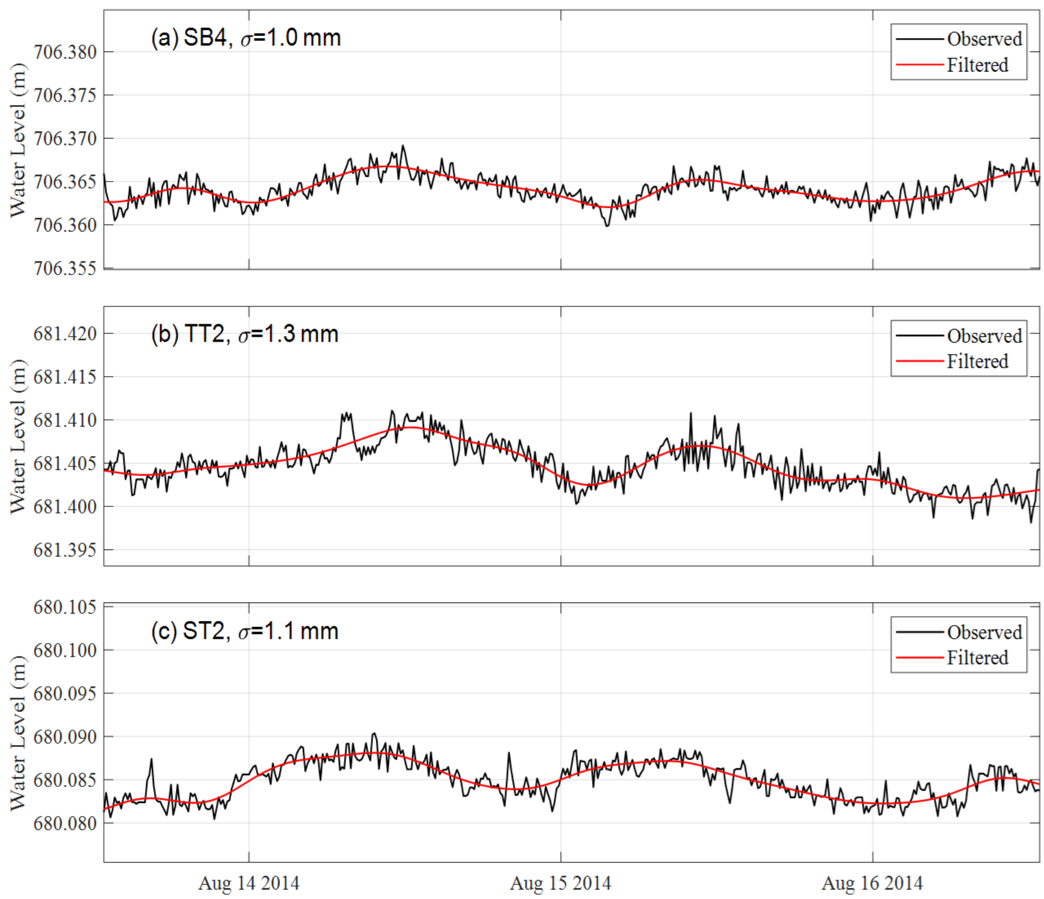

Figure 3-4: Observed and filtered water levels at the study ponds

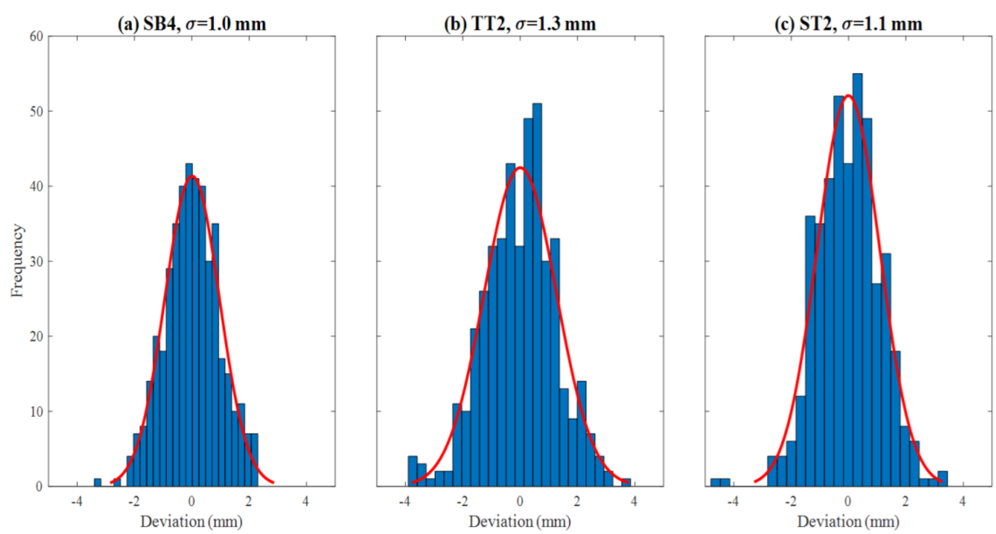

Figure 3-5: Histogram of noise (deviation of measured from filtered water levels) overlaid with the normal distribution (red line) for the study ponds.

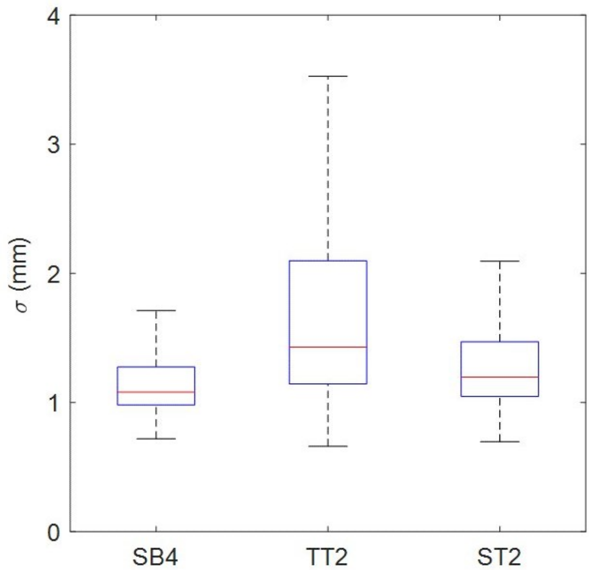

Figure 3-6: Boxplots of noise standard deviation (σ) values, computed using a 72-hour sliding window across the observation period.

3.2.2.1 Analytical Error Analysis

An analytical error analysis was conducted to investigate the amplification of water level noise by reverse level pool routing. First, the noise (i.e., random error in the measured water level) was modeled by a normal distribution as follows:

$$\epsilon \sim \mathbf{N}(0, \sigma) \tag{3-5}$$

where ϵ is noise, and $\mathbf{N}$ denotes the normal distribution with a mean (μ) of zero and a constant standard deviation (σ), or:

$$\mu_{(\epsilon)} = 0; \qquad \sigma_{(\epsilon)} = \sigma \tag{3-6}$$

Therefore, the noisy water level (denoted as h^*) at time t, is also a normal random variable, different from the true water level (h) and given by:

$$h^* = h + \epsilon \tag{3-7}$$

Taking the mean and standard deviation of (3-7) gives:

$$\mu_{(h^*)} = h; \qquad \sigma_{(h^*)} = \sigma \tag{3-8}$$

indicating that the measured water level is a random normal variable with the following distribution:

$$h^* \sim \mathbf{N}(h, \sigma) \tag{3-9}$$

Since the water level time series is used to calculate the outflow and pond volume a noisy water level time series will produce noisy outflow and volume time series defined as O^* and V^*. The resulting noisy back-routed inflow time series will then be given from Equation (3-2) as:

$$I^{*n} = O^{*n} + \frac{V^{*n+1} - V^{*n-1}}{2\Delta t} \tag{3-10}$$

For small perturbations, i.e., $\epsilon \ll h$, noisy volume ($V^* = V(h^*)$) and outflow ($O^* = f(h^*)$) can be linearized based on Taylor's expansion as follows:

$$\begin{aligned} V^{*n} &= V(h^n + \epsilon^n) \\ &= V^n + \epsilon^n \frac{\partial V^n}{\partial h} + \frac{(\epsilon^n)^2}{2} \frac{\partial^2 V^n}{\partial h^2} + \cdots \end{aligned} \tag{3-11}$$

$$
\begin{aligned}
O^{*n} &= O(h^n + \epsilon^n) \\
&= O^n + \epsilon^n \frac{\partial O^n}{\partial h} + \frac{(\epsilon^n)^2}{2} \frac{\partial^2 O^n}{\partial h^2} + \cdots
\end{aligned} \tag{3-12}
$$

Substituting Equations (3-11) and (3-12) into Equation (3-10) and dropping the higher order terms:

$$
\begin{aligned}
I^{*n} = I^n &+ \frac{\partial}{\partial h}\left(\epsilon^n O^n + \frac{\epsilon^{n+1} V^{n+1} - \epsilon^{n-1} V^{n-1}}{2\Delta t}\right) \\
&+ \frac{1}{2} \frac{\partial^2}{\partial h^2}\left((\epsilon^n)^2 O^n + \frac{(\epsilon^{n+1})^2 V^{n+1} - (\epsilon^{n-1})^2 V^{n-1}}{2\Delta t}\right)
\end{aligned} \tag{3-13}
$$

Computing the expected value on both sides of Equation (3-13), and considering Equation (3-8), the expected value of the noisy inflow times series is:

$$
\mu_{I^{*n}} = I^n + \frac{\sigma^2}{2} \frac{\partial^2 I^n}{\partial h^2} \tag{3-14}
$$

Given that $\sigma^2 \ll I^{*n}$, it can be concluded that at each time step, the expected value of the noisy inflow is the same as the exact inflow, or

$$
\mu_{(I^{*n})} = I^n \tag{3-15}
$$

Further, taking the standard deviation of both sides of Equation (3-13) yields:

$$
\sigma_{I^{*n}} = \sigma \sqrt{\left(\frac{\partial O^n}{\partial h}\right)^2 + \frac{1}{4(\Delta t)^2}\left[\left(\frac{\partial V^{n+1}}{\partial h}\right)^2 + \left(\frac{\partial V^{n-1}}{\partial h}\right)^2\right]} \tag{3-16}
$$

Based on Taylor's expansion, the volume derivatives under the radical can be expanded about time step n, and given that $\partial V/\partial h = A$, Equation (3-16) reduces to:

$$\sigma_{I^{*n}} = \sigma\sqrt{\left(\frac{\partial O^n}{\partial h}\right)^2 + \frac{1}{2}\left(\frac{A^n}{\Delta t}\right)^2} \tag{3-17}$$

Considering the order of magnitudes of the terms in Equation (3-17) ($O\sim10^{-3}$ m³/s, $A\sim10^4$ m², $\Delta t\sim10^2$ s, and $h\sim10^0$ m), the second term under the radical is several orders of magnitudes larger than the first term, therefore:

$$\frac{\sigma_I}{\sigma} = \frac{A}{\sqrt{2}\Delta t} \tag{3-18}$$

where $A/(\sqrt{2}\,\Delta t)$ is defined as the amplification factor of the reverse level pool routing using the centred scheme and σ_I is the standard deviation of the noisy inflow, I^*. However, in Equation (3-18) and throughout the remainder of this chapter, the superscript (*) is omitted for clarity and readability. It can be seen in Eq. (3-18) that in reverse level pool routing, by decreasing Δt the amplification factor increases.

3.2.2.1 Calculation of Amplification Factor using Monte Carlo Simulations

In order to verify the validity of Equation (3-18), amplification factors were calculated using the same Monte Carlo technique described earlier. The exact water level times series at each pond were perturbed with σ values between 1mm and 100mm, and the corresponding amplification factors (σ_I/σ) were calculated.

3.2.3. **Noise Mitigation by Filtering**

The goal of this section is to quantify the impact of low-pass filtering the water level time series on the back-routed inflow. The simulation procedure here is similar to that outlined in

Section 3.2.2.1, with two key differences. Firstly, instead of a hypothetical hydrograph, observed inflows were routed and secondly, low-pass filtering was applied to the observed and perturbed water levels.

The measured inflows between January 7 and May 23 2015, were used for the SB4 and TT2. For these two ponds, the “observed” RMSE” was calculated by comparing the observed inflows with inflows calculated by back-routing the observed water levels. The observed RMSE could not be evaluated for the ST2 pond, since no inflow measurements were available. Additionally, the "simulated" RMSE was calculated for all the ponds following the steps listed in Table 2. In calculating simulated RMSE, random noise time series with σ = 1, 2, 4, and 6 mm were used. The Butterworth low-pass filter (Butterworth 1930) was used here, which has been applied in several previous hydrological applications (e.g., Henley et al. 2011; Pagendam and Percival 2015). Cut-off frequencies (fc) of 1/1.5, 1/2, 1/3, 1/4.5, 1/6, 1/9, 1/12, 1/18, and 1/24 hr^{-1} were applied to the measured water level time series. It should be noted that the sampling frequency (fs) was 6 hr^{-1}.

Table 2: Steps for calculating simulated RMSE

Step	Description
1	Generate exact water level time series (h) by routing the observed inflow time series into SB4 and TT2. For ST2, use the inflow time series observed at TT2.
2	Generate 10,000 normal random noise time series (ϵ) with a mean of zero and a standard deviation of σ, i.e., $\epsilon \sim \mathbf{N}(0, \sigma)$.
3	Generate 10,000 "perturbed" water level time series (h^*) by adding the noise time series to the exact water level time series, i.e., $h^* = h + \epsilon$.
4	Low-pass filter the 10,000 perturbed water level time series using a cut-off frequency (fc) to create 10,000 filtered water level time series.
5	Generate 10,000 simulated inflow time series (I^*) by back-routing the filtered water level time series.
6	Calculate the RMSE for each of the 10,000 pairs of observed and simulated inflow time series, and compute their average as the "simulated" RMSE for the selected σ and fc.
7	Repeat Steps 2 to 6 for each pond while varying σ and fc.

3.3. RESULTS AND DISCUSSION

3.3.1. Amplification Factors of the Reverse Level Pool Routing

Based on Monte Carlo simulations, the simulated amplification factor (σ_I/σ) was calculated for each pond. This ratio remained nearly constant for each pond for values of σ between 1mm and 100mm. Additionally, analytical amplification factors were calculated using Equation (3-18) using Δt = 600 s and A equal to the area at the normal water level (NWL). Table 3 shows that simulated and analytical amplification factors are nearly identical, confirming the validity of Equation (3-18). Furthermore, the lowest and highest σ_I/σ ratios were obtained at ST2 and TT2, respectively, which is consistent with their respective areas.

Table 3: Amplification factor derived based on the analytical error analysis and simulation

Pond		SB4	TT2	ST2
Area (m²)		18,200	21,800	9,000
σ_I/σ (m³/s/mm)	Analytical	0.0214	0.0257	0.0106
	Simulation	0.0213	0.0256	0.0109

Time series of water levels and inflows are plotted in Figure 3-7 to Figure 3-9 to illustrate how water level noise is amplified by the reverse level pool routing. The 95% confidence intervals shown in these figures were calculated based on 10,000 simulations. The magnitudes of the inflow oscillations (σ_I) at SB4, TT2, and ST2 are 0.0428, 0.0514, and 0.0220 m³/s, respectively, which correspond to the same ratios reported in Table 3.

In Figure 3-10 plots of the frequency distribution of inflow residuals (i.e., deviation of 10,000 back-routed inflows from the exact inflow) are presented. These residuals are calculated at $t = 4$ hr (Figure 3-7 to Figure 3-9), but the distribution is the same at all time steps and only depends on σ and the pond's characteristics. The residual distributions closely follow the theoretical normal distributions overlaid in the figures. This shows that, perturbing water levels with $\epsilon \sim \mathbf{N}(0, \sigma)$ leads to inflow deviations given by:

$$I - I^* \sim \mathbf{N}(0, \sigma_I) \tag{3-19}$$

where the σ_I/σ ratio is given by Equation (3-18). In fact, the mean of 10,000 simulated inflows was exactly the same as the exact inflow, and hence not shown in Figure 3-7 to Figure 3-9. Additionally, the magnitudes of σ_I are reflected in the width of the confidence intervals in Figure 3-7 to Figure 3-9. Given the approximately normal distribution of simulated inflows, the width of the 95% confidence interval is $\sim 4\sigma_I$ according to the empirical rule.

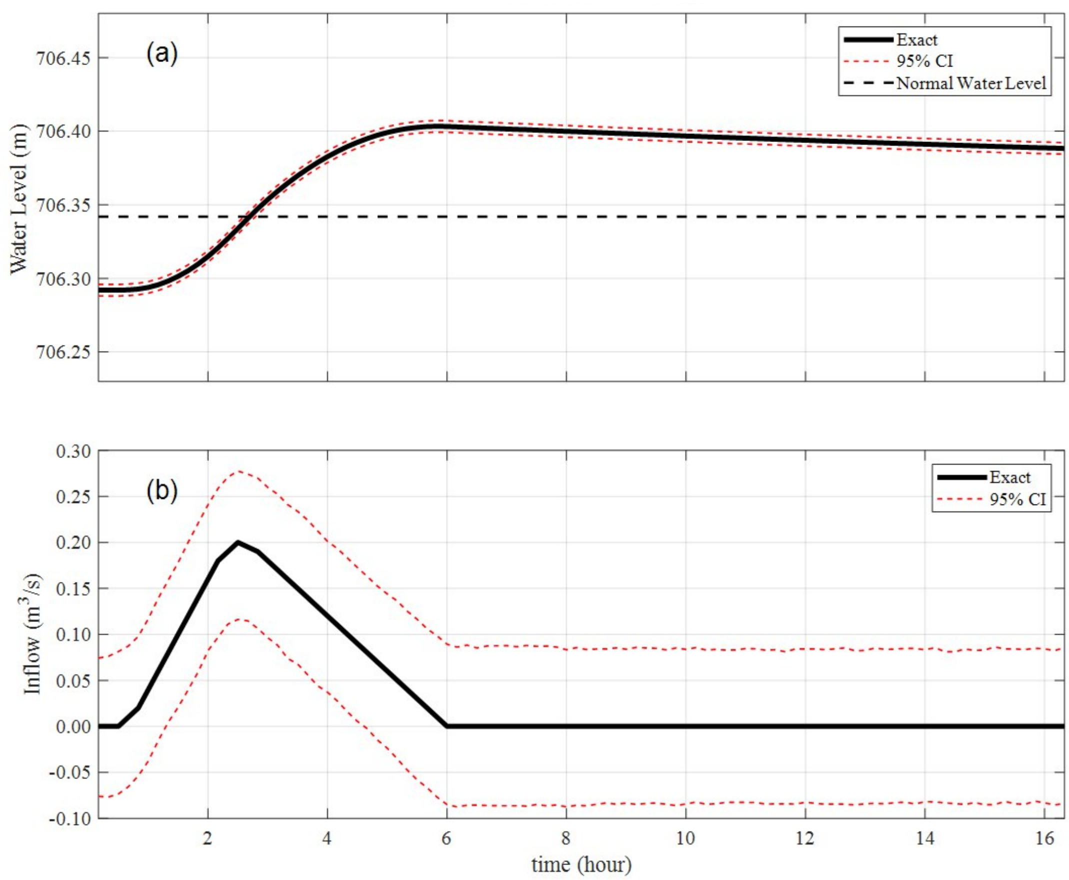

Figure 3-7: 95% confidence intervals of (a) water level perturbed by σ=2 mm and (b) inflow estimated by reverse routing at SB4 based on 10,000 Simulations. σ_I=0.0428 m³/s, Δt=600 s.

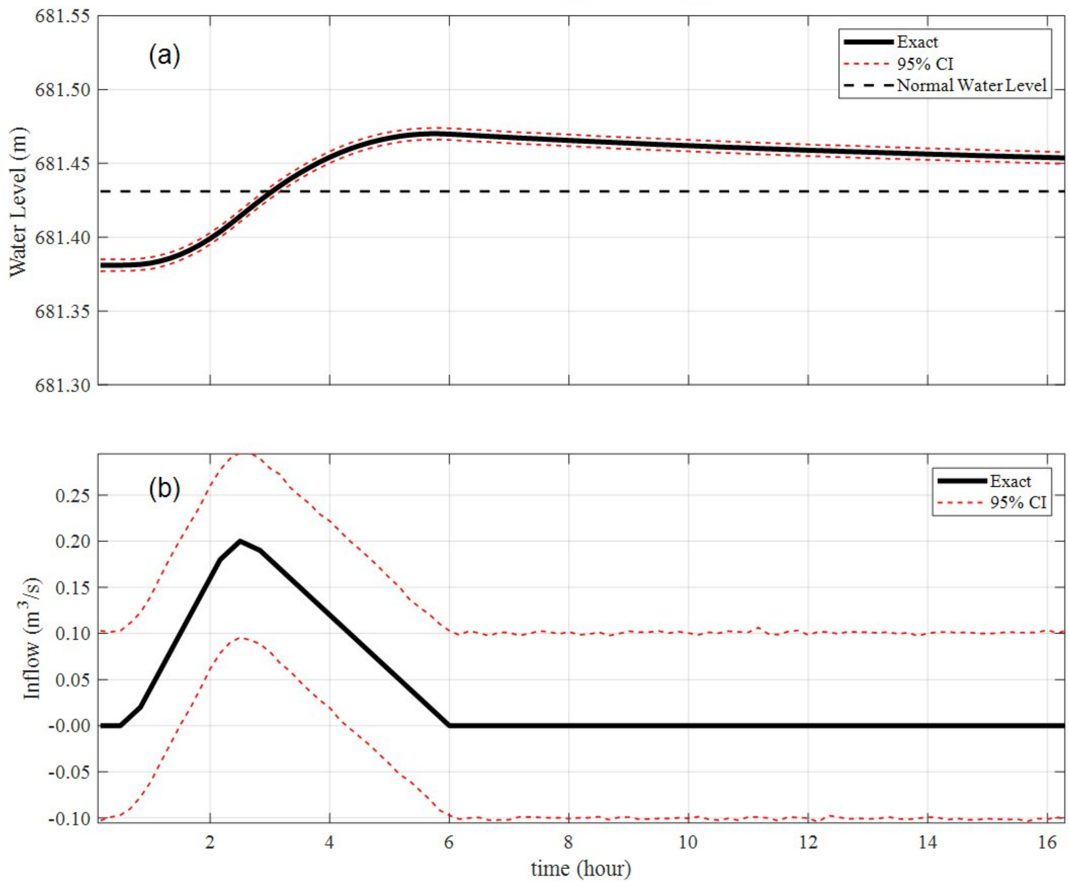

Figure 3-8: 95% confidence intervals of (a) water level perturbed by σ=2 mm and (b) inflow estimated by reverse routing at TT2 based on 10,000 Simulations. σ_I=0.0514 m³/s, Δt=600 s.

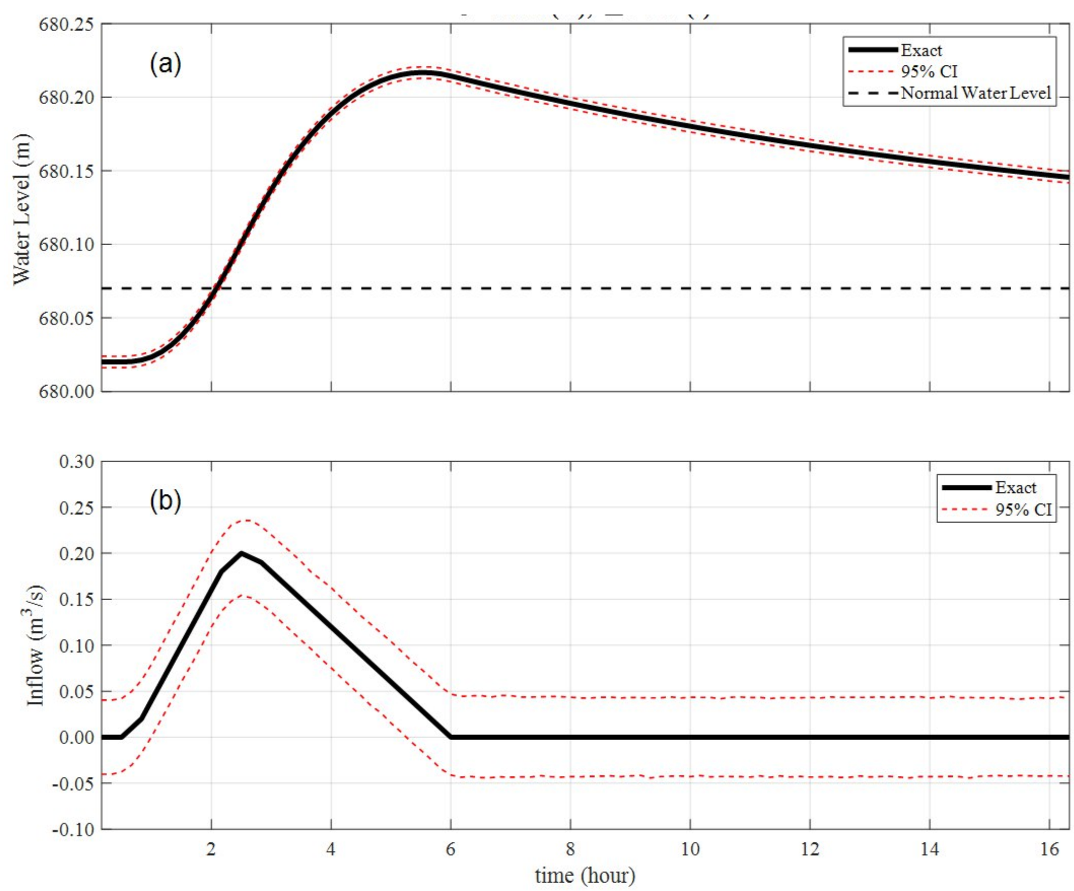

Figure 3-9: 95% confidence intervals of (a) water level perturbed by σ=2 mm and (b) inflow estimated by reverse routing at ST2 based on 10,000 Simulations. σ_I=0.0220 m³/s, Δt=600 s.

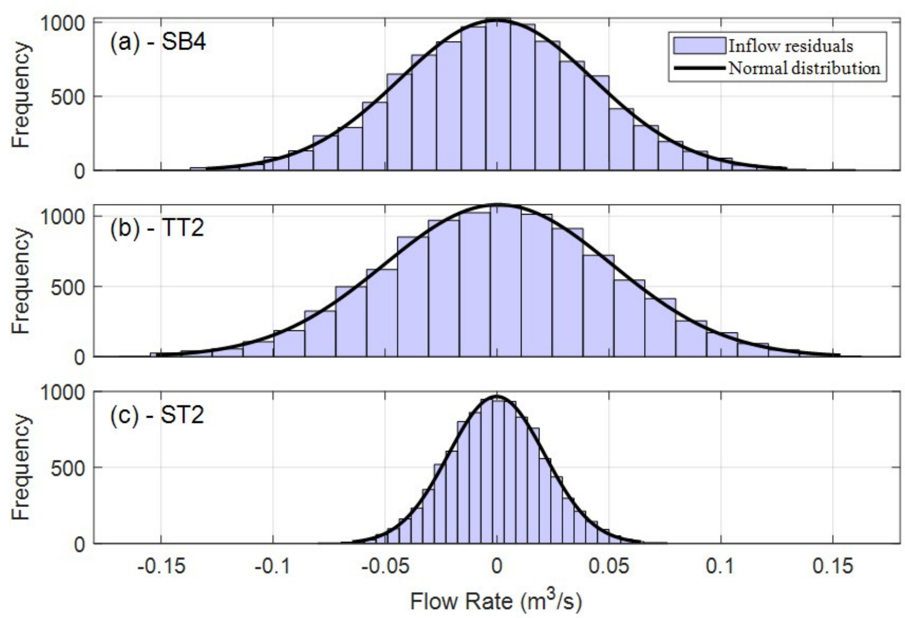

Figure 3-10: Distribution of inflow residuals at the (a) SB4, (b) TT2, and (c) ST2 ponds.

According to Equation (3-18) and evident from Figure 3-7 to Figure 3-9, σ_I is independent of the magnitude of inflow. Therefore, the impact of noise is more significant when inflows are relatively small or zero, a condition very common in urban stormwater ponds. For instance, while no inflow enters the ponds after t = 6 hr (bottom panels of Figure 3-7 to Figure 3-9), there is a 50% probability of negative inflows estimated by the reverse routing approach. Conversely, the likelihood of a negative inflow being calculated decreases significantly when inflows are sufficiently large, such as for $1 < t < 5$ hr. Therefore, the propagation of errors from the measured water levels to the estimated inflows results in more frequent non-physical negative inflows on urban stormwater ponds receiving intermittent inflows, compared to the bodies of water receiving continuous base flow.

3.3.2. **Noise Mitigation by Filtering of the Measured Water Level**

Filtering the observed water level time series was found to significantly reduce the magnitude of oscillations in the back-routed inflows. For example, in Figure 3-11 to Figure 3-13 time series of observed water levels and corresponding back-routed inflows into the study ponds in response to the rain event of early May 2015. The inflows are estimated from the unfiltered water levels as well as from water levels filtered with fc=1/6 hr^{-1}, which, as will be shown, was found to be the optimum cut-off frequency.

Based on available inflow measurements for SB4 and TT2 (Figure 3-11 and Figure 3-12), the inflows back-routed from the filtered water levels effectively replicated the hydrographs corresponding to this rain event. Additionally, despite the absence of inflow measurements at ST2, Figure 3-13 shows that the reverse level pool routing predicted an inflow hydrograph consistent with those observed at SB4 and TT2. In contrast to inflows back-routed from unfiltered water levels, filtering led to estimated inflows that are much smoother, with fewer and significantly smaller negative values. Notably, without filtering, the noisier water levels observed in TT2 on May 5 (Figure 3-12a) resulted in significantly larger inflow oscillations, which were effectively diminished by filtering (Figure 3-12b).

Comparing the back-routed inflows (fc=1/6 hr^{-1}) with those observed in SB4 and TT2 (Figure 3-11 and Figure 3-12), the TT2 peak has been more significantly attenuated by filtering. The inflow peak on May 6 into TT2 consisted of two pulses of inflow occurring close to each other. Water levels corresponding to such peaks contain more high-frequency components (on the order of fc), which are smoothed by the low-pass filters, leading to a flatter peak than was observed.

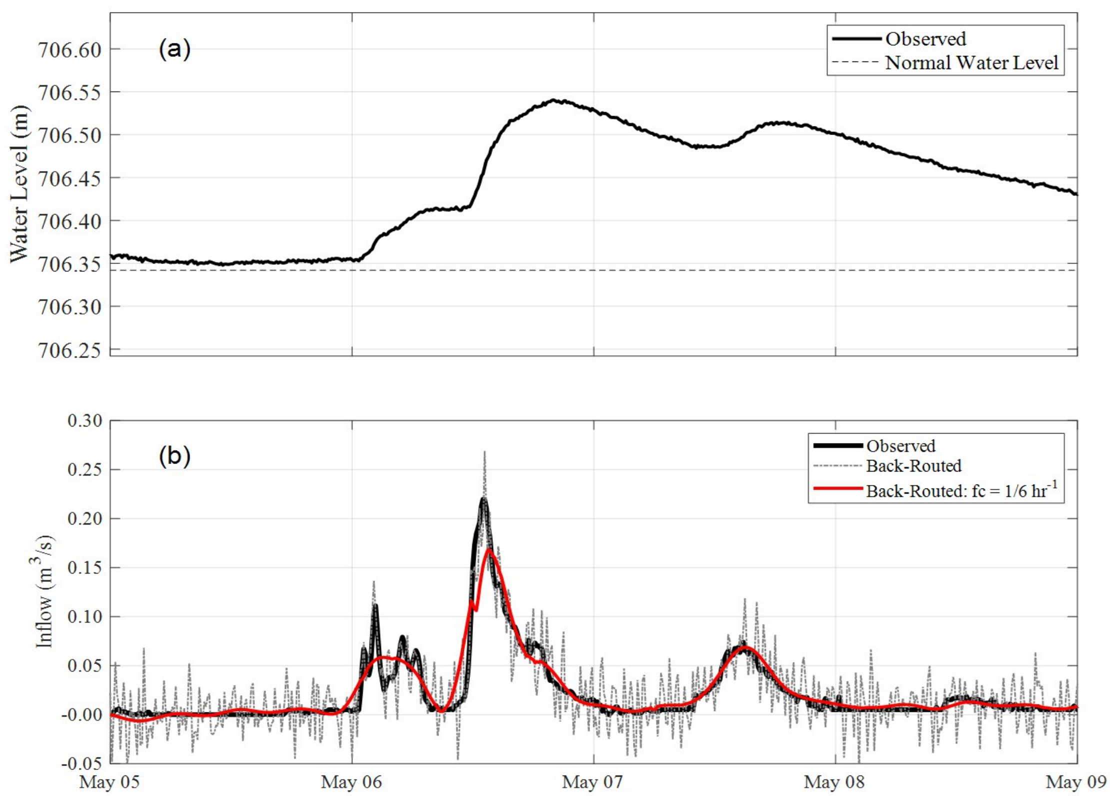

Figure 3-11: (a) Observed water level and (b) observed and back-routed inflows for the SB4 pond between May 5 and 9, 2015.

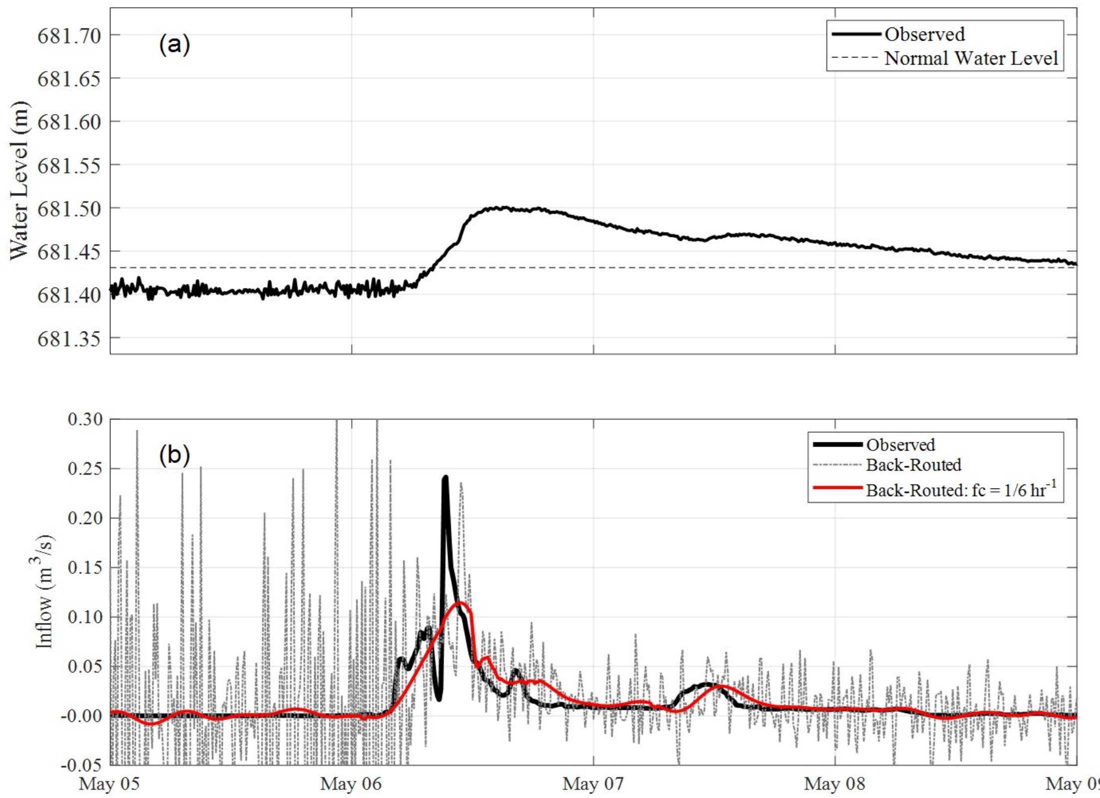

Figure 3-12: (a) Observed water level and (b) observed and back-routed inflows for the TT2 pond between May 5 and 9, 2015.

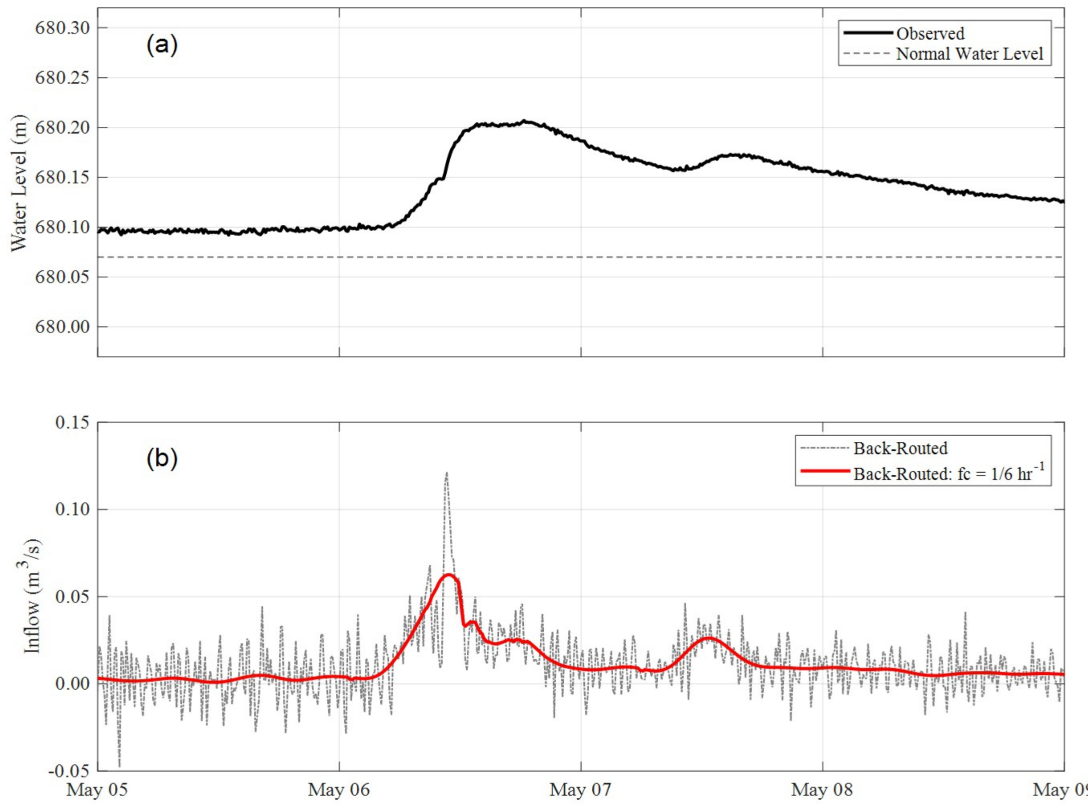

Figure 3-13: (a) Observed water level and (b) back-routed inflows for the ST2 pond between May 5 and 9, 2015.

Figure 3-14 to Figure 3-16 illustrate the effect of fc on the back-routed inflows between March 24 and 29, 2015, during which warmer weather led to diurnal peaks caused by meltwater flowing into the study ponds. Estimating inflows based on a relatively high fc (1/1.5 hr^{-1}) shows smaller peak attenuation at SB4 (Figure 3-14) and TT2 (Figure 3-15); however, non-physical ripples are evident. Conversely, employing a relatively low fc (1/18 hr^{-1}) significantly distorted the shape of hydrographs. While the resulting inflows are smooth, the problem of negative inflows was not resolved.

It can be seen that filtering water levels with fc=1/6 hr^{-1} has led to smooth results with minimal distortion and oscillations. Although no flow observation was available at ST2, Figure

3-16 illustrates that fc=1/6 hr^{-1} provides a hydrograph with peaks very similar to those estimated with fc=1/1.5 hr^{-1} and much less oscillations.

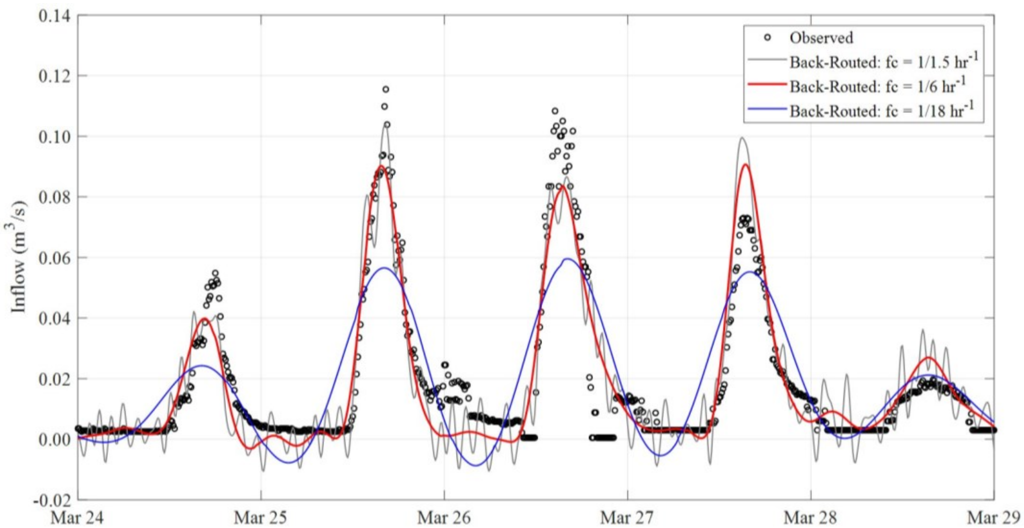

Figure 3-14: Observed and back-routed inflows for the SB4 pond between March 25 and 29, 2015.

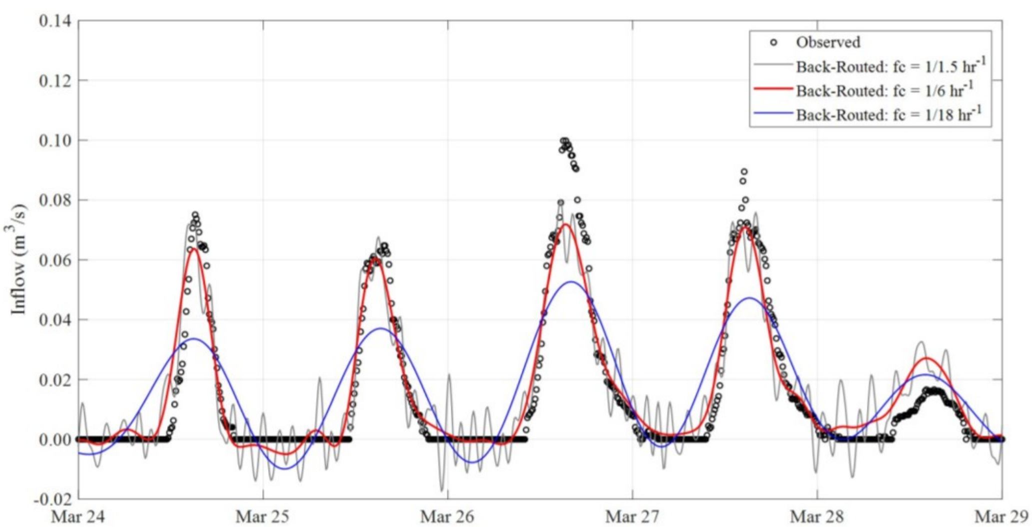

Figure 3-15: Observed and back-routed inflows for the TT2 pond between March 25 and 29, 2015.

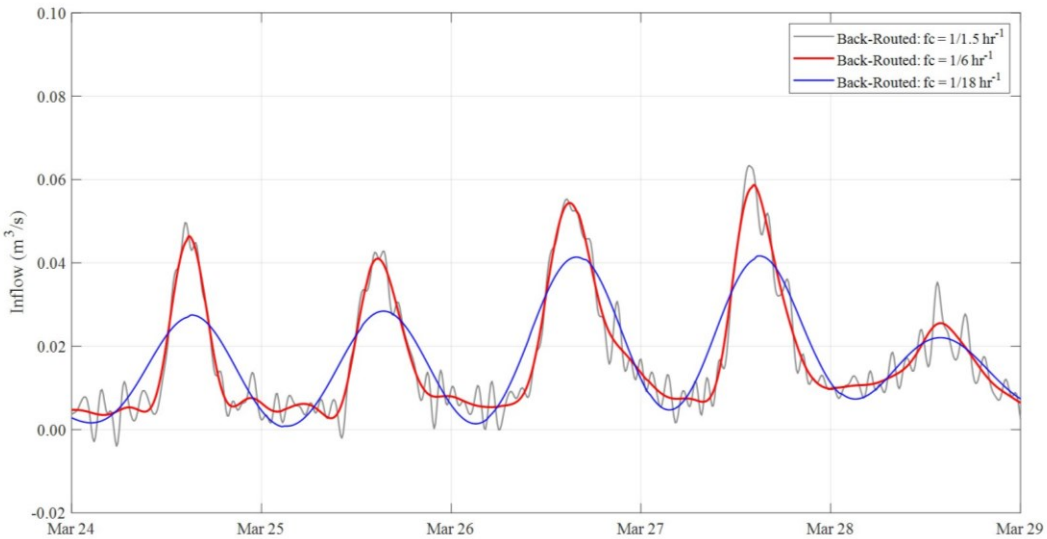

Figure 3-16: Back-routed inflows for the ST2 pond between March 25 and 29, 2015.

Table 4, Figure 3-17, and Figure 3-18 demonstrate how filtering water levels can improve the performance of the reverse level pool routing. While lower fc values (e.g., 1/24 hr^{-1}) more aggressively remove noise, they also more severely distort the dataset (Koussis and Mazi 2015; Leonhardt et al. 2014). The observed RMSE of inflows was minimized for SB4 by applying the Butterworth filter with fc between 1/3 to 1/6 hr^{-1}, and for TT2 with fc between 1/4.5 to 1/9 hr^{-1}. RMSE values of inflows based on unfiltered water levels were 0.0218 and 0.0480 m^3/s at SB4 and TT2, respectively. Filtering with fc=1/6 hr^{-1}, however, reduced the RMSE by 75% and 87%, respectively. Values of V_N, defined as the percentage of the volume of negative inflows relative to the volume of positive inflows over the simulation period are also presented in Table 2. Without filtering, the volume of negative inflows was 49% and 73% of the volume of positive inflows for SB4 and TT2, respectively. However, filtering with fc=1/6 hr^{-1} reduces these percentages to 6% and 17%, respectively. Employing lower fc values does not significantly reduce the volume of negative inflows, except for fc=1/24 hr^{-1} which significantly distorts the dataset.

The simulated RMSE is presented in Figure 3-17 to Figure 3-19 for all three ponds. While the trends of observed and simulated RMSE exhibit similarities, the observed RMSE does not exactly align with any of the simulated curves. This was expected because the simulated RMSE only reflects water level errors, whereas the observed RMSE includes measurement errors of both water levels and inflows. Furthermore, simulated RMSE calculations assume random and independent noise with a constant σ, however real-world noise may not always be random, and its magnitude can vary throughout the season. Figure 3-17 to Figure 3-19 indicate that as expected RMSE depends on the magnitude of water level noise, σ, the cut-off frequency of the low-pass filter, fc, and the characteristics of the pond. Both high and low fc can lead to higher RMSE. Relatively high values of fc (e.g., 1/1.5 hr^{-1}) may not effectively remove noise, and relatively low values of fc (e.g., 1/24 hr^{-1}) significantly distort the real signal. The simulated RMSE values were minimized at fc between 1/3 and 1/9 hr^{-1}, depending on the magnitude of σ.

Moreover, consistent with the results presented in Table 3, simulated RMSE values for SB4 and TT2 are higher than those for ST2. Due to consistent trends of RMSE across the ponds, an fc = 1/6 hr^{-1} was selected for filtering ST2 water levels. Furthermore, given the smaller area of ST2 and its relatively low magnitude of observed noise (e.g., Figure 3-5 and Figure 3-6), the overall performance of the reverse level pool routing in this pond is expected to be better than in the other two ponds.

Table 4: Impact of filtering on the RMSE and negative inflows for the SB4 and TT2 ponds.

fc (hr^{-1})	fc/fs	SB4 RMSE (m^3/s)	SB4 V_N (%)	TT2 RMSE (m^3/s)	TT2 V_N (%)
Unfiltered		*0.0218*	*49*	*0.0480*	*73*
1/1.5	1/9	0.0078	18	0.0155	47
1/2	1/12	0.0064	13	0.0116	39
1/3	1/18	0.0056	9	0.0082	28
1/4.5	1/27	0.0054	7	0.0067	20
1/6	1/36	0.0055	6	0.0065	17
1/9	1/54	0.0066	6	0.0070	16
1/12	1/72	0.0076	6	0.0080	15
1/18	1/108	0.0088	6	0.0096	14
1/24	1/144	0.0093	3	0.0110	8

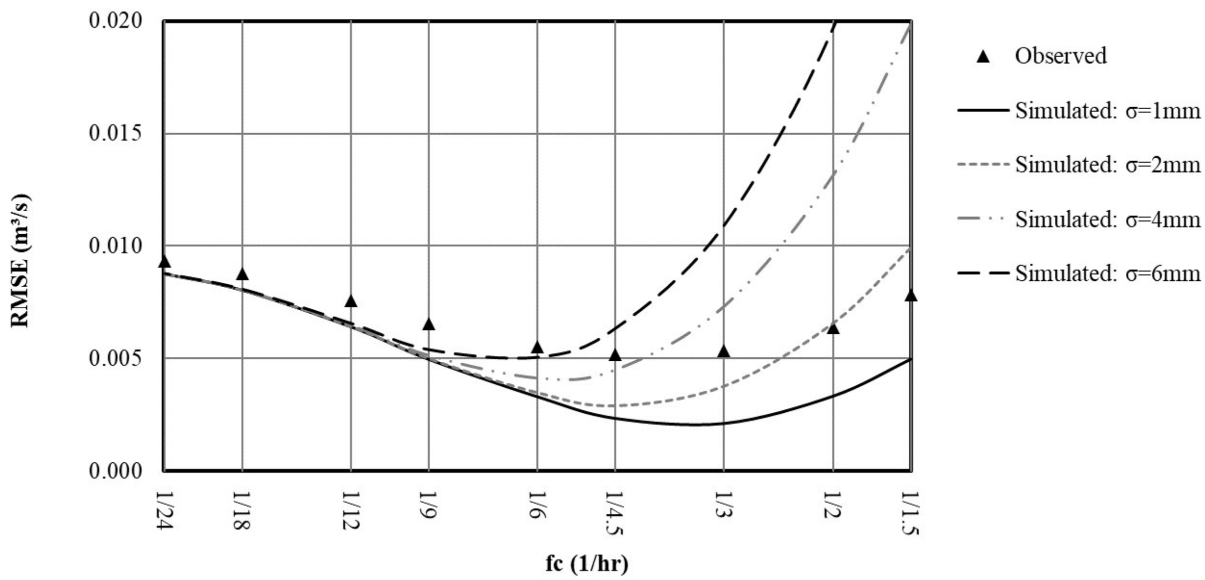

Figure 3-17: Observed and simulated RMSE of inflows for the SB4 pond.

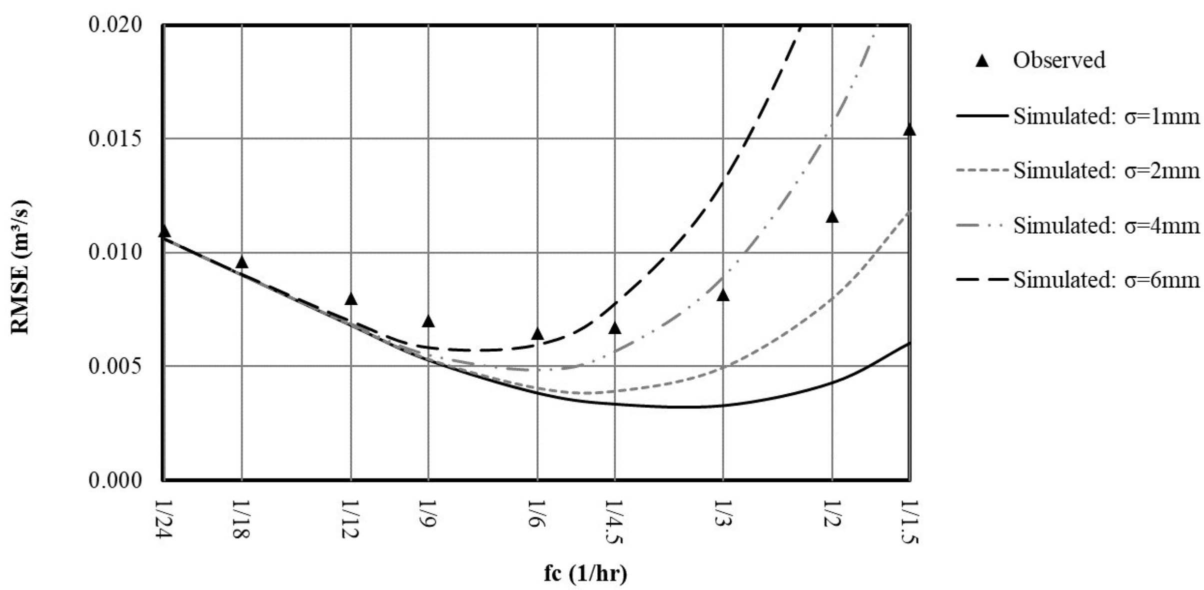

Figure 3-18: Observed and simulated RMSE of inflows for the TT2 pond.

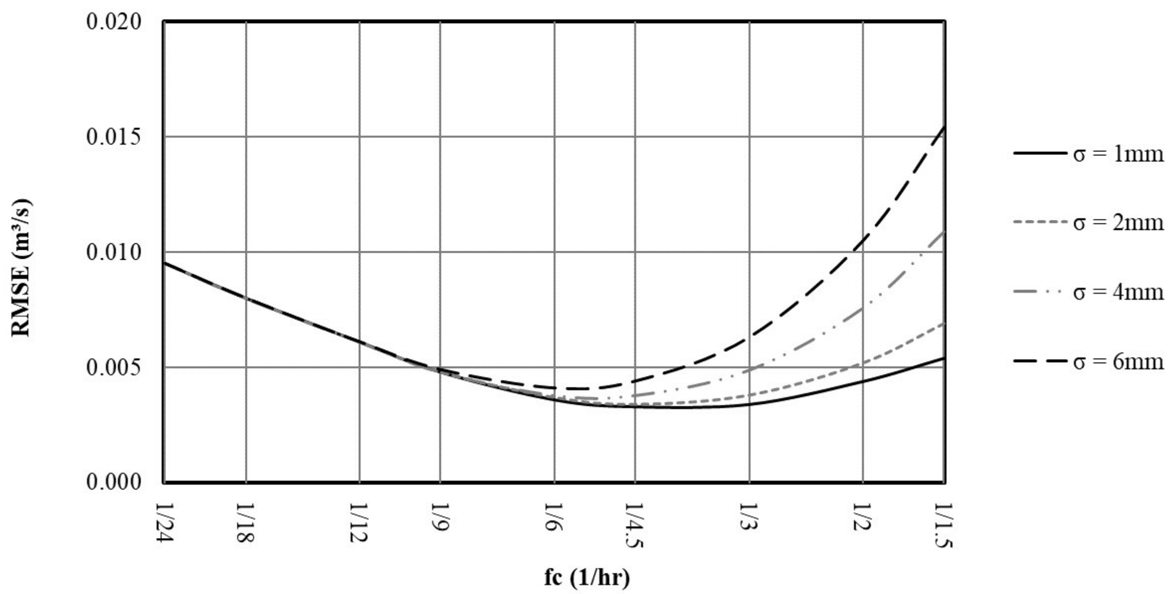

Figure 3-19: Simulated RMSE of inflows for the ST2 pond.

3.3.3. **Elimination of Negative Inflows**

During dry periods, when there is zero or near-zero inflow, the reverse routing approach has approximately a 50% chance of calculating a negative inflow at each time step. Although filtering water levels is expected to decrease the magnitude of negative inflows, it does not eliminate them entirely. It seems logical to remove these negative values and scale down the positive inflows to ensure the inflow volume is not changed. However, such post-processing may fail to preserve the water balance at smaller time scales and, depending on the relative magnitudes of the negative inflows, may actually violate conservation of mass.

3.4. **CONCLUSION**

The reverse level pool routing method inevitably amplifies noise in the measured water levels and corrupts the estimated inflows with spurious oscillations. The centred discretization scheme used here resulted in the least noise amplification compared to the forward and trapezoidal schemes. The noise amplification factor, σ_I/σ, was derived analytically and verified by the results of simulations. This factor is directly proportional to the surface area of the pond

(A), and inversely proportional to the numerical time step (Δt). While the magnitude of inflow oscillations is independent of the magnitude of inflow, oscillations have a more significant impact during dry periods, which are typical of urban stormwater ponds. The result is that reverse level pool routing predicts non-physical negative inflows when using unfiltered water level time series as input.

It should be noted that in reverse problems, higher-order schemes do not necessarily result in more accurate results. For example, it has been shown here that the first-order forward scheme was superior to the second-order trapezoidal scheme. Additionally, as presented in Equation (3-18) unlike level pool routing, errors in reverse level-pool routing increase as the time step decreases.

The noise amplification problem was mitigated by low-pass filtering of water levels. The Butterworth filter with a cut-off frequency (fc) of 1/6 hr^{-1} for the sampling rate of fs = 6 hr^{-1} provided the optimal results. This fc value was shown to minimize the RMSE of predicted inflows at the SB4 and TT2 ponds, while reasonably preserving the physical characteristics of the inflow hydrographs. The RMSE of inflows back-routed from water levels observed at the SB4 and TT2 ponds were 0.022 and 0.048 m^3/s respectively. Filtering reduced these values by 75% and 87%, respectively. The greater reduction at TT2 is attributed to noisier water levels, reflected in the higher RMSE, therefore the filtering had a greater impact. Similarly, filtering reduced the volume of negative inflows, as a percentage of the volume positive inflows, from 49% to 6% at SB4 and from 73% to 17% at TT2. Similar to SB4 and TT2, an fc=1/6 hr^{-1} was used for ST2, as all study ponds are in the same environment and the same instrumentation was used for measurements, thus similar noise magnitudes and behavior were expected.

Further post-processing of inflows to remove negative values was shown to violate the mass balance at smaller time scales and was not used here. If the estimated inflows are to be used for hydrodynamics and water quality modeling, and negative inflows do not disrupt the models, post-processing is not recommended, especially for the modeling of urban stormwater ponds because of the frequent occurrence of dry periods.

The different impacts of noise during dry and wet periods, as well as the variability of noise magnitudes over the simulation period (e.g., due to wind), suggest that in future studies, the performance of reverse level pool routing can be further improved by dynamically adjusting fc. This "conditional filtering" approach requires an algorithm to determine the optimal fc based on prevailing conditions. For example, if the algorithm can distinguish between wet and dry periods, it can apply relatively higher and lower fc values accordingly. Preliminary attempts to implement conditional filtering in this study resulted in a slightly improved performance of the reverse level pool routing (results not presented). However, since employing a single fc provided sufficiently accurate results for the purpose of this study, and considering the subjective nature of defining the criteria for selecting optimal fc, further exploration of this approach was not pursued here.

Chapter 4. ASSESSMENT OF HYDRODYNAMICS AND WATER QUALITY MODELLING OF A STORMWATER POND

The physical, chemical, and biological processes that take place in water bodies are extremely dynamic, interconnected, and impacted by a wide range of factors. The coupled three-dimensional (3D) hydrodynamic and water quality model, ELCOM-CAEDYM, has been successfully applied to simulate biogeochemical processes in different aquatic systems, including stormwater ponds. However, the model requires extensive calibration of various model parameters to appropriately address the state variables and describe the complex ecological processes (Hipsey et al. 2013; Hodges and Dallimore 2013a; Missaghi et al. 2014).

This chapter describes the calibration, validation, and the evaluation of ELCOM-CAEDYM for modelling the hydrodynamics and water quality of one stormwater pond —South Terwillegar2 (ST2)— in the city of Edmonton. The purposes of this chapter are: (i) to evaluate the ability of ELCOM-CAEDYM to model algae biomass by focusing on total chlorophyll-a (TCHLA) along with simulating the desired model state variables (i.e., temperature, dissolved oxygen, and nutrients) which support the simulation of algae, and (ii) to perform a sensitivity analysis to investigate the impact of model parameters on modelled state variables with a focus on TCHLA.

4.1. METHODOLOGY

4.1.1. Model Descriptions

2.2.3.1 ELCOM

The Estuary and Lake COmputer Model (ELCOM) was used to predict the temporal and spatial variation of physical processes and simulate the advection and diffusion of momentum and scalars in the study pond. A comprehensive description of ELCOM as well as governing equations and fundamental models for hydrodynamics and thermodynamics can be found in Hodges (2000), Hodges et al, (2000), and Hodges and Dallimore (2013a). ELCOM is based on the 3D unsteady Reynolds Averaged Navier-Stokes (RANS) equations for incompressible flow along with the scalar transport equation, i.e., temperature and salinity. The RANS equations are solved based on a semi-implicit scheme that discretizes momentum advection terms, and then the scalars are transported by the ULTIMATE QUICKEST scheme. The computational grid cells consist of a uniform rectangular mesh in the horizontal direction, which can accommodate non-uniform vertical spacing when required. Scalars are defined at cell centres and velocities on cell faces.

ELCOM assumes a hydrostatic pressure distribution and employs the Boussinesq approximation for considering density effects. The horizontal Reynolds stress terms are approximated by their correlation with eddy viscosity. The vertical Reynolds stress terms and upper mixed layer depths are quantified by extending a one-dimensional mixed-layer approach to three dimensions. The mixed-layer model is based on the balance between the available potential energy in the stratified water column and the kinetic energy. The free-surface elevation is determined by vertical integration of the continuity equation for incompressible flow from bottom to the top of the water column and employing the Reynolds averaging filter to the kinematic boundary condition.

The heat exchange at the water surface is governed by the standard bulk transfer model described, for example, by Hodges (2000). The energy transfer across the free surface is divided into non-penetrative and penetrative components. The penetrative component includes only the short-wave radiation, which is calculated as:

$$Q_{\mathrm{sw}} = Q_{sw(total)}\,(1 - r_a) \tag{4-1}$$

where $Q_{sw(total)}$ and Q_{sw} in (W/m^2) are the incident short-wave and penetrating short-wave at water surface, respectively, and r_a is the albedo coefficient, which theoretically varies between zero and one. The decay of Q_{sw} through the water column is modelled using the Beer-Lambert law:

$$Q_{\mathrm{z}} = Q_{sw}\exp(-k_{ext}d) \tag{4-2}$$

where Q_z (W/m^2) is the short-wave penetration at depth d (m) below the water surface, and k_{ext} (1/m) is the light extinction coefficient. The non-penetrative component includes long-wave radiation, sensible heat transfer, and evaporative heat loss. ELCOM employs a constant value for the latent heat and sensible heat transfer coefficients under stable atmospheric conditions.

The computing stages of ECLOM are summarized here. At the beginning of each time step, the heat budget at the uppermost grid cell of each water column is calculated. First, short-wave radiation is exponentially absorbed and decayed over the depth of the water column. This heat transfer may result in density variations between the mixed layer and the underlying layer. When there is an unstable density gradient, the lower layer mixes with the top mixed layer, resulting in release of energy. This released energy is added to the available energy in the mixed layer. Momentum introduced by wind also contributes to the available energy at the surface layer. Additionally, the energy present in the mixed layer can be is increased by the energy arising from velocity shear between the mixed layer and the lower layer. Next, using the mixed-layer approach on a layer-by-layer basis, the energy required to add a grid cell to the mixed layer above it is compared to the available energy. If available energy is sufficient, mixing occurs. Finally, the model computes changes in the free-surface, velocity fields, horizontal diffusion of momentum, and advection and horizontal diffusion of scalars are computed (Hodges et al. 2000; Lee et al. 2013; Paturi et al. 2012).

3.2.2.1 CAEDYM

The Computational Aquatic Ecosystem Dynamics Model (CAEDYM) is a biogeochemical model that is coupled with a hydrodynamic model (i.e., ELCOM in this study). CAEDYM simulates the dynamics of nutrients, dissolved oxygen (DO), inorganic suspended solids, phytoplanktons (algae), and other optional biotic compartments. Depending on the research objectives, users can define their ecological configurations; however, the major nutrients and at least one group of algae must be defined. Detailed descriptions of the model have been described in the literature (e.g., Bruce and Imberger 2009; Gal et al. 2009; Hipsey et al. 2013; Leon et al. 2011; Romero et al. 2004). The main equations used in CAEDYM are presented in Appendix B, Section B.1.

CAEDYM and ELCOM are dynamically coupled. At each time step, ELCOM provides physical variables such as temperature, light, and velocity to CAEDYM to simulate biogeochemical variables. Similarly, CAEDYM feeds parameters required for physical processes simulated by ELCOM. For example, ELCOM provides CAEDYM with the proportion of short-wave radiation received at the surface (Q_{sw}) that is converted to the photosynthetically active component (PAR). Subsequently, CAEDYM calculates and returns the light extinction coefficient to ELCOM (k_{ext} in Equation (4-2)), taking into account influences from algae, inorganic particles, particulate matter, and dissolved organic carbon concentrations. The fate of state variables is also influenced by inflows, outflows, advection, and mixing, all of which are modelled by ELCOM.

Dissolved oxygen (DO), dissolved nutrients, and inorganic suspended solids are simulated by CAEDYM in both the water column and a single sediment layer. CAEDYM can model sediment diagenetic processes and their interaction with the water column using either static or dynamic approaches. The static approach, widely used in the literature (Missaghi and Hondzo 2010; Nakhaei et al. 2021; Özkundakci et al. 2012; e.g., Trolle et al. 2011) and adopted in this study, models the sediment-water interaction through empirical relationships. These relationships are defined based on several parameters and variables, including temperature, DO, transfer rate of nutrients, and DO half-saturation for nutrient sediment and sediment oxygen demand. Some of the major relationships are listed in Appendix B.1 and further description can be found in CAEDYM science manual (Hipsey et al. 2013).

DO dynamics are modelled by considering several processes, including oxygen exchange across the water surface, algal production and respiration, sediment oxygen consumption, nitrification, and organic matter mineralization. The oxygen flux across the water surface is modelled based on model of Wanninkhof (1992) as a function of the oxygen transfer coefficient and concentration of DO at the air-water interface. The concentration of DO in the air phase is modelled according to Riley and Skirrow (1975) flux equation, taking into account atmospheric pressure and temperature. In the static approach employed in this study, sediment oxygen consumption is determined by temperature and DO concentration in the layer immediately above the sediment (Hipsey et al. 2013).

CAEDYM tracks the cycle of the inorganic and organic forms of nutrients, including carbon, phosphorous and nitrogen (Figure 4-1). The nutrient components include dissolved organic nutrient (DOM), particulate organic nutrient (POM), dissolved inorganic nutrient (DIM), particulate inorganic nutrient (PIM), and algae internal nutrient for the i-th algae group (AIMi). Organic nutrients are modelled in both filterable and particulate forms, and there is also the option to model them in labile and refractory forms. Inorganic nutrients are only modelled in the filterable from; however, their absorption and desorption onto inorganic suspended solids are tracked. It should be mentioned that resuspension was not modelled here.

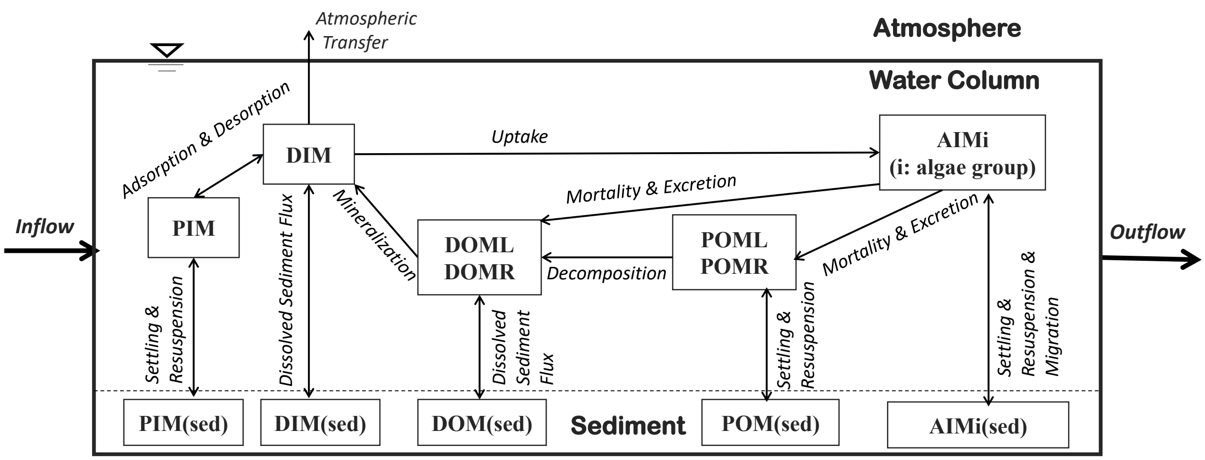

Figure 4-1: Schematic representation of nutrient dynamics tracked by CAEDYM, adopted from (Hipsey et al. 2013).

CAEDYM requires four mandatory phosphorus state variables: soluble reactive phosphorus (SRP or PO4), labile dissolved organic phosphorus (DOPL), labile particulate organic phosphorous (POPL), and algal internal phosphorous for each algae group (AIPi). The model also requires five mandatory nitrogen state variables: nitrate (NO3), ammonium (NH4), labile dissolved organic nitrogen (DONL), labile particulate organic nitrogen (PONL), and algal internal nitrogen for each algae group (AINi). This study considered all mandatory phosphorous and nitrogen variables, as well as two optional variables: particulate inorganic nitrogen (PIN) and particulate inorganic phosphorus (PIP). Algae dynamics are governed by growth and loss processes. Algae growth is a function of temperature, light, and nutrients as follows:

$$\mu_i = f_{A_i}^{T_1}(T)\mu_{\max_i} f(I)\min[(f(P), f(N)] \tag{4-3}$$

where i is the index of the algae group, A is the concentration, μ and $\mu_{\max}$ are the potential growth and maximum potential growth rates (1/day), respectively, and $f_{A_i}^{T_1}(T)$, $f(I)$, $f(P)$ and $f(N)$ are temperature, light, phosphorous and nitrogen limiting factors, respectively. The limiting factors vary between zero and one, where smaller values indicate greater limitations.

Detailed equations describing temperature dependencies and light and nutrient limiting factors are presented in Appendix B, Section B.1. In particular, the temperature limiting factor is:

$$f_i^{T_1}(T) = \vartheta_i^{T-20} + \vartheta_i^{c_j(T-a_j)} + b_i \tag{4-4}$$

where

ϑ_i = Temperature multiplier
a_i = Constant, $f(\vartheta_i, T_{std}, T_{\max}, c)$,
b_i = Constant, $f(\vartheta_i, T_{std}, a_i, c)$
c_i = Constant, $f(a_i, b_i)$
a_i, b_i, and c_i, solved numiricaly to satisfy following conditions:
$f_i^{T_1}(T) = 1 \quad if\ T = T_{std} = 20$
$f_i^{T_1}(T) = 0 \quad if\ T = T_{\max}$
$\dfrac{\partial f_i^{T_1}(T)}{\partial T} = 0 \quad if\ T = T_{opt}$

The maximum productivity occurs at the optimum temperature (T_{opt}), beyond which, productivity decreases and reaches zero at the maximum temperature ($T_{\max}$). For temperatures below the standard temperature (T_{std}=20°C), the temperature limiting factor, $f_{A_i}^{T_1}(T)$, closely follows $f_{A_i}^{T2}(T)$ which is defined as:

$$f_i^{T_2}(T) = \vartheta_i^{T-20} \tag{4-5}$$

CAEDYM was configured to model algae internal nutrient concentrations using the dynamic nutrient uptake equation, constrained by user-defined minimum and maximum values (Appendix B, Section B.4.2). Additionally, it was assumed that the algae groups were not photo-inhibited. The model combines the processes contributing to algae loss (respiration, mortality, and excretion) as represented by the second term on the right-hand side Equation (4-6). Algae vertical migration and settling were modelled using the constant settling method. It should be noted that resuspension was not configured as part of the model settings. Therefore, the dynamics of algae groups were calculated as follows:

$$\frac{\partial A_i}{\partial t} = \left\{ \underbrace{\mu_i}_{\text{Potential Growth}} - \underbrace{k_{r_i} f^{T_2}(T)}_{\text{Respiration, Mortality, and Excretion}} - \underbrace{\frac{V_{s_{A_i}}}{\Delta z}}_{\text{Settling}} \right\} A_i \qquad (4\text{-}6)$$

where:

A_i = Concentration of the i^{th} algal group $\left(\mathrm{g/m^3}\right)$
Δz = Vertical thickness of compoutational surface layer (m)
k_{r_i} = Algal respiration, mortality, and excretion rate (1/day)
$V_{s_{A_i}}$ = Settling Velocity of A_i (m/day)

CAEDYM was configured to express the concentration of algae in units of chlorophyll-a per unit volume (e.g., mg/L).

4.1.2. **Model Setup, initial data, and boundary conditions**

The computational domain was defined by discretizing the surveyed bathymetry of the ST2 pond into 4 m by 4 m horizontal grids and vertical grids of 10 cm as presented in Appendix B, Figure B-1. Despite testing resolutions from 1 m to 4 m, there was no significant impact on the simulation. Therefore, a 4m horizontal grid size was chosen for computational efficiency. All depths and vertical locations in this chapter are referenced to the elevation datum of 681.75 m above sea level. This datum is aligned with the highest surveyed bathymetric elevation of the pond, approximately 1.68 m above the normal water level (NWL) elevation 680.07 m. This reference was selected conservatively to account for potential increases in water levels during the simulation period. Three inlets (NW, SARM, SW) and one outlet (SE) locations were included in the bathymetry file. The required input data for initialization and boundary forcing were obtained from field measurements described in Chapter 2. Mandatory and optional CAEDYM state variables were defined based on water quality measurements and the equations presented in Table B-1, Appendix B.

Data from in-pond instruments at the sampling locations were used to define temperature and DO initial conditions. Due to safety concerns regarding H2S gas and restricted access, water quality sampling within the inlet structures was not feasible. Therefore, water quality and temperature boundary conditions were defined based on measurements taken in close proximity to each inlet structure. Meteorological data including air temperature, relative humidity, wind speed, wind direction, precipitation, air pressure, and solar radiation were collected from the weather station installed near the pond. The cloud cover was estimated according to Reed (1977) as a function of potential and measured short-wave radiations. Outflows were estimated from the rating curve developed for ST2, and consequently, the inflows were estimated using the reverse level pool routing method described in Chapter 3. All environmental forcing including flow and meteorological data were introduced to the model in time steps of 10 min.

In this study, CAEDYM was configured to simulate the dynamics of total chlorophyll-a (TCHLA), dissolved oxygen (DO), total phosphorus (TP), and total nitrogen (TN). The model was set up to calculate the combined concentrations of three major algae groups dominant in the water quality samples: chlorophyte (CHLR), cyanobacteria (CYANO), and dinoflagellates (DINOF). A simulation time step of 10 seconds was chosen, satisfying the Courant–Friedrichs–Lewy (CFL) stability condition. Simulated variables were outputted hourly to facilitate further analysis.

4.1.3. **Model Calibration, Validation, and Sensitivity Analysis**

ELCOM-CAEDYM was initially set up with the configuration and parameters identical to those used in a prior application to urban stormwater ponds (i.e., Nakhaei et al. 2018, 2021).

Based on error statistics and visual assessments, this configuration did not provide satisfactory results for the ST2 pond. Consequently, a two-stage calibration approach was adopted. First, ELCOM was calibrated through tuning of its parameters and then validated. Next, the coupled ELCOM-CAEDYM model was calibrated by tuning the CAEDYM parameters, followed by validation of the coupled model. The calibration and validation periods are listed in Table 4-1.

Table 4-1: Simulation periods for model calibration and validation.

Model	Calibration period	Validation period
ELCOM	2014-05-16 to 2014-10-03	2015-05-01 to 2015-10-14
CAEDYM	2015-06-10 to 2015-10-13	2014-05-28 to 2014-10-27

Root mean square error (*RMSE*), normalized root mean square error (*RMSEN*), and mean bias error (*MBE*) were used to quantify model performance. These statistical measures are widely used in the literature to assess the performance of hydrodynamic and water quality models (e.g., Carraro et al. 2012; Mcdonald and Muricken 2009; Nakhaei et al. 2021; Trolle et al. 2008b). *RMSE* is calculated as:

$$RMSE = \sqrt{\frac{1}{n}\sum_{i=1}^{n}\left(\varphi_i - \varphi_i^0\right)^2} \tag{4-7}$$

where n is the number of observations, and φ_i and φ_i^0 are the i^{th} observed and simulated variables, respectively. Since *RMSE* has the same units as φ, it can be normalized and represented as a relative percentage:

$$RMSEN = 100 \times (RMSE)/\bar{\varphi} \tag{4-8}$$

where *RMSEN* is the normalized root mean square error in (%) and $\bar{\varphi}$ is the average value of the observed variable. Mean bias error (*MBE*), presented in the same units as φ, is an indicator of the overall tendency of the model to overestimate (*MBE*>0) or underestimate (*MBE*<0) the state variables:

$$MBE = \frac{1}{n}\sum_{i=1}^{n}(\varphi_i - \varphi_i^0) \tag{4-9}$$

Furthermore, the model's performance was also evaluated qualitatively through visual comparison of the patterns and dynamics of observed and estimated variables, similar to previous studies (Bruce et al. 2006; Gal et al. 2009; Hipsey et al. 2006; Missaghi and Hondzo 2011).

3.2.2.1 Calibration of ELCOM Model Parameters

Since ELCOM simulates physical processes based on fundamental equations, it typically requires minimal calibration. Several studies have confirmed this by successfully simulating temperature in various bodies of water with different levels of calibration efforts, ranging from utilizing the uncalibrated model to applying only minimal calibration (Hannoun et al. 2006; León et al. 2005; Missaghi and Hondzo 2010; Romero et al. 2004). A previous application of ELCOM for simulating water temperature in similar stormwater ponds concluded that optimizing albedo and light extinction coefficient, while considering atmospheric stability adjustments, increases the accuracy of simulations (Nakhaei et al. 2018). The accuracy of simulation also depends on accurately defining boundary conditions and environmental forcing.

In this study, 72 calibration scenarios were defined considering atmospheric stability correction, albedo, NWL, light extinction coefficient, cloudiness, and pond's horizontal gird resolution. ELCOM was more sensitive to NWL, albedo and light extinction coefficient. The most important model parameters, albedo and light extinction coefficient, were varied between their lowest and highest published values to achieve the best fit between simulated and observed temperature. The default albedo in ELCOM is 0.08, a value used in many studies with satisfactory results (e.g., Hannoun et al. 2006; Lee et al. 2013; Owens et al. 2014). Nakhaei et al.

(2018), however, reported calibrated albedo values for urban stormwater ponds ranging between 0.30 and 0.35. Therefore, in this study, to determine the calibrated albedo coefficient, the albedo was varied between 0.08 and 0.40. The light extinction coefficient was estimated based on an empirical relationship with Secchi disk depths (Beeton 1958; Dipper 2022; Zhen-Gang 2017) and presented as follows:

$$k_{ext} = 100\frac{1.45}{d_{SD}} \tag{4-10}$$

where k_{ext} is the light extinction coefficient (m^{-1}) and d_{SD} is the Secchi disk depth (cm). The Secchi disk depths in the pond were between 5 cm and 100 cm, resulting in k_{ext} between 29 m^{-1} and 1.45 m^{-1}, respectively. Notably, the average observed Secchi disk depth was 40 cm, corresponding to the k_{ext} value of 3.6 m^{-1}. Furthermore, the inflow and outflow rates were adjusted by varying the NWL elevation within ±4.0 cm of the average surveyed water levels (i.e., 680.08 m). The model was calibrated by selecting the parameters and NWL that resulted in the smallest *RMSE* between observed and simulated water temperature.

3.2.2.1 Calibration of CAEDYM Model Parameters

CAEDYM was calibrated by primarily focusing on simulated TCHLA as the key water quality variable in this study. Initially, CAEDYM parameters were set to values obtained from a previous study (Nakhaei et al. 2021), and the model was configured to simulate five of the seven algae groups that it can simulate. These five groups, cyanobacteria (CYANO), chlorophyte (CHLR), dinoflagellates (DINOF), cryptophyte (CRYPT), and freshwater diatom (FDIAT), were observed during the taxonomic analysis, although with varying concentrations and intermittent occurrences. On average across all the samples, CHLR, CYANO and DINOF accounted for 49%, 23% and 26% of the total algae mass, respectively. Preliminary simulations showed the dominance of the CRYPT group over the CHLR group, despite CRYPT being rarely observed in the samples (less than 2% of the total algae mass on average). Consequently, CRYPT was eliminated from the model. This adjustment not only improved the temporal variation of TCHLA but also established CHLR as the dominant algae group, aligned with field measurements. Furthermore, the removal of FDIAT did not affect the model results. Therefore, the calibration proceeded focusing on the CHLR, CYANO, and DINOF algae groups.

CAEDYM has a large number of adjustable parameters; however, water quality studies commonly attempt to calibrate the model by tuning a much smaller subset of these parameters according to the purpose of their research. By examining parameters considered in the calibration process of similar studies, specifically those targeting the simulation of TCHLA biomass (i.e., Leon et al. 2011; Missaghi and Hondzo 2011; Nakhaei et al. 2021), initially 46 CAEDYM parameters were selected. These parameters, along with their reported minimum and maximum values, are presented in Table 4-2. The calibration process started with the tuning of 15 parameters, marked with an asterisk in Table 4-2. These parameters were chosen because they were either identified as highly influential in the sensitivity analysis conducted by Missaghi (2014) or had varying assigned values across the similar studies (i.e., Leon et al. 2011; Missaghi and Hondzo 2011; Nakhaei et al. 2021). Next, the model was run over the calibration period using both the maximum and minimum values of each parameter, while the remaining parameters were kept at their initial values suggested by Nakhaei et al. (2021). If the pond-averaged simulated variables, particularly TCHLA, showed a change below 2%, the parameter was retained at its initial value and considered calibrated. Nine out of the 15 parameters, marked by the † symbol in Table 4-2, resulted in changes greater than 2%. These parameters were fine-tuned through the calibration process, in which CAEDYM was run with incremental adjustments made to each parameter to determine the values that optimized model performance. The performance assessment involved both a visual evaluation of simulated variables, with a focus on TCHLA and DO, and an examination of RMSE. Calibrating these nine parameters was sufficient to consider the CAEDYM model calibrated, making the tuning of the remaining parameters unnecessary.

Quantitative statistics, while valuable for summarizing model performance, have their limitations. For example, RMSE can be disproportionately large due to outliers or errors in the timing and location of simulated values, even when the temporal and special trends of simulated variables generally align with the observed trends. Therefore, in addition to quantitative statistics, the model's performance was evaluated through visual inspection of time series of simulated and measured variables.

Table 4-2: CAEDYM parameters identified important for calibration, including their symbols, units, maximum and minimum values from literature, and assigned. Biological parameters are presented for the CHLR group.

Parameters	Symbol	Unit	Min	Max	Assigned
Biological parameters					
Average Ratio of C to Chlorophyll-a	Ycc*	mg C/mg Chla	0.3	400	40
Algal Constant settling velocity	ws	m/s	-1.16E-06	1.00E-05	-2.30E-07
Critical shear stress	$tcpy$	N/m2	0.001	0.01	0.001
Half saturation constant for nitrogen uptake	K_N	mg/L	0	30	0.07
Half saturation constant for phosphorus	K_P	mg/L	0.001	6	0.02
Light half saturation constant for algal limitation	[illegible] *†	μE/m^{2}s	100	145	130
Light saturation for maximum production	I_{st} *†	μE/m^{2}s	75	710	100
Maximum internal nitrogen concentration	[illegible]$_{max}$ *	mg N/mg Chla	5	14.4	9
Maximum internal P concentration	IP_{max} *†	mg P/mg Chla	0.08	21	2.4
Maximum potential growth rate of phytoplankton	[illegible] *†	1/day	0.7	4.66	0.6
Maximum rate of nitrogen uptake	UN_{max} *	mg N/mg Chla/day	0.12	6.48	3.5
Minimum internal nitrogen concentration	IN_{min}	mg N/mg Chla	1	36	3
Minimum internal P concentration	IP_{min} *†	mg P/mg Chla	0.008	1	0.1
Phytoplankton optimum temperature	T_{opt} *†	°C	21	34	25
Phytoplankton maximum temperature	T_{max} *†	°C	28	39	31
Respiration mortality and excretion	K_r *†	1/day	0.001	0.28	0.02
Standard growth temperature	T_{sta} *	°C	14	20.8	20
Temperature multiplier for respiration	ϑ_{res}	--	1.03	1.13	1.06
Temperature multiplier function for phytoplankton growth	ϑ_{growth} *†	--	1.02	1.14	1.06
Chemical parameters					
Aerobic/anaerobic factor for both sediment and water colu	fanB	--	0.3	0.8	0.3
Density of particulate organic matter (POM) particles	POMDensity*	kg/m^3	1010	2600	1005
Diameter of POM particles	POMDiameter	m	0.00005	0.00005	0.00005
Half saturation constant for nitrification	KOn	mg O/L	0.081	4	0.5
Half saturation constant for denitrification dependence on D	KN2	mg/L	0.01	6.5	0.4
Half saturation of POM/DOM decomposition on DO	KDOB	mg/L	1.5	1.5	1.5
Maximum mineralization of DONL to NH4	DON1max	1/day	0.002	1	0.003
Maximum mineralization of DOC labile to DIC	DOC1max*†	1/day	0.001	0.15	0.011
Maximum mineralization of DOPL to PO4	DOP1 max	1/day	0.002	1	0.01
Maximum transfer of POCL to DOCL	POC1 max	1/day	0.001	0.07	0.07
Maximum transfer of PONL to DONL	PON1 max	1/day	0.001	0.05	0.005
Maximum transfer of POPL to DOPL	POP1 max	1/day	0.01	0.1	0.03
Maximum denitrification rate under anoxia at 20	koN2	1/day	0.3	0.6	0.15
Nitrification rate coefficient	koNH	1/day	0.005	0.6	0.5
Photo-respiration phytoplankton DO loss Specific	prc	--	0.02	0.02	0.02
Specific light attenuation due to the action of POC	KePOC	mg/L/m	0.02	0.02	0.02

Table 4-2 **(Continue…)**

Sediment related parameters					
Controls sediment release of PO4 via O	KOxS-PO4	mg/L	0.05	3	1
Half saturation for DO sediment flux	KSOs	mg O/L	0.2	5	0.7
Half saturation for sediment NH4 release dependence on D	KDOS-NH4	mg/L	0.25	0.5	0.5
Half saturation for sediment NO3 release dependence on D	KDOS-NO3	mg/L	0	0.3	0.3
Half saturation for sediment DOC release dependence on I	KDOS-DOC	mg/L	0	0.005	0.005
Maximum NH4 sediment flux	$SmpNH_4$	g/m2/day	0.002	0.1	0.09
Maximum release rate of DOC from sediment at 20	SmpDOCL	g/m2/day	0.005	0.005	0.005
Maximum release rate of NO3 from Sediment at 20	$SmpNO_3$	g/m2/day	0.01	0.1	0.03
Sediment release rate of PO4	$SmpPO_4$*	g/m2/day	0.0003	49	0.04
Static sediment exchange rate of O2	rSOs	g/m2/day	0.2	3.95	1.3
Temperature multiplier for sediment nutrient fluxes	ϑ_{sed}	--	1.04	1.1	1.05

* Parameters calibrated in this study

Ɨ † Selected for "Sensitivity Analysis"

3.2.2.1 Sensitivity Analysis of CAEDYM model parameter

The sensitivity analysis quantifies the impact of perturbation of model parameters, denoted as θ (e.g., *Pmax* and *Kr*) from their calibrated values, denoted as θ^c, on the simulated variables, denoted as φ (e.g., TCHLA and DO). However, in the case of comprehensive models like CAEDYM, characterized by an excessive number of parameters, conducting a complete sensitivity analysis that includes all model parameters is impractical (Romero et al. 2004). As a result, sensitivity analyses for CAEDYM are commonly limited to a smaller subset of parameters. For example, Missaghi et al. (2014) performed a sensitivity analysis of Lake Minnetonka's model and identified seven CAEDYM parameters as the most influential. However, Lake Minnetonka is significantly larger (area of 60 Km^2 and maximum depth of 34 m) than the study pond, and hence, the parameters deemed most influential and their relative importance may not be the same for the study pond. Therefore, in this study, a sensitivity analysis was carried out for the CAEDYM model developed for the study pond.

The selected parameters for sensitivity analysis marked by the † symbol in Table 4-2 were perturbed by $\pm\Delta\theta$ and inputted into CAEDYM to simulate the time series of perturbed variables throughout the calibration period. Later in this chapter, the Table 4-7 provides details of selected parameters and their perturbations. T_{max} was perturbed by 1°C, and T_{opt} was perturbed by 1°C and 2°C. For the remaining parameters, the perturbation was set as the minimum of $(\theta^{max} - \theta^c)$ and $(\theta^c - \theta^{min})$, where θ^{max} and θ^{min} are the maximum and minimum reported values (Table 4-2). Next, the resulting simulated variables were averaged over the computational cells to generate the pond-integrated time series, φ_θ. These time series were assessed visually, as will be discussed later. Next, the pond-integrated time series were averaged over the simulation period to give the pond-averaged values, $\bar{\varphi}_\theta$. Finally, the sensitivity of variable φ to the parameter θ was quantified by defining a sensitivity index, SI_θ^φ, adopted from Abtahi (2023) and Sun et al. (2012) as follows:

$$SI_\theta^\varphi = 100 \times \frac{|\bar{\varphi}_{\theta+\Delta\theta} - \bar{\varphi}_{\theta-\Delta\theta}|}{\bar{\varphi}_\theta} \quad (4\text{-}11)$$

For each simulated variable, the most sensitive parameters are those with greater values of SI_θ^φ.

4.2. RESULTS AND DISCUSSION

The model output for selected variables was processed and compared with observed data, and the results are presented here. It should be noted that all depths presented in the figures are referenced to the lake's outline at an elevation of 681.75 meters, which is 1.68 meters above the normal water level (NWL) elevation of 680.07 m.

4.2.1. ELCOM Calibration

The representative scenarios and corresponding error statistics are presented in Table 4-3. The RMSE, RMSEN, and MBE were calculated based on temperatures measured by the deployed instruments. These statistics revealed that temperature was more sensitive to NWL, so NWL was calibrated first. By adopting the predefined albedo value of 0.30 and the extinction coefficient determined from the average observed Secchi depth (i.e., 40 cm), the best performance occurred at NWL of 680.07 m. Next, the model performance was further enhanced at albedo of 0.2. Tuning of Secchi disk depth did not improve performance significantly (Appendix B, Figure B-2); therefore, the Secchi depth of 40 cm was selected, as it was derived from direct measurements. The calibrated parameters used in this study are shown in Table 4-3 under Scenario 11.

Table 4-3: Performance of representative calibration runs of ELCOM in estimation of temperature during the calibration period.

ELCOM Scenario	NWL (m)	Albedo	Secchi Disk (cm)	RMSE (°C)	RMSEN (%)	MBE (°C)
1	680.04	0.20	40	1.60	9.60	-0.98
2	680.04	0.30	40	1.96	11.63	-1.55
3	680.05	0.20	40	1.45	8.75	-0.73
4	680.05	0.30	40	1.77	10.53	-1.31
5	680.06	0.20	40	1.36	8.24	-0.44
6	680.06	0.30	40	1.60	9.56	-1.05
7	680.07	0.08	40	1.60	9.61	0.54
8	680.07	0.15	40	1.41	8.54	0.13
9	680.07	0.20	10	1.35	8.16	-0.22
10	680.07	0.20	20	1.35	8.18	-0.21
11*	**680.07**	**0.20**	**40**	**1.37**	**8.30**	**-0.17**
12	680.07	0.20	60	1.39	8.42	-0.14
13	680.07	0.20	80	1.42	8.60	-0.11
14	680.07	0.20	100	1.44	8.73	-0.10
15	680.07	0.25	40	1.41	8.49	-0.50
16	680.07	0.30	40	1.53	9.17	-0.81
17	680.07	0.40	40	1.98	11.69	-1.51
18	680.08	0.08	40	2.04	12.82	1.08
19	680.08	0.15	40	1.77	11.24	0.64
20	680.08	0.20	40	1.65	10.48	0.31
21	680.08	0.25	40	1.62	10.25	-0.03
22	680.08	0.30	40	1.68	10.48	-0.38
23	680.08	0.30	40	1.68	10.48	-0.38
24	680.09	0.20	40	2.08	14.01	0.72
25	680.09	0.30	40	2.04	13.48	-0.02

* Accepted scenario as calibrated run. Bold text indicates the values of calibrated parameters and resulting statistics.

Figure 4-2 displays measured and simulated average temperatures at NW, SW, and SE sampling locations. At the SARM inlet, only the simulated temperature is displayed, as measurements were not taken during the calibration period. The figure also presents the pond-integrated temperature (17.2°C), an average across the computational cells and over the simulation period. The calibrated model accurately simulated average temperatures at NW, SW, and SE, with only slight underestimations. These results are consistent with the error statistics in: RMSE of 1.37°C, RMSEN of 8.3%, and MBE of -0.17°C. Notably, the SW and SE locations are more representative of the pond, while the NW and SARM inlets are 4.2°C and 1.4°C colder, respectively, than the pond. These colder temperatures are primarily due to the impact of colder inflows into the pond. Finally, the model accurately captured the overall temperature rise along the pond's main axis. Both measurements and simulation results demonstrated an average temperature increase of 0.6°C from SW to SE locations.

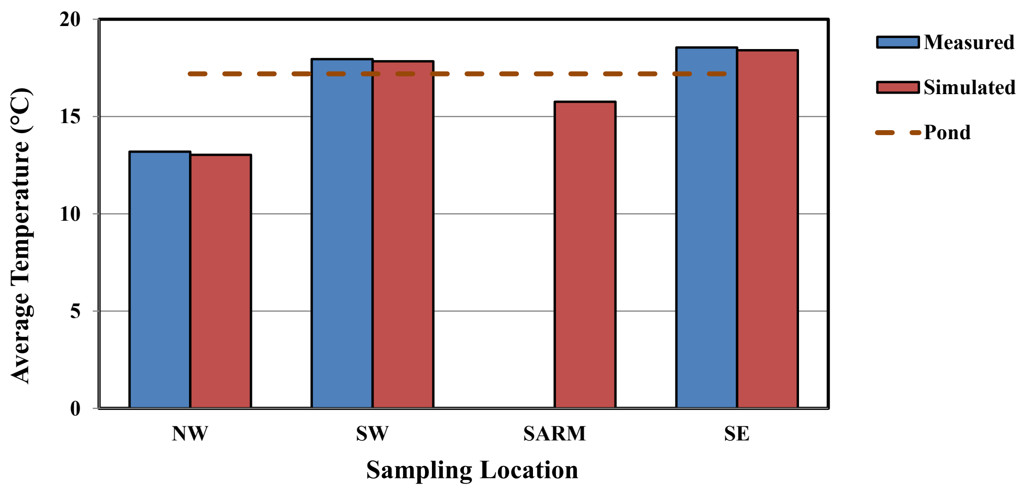

Figure 4-2: Measured and simulated average temperatures at sampling locations during the calibration. The dashed line shows the pond-integrated temperature.

More detailed error statistics presented in Table 4-4 were calculated based on point-to-point comparisons of measured and simulated temperature time series at different locations (Figure 4-3 to Figure 4-5). In general, the model performed better and more consistently at SW and SE locations, with an RMSE range of 1.2°C to 1.5°C. In contrast, the NW inlet displayed a higher average and a broader range of error, with the smallest and largest RMSE values occurring near the bed and the surface, measuring 0.4°C and 2.4°C, respectively. The low error at the bottom of the NW inlet is a result of boundary condition influence. The relatively higher error near the surface can be attributed to the deep, narrow, and isolated bathymetry of the NW inlet, which limits ELCOM’s ability to accurately model temperature profile. Another reason for the higher RMSE at NW could be the shading at this location, which results in lower surface temperatures not accurately captured by ELCOM.

Table 4-4: Performance of calibrated ELCOM in estimation of temperature at different depths of NW, SW, and SE locations during calibration period.

	NW				SW				SE			
Depth below Outline (m)	**Mean** (°C)	**RMSE** (°C)	**RMSEN** **(%)**	**MBE** (°C)	**Mean** (°C)	**RMSE** (°C)	**RMSEN** **(%)**	**MBE** (°C)	**Mean** (°C)	**RMSE** (°C)	**RMSEN** **(%)**	**MBE** (°C)
-2.1	---	---	---	---	---	---	---	---	19.3	1.2	6.5	-0.5
-2.2	16.4	2.2	13.5	0.4	18.9	1.2	6.1	-0.4	---	---	---	---
-2.4	---	---	---	---	---	---	---	---	18.9	1.2	6.4	-0.3
-2.5	---	---	---	---	18.5	1.2	6.6	-0.2	---	---	---	---
-2.6	14.1	2.4	17.2	-0.6	---	---	---	---	---	---	---	---
-2.7	---	---	---	---	18.0	1.3	7.1	0.0	18.7	1.2	6.6	-0.2
-2.8	12.7	1.7	13.3	-0.5	---	---	---	---	---	---	---	
-2.9	---	---	---	---	---	---	---	---	18.4	1.2	6.6	-0.1
-3.0	---	---	---	---	17.5	1.3	7.5	-0.1	--	---	---	
-3.1	---	---	---	---	---	---	---		18.2	1.3	7.0	0.0
-3.3	11.5	0.6	5.6	-0.1	16.9	1.4	8.4	0.1	17.8	1.5	8.3	0.3
-3.7	11.3	0.4	3.5	0.0	---	---	---	---	---	---	---	---

Time series plots in Figure 4-3 to Figure 4-5 provide visual confirmation of ELCOM's performance, demonstrating the model's successful simulation of temperatures across various time scales, from diurnal variations to the seasonal averages. The model particularly performed well at the SW and SE locations, with acceptable performance at NW. Furthermore, the time series indicates that water temperature more closely follows the trends in air temperature at layers closer to the surface. (Figure 4-6). A notable feature observed in the time series plots is that simulated temperature sometimes has larger diurnal amplitudes than the measured values. This may be due to inaccuracies in the estimated cloudiness used in the model, as cloudiness measurements were unavailable for this study. Consequently, near-surface temperatures were sometimes over- or under-estimated when the actual cloudiness ratio deviated from the estimated value. Also, while the model did account for atmospheric instability by adjusting the heat exchange coefficients there may still be errors associated with this approach. Nonetheless, the difference between observed and simulated diurnal amplitudes decreased with increasing depth.

The model's capability to represent the thermal characteristics of the pond was further assessed through visual examination of color plots in Figure 4-7 to Figure 4-10. Mixed periods, characterized by a uniform temperature spanning from the surface to the bed, and stratified periods, during which a temperature difference (here exceeding 1°C) exists between the top and bottom layers are both evident in these plots. For example, throughout most of August, characterized by dry and warm conditions (Figure 4-6), ELCOM effectively simulated the stratification observed at sampling locations. Additionally, the color plots illustrate that in the second week of September, when air temperatures dropped below 5°C (Figure 4-6), the vertical mixing observed at all the sampling locations was accurately captured by the model (Figure 4-7 to Figure 4-10). Moreover, these plots allow for the identification of surface mixed layers, characterized by relatively uniform temperature, as well as thermocline, characterized by rapid temperature gradient. For instance, during the warm and dry period in early August, the depth of the mixed layers extends deeper at all locations, reaching the bottom of the pond at some locations, inducing mixing around August 10. The model has also effectively predicted the depth of thermocline, with shallower depths at NW and deeper depths at the SW and SE locations. These plots also effectively display how the thermal structure was influenced by inflows. The inflows have a cooling impact near the inlets. With higher inflow rates, this cooling influence extends both horizontally along the bottom layers, resulting in lower temperatures towards the outlet, and vertically upward, leading to shallower surface mixed layers. This effect was particularly evident during the significant inflow in July 25, when a large inflow caused the water columns at all the sampling locations became fully mixed. The plots show that ELCOM also accurately captured this phenomenon (Figure 4-7 to Figure 4-10).

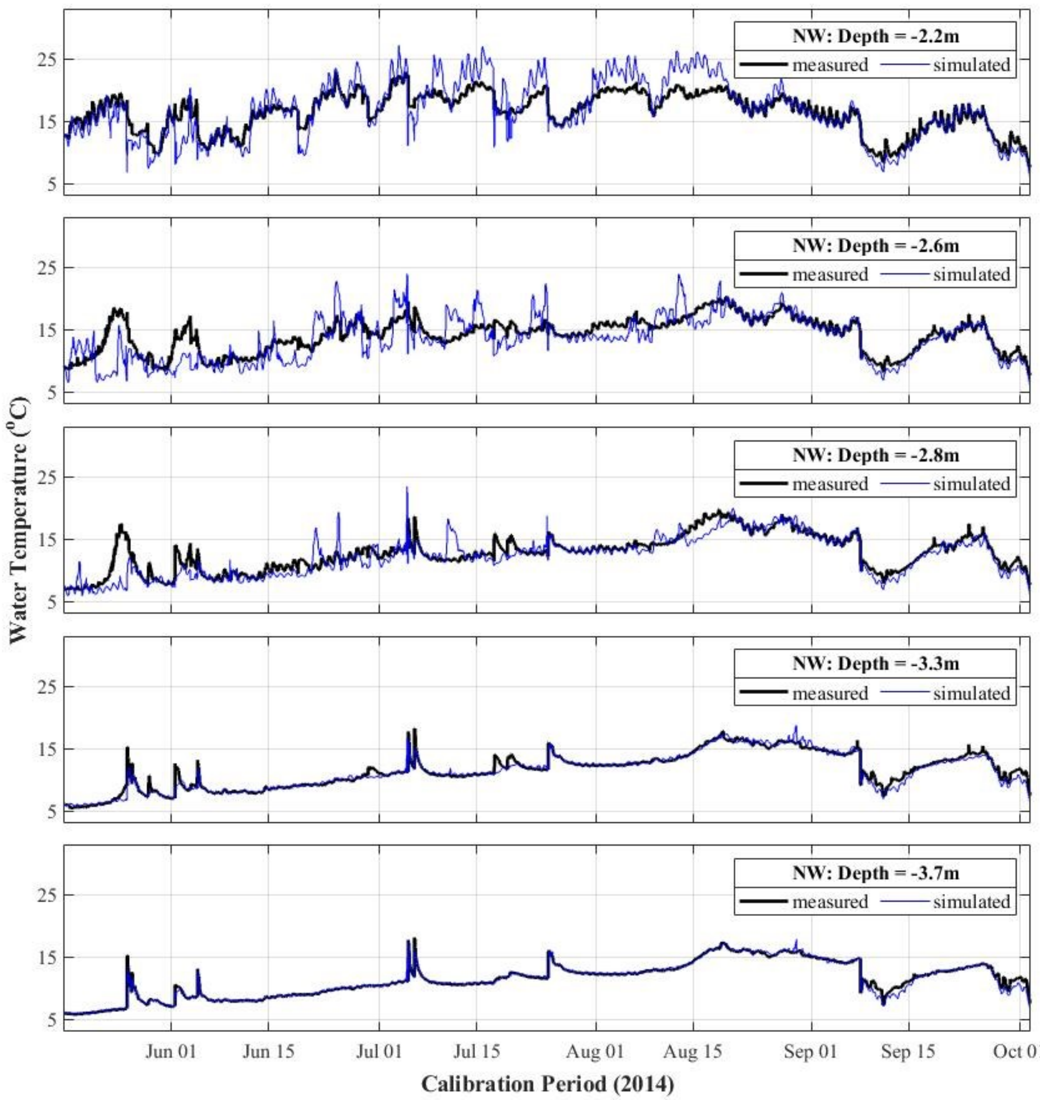

Figure 4-3: Comparison of observed and modelled temperature time series at different depths of the NW sampling location over the calibration period.

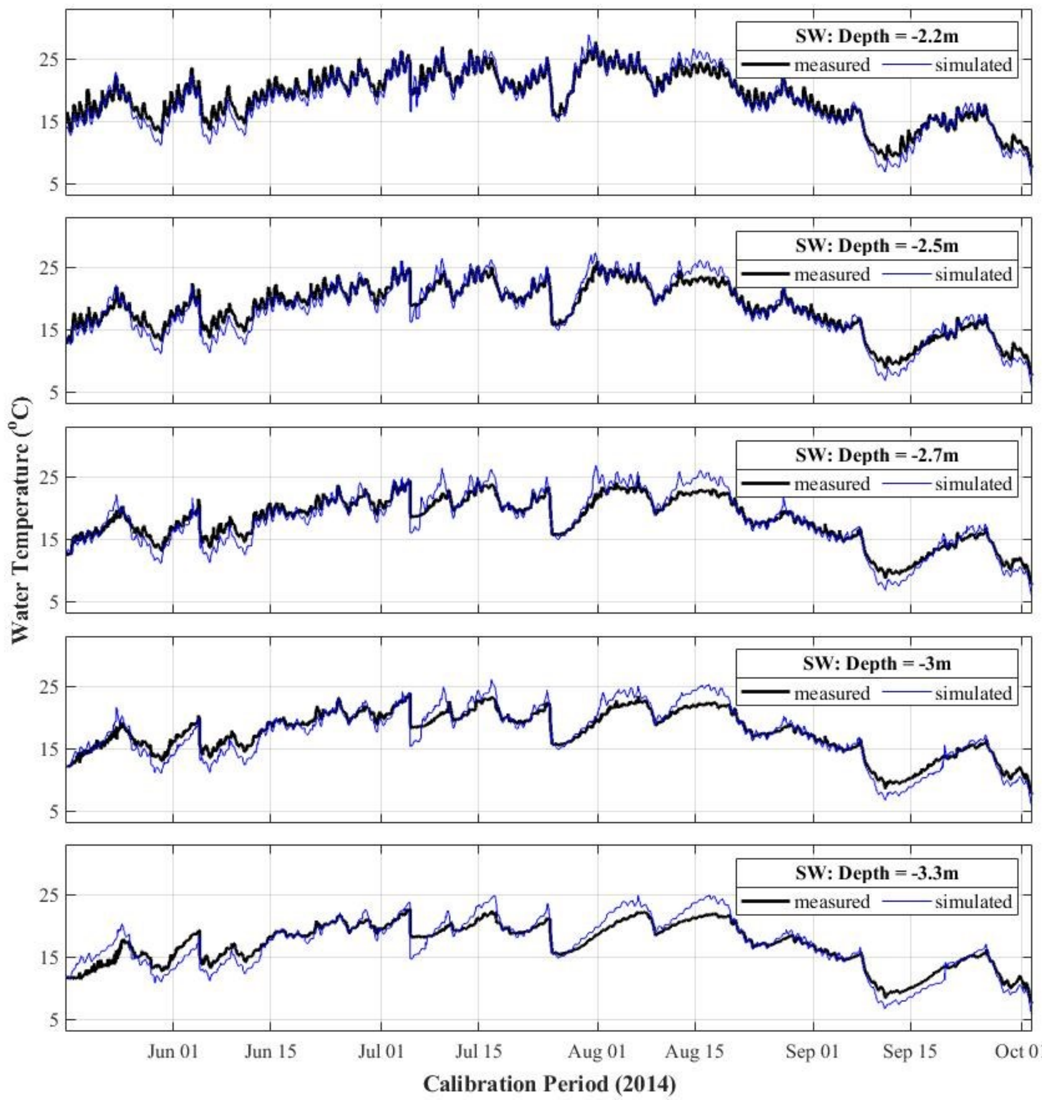

Figure 4-4: Comparison of observed and modelled temperature time series at different depths of the SW sampling location over the calibration period.

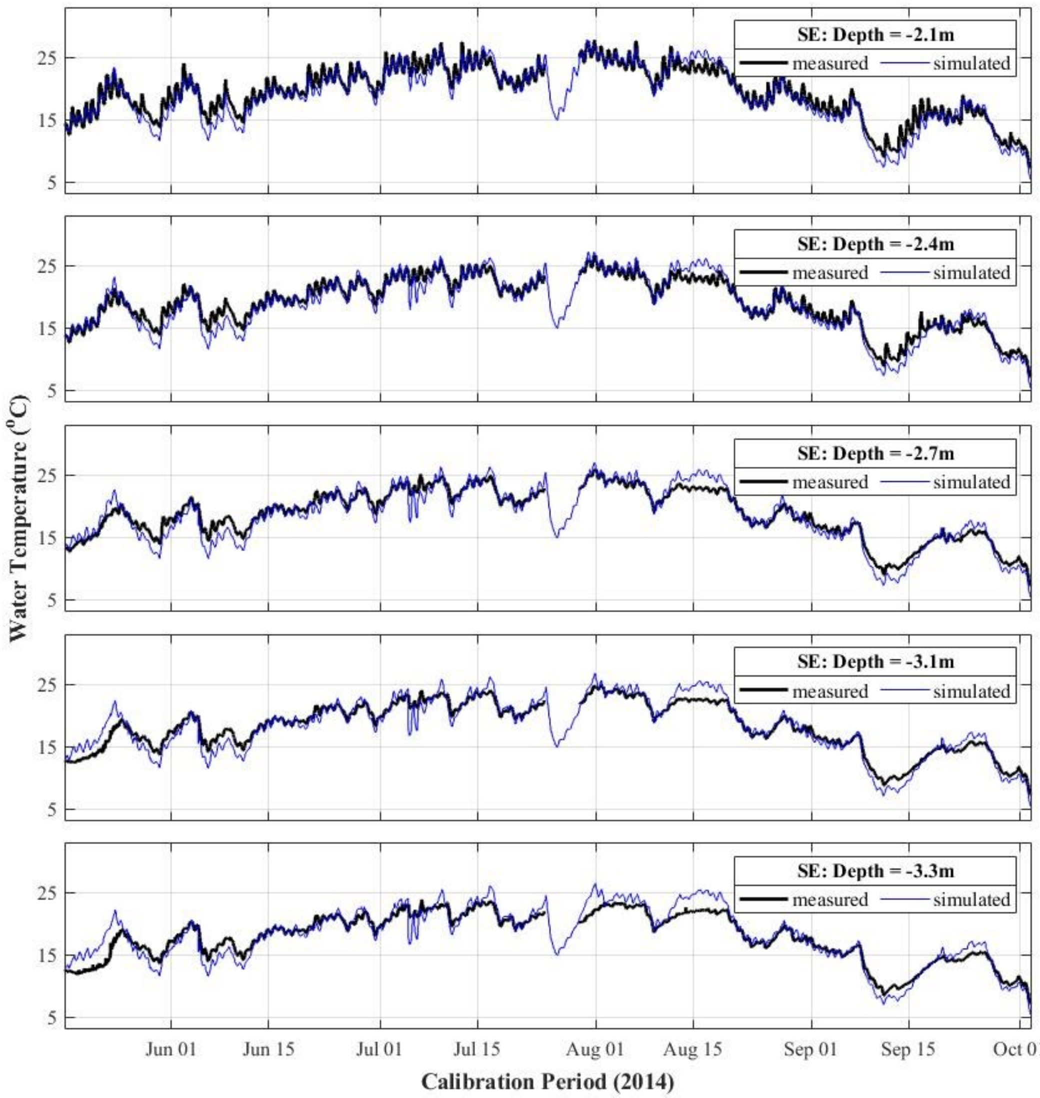

Figure 4-5: Comparison of observed and modelled temperature time series at different depths of the SE sampling location over the calibration period.

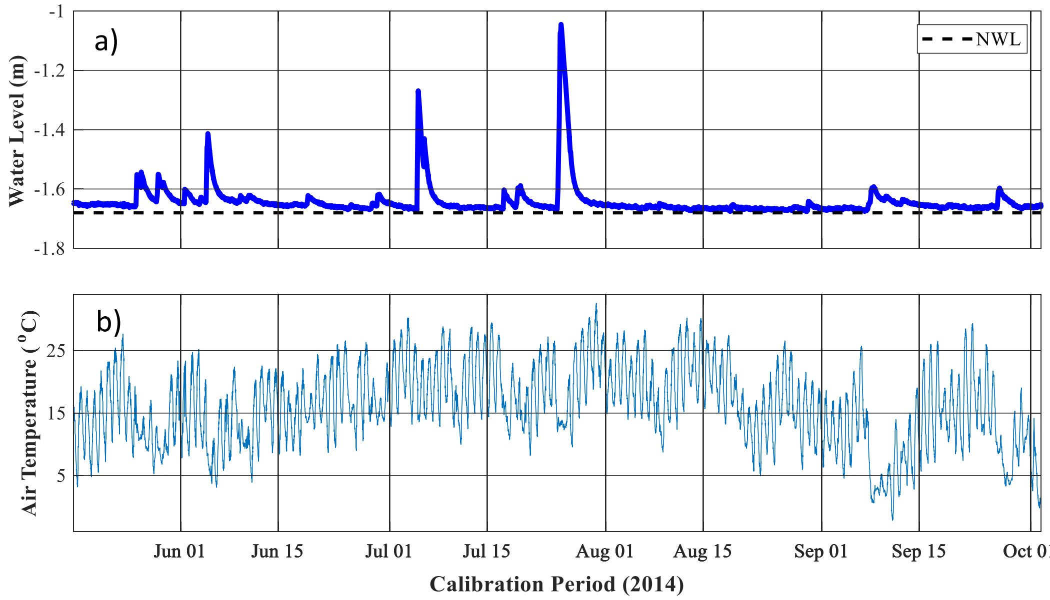

Figure 4-6: a) Water level and b) air temperature during calibration period (2014).

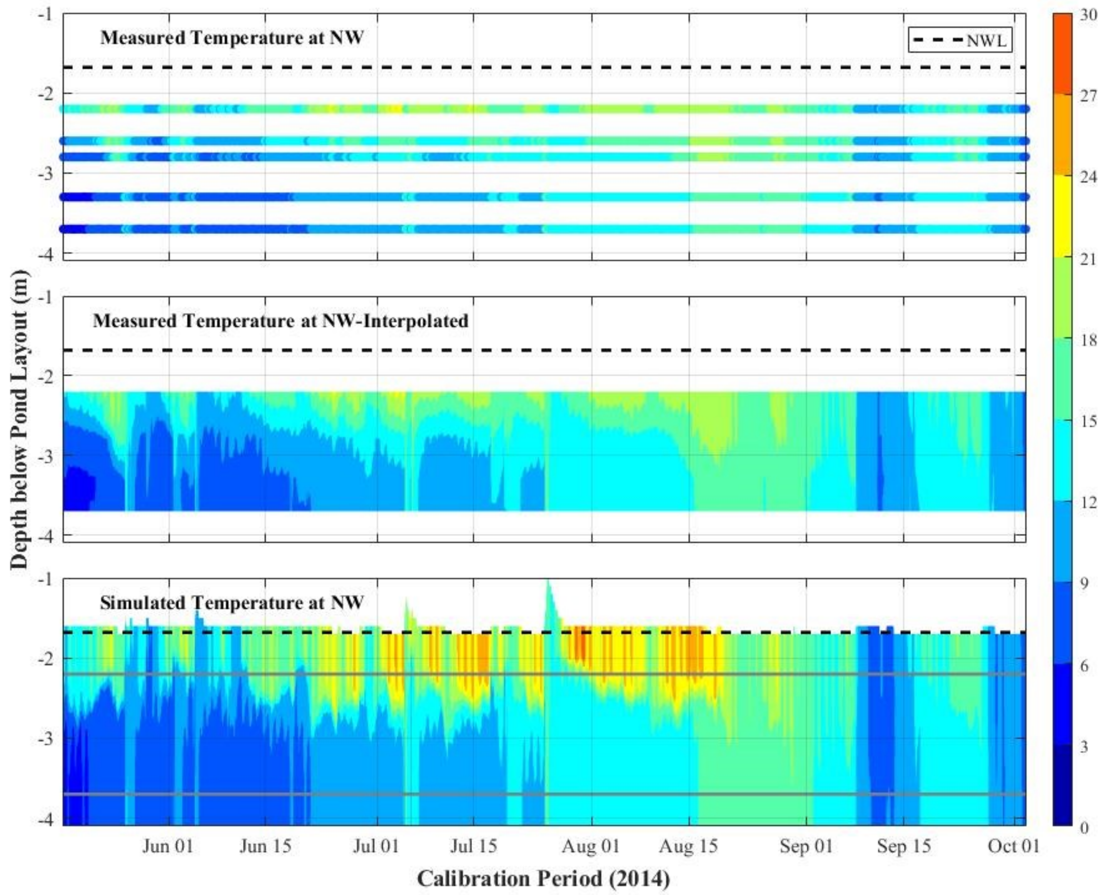

Figure 4-7: Measured and modelled temperatures at NW sampling location during the calibration period. The dashed lines represent the normal water level at elevation 680.07m.

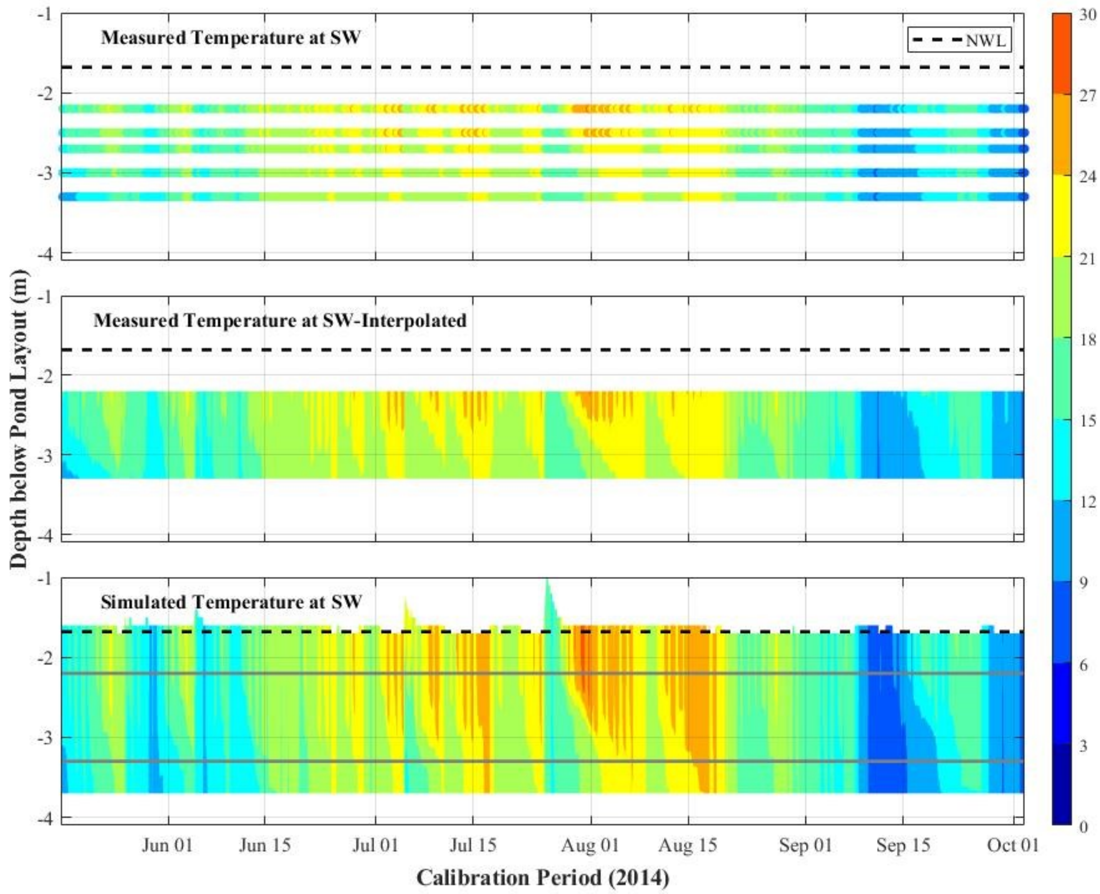

Figure 4-8: a) measured and modelled temperatures at SW sampling location during the calibration period. The dashed lines represent the normal water level at elevation 680.07m.

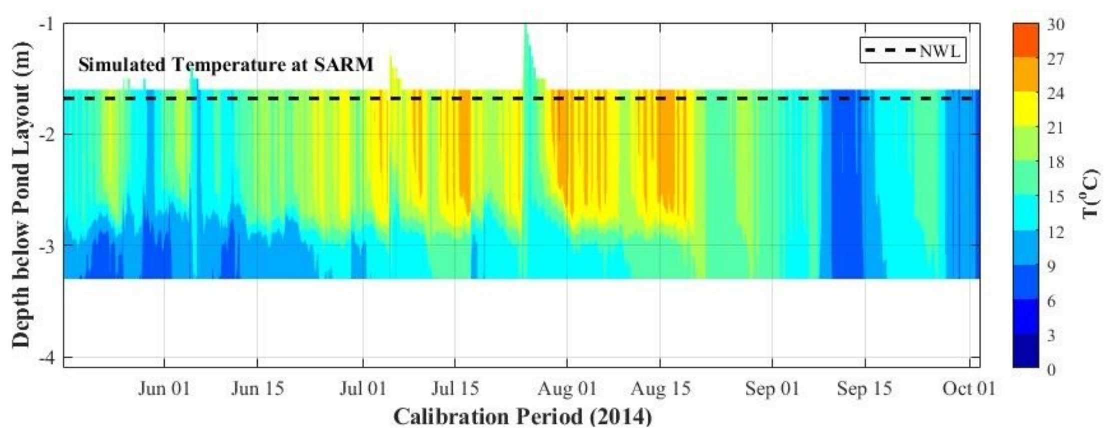

Figure 4-9: Simulated temperatures at SARM sampling location during the calibration period. The dashed line represents the normal water level at elevation 680.07m.

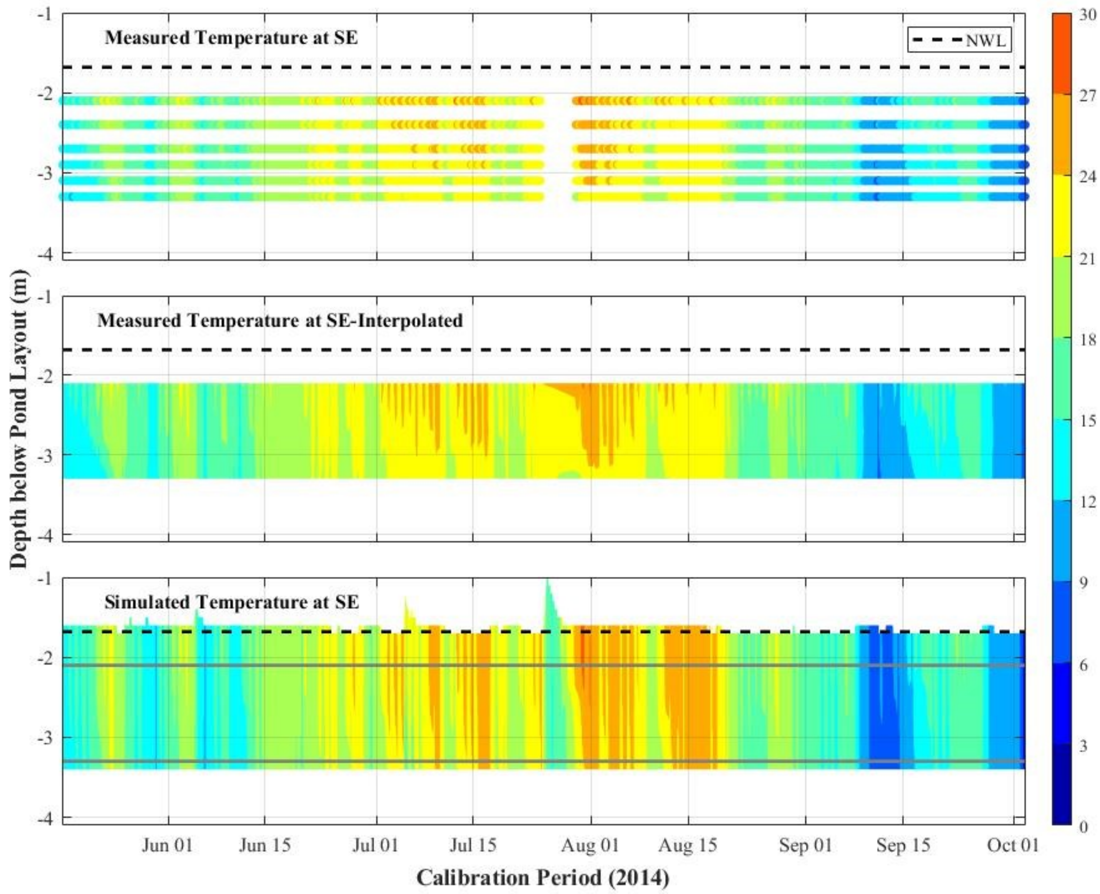

Figure 4-10: measured and modelled temperatures at SE sampling location during the calibration period. The dashed lines represent the normal water level at elevation 680.07m.

Figure 4-11 displays the stratification occurrence, defined as percent of time when the top-bottom temperature difference at a location exceeded 1°C. The figure indicates that ELCOM underestimated stratification at the NW, SW, and SE locations, by 4%, 19%, and 25%, respectively. This was expected since the temperature contour plots (Figure 4-7 to Figure 4-10) consistently showed the model simulating the thermocline at greater depths. Nonetheless, the model's performance was consistent as underestimation was observed everywhere, and additionally, both observed and simulated stratification occurrences decreased from the inlets towards the outlet. The increased stratification at the NW inlet is due to the colder near-bed inflows which resulted in higher top-bottom temperature differences compared to the SW and SE locations. Moreover, the NW location is deep and isolated enough that a significant top-bottom temperature difference often persisted, meaning the pond remained stratified over most of the validation period.

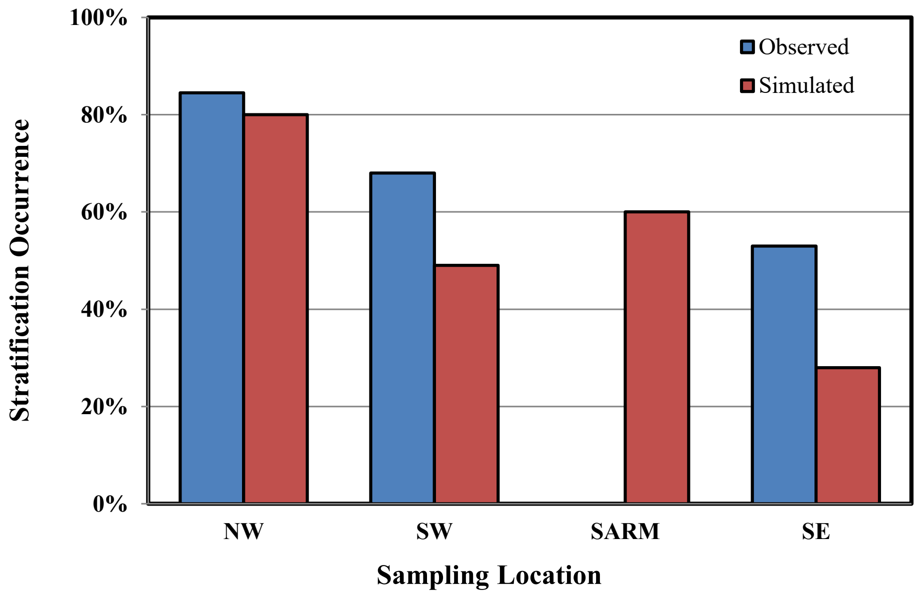

Figure 4-11: Observed and simulated stratification occurrence (%) during the calibration period.

4.2.2. **ELCOM Validation**

Measured and simulated average temperatures at NW, SW, and SARM sampling locations during the validation period are presented in Figure 4-12. Only the simulated temperature is presented at the SE outlet, as no in-pond instrument was deployed during the validation period. The figure also displays the pond-integrated temperature (17.9°C). Similar to the calibration period, the model accurately simulated average temperatures at NW, SW, and SARM. The average MBE across all locations indicated a minor overestimation of temperature by 0.5°C, while the average RMSE and RMSEN were 1.9°C and 12.3%, respectively (Table 4-5). Similar to the calibration period, the NW inlet has the lowest temperature, on average 3.9°C colder than the pond. However, the SARM inlet's temperature was within 1°C of SW and SE temperatures, which is mainly attributed to the lower inflows during the validation period. Both measured and simulated temperatures generally increase along the pond's major axis, with exception of at the SARM inlet. The model simulated a warm-up of 0.4°C from the SW sampling location to the SE outlet.

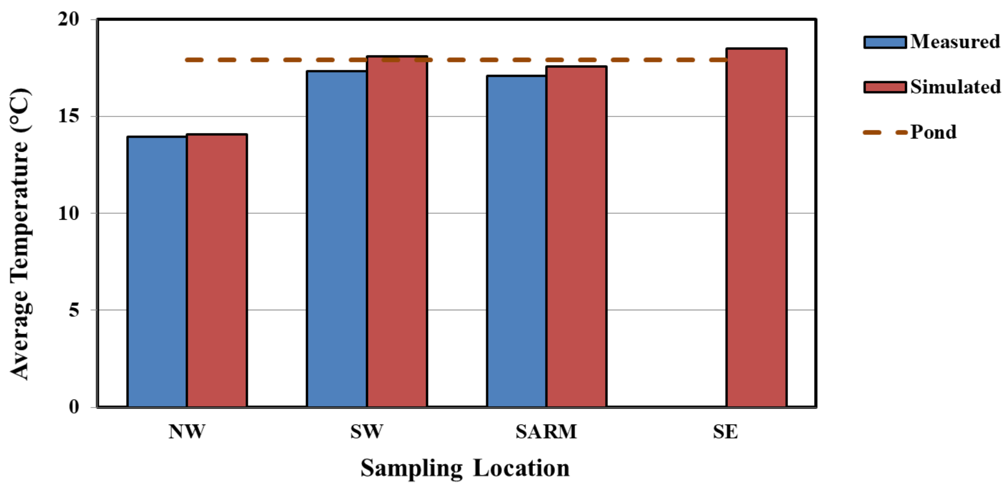

Figure 4-12: Measured and simulated average temperatures at sampling locations during the validation period. The dashed line shows the pond-integrated temperature.

Table 4-5 presents detailed error statistics for the validation period, derived by comparing the simulated temperatures with measurements at deployed depths (Figure 4-13 to Figure 4-15). The lowest RMSE of 1.0°C was observed near the bed of the NW inlet, while the highest RMSE of 3.1°C was near the bed of the SARM inlet. Similar to the calibration period, model performance was consistent at the SW location, with an RMSE range of 1.6°C to 1.9°C.

Comparison of temperature time series (Figure 4-13 to Figure 4-15) with the time series of water level and air temperature (Figure 4-16) reveals that ELCOM tended to overestimate the near-bed temperature during dry and warm periods. For example, in early to mid-July 2015, the simulated mixed layer extended deeper than the observed one, resulting in a higher error near the bed. This is similar to previous studies that found that ELCOM tended to overestimate the thermocline depth and the mixed layer thickness (Huang et al. 2010; Nakhaei et al. 2018; Paturi et al. 2012). Additionally, as discussed in the calibration section, the simulated diurnal patterns exhibited larger amplitudes than the observed ones, likely due to a constant representation of cloudiness. However, this discrepancy decreases near the bed.

Table 4-5: ELCOM's error statistics for temperature estimation at different depths and locations of ST2 during the validation period.

	NW				SW				SARM			
Depth below Outline (m)	**Mean (°C)**	**RMSE (°C)**	**RMSEN (%)**	**MBE (°C)**	**Mean (°C)**	**RMSE (°C)**	**RMSEN (%)**	**MBE (°C)**	**Mean (°C)**	**RMSE (°C)**	**RMSEN (%)**	**MBE (°C)**
-1.7	18.1	1.7	9.6	-0.4	---	---	---		18.4	1.4	7.6	-0.4
-2.1	16.7	1.8	10.7	0.3	17.9	1.6	9.2	0.5	---	---	---	
-2.2	---	---	---		---	---	---		17.9	1.8	9.8	0.5
-2.3	---	---	---		17.5	1.9	10.6	0.8	---	---	---	
-2.5	15.3	2.3	14.9	0.7	---	---	---		17.3	2.1	12.4	0.8
-2.6	---	---	---		17.2	1.9	11.1	0.8	---	---	---	
-2.9	12.0	2.5	20.7	0.3	16.7	1.9	11.6	1.0	14.7	3.1	20.3	1.1
-3.2	12.1	2.2	18.1	0.1	---	---	---		---	---	---	
-3.5	11.9	1.6	13.4	0.0	---	---	---		---	---	---	
-3.8	11.5	1.0	8.7	0.0	---	---	---		---	---	---	

The temperature color plots presented in Figure 4-17 to Figure 4-20) show that the predicted mixed and stratified periods closely match the observed patterns. Moreover, while ELCOM overestimated the depth of the mixed surface layer it accurately replicated the timing of he observed temporal variations. For example, during extended periods of warm and dry weather, such as the last week of June, the first half of July, and the second week of August (Figure 4-16), ELCOM replicated the deepening of the surface mixed layer at all sampling locations. Additionally, ELCOM simulated the generally thermally mixed conditions at SW and SE, and generally stratified conditions at the NW and SARM inlets. Furthermore, the pond mixing driven by the significant inflows of mid-July (Figure 4-16) or caused by the colder weather of early September have been closely captured by the simulated results.

Figure 4-21 illustrates that, similar to the calibration period, stratification occurrence generally decreased along the pond's major axis, with an increase at the SARM inlet. Overall, ELCOM underestimated the stratification occurrence by approximately 14%. The maximum error observed at SARM (28%) is a direct result of the 1.1°C overestimation of near-bed temperatures (Table 4-5 and Figure 4-15), leading to less predicted stratification at this location (Figure 4-19). The minimum error observed at NW (4%), however, is due to the strong influence of boundary conditions on the simulated temperatures near the bed, resulting in an MBE of nearly 0°C (Table 4-5 and Figure 4-13).

In both the calibration and validation periods, ELCOM generally performed satisfactorily in estimating the magnitude of water temperature and effectively capturing the temporal and spatial variations. The error statistics fall within or are less than the range of values reported in literature (e.g., Bolkhari 2014; Carraro et al. 2012; Nakhaei et al. 2018; Paturi et al. 2012).

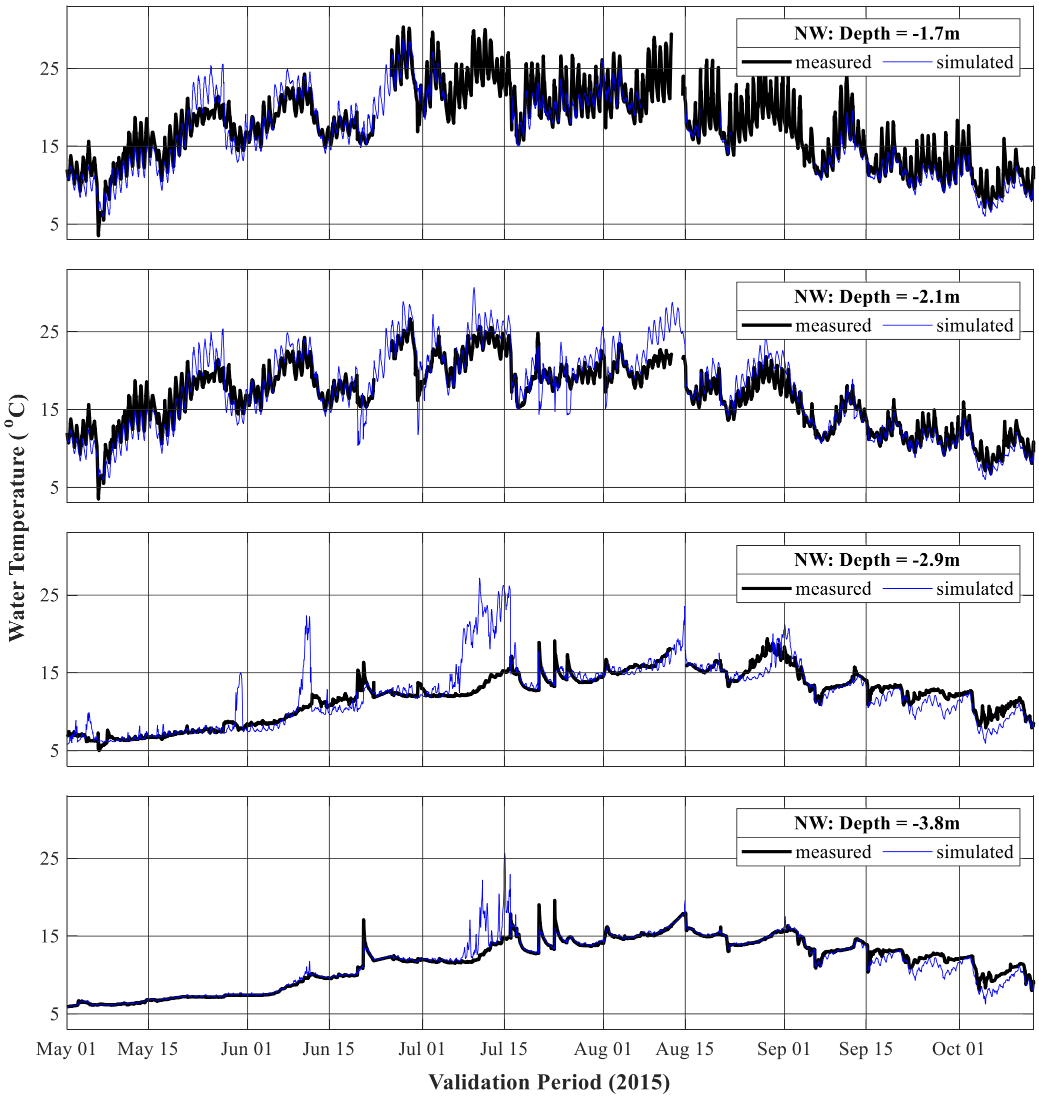

Figure 4-13: Comparison of observed and modelled temperature time series at different depths of the NW sampling location over the validation period.

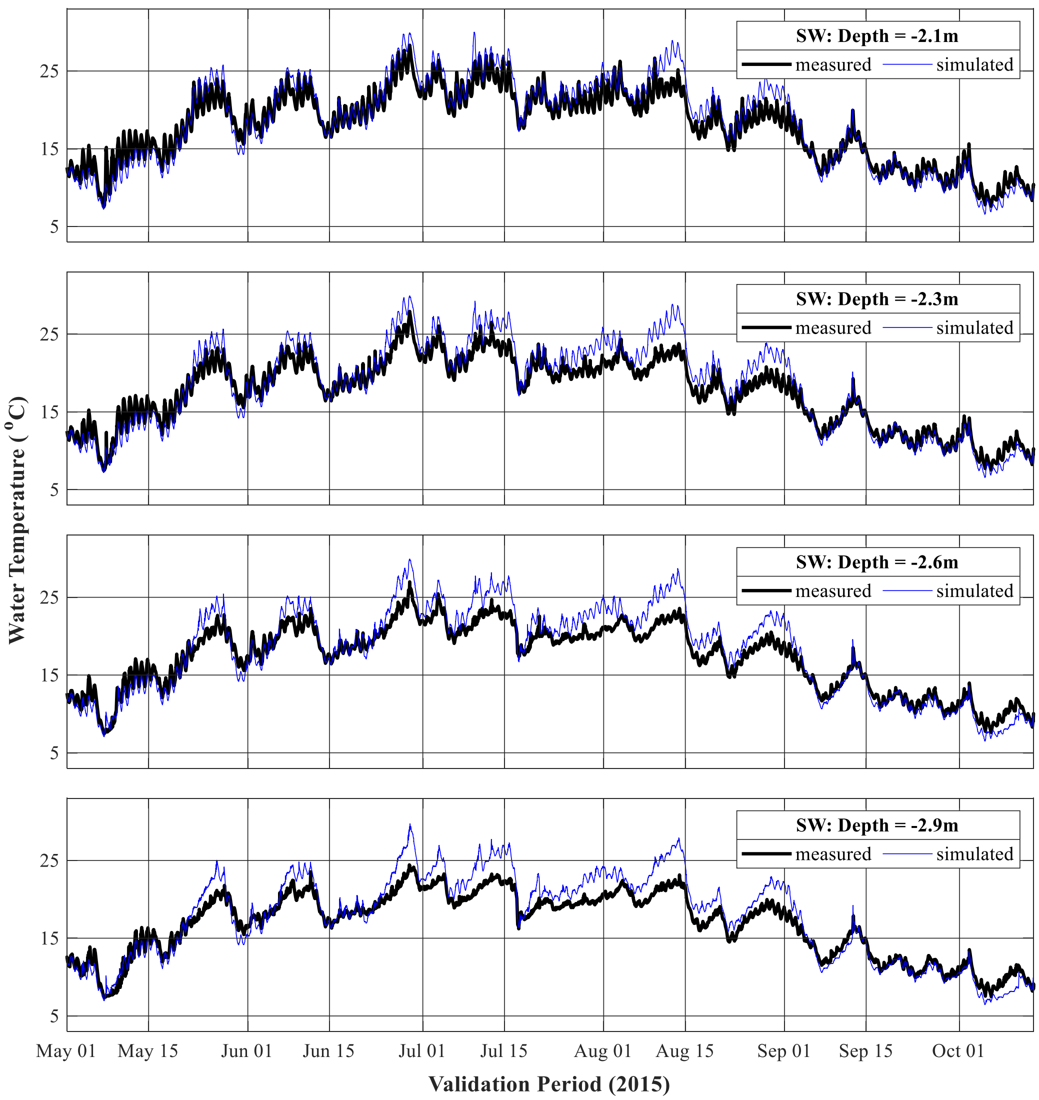

Figure 4-14: Comparison of observed and modelled temperature time series at different depths of the SW sampling location over the validation period.

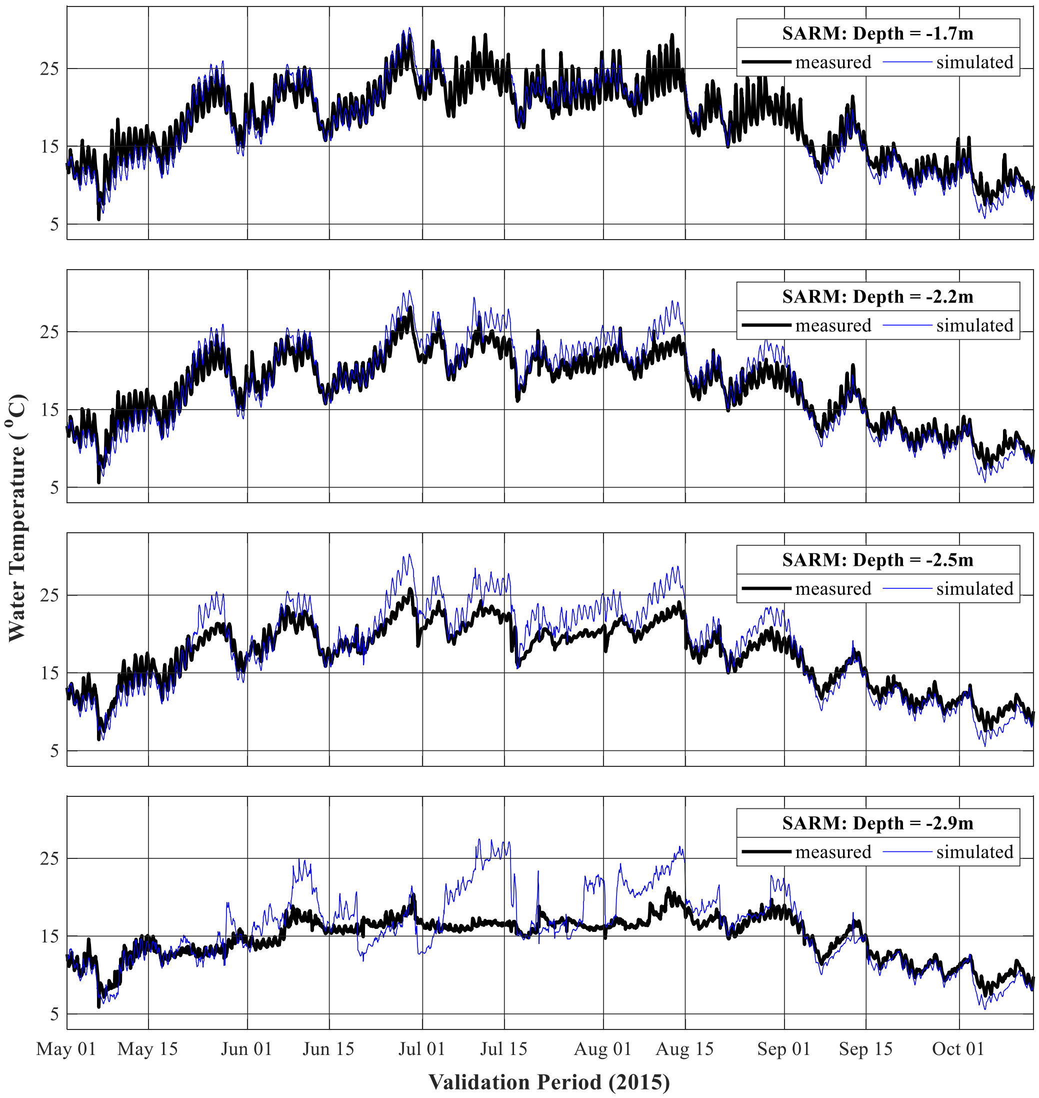

Figure 4-15: Comparison of observed and modelled temperature time series at different depths of the SARM sampling location over the validation period.

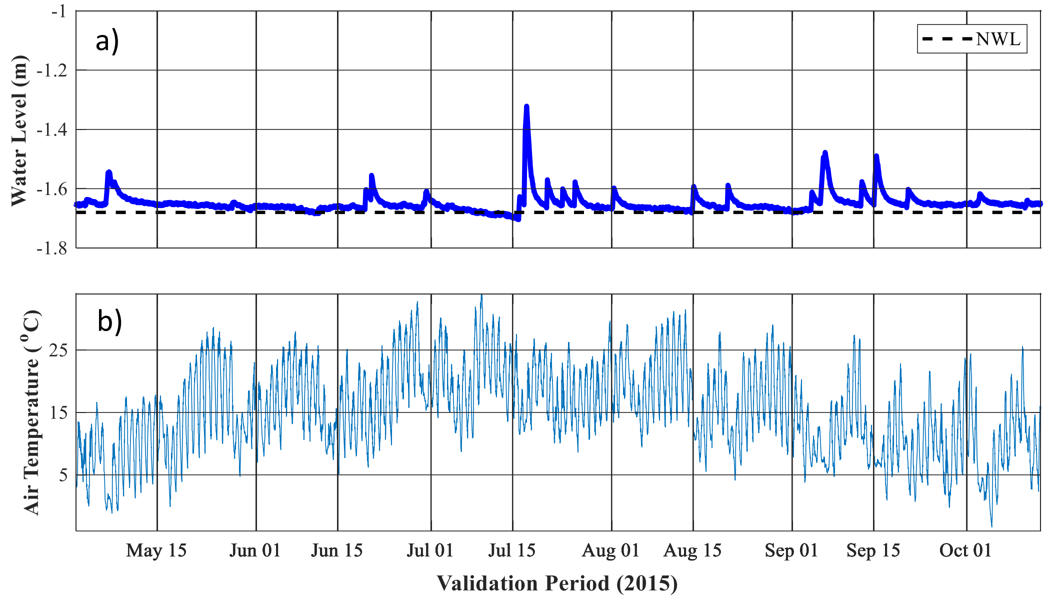

Figure 4-16: a)Water level and b) air temperature during the validation period (2015).

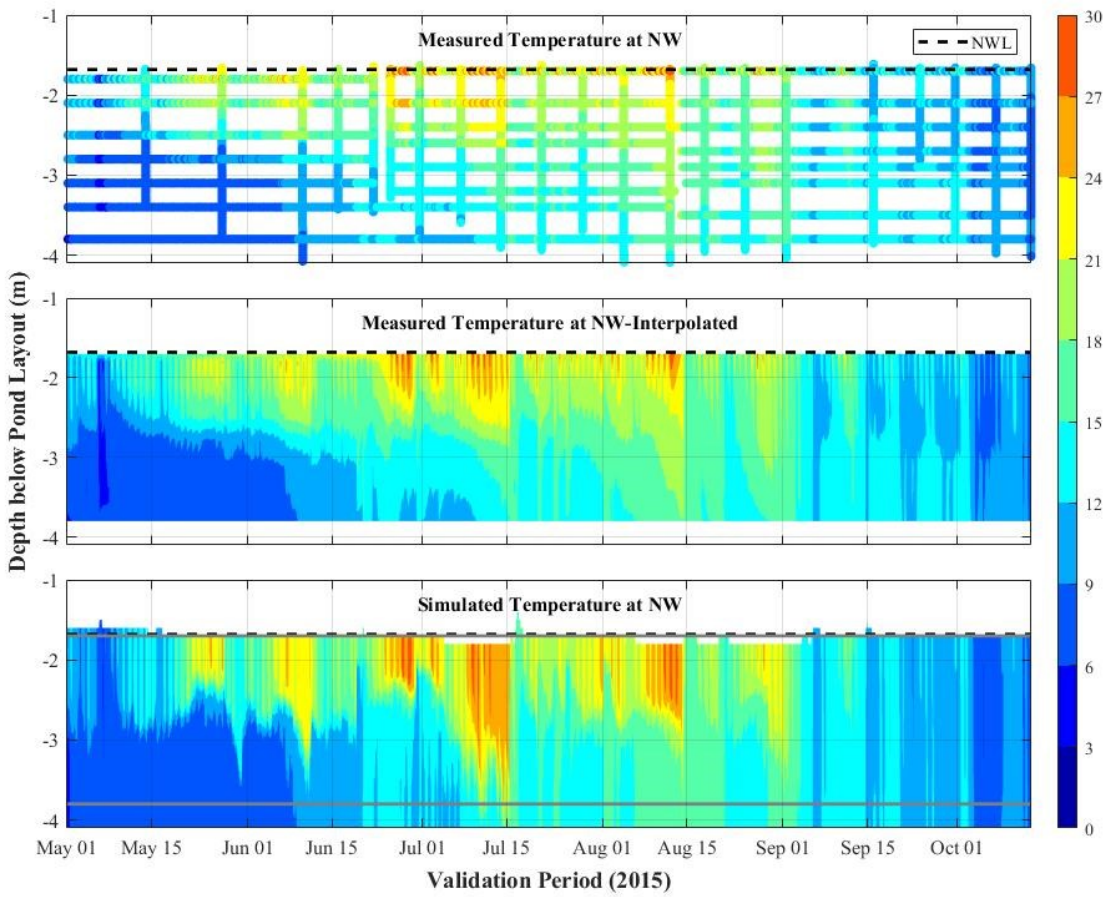

Figure 4-17: a) Observed and b) modelled temperatures (°C) at NW sampling location during the validation period. The dashed lines represent the normal water level at elevation 680.07m.

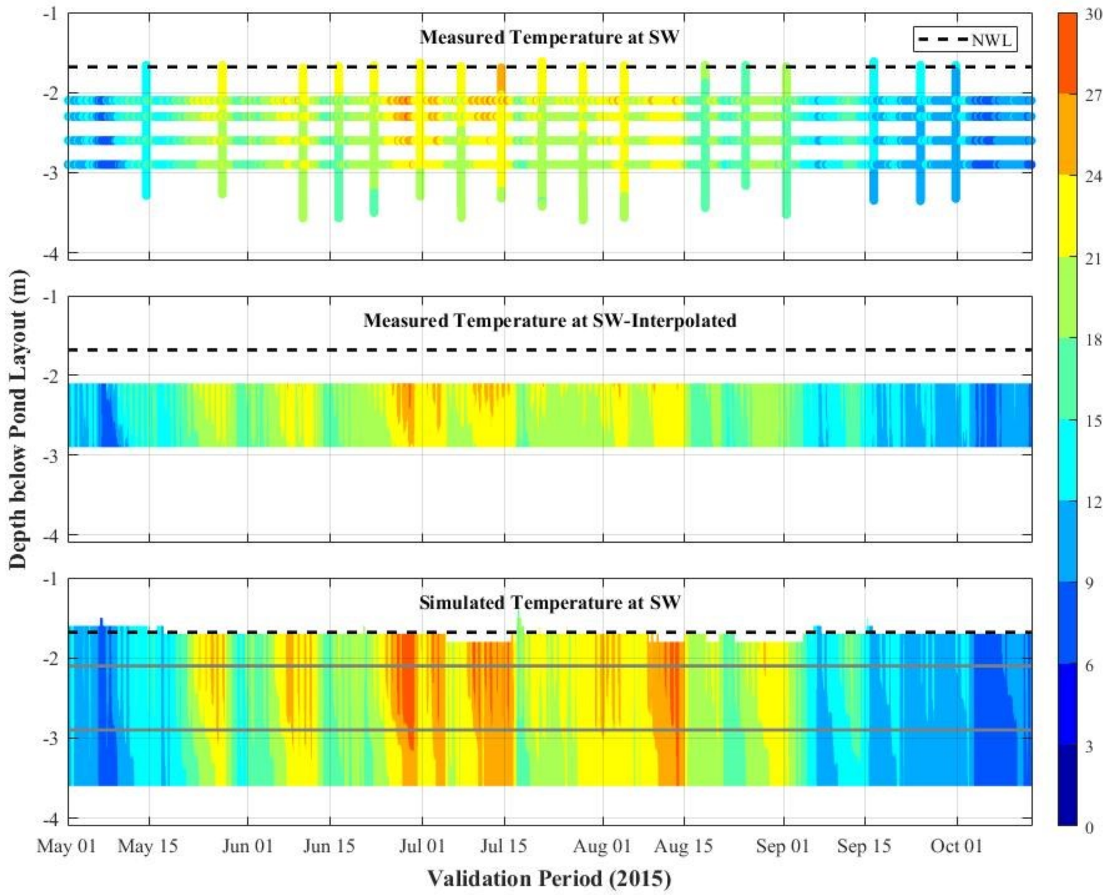

Figure 4-18: a) Observed and b) modelled temperatures (°C) at SW sampling location during the validation period. The dashed lines represent the normal water level at elevation 680.07m.

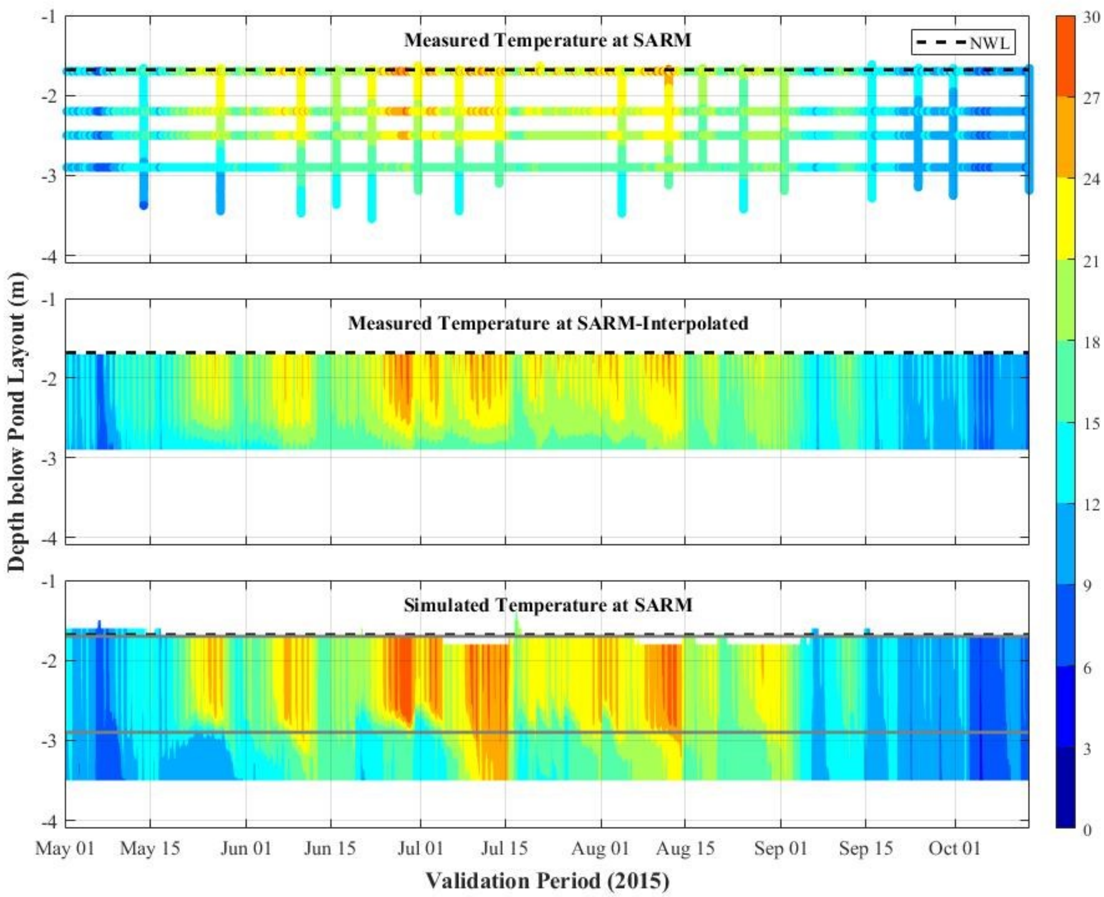

Figure 4-19: a) Observed and b) modelled temperatures (°C) at SARM sampling location during the validation period. The dashed lines represent the normal water level at elevation 680.07m.

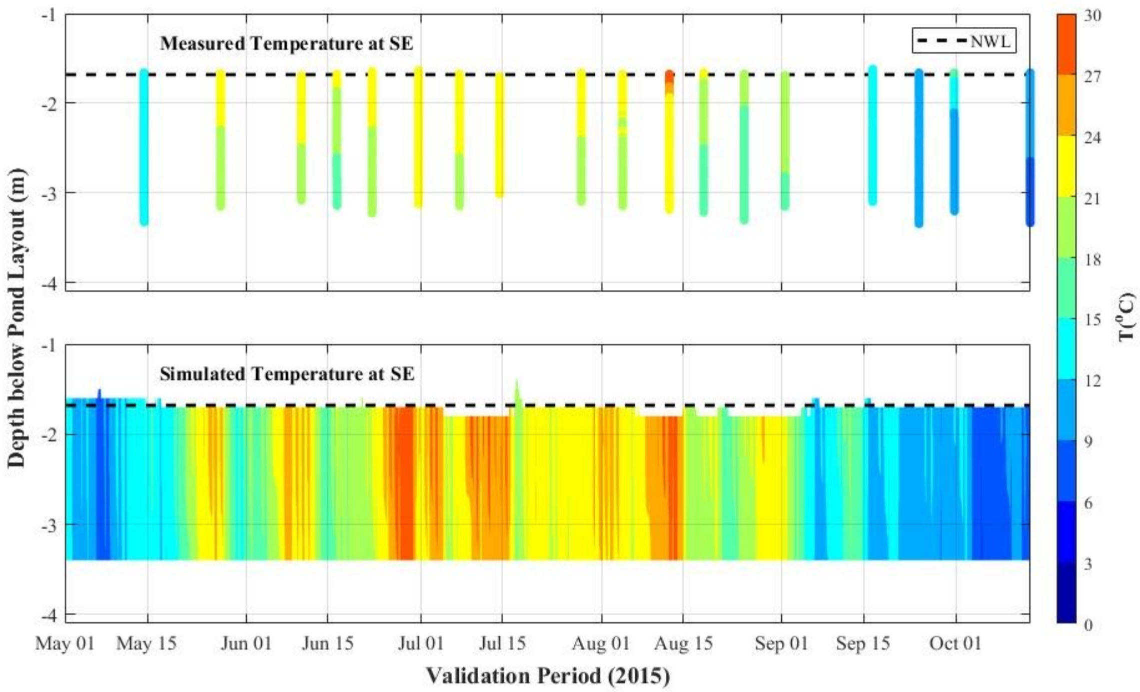

Figure 4-20: Percentage of occurrence of measured and modelled stratification in sampling locations during calibration period. The dashed lines represent the normal water level at elevation 680.07m.

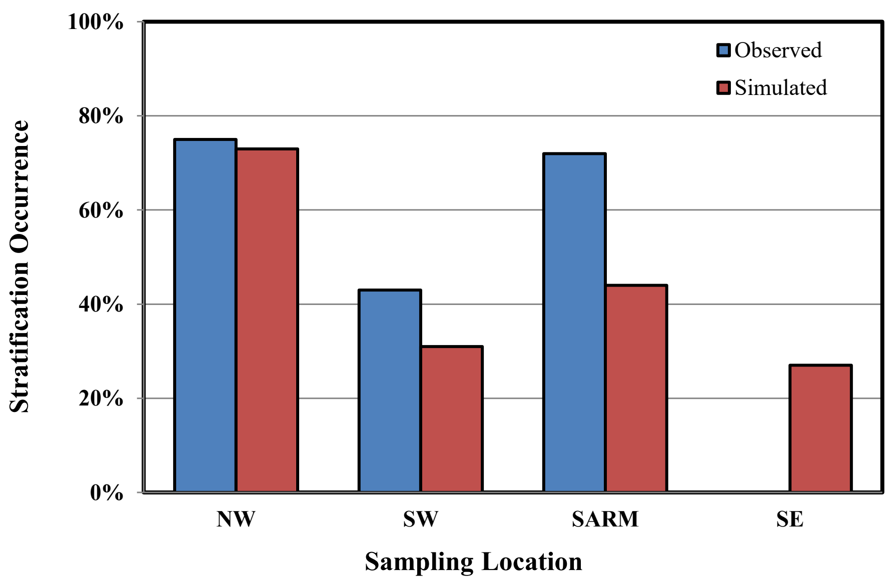

Figure 4-21: Observed and simulated stratification occurrence (%) during the validation period

4.2.3. CAEDYM Calibration and Validation

Table 4-6 provides quantitative performance details of the CAEDYM model in simulating model variables TCHLA, DO, TP, and TN, throughout the calibration and validation periods. The statistics presented in this table are based on TN, TP, and TCHLA measurements derived from water quality samples, and DO measured by deployed instruments.

3.2.2.1 Total Nitrogen (TN)

Figure 4-22 displays color plots of simulated TN at the sampling locations during both the calibration and validation periods, overlaid with field measurements. The color plots illustrate that CAEDYM overestimated TN especially near the surface. This is reflected in an average MBE of 1.20 mg/L and 0.16 mg/L during calibration and validation periods, respectively (Table 4-6). Also, the average RMSE was 1.42 mg/L during the calibration period and 0.47 mg/L during the validation period. Further details can be found in the Appendix B, Section B.4.4. It worth noting that, the effects of TN boundary conditions, and consequently simulated TN on TCHLA found to be negligible, as will be discussed in Chapter 5.

Table 4-6: Performance of CAEDYM in simulation of selected variables at ST2 pond. Measured and modeled values are average over their respective simulation period.

Variable	Period	Location	Measured*	Modelled*	MBE*	RMSE*	RMSEN (%)
TN	Calibration	Average	1.41	2.60	1.20	1.42	101
		NW	2.05	2.95	0.90	1.22	59
		SW	0.97	2.50	1.53	1.64	169
		SARM	0.86	2.19	1.33	1.50	174
		SE	0.97	2.33	1.36	1.50	154
	Validation	Average	1.27	1.43	0.16	0.47	37
		NW	1.73	1.48	-0.25	0.36	21
		SW	0.97	1.52	0.55	0.61	63
		SARM	1.18	1.34	0.16	0.31	26
		SE	0.75	1.42	0.67	0.72	96
TP	Calibration	Average	0.16	0.08	-0.08	0.12	78
		NW	0.16	0.11	-0.05	0.11	70
		SW	0.16	0.07	-0.10	0.13	76
		SARM	0.16	0.06	-0.10	0.15	91
		SE	0.15	0.06	-0.09	0.13	85
	Validation	Average	0.12	0.10	-0.02	0.18	146
		NW	0.11	0.10	-0.02	0.05	41
		SW	0.06	0.11	0.06	0.07	118
		SARM	0.10	0.09	-0.01	0.06	61
		SE	0.23	0.10	-0.13	0.41	176
DO	Calibration	NW	2.03	2.31	0.28	2.23	110
	Validation	SE	4.80	6.04	1.24	3.25	68
TCHLA	Calibration	Average	42.8	30.2	-12.63	25.26	59
		NW	34.4	19.2	-15.13	32.46	94
		SW	53.9	35.3	-18.61	23.45	44
		SARM	44.4	36.6	-7.77	12.35	28
		SE	46.7	40.0	-6.66	18.85	40
	Validation	Average	32.2	27.9	-4.35	52.64	163
		NW	63.3	30.6	-32.73	83.59	132
		SW	5.6	20.9	15.33	19.8	356
		SARM	25.3	32.0	6.63	21.05	83
		SE	3.9	20.8	16.92	20.85	542

*Units are in mg/L except for TCHLA which is in mcg/L.

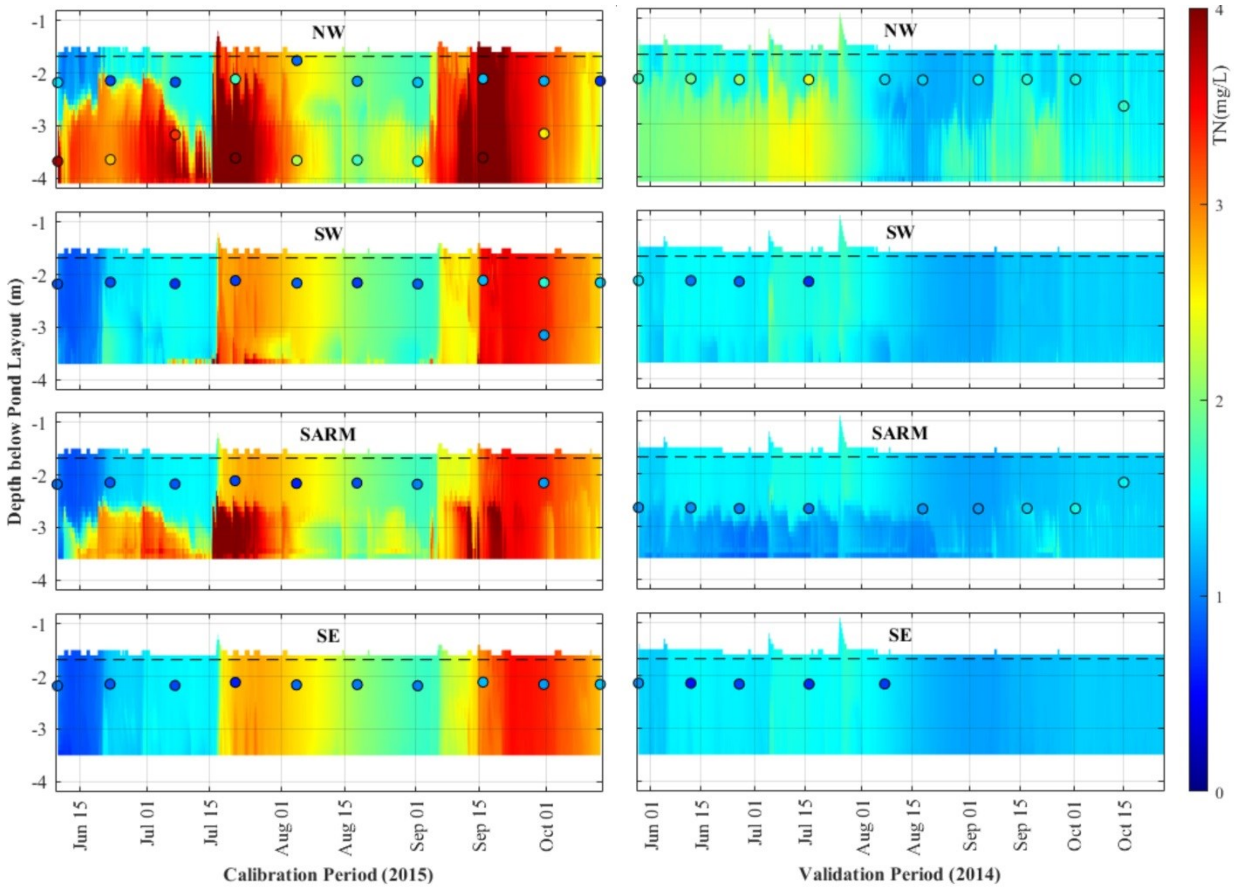

Figure 4-22: Comparison of measured (circles) and simulated (color plots) TN at four sampling locations during calibration and validation periods. The dashed lines represent the NWL at elevation 680.07 m.

3.2.2.1 Total Phosphorous (TP)

Figure 4-23 presents color plots comparing measured and simulated TP at sampling locations during both calibration and validation periods. However, during the calibration period, from early August to early September, CAEDYM underestimated near surface TP across all the sampling locations. More detailed comparisons are presented in Figure 4-24 for NW sampling locations, and in Appendix B, Section B.4.4 for other sampling locations. Efforts to rectify this issue by tuning model parameters such as the maximum potential phosphorous release rates did not improve the model's performance. The discrepancy in measured and simulated TP throughout the water column, as well as model's inability to capture short-term variations (e.g., monthly), has been also observed in other studies (e.g., Nakhaei et al. 2021; Özkundakci et al.

2011; Trolle et al. 2008b). Referring to Table 4-6, during the calibration period, RMSE values at the sampling locations ranged from 0.11 to 0.15 mg/L, while during the validation period, RMSE values ranged from 0.05 to 0.41 mg/L.

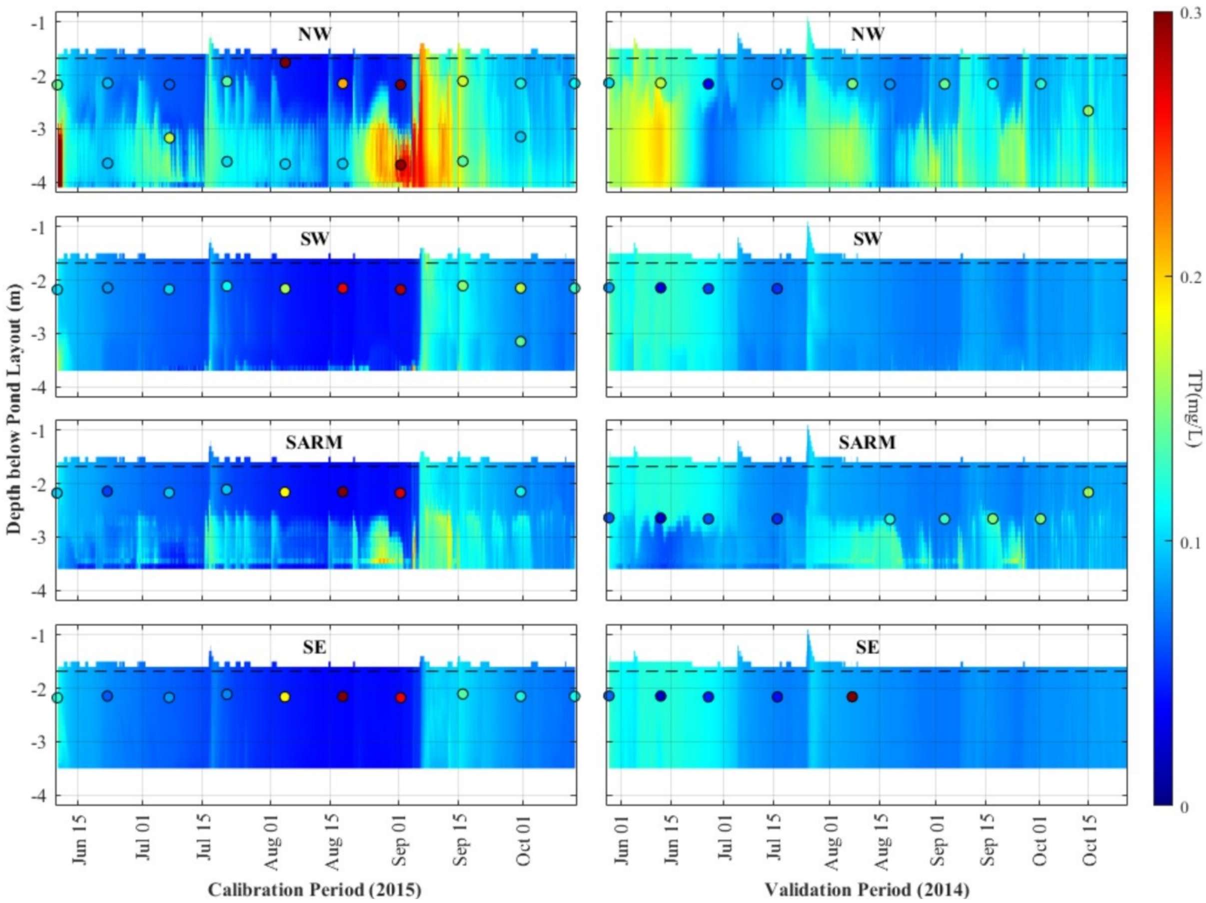

Figure 4-23: Comparison of measured and simulated TP at four sampling locations during calibration and validation periods. Color plots and circles indicate simulation results and field measurements, respectively. The dashed lines represent the NWL at elevation 680.07 m.

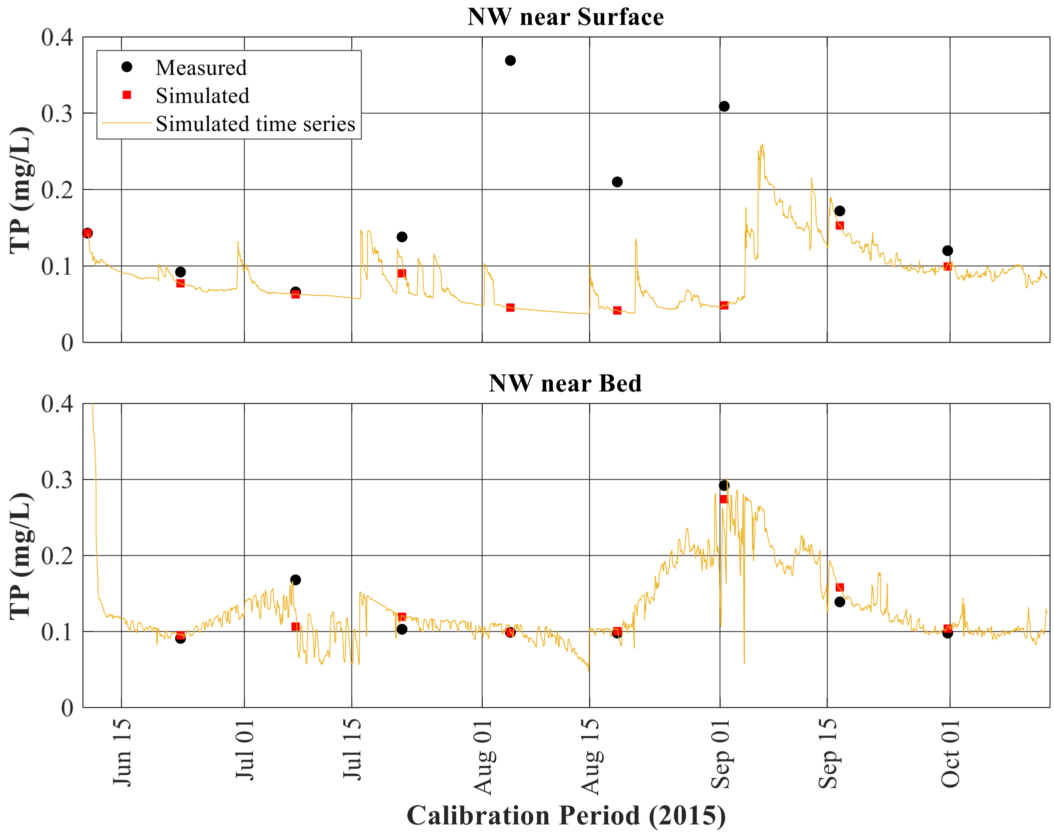

Figure 4-24: Comparison of observed and simulated TP at NW sampling location during calibration period near the surface (a) and near the bed (b).

3.2.2.1 Dissolved Oxygen (DO)

Figure 4-25 compares measured and simulated DO time series at the NW inlet, where DO measuring instruments were deployed near the surface and bed during the calibration period. The measured and simulated DO agree reasonably well, with an average RMSE of 2.23 mg/L (Table 4-6), although the agreement near the bed is influenced by the boundary conditions. CAEDYM tended to overestimate DO at both near bed and near surface towards the end of the season. A comparison of simulated and profiled DO at all sampling locations is presented in Appendix B, Section B.4.4.

Simulated DO during validation period was also compared to measurements obtained from instruments deployed near the surface and bed at the SE location and presented in Figure 4-26.

Similar to the calibration run, CAEDYM overestimated DO near the end of the season. From early Jun to late July, while CAEDYM reasonably simulated the average DO, it could not reproduce the observed diurnal variations. This is likely due to inability of the model to accurately simulate the dynamics of dissolved oxygen through photosynthesis and respiration. That is, the model likely underestimated the concentration of DO produced by photosynthesis during the day and consumed by respiration during the night. These discrepancies are more apparent in the near-surface measurements, where more algae are expected to be present. As such, the RMSE of the validation run increased to 3.25 mg/L.

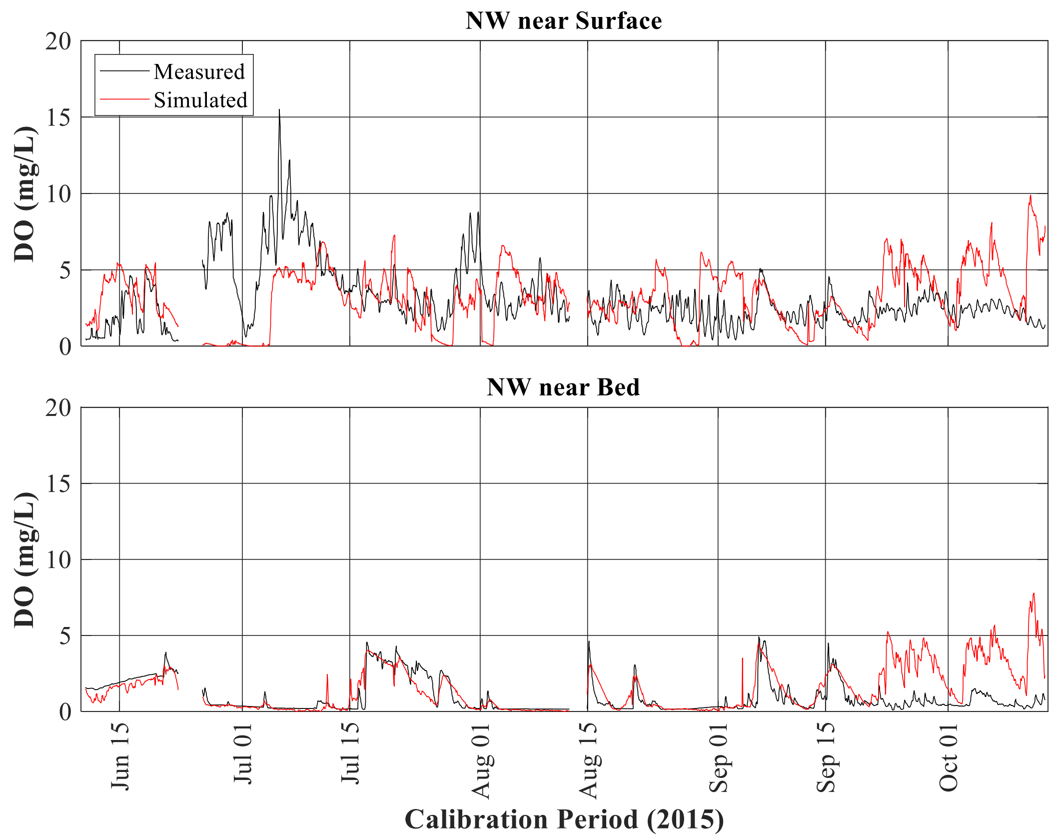

Figure 4-25: Comparison of measured and simulated DO near surface (top) and bed (bottom) at NW during calibration period.

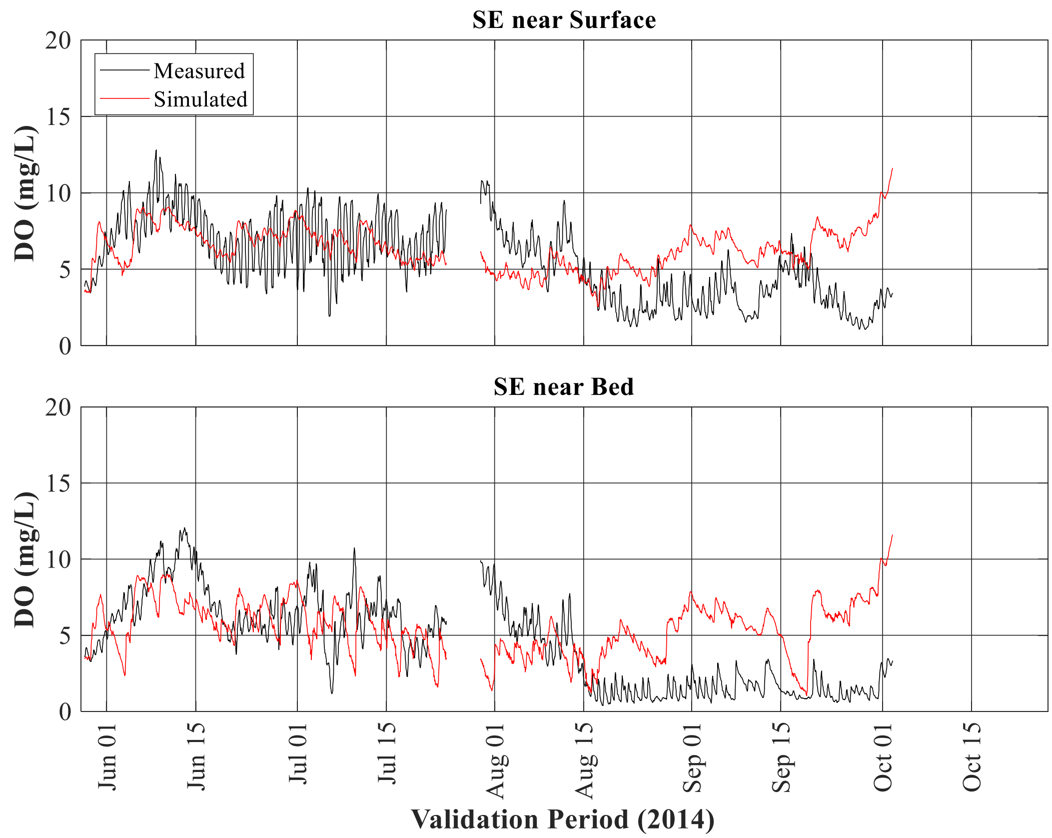

Figure 4-26: Comparison of measured and simulated DO near surface (top) and bed (bottom) at SE during validation period.

3.2.2.1 Total Chlorophyll-a (TCHLA)

Table 4-6 shows that RMSE during the calibration period varied from 12.35 mcg/L at SARM to 32.46 mcg/L at NW. The average RMSE increased from 25.26 mcg/L in the calibration period to 52.64 mcg/L in the validation period. Simulated TCHLA during the calibration and validation periods at sampling locations are presented in Figure 4-27, overlaid with measured water quality samples (single dots), deployed instruments (sequence of horizontal dots), and profiled measurements (sequence of vertical dots). The model was able to capture the overall temporal and spatial variability of TCHLA with some discrepancies. For example, during the calibration period, the model did not capture the sudden increase in TCHLA measured by deployed instruments and profiling in early July at NW (Figure 4-27a). Previous studies have found that phytoplankton patchiness could be the cause of high temporal variability in observed data (Bolkhari 2014; Missaghi and Hondzo 2011).

Figure 4-28 compares simulated TCHLA with measured TCHLA from the deployed instruments (EXO2) at the NW location. The EXO2 was initially deployed at a depth of -2.2 m (Figure 4-28a); however, it was retrieved and deployed at a depth of -3.0 m around mid-August (Figure 4-28b). Since the EXO2 sensors were not calibrated, the TCHLA readings are relative and only show temporal trends, which generally align with the simulation trends.

The average TCHLA, measured via profiling at various sampling locations was also compared with the corresponding depth-averaged simulated TCHLA (Figure 4-29). This figure indicates that CAEDYM effectively captured the temporal and spatial variations of TCHLA. The TCHLA underestimation between mid-August and mid-September can be attributed to the underestimation of TP during this period as discussed earlier.

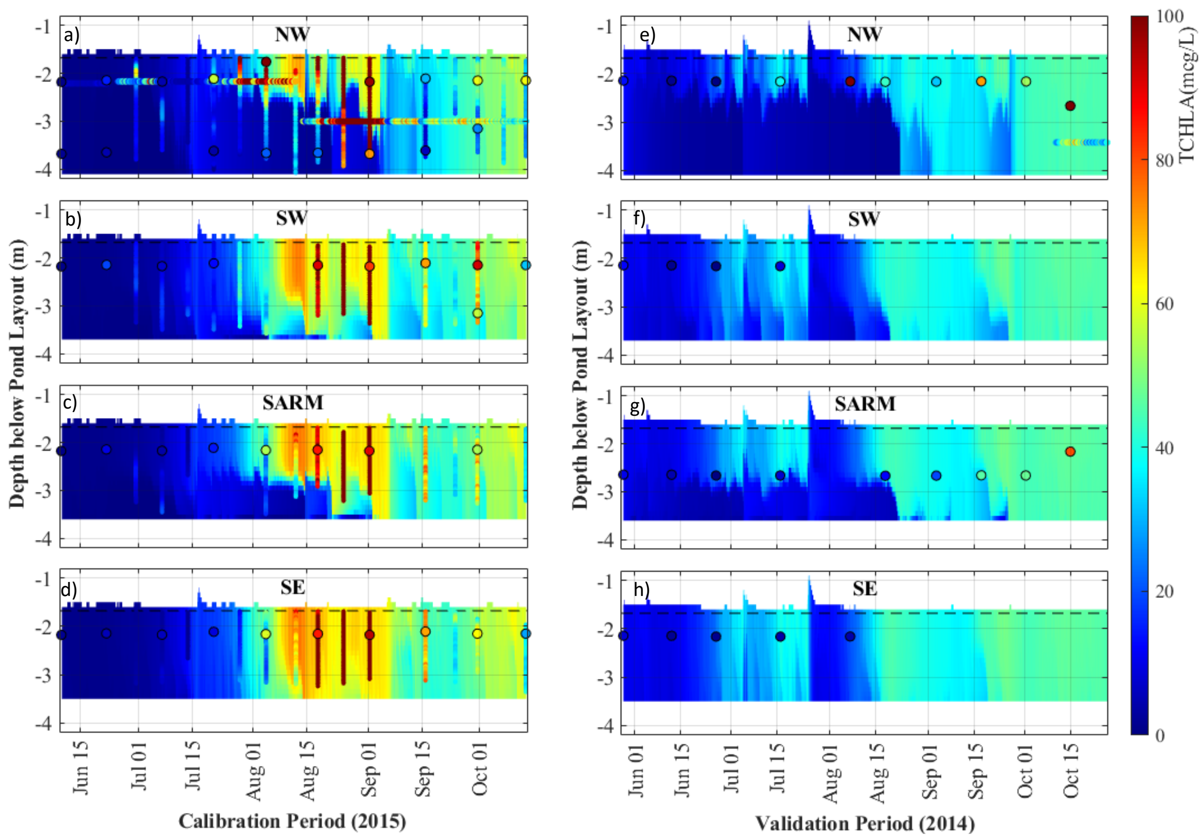

Figure 4-27: Comparison of measured and simulated Total Chlorophyll-a (TCHLA) at four sampling locations during both calibration and validation periods. The color plots depict simulation results, while single circles, vertical and horizontal sequences of circles represent measured TCHLA through water quality sampling, profiling, and deployed instruments, respectively. The dashed lines are corresponded to the NWL at elevation 680.07 m.

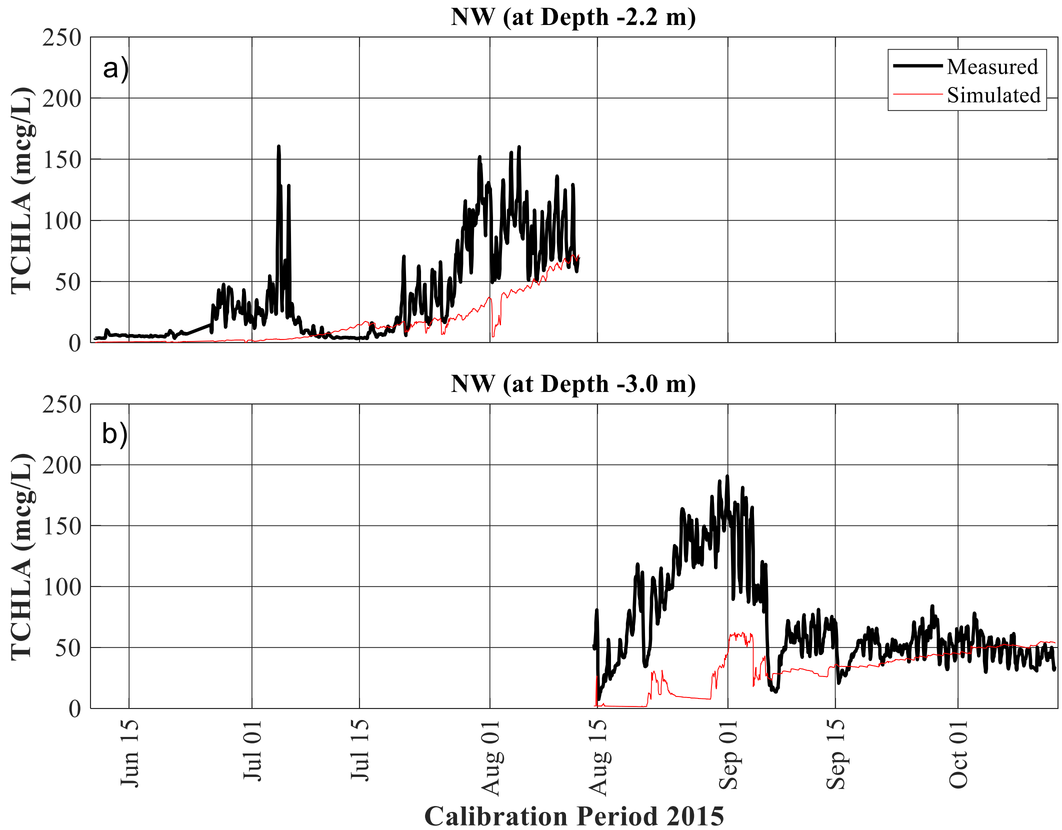

Figure 4-28: Simulated and measured TCHLA with the deployed EXO2: a) at depth of -2.2 m, b) measured at depth of -3.0 m from outline of pond.

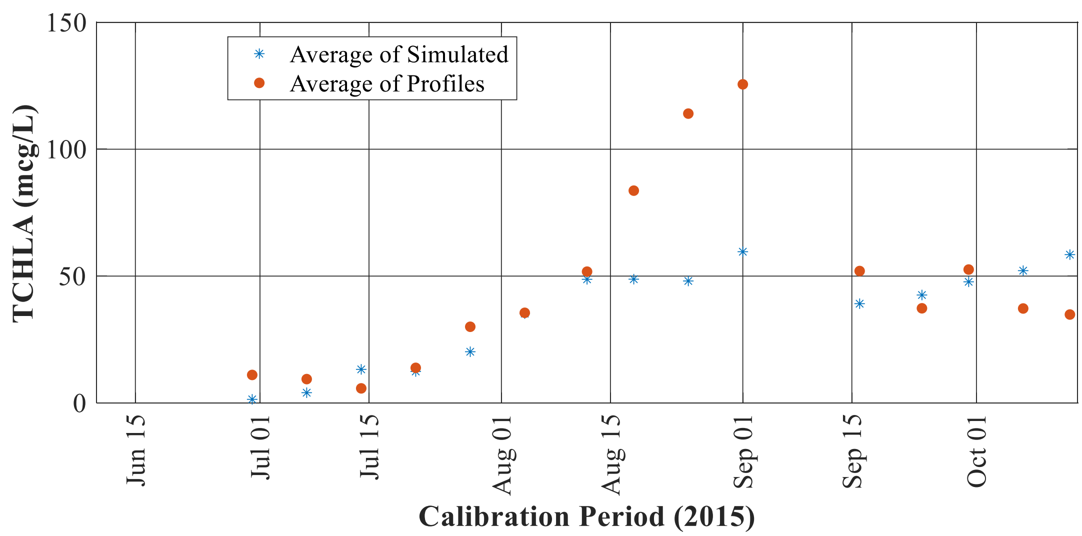

Figure 4-29: Average simulated and profiled TCHLA at sampling dates.

4.2.4. **Sensitivity Analysis of CAEDYM model parameter (Results)**

Using the information gained throughout the calibration and validation processes, a number of model parameters were selected for the sensitivity analysis, as shown in Table 4-7. The sensitivity of TCHLA, DO, TN, and TP to the selected model parameters was calculated based on simulations conducted using three values for each model parameter shown in this table, and the computed sensitivity index (SI) values are presented in Figure 4-30.

Figure 4-30a shows that TCHLA is the most sensitive variable overall, with an average SI of 93.1%, followed by DO, TN, and TP, with average SI values of 16.3%, 9.7%, and 8.4%, respectively. Modelled TCHLA concentrations are most sensitive to μ_{max}, K_r, IP_{min}, and IK. Therefore, TP, TN, and DO are also sensitive to these four parameters due to interdependencies across simulated variables.

Table 4-7: Nominated model parameters along with three values selected for sensitivity analysis of CAEDYM.

Parameter	θ^c	$\theta^c - \Delta\theta$	$\theta^c + \Delta\theta$	Average SI (%)	Average Rank
DOC1max	0.011	0.001	0.021	3.3	9
IK	130	70	200	38.8	4
IP_{min}	0.100	0.008	0.200	47.6	3
K_r	0.020	0.001	0.039	71.2	2
μ_{max}	0.60	0.30	0.90	102.9	1
POMDensity	1005	1000	1010	12.1	7
ϑ_{growth}	1.06	1.00001	1.12	6.2	8
T_{opt}, $\Delta\theta = 1°C$	25	24	26	12.7	6
T_{opt}, $\Delta\theta = 2°C$	25	23	27	22.1	5
T_{max}, $\Delta\theta = 2°C$	33*	31	35	1.9	10

*θ^m for T_{max} was adjusted from 31°C to 33°C to satisfy the condition of $T_{max} \geq T_{opt} + 6$ considered in the CAEDYM.

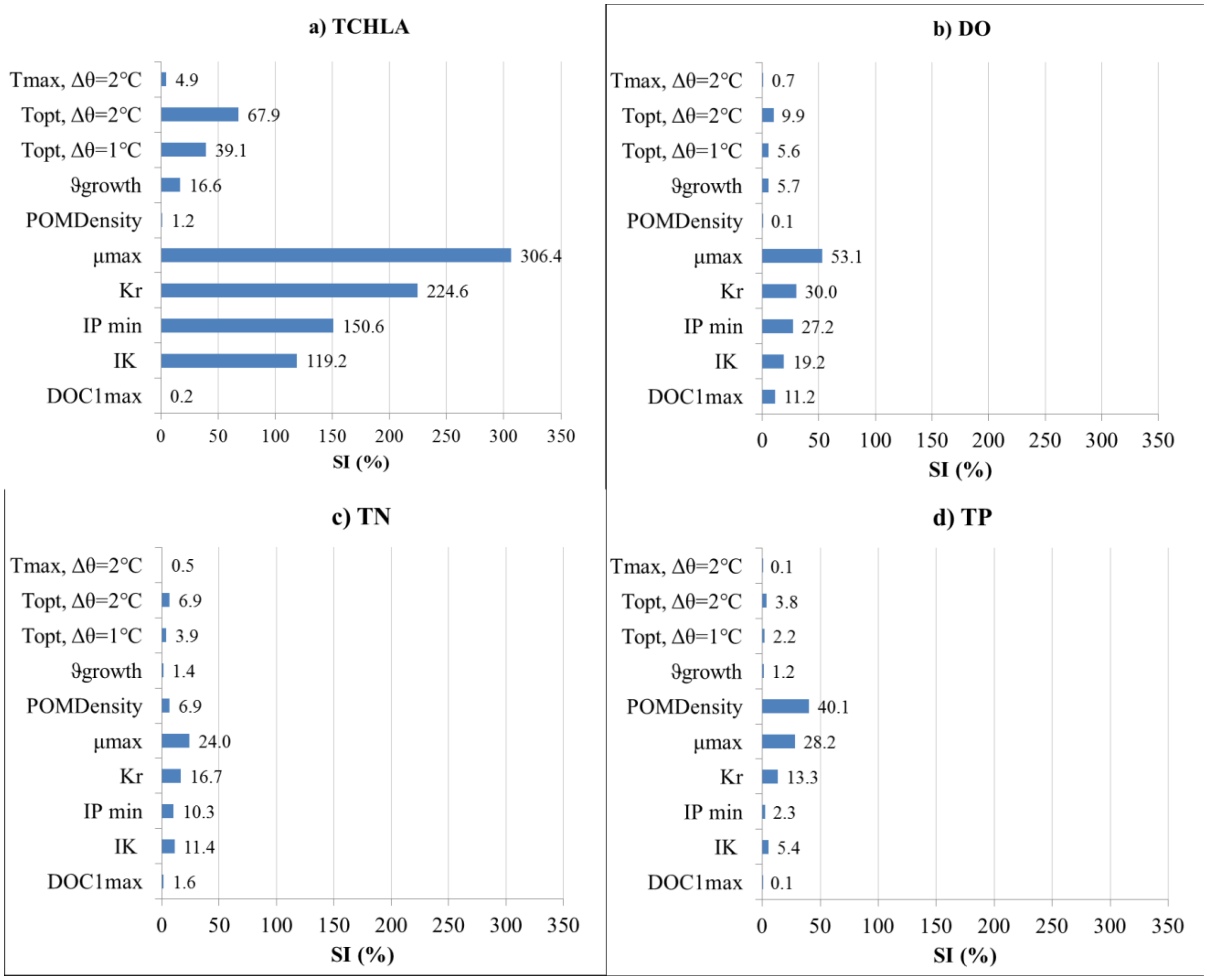

Figure 4-30: Sensitivity index (SI %) of model outputs: a) TCHLA, b) DO, c)TN, and D) TP, to selected model parameters.

4.3. Conclusion

A 3D coupled hydrodynamics and water quality model, ELCOM-CAEDYM, was used in this study to simulate the temporal and spatial variations of variables measured at the South Terwillegar2 (ST2) stormwater pond in the city of Edmonton.

ELCOM accurately simulated water temperatures, which was considered the most important variable representing pond hydrodynamics. This was accomplished by calibrating the model through adjustments of inflows and model parameters such as, albedo and Secchi depth, and accounting for atmospheric instability. The model captured temperature variations across various time scales, from diurnal fluctuations to the seasonal averages. Moreover, the spatial variation of temperature was successfully replicated across the pond. ELCOM also captured the thermal structure of the pond, including periods of thermally mixed and stratified, along with responses to abrupt external changes such as significant changes in inflows and weather conditions. The error statistics over the calibration and validation periods consistently remained within or below the established range of values reported in similar studies.

The water quality model, CAEDYM, was able to simulate TCHLA and DO with acceptable accuracy. It effectively captured both the temporal and spatial trends of TCHLA. Similarly, it effectively represented DO dynamics, although it struggled to resolve the diurnal variations. While the model performance in simulating TP was acceptable, it encountered challenges in predicting TN. The under-performance of the model in simulating nutrient components was partly attributed to the accuracy of boundary conditions. Nevertheless, RMSE values obtained in this study were comparable with those reported in similar studies (e.g. Nakhaei 2021).

The sensitivity analysis of CAEDYM revealed that TCHLA is the most sensitive variable overall, followed by DO, TN, and TP. Although TCHLA exhibits sensitivity to a larger number of model parameters, μ_{max}, K_r, IP_{min}, and IK were identified as most influential. Therefore, the findings of this study provide valuable guidance for calibration and can reduce the number of calibration attempts in similar studies.

Chapter 5. INVESTIGATING THE BEHAVIOUR OF THE STUDY STORMWATER POND UNDER VARIOUS BOUNDARY CONDITIONS AND DEPTH SCENARIOS USING ELCOM-CAEDYM MODEL

5.1. INTRODUCTION

Water quality models have been widely used as planning, design and decision-making tools for evaluating water quality of aquatic systems under various management and climate change scenarios (e.g., Conn and Fiedler 2006; Gal et al. 2004, 2009; Gilboa et al. 2022; Jin et al. 2007; León et al. 2005; Lewis et al. 2004; Yajima and Choi 2013). However, the accuracy and reliability of simulations depend not only on the model structure and parameterization but also on reliable input data, particularly boundary conditions.

Inevitably, uncertainties always exist in input data due to measurement errors and assumptions made to establish boundary conditions. It is important to assess the impact of such errors and assumptions on the model's response. Moreover, to assess the response of the aquatic systems under proposed management or future climate scenarios, the model is run under altered boundary conditions or within a modified physical domain. This "sensitivity approach" (Elliott 2011) has been employed in previous studies to predict the impact of future scenarios by altering variables such as temperature, precipitation, and nutrient loadings beyond the historical levels in the aquatic ecosystem (e.g., Cui et al. 2016; Elliott et al. 2006; Gal et al. 2009; Linden et al. 2015; Trolle et al. 2008b; a).

The content presented in this chapter distinguishes itself from previous studies due to its focus on the urban stormwater pond scale, the utilization of a model calibrated and validated through extensive field measurements, and analysis of the model's response to a diverse range of input data. In this study, the impacts of nutrient loadings, geometry, hydrological, and climate scenarios on the water quality of the selected stormwater pond, South Terwillegar 2 (ST2), will be analyzed. The calibrated ELCOM-CAEDYM model is used to simulate total chlorophyll-a (TCHLA) under different scenarios. For each scenario, key factors influencing the algae dynamics (e.g., retention time, thermal stratification, as well as nutrients, light, and temperature limiting factors) were identified and discussed. This provides insights into the suitability and sensitivity of the ELCOM-CAEDYM model for managing urban stormwater ponds.

5.2. METHODOLOGY

5.2.1. Modelling Scenarios

The calibrated model run, spanning from June 10th to October 13th, 2015, serves as the "base-run", to define the scenarios and compare their impacts. Next, by perturbing the pond geometry (depth and bed topography) and boundary conditions (inflows, nutrient load, wind, and temperature), 15 scenarios were defined (Figure 5-1). These perturbations were created by applying either multipliers or increments to the input data values. Subsequently, all scenarios were run over the simulation period, using initial and boundary conditions identical to those of the base-run, except for the revised boundary conditions imposed by that specific scenario. In the following, further details about each specific scenario are provided.

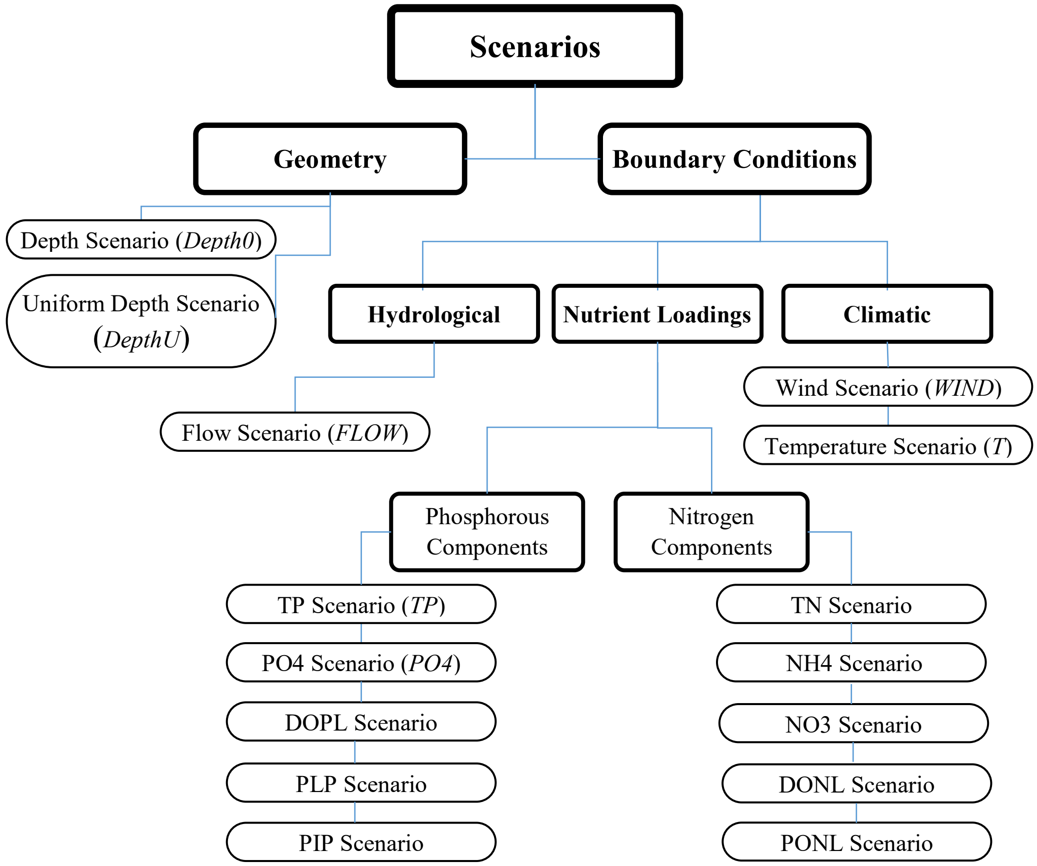

Figure 5-1: Classification of Defined Scenarios based on Perturbation of Geometry and Boundary Conditions.

3.2.2.1 Geometry

The depth and bed topography of a water body have a significant impact on its hydrodynamics and water quality (Conn and Fiedler 2006; Ji 2017). Therefore, to investigate the impacts of pond's depth and its variations, two scenarios were defined: Depth0 and DepthU. Here, all the depths are given relative to the outline of the study pond, which, as described in Chapter 2, has an elevation of 680.75 m above sea level. Therefore, the normal water level (NWL) with elevation of 680.07 m is indicated by a depth of -1.68 m.

In the Depth0 scenario, the bed elevations of computational cells were uniformly changed by the same amount, ranging from -1.0 to 0.8 m, in increments of 0.1 to 0.5 m (Table 5-1). This consistent change preserves the relative bed topography. In the DepthU scenario, a constant value was assigned to bed elevations of the computational cells creating a pond with a uniform depth. The bed elevations ranged between -3.33 and -2.13 m, relative to the pond's outline, in increments of 0.1 to 0.2 m (Table 5-1). It should be noted that the significantly different bathymetry of the DepthU scenario is not representative of the study pond, and this scenario serves only as a reference to investigate the impacts of bed non-homogeneity. In both scenarios, only the computational cells with bed elevations less than -2.1 m (i.e., 0.42 m below the NWL) were altered. The -2.1 m threshold ensures that all the altered cells remain submerged in all the runs of both scenarios, ensuring a consistent elevation-surface area relationship. Subsequently, the water depth was averaged for each of the runs in the Depth0 and DepthU scenarios over the simulation period. Then, the depth multipliers, denoted as λ[Depth0] and λ[DepthU], were calculated for each run by dividing the simulated average water depth by that of the base-run. For example, by deepening the bed by 0.2 m, the average simulated water level was 1.04 m, which is 1.15 times deeper than that of the base-run, which was 0.91 m. These multipliers presented in Table 5-1 provide a more consistent basis for comparisons between the two depth scenarios.

Table 5-1: Depth modifications and average multiplier in Geometry scenarios.

Depth0 Scenario		
Depth Increment (m)	**Pond Averaged Depth (m)**	**λ[Depth0]**
-1.0	1.56	1.72
-0.5	1.23	1.36
-0.2	1.04	1.15
-0.1	0.97	1.08
0.0	0.91	1.00
0.1	0.85	0.93
0.2	0.8	0.88
0.5	0.74	0.82
0.6	0.7	0.77
0.7	0.61	0.67
0.8	0.53	0.59

DepthU Scenario		
Bed Elevation (m)*	**Pond Averaged Depth (m)**	**λ [DepthU]**
-3.33	1.43	1.58
-3.13	1.26	1.39
-2.93	1.09	1.20
-2.73	0.92	1.01
-2.63	0.83	0.92
-2.53	0.74	0.82
-2.43	0.65	0.72
-2.33	0.57	0.63
-2.23	0.49	0.54
-2.13	0.39	0.44
*Relative to pond's outline		

3.2.2.1 Hydrological

The preparation of input data for the "Flow scenario" required additional steps due to the interrelation between inflow, outflow, and water level time series, as described in Appendix C. The inflows and, accordingly, outflows were perturbed such that the resulting water levels matched those of the base-run. To calculate the perturbed inflow time series, first the elevation of the weir crest was varied within a range of -5 to +5 cm (Table 5-2). The perturbed outflows were then calculated by inputting the base-run water levels into the outlet structure stage-discharge relationship. Finally, the perturbed inflows were back-calculated using the reverse level pool routing. The average perturbed inflows over the simulation period vary between 7.49×10^{-4} and 1.40×10^{-2} m^3/s, corresponding to flow multipliers (λ[Flow]) of 0.18 and 3.35, respectively (Table 5-2).

Table 5-2: Flow scenario multipliers and corresponding average inflows and weir height modifications.

λ [Flow]	Average Inflows (m^3/s)	Weir height perturbation (cm)
0.18	0.0007	5.0
0.28	0.0012	4.0
0.36	0.0015	3.0
0.51	0.0021	2.0
0.58	0.0024	1.5
0.73	0.0030	1.0
0.87	0.0036	0.5
1.00	0.0042*	0.0
1.21	0.0050	-0.5
1.40	0.0058	-1.0
1.48	0.0062	-1.5
1.83	0.0076	-2.0
2.27	0.0095	-3.0
2.79	0.0116	-4.0
3.35	0.0140	-5.0

* base-run values

3.2.2.1 Climatic

Climatic scenarios (Figure 5-1) were defined by altering the observed wind speeds and air temperatures. In the Wind scenario, wind speeds were scaled by wind multipliers (λ[WIND]) ranging from 0.25 to 2.00, in increments of 0.25. Additionally, for the Temperature scenario, air temperatures were varied by using offsets (λ[T]) ranging from -4 to 4°C, in increments of 0.5 and 1.0°C (Table 5-4). In addition to analyzing the model's sensitivity to potential errors in climatic boundary conditions, the wide ranges of λ[T] and λ[WIND] can illustrate how state variables would respond to significant changes in boundary conditions.

3.2.2.1 Nutrients Loading

The nutrient scenarios were defined by varying the phosphorous and nitrogen component loadings through inflow boundary conditions. The phosphorous and nitrogen components (PO4, PIP, DOPL, POPL, TP, NO3, NH4, DONL and TN) were individually manipulated by the nutrient multiplier, λ[Nutrient], with values of 0.5, 0.67, 0.75, 0.9, 1.1, 1.25, 1.5, and 2.0.

5.2.2. **Processing of Model Outputs**

ELCOM-CAEDYM simulates and outputs a wide range of state variables (e.g., water temperature, dissolved oxygen, and nutrient concentrations), as well as biogeochemical rates (e.g., productivity, respiration, and settling). Most simulated variables can be extracted from specific cells or the top/middle/bottom water layers, and at specified times, enabling detailed spatial and temporal analysis. Additionally, ELCOM-CAEDYM can output the average of selected state variables over the computational cells (Hipsey et al. 2013; Hodges and Dallimore 2013b, 2016).

For this study, the ELCOM-CAEDYM model was configured to output hourly state variables. Profiles of retention time (RT), water temperature (T), total chlorophyll-a (TCHLA), dissolved oxygen (DO), total phosphorous (TP) and total nitrogen (TN) were extracted at designated sampling locations, namely the NW, SW, SARM inlets and the SE outlet. This allowed for the calculation of depth-averaged time series of these variables, as well as their temporal average over the simulation period. It should be noted that the model does not provide spatial average values for some state variables, in particular RT. Additionally, the variable "retention time" outputted by ELCOM-CAEDYM is basically the "water age" which is the average age of water in a cell (Hodges and Dallimore 2016). The model outputs RT at the surface (top), middle (mid), and near-bed (bed) layers. Therefore, spatial average of RT values were calculated by averaging top, mid, and bed RT values.

3.2.2.1 Trophic State of the Pond

TCHLA concentrations were used to determine the trophic state of the study pond based on the trophic index of Carlson (1977) given in Table 5-3.

Table 5-3: Criteria of the tropic state.

Trophic State	**Criteria (mcg/L of TCHLA)**
Oligotrophic	TCHLA < 2.6
Mesotrophic	2.6< TCHLA < 20
Eutrophic	20 < TCHLA < 56
Hypereutrophic	TCHLA > 56

3.2.2.1 Thermal Stratification

To assess stratification strength and occurrence, additional calculations were performed on the simulated water temperatures. The strength of thermal stratification, ΔT, is defined as the temperature difference between the surface and the bed of a water column. The water column was considered to be "stratified" when ΔT≥1°C and "strongly stratified" when ΔT≥10°C. These thresholds have been used in similar studies (Ahmed et al. 2022).

The stratification occurrence FΔT, is defined as the percentage of the simulation period during which the stratification strength (ΔT) exceeds a predefined threshold. For example, F1 and F10 represent the percentage of time during which a water column is stratified and strongly stratified, respectively. Furthermore, the pond FΔT and ΔT were calculated by averaging over all computational cells. Stratification strength and occurrence provide insight into the pond's thermal stability and help identify locations or scenarios where stratification is more persistent.

3.2.2.1 Physical Transport Rate

The temporal and spatial variations of total chlorophyll-a (TCHLA) in a body of water are influenced by both biogeochemical factors (e.g., temperature, light and nutrient) and physical transport factors (e.g., advection and diffusion). Due to the interdependence of these factors, isolating their individual effects on TCHLA can be challenging. Following an approach similar to Ji (2017) and Qin (2017), the fractional biomass change rate (*G*) can be considered as the sum of the biogeochemical rate (*g*) and physical transport rate (*hd*), and hence, *hd* can be back-calculated based on other outputted variables. First, pond-averaged *G* (1/day) is calculated as:

$$G_t = \frac{1}{\Delta t}\left(\frac{A_{t+\Delta t}}{A_t} - 1\right) \tag{5-1}$$

where the subscript t indicates time, Δt is the time step (1/24 day), and A_t is the pond-averaged TCHLA (mcg/L) at time t. Following the discussion in the previous chapter, the time series of pond-averaged *g* (1/day) is then calculated:

$$g_t = \mu_t - res_t + set_t \tag{5-2}$$

where μ, is the potential growth rate (1/day), *res* represents the respiration, mortality and excretion rate (1/day), and *set* is the settling rate (1/day). The pond-averaged rates on the right-hand side of Equation (5-1) and Equation (5-2) are outputted by the model. As discussed in the previous chapter, μ is a function of light, temperature, and nutrient limiting factors and reaches its maximum values when the limiting factors approach one and decreases as the limiting factors approach zero. Finally, the pond-averaged *hd* (1/day) is calculated as:

$$hd_t = G_t - g_t \tag{5-3}$$

5.3. RESULTS AND DISCUSSIONS

This section presents the results of the different scenarios, focusing on state variables related to or potentially influencing total chlorophyll-a concentrations (TCHLA). These variables include water temperature (T), stratification strength (ΔT), stratification occurrence (FΔT), retention time (RT), limiting factors, physical transport rate (*hd*), biogeochemical rate (*g*), as well as dissolved oxygen (DO).

Values reported for the pond are pond-integrated, meaning they are spatially averaged across the entire pond, whereas those reported for the sampling locations are depth-averaged. Additionally, these values are averaged over the simulation period. The presented time series of averaged of variables are also either spatially averaged across horizontal layers or all cells of the pond, or depth-averaged for the sampling locations. For example, "pond RT" refers to the pond-integrated retention time averaged over the simulation period. Furthermore, alterations in state variables within each scenario are reported relative to the base-run values. Moreover, reported statistics involving all scenarios (such as averages, maximums, or ranges) exclude the DepthU scenario due to its significantly different bathymetry.

Moreover, R^2 and p-value statistics were reported only when the assumptions of linear regression were met as determined through visual inspection of the corresponding scatter and residual plots. When these assumptions were not satisfied (e.g., evident non-linearity, presence of outliers, non-randomness of residuals), either the Kendall test (Appendix C) was employed, or general trends and average changes were presented. Linear regression and Kendall tests were considered statistically significant when p-values were less than 0.01.

5.3.1. **Nutrient Scenarios**

To assess the impact of nutrient scenarios on water quality, their effects on nutrient limiting factors and subsequently on TCHLA were examined. Given that in these scenarios, other variables (e.g., T, *hd*, ΔT, and RT) changed less than 1%, their results are not presented or discussed here.

3.2.2.1 Phosphorous Scenarios

Figure 5-2 depicts the response of pond-integrated phosphorous limiting factor, f(P), and TCHLA to perturbations in individual phosphorous components (POPL, PIP, DOPL and PO4), and to perturbations in TP. Notably, f(P) and consequently TCHLA are more sensitive to PO4 and DOPL, given their greater availability for uptake by algae (Ji 2017). The response of TCHLA to these two components and to TP is linear (R^2=0.98, p-Value<0.01). However, PIP and DOPL components have negligible impact on TCHLA, with variations under 2% over the range of λ[Nutrient]. As expected, the influence of TP is more significant than the individual influences of each component. For example, Figure 5-2b indicates that a ±50% change in TP leads to +25% and -36% change in TCHLA, respectively, while a ±50% change in DOPL or PO4 leads to approximately ±10% TCHLA variations.

It should be noted that phosphorus load influences the potential growth rate (μ) only during the periods when phosphorus is indeed the limiting factor. This is particularly evident in Figure 5-3a during the period of late July to early September, when f(P) is significantly below 1.0. During this time, the effect of changing TP on μ becomes apparent (Figure 5-3b), leading to higher concentrations of TCHLA for larger λ[Nutrient], as shown in Figure 5-3c.

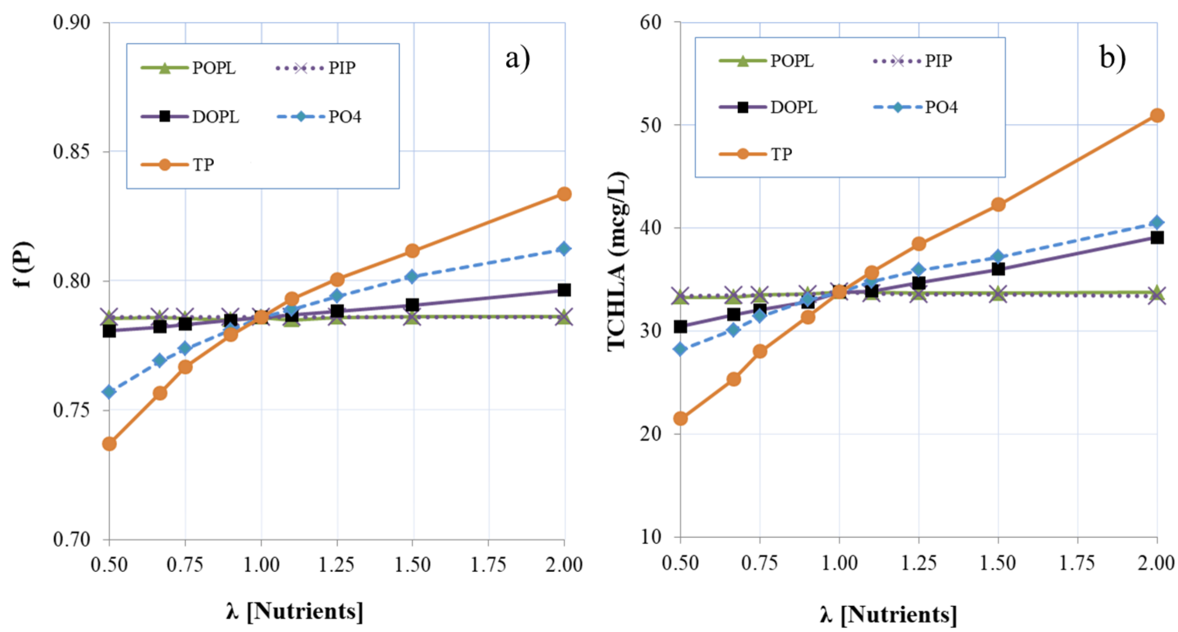

Figure 5-2: Response of pond-integrated (a) f(P) and (b) TCHLA to phosphorous scenarios.

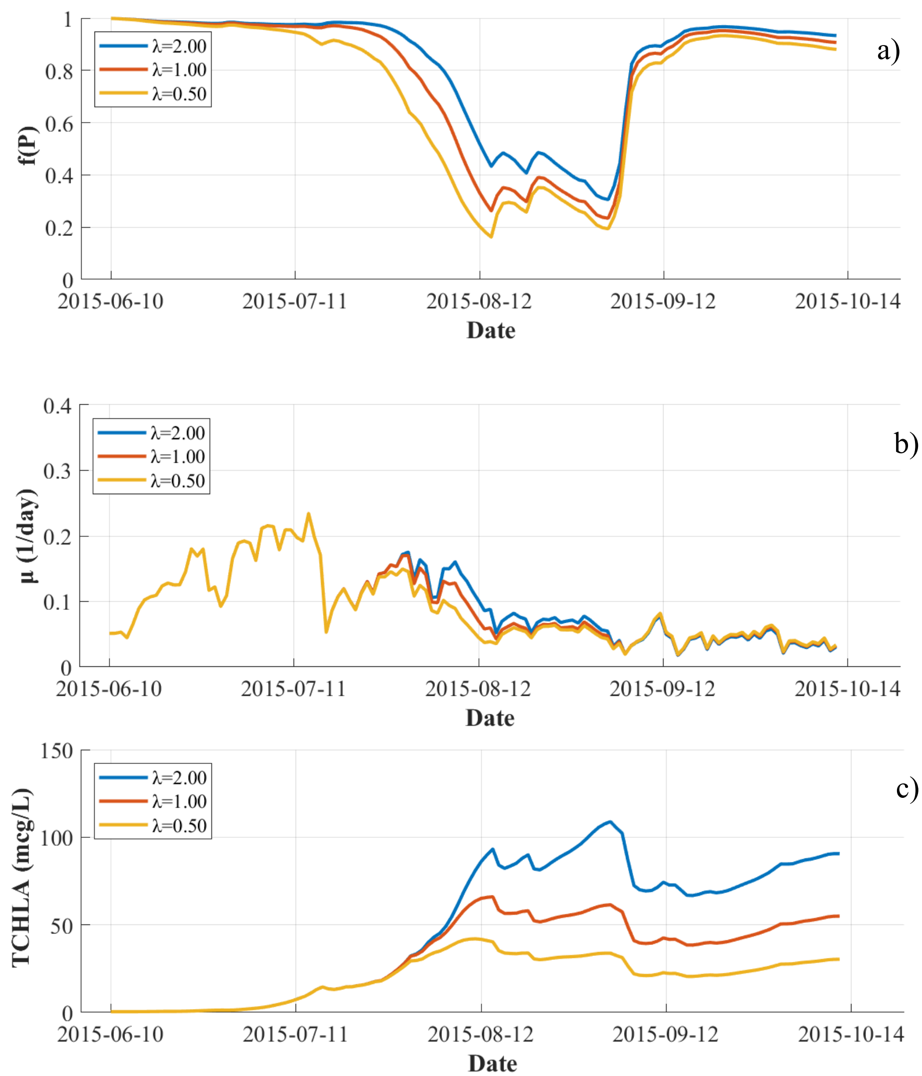

Figure 5-3: Time series of daily-averaged (a) phosphorous limiting factor, (b) gross growth rate, and (c) Total Chlorophyll-a concentration under Total Phosphorous scenario with different λ[TP].

3.2.2.1 Nitrogen Components

Varying the nitrogen components by 0.25<λ[TN]<2.0 changed the pond-integrated f(N) by up to 50%, but had minimal impact on TCHLA. This is due to f(P) being the dominant nutrient limiting factor over most of the simulation period. Nitrogen only became the nutrient limiting factor during the early season when f(P) ≈ 1.0. However, even during this period, f(N) changed by less than 2% over the range of λ[TN]. Consequently, across the range of λ[TN], pond TCHLA changed less than 4% compared to the base-run values. For brevity, results are not presented here.

5.3.2. **Impact of Different Scenarios on Water Temperature**

The average of perturbed air temperature and pond-integrated water temperature presented in Table 5-4, have a linear relationship (R^2=0.99, p-value<0.01). During the simulation period, the pond-integrated water temperature for the base-run was 18.5°C and at the NW, SW, SARM, and SE sampling locations it was 14.9°C, 17.8°C, 17.0°C, and 18.8°C, respectively. In other words, water temperatures are lower at the inlets compared to the outlet and the pond-integrated value. A comparison of different runs and scenarios presented in Figure 5-4 also highlights the consistent pattern of lower temperatures near the inlets. Figure 5-4 a&b show how the average temperatures of the pond and sampling locations respond to changes in depth. In both the Depth0 and DepthU scenarios, average temperatures do not change significantly (less than 1°C) with variations in depth, and the response is not monotonic. In general, shallower ponds tend to have larger diurnal temperature fluctuations as well as higher variability at timescales ranging from several days to a week (Appendix C, Figure C-1), primarily due to their lower water volume and, consequently, reduced heat capacity. As a result, compared to deeper ponds, shallower ponds warm up faster during the day and cool down more quickly at night. Shallower ponds also heat up more and cool down more in response to longer timescale climatic forcing. For instance, Figure C-1 shows that the difference between the maximum and minimum daily pond-averaged temperatures during the simulation period was 16.7°C and 22.8°C for λ[Depth0] of 1.72 and 0.59, respectively. Figure 5-4b shows that the temperatures are more uniformly distributed across a pond in the DepthU scenario, indicating that homogeneity of the bathymetry also plays an important role in the spatial variations in water temperature.

Table 5-4: Temperature scenario perturbations and corresponding averaged air and pond-integrated temperatures.

λ [T] (°C)	Average Air Temperature (°C)	Pond-integrated Temperature (°C)
-4.0	11.7	15.6
-3.0	12.7	16.3
-2.0	13.7	17.0
-1.0	14.7	17.8
-0.5	15.2	18.1
0.0	15.7	18.5
0.5	16.2	18.8
1.0	16.7	19.2
2.0	17.7	19.9
3.0	18.7	20.6
4.0	19.7	21.3

The results of the Flow scenario, as depicted in Figure 5-4c, indicate a negative association between the pond-averaged temperature and λ[Flow]. This trend is primarily attributed to the increased volume of colder inflows. Specifically, pond temperature decreases linearly with a slope of -0.45°C/λ[Flow] (R^2=0.99, p-value<0.01). Note that the NW inlet experiences a greater impact since it receives the majority of inflow. However, the trend is nonlinear at this location: a decreases rate of -1.64 and -0.38°C/λ[Flow] for the range of λ[Flow] less than and greater than 1.5, respectively.

In Figure 5-4d, a negative association between temperature and wind speed is evident across the entire pond. This can be attributed to the enhanced evaporative heat flux as well as enhanced mixing due to higher wind speeds. There is a statistically significant logarithmic relationship between pond-averaged temperature and wind speed. Furthermore, stronger winds lead to smaller temperature differences across the pond. However, the NW location displays a lower sensitivity to wind speed perturbations due to its narrow and deep bathymetry, which likely inhibits mixing.

Pond-averaged and sampling location temperatures increase linearly with air temperature (Figure 5-4e). The linear regression is significant across the pond (R^2=0.99). Once again, the NW inlet demonstrates a relatively lower sensitivity to air temperature. For example, the pond-averaged temperature was 2.5 times more sensitive to increasing air temperatures compared to the NW. The reduced sensitivity is linked to the locally deep and narrow bathymetry of the NW inlet, where its temperature is influenced by the relatively cold inflow that tends to get trapped in this low spot. Furthermore, when comparing all scenarios (Figure 5-4), an increase of water temperature from the major inlet at the NW towards the SE outlet is evident. Excluding the DepthU scenario, the SE-NW temperature differences range from 2.1°C at λ[T]=-4°C to 5.8°C at λ[T]=+4°C and λ[Wind]=0.25. The implications of these elevated outflow temperatures on the environment can vary depending on the specific characteristics of the downstream receiving water and may need to be considered in management plans.

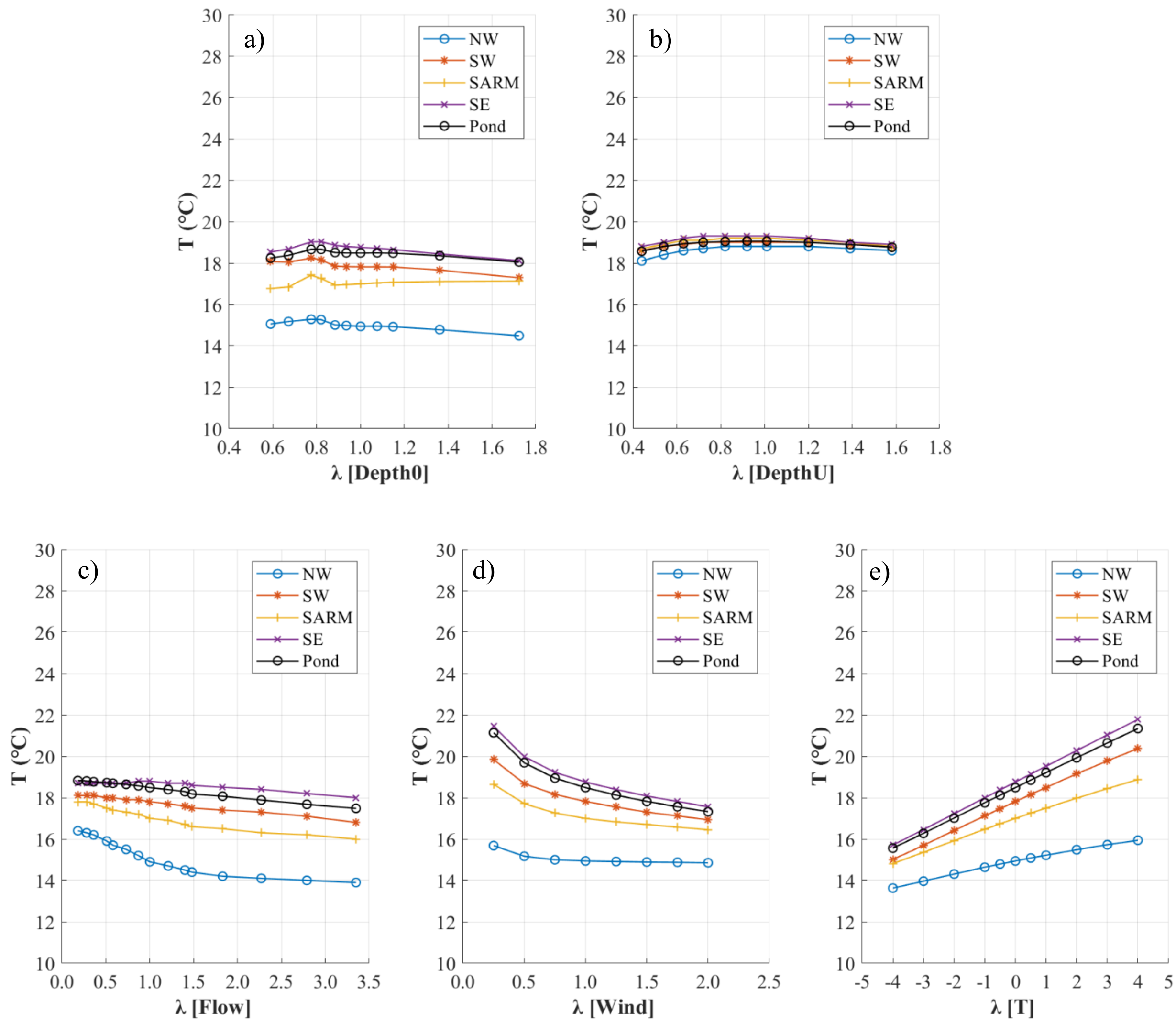

Figure 5-4: Response of water temperature, T (°C) to different scenarios: a) Depth, b) Uniform Depth, c) Flow, d) Wind, and e) Temperature scenario.

5.3.3. Impact of Different Scenarios on Thermal Stratification

Figure 5-5 illustrates how F1 (i.e., a stratification criteria of ΔT=1) responds in different scenarios. Results for other stratification criteria are presented in Appendix C, Figure C-2 to Figure C-6. The significant impact of the local bathymetry is evident from the higher F1 values in the Depth0 scenario compared to the DepthU scenario. As expected, the deeper sampling locations have higher F1 compared to the pond average due to the increased vertical separation between the warmer surface and colder bottom layers. However, across the range of λ[Depth0], F1 at the NW inlet varied less than 10% (Figure 5-5a) which was the smallest value compared to the other locations. This can be attributed to the deep and relatively isolated bathymetry of the NW inlet, and the fact that near-bed temperatures at this location are primarily influenced by the colder inflows rather than changes in depth.

Figure 5-5b shows that across the range of λ[DepthU], the F1 values were within 5% of the pond averaged value at all locations except the NW inlet. The NW F1 values are up to 18% higher (at λ[DepthU]=0.44) compared to other locations, but with increased depth, the discrepancy diminishes to less than 2% at λ[DepthU]=1.58. This occurs because the near-bed temperatures in a deeper pond approach inflow temperatures.

Figure 5-5c indicates that, in the Flow scenario, F1 increases linearly for the pond from 36% to 56% across the entire range of λ[Flow]. However, at the sampling locations, F1 variation is non-monotonic and less sensitive to λ[Flow]. More detailed comparisons are presented in Appendix D, Figure C-7, illustrating variations in average temperature versus λ[Flow] at the sampling locations and the pond, both at the top (Figure C-7a) and bottom (Figure C-7b), along with their difference, i.e., ΔT (Figure C-7c). These results suggest that ΔT and, consequently, F1 are more influenced by variations in near bed temperatures than surface temperatures in the flow scenario. This is attributed to the placement of inlets at the bottom of the pond, which introduce cold inflows near the bed.

Figure 5-5d shows that higher wind speeds are associated with lower F1 across the pond. The trend is linear at the SW and SE sampling locations and the pond, with slopes of about 20% per unit of λ[Wind], respectively (R^2>0.98, p-value<0.01). The trends at the NW and SARM inlets are almost linear, but on average, F1 shows lower sensitivity with slopes of about 10% per unit of λ[Wind (R^2>0.93, p-value<0.01). The reduced responses at the inlets can be attributed to the influence of cold inflows, which contribute to more locally stable stratification. More detailed results are presented in Appendix C, Figure C-8d, showing that with increasing wind speed, the temperatures of the top and bottom layers gradually converge. Over the range of λ[Wind], the top and bottom temperatures decrease by 5.0°C and 2.6°C, respectively. The greater reduction in top temperature is attributed to the higher cooling effect of the evaporative heat flux at the surface.

Figure 5-5e illustrates a linear positive correlation between λ[T] and F1 across the pond, with an average slope of 2.2%/°C. That is, for every 1.0°C increase in air temperature, the occurrence of stratification increased on average by 2.2%. This is because, as shown in Appendix C, Figure C-8e, the top temperature increased at a higher rate compared to the bottom temperature. For every 1.0°C increase in air temperature, the water temperature increased on average by 0.81°C and 0.67°C at the top and bottom, respectively.

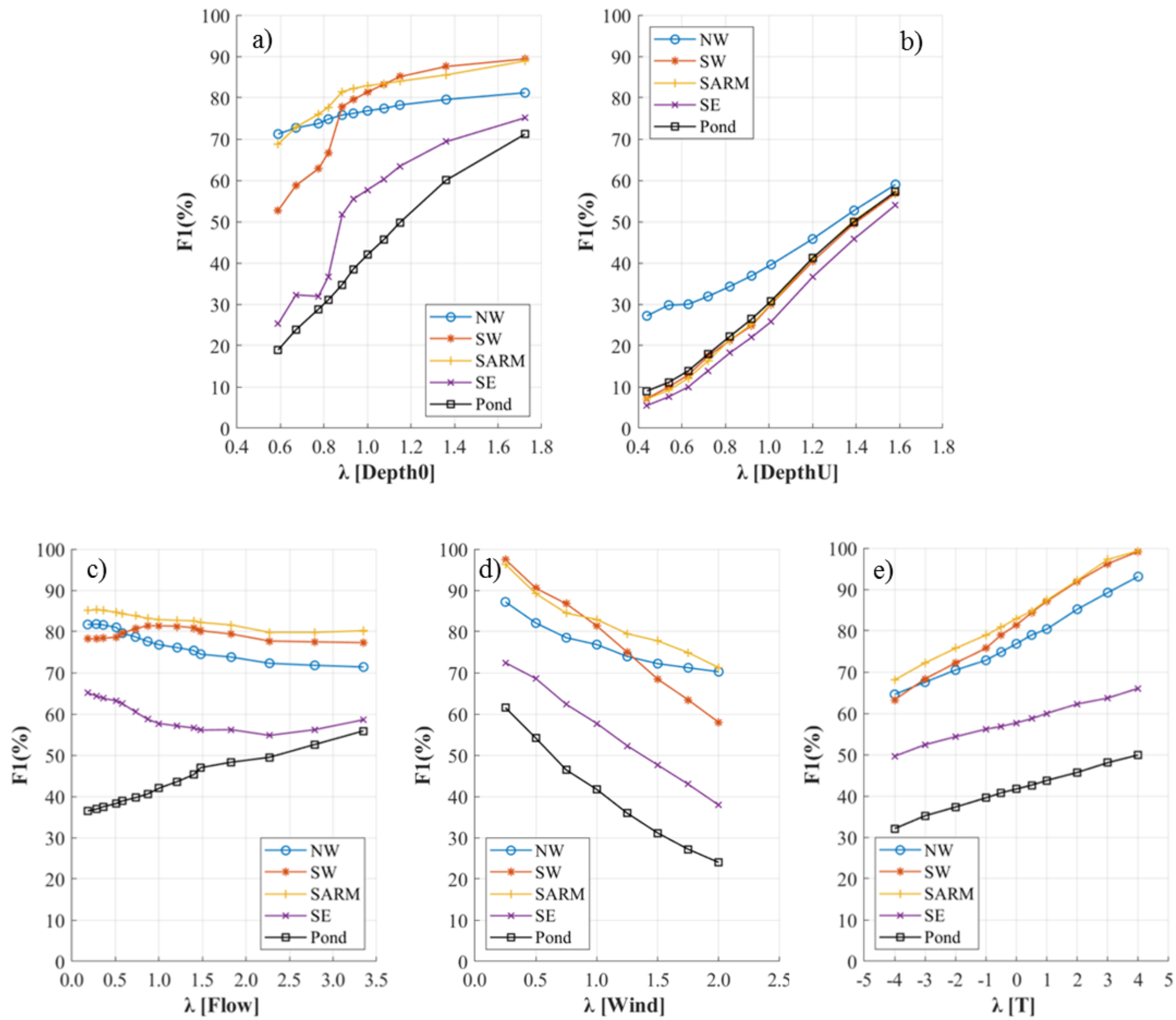

Figure 5-5: Response of F1 ratio (%) to defined scenarios: a) Depth, b) Uniform depth, c) Flow, d) Wind, and e) Temperature scenarios.

5.3.4. Impact of Different Scenarios on Retention Time

Figure 5-6 illustrates the response of retention time (RT) to the different scenarios. The NW inlet has the shortest RT across all the scenarios, averaging 9.3 days less than the pond RT (16.8 days). This is expected, as 74% of inflow enters the pond through this inlet. Similarly, the SARM inlet RT is on average 3.4 days less than the pond. In contrast, the SE outlet has the longest RT, with a mean of 1.9 days longer than that of the pond.

Figure 5-6a shows that RT increased linearly with λ[Depth0], although at different rates across the pond. A 50% increase in depth increased the average RT from 18 to 26 days, which is a 44% increase. The rates of increase at the SE and SW locations were almost the same as the pond average, but lower at the inlet locations. All linear regressions are significant with $R^2>0.98$. With the uniform bathymetry of the DepthU scenario, these slopes converge to approximately 13.5 day/λ[DepthU] (Figure 5-6b). As discussed earlier, the NW inlet has the shortest RT among the sampling locations, with 6.0 to 15.3 days shorter than the pond RT. However, the uniform bathymetry of the DepthU scenario reduces this difference to approximately 2 days (Figure 5-6a and b).

RT decreases monotonically with λ[Flow] across the pond (Figure 5-6c). A linear regression between the logarithm of λ[Flow] and RT is significant for all the locations and the pond ($R^2>0.96$). Due to this nonlinear relationship, pond RT decreases at a higher rate for λ[Flow]<1.5, resulting in a reduction of approximately 20 days. However, further increases of flow (1.5<λ[Flow]<3.4) contributed to less than 5 additional days of decrease.

The average RT versus λ[Wind] relationship (Figure 5-6d) exhibits a non-linear decreasing trend at SW, SE, and the pond, while the trend is non-monotonic at the NW and SARM inlets. Nevertheless, these variations are less significant compared to the Depth and Flow scenarios. For instance, pond RT changes by less than 5 days over the range of λ[Wind]. Furthermore, wind speeds exceeding those of the base-run do not exert a substantial influence on the RT throughout the pond; doubling wind speed reduces pond RT by less than 0.5 days.

In the Temperature scenario (Figure 5-6e), small variations of RT were observed across the range of λ[T]. Additionally, the trends of these variations are inconsistent across the pond. For example, at the NW inlet and SE outlet, a decreasing rate of 0.3 day/λ[T] and an increasing rate of 0.1 day/λ[T], respectively, was observed.

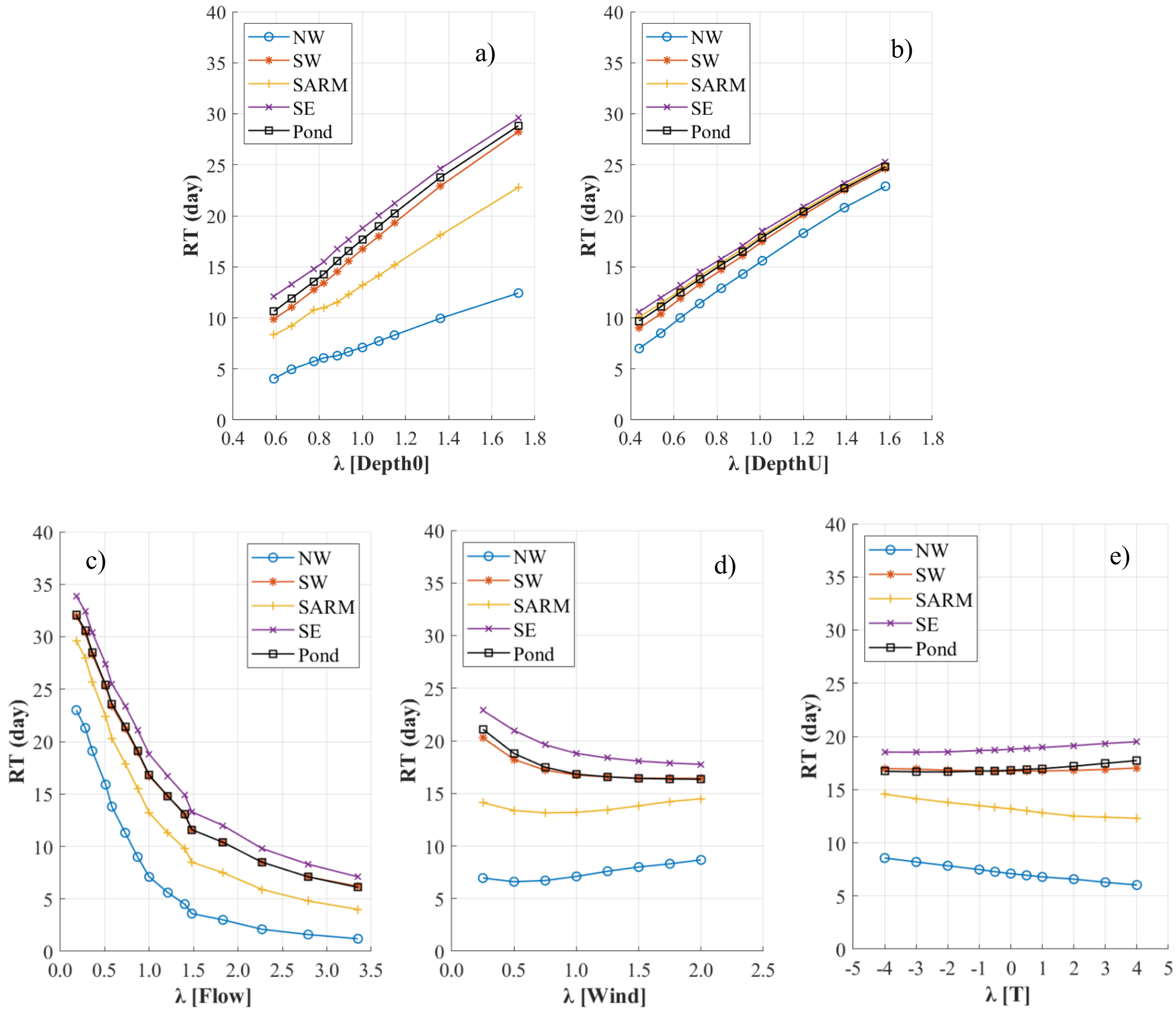

Figure 5-6: Response of retention time, RT (days) to defined scenarios. a) Depth, b) Uniform Depth, c) Flow, d) Wind, and e) Temperature scenarios.

5.3.5. Impact of Different Scenarios on Total Chlorophyll-a (TCHLA)

As mentioned earlier, TCHLA dynamics are controlled by the fractional biomass change rate, *G*, which is the sum of the physical transport rate, *hd*, and the net growth rate, *g*. While *g* is reasonably well understood as a function of f(I), f(T), f(P), and f(N) limiting factors as well as the respiration/mortality/excretion (*res*) and settling (*set*) rates, it is not fully clear how ECLOM-CAEDYM calculates and employs *hd*. In this section, the impact of different scenarios on TCHLA is described by investigating changes in the aforementioned key factors.

Figure 5-7 illustrates that TCHLA responds differently to each scenario. However, within the runs of each scenario, there is a consistent response at the sampling locations and pond. Despite the NW inlet showing lower concentrations compared to the pond average (ranging from 5 to 15 mcg/L across scenarios), its trend closely aligns with the other locations. Therefore, in the following discussion, only pond-averaged TCHLA and the key factors are detailed. Figure 5-8 illustrates the pond-averaged values of these factors for Depth0, DepthU and Flow scenarios. The settling rate is not presented, as its relative magnitude is negligible compared to *res*. It also should be noted that since the potential growth rate, μ, is proportional to the product of the limiting factors, its relative change is equal to the sum of relative changes of the limiting factors, i.e., $\Delta\mu/\mu = \Delta f(I)/f(I) + \Delta f(Nutrient)/f(Nutrient) + \Delta f(T)/f(T)$. Panels a1 and a2 of Figure 5-8 illustrate that the relative change in f(I) has the greatest magnitude compared to other limiting factors, indicating light is the most influential factor in Depth0 and DepthU scenarios. This conclusion is further supported as μ (shown in panels b1 and b2) and f(I) exhibit a consistent decreasing trend with depth. Given the relatively small changes in *res*, *g* also decreases with increasing depth. Conversely, *hd* increases monotonically with depth, as depicted in panels c1 and c2. The interplay of decreasing *g* and increasing *hd* results in a maximum *G* at λ[Depth0]=0.77 (panel c1), while in the DepthU scenario, *G* decreases monotonically (panel c2). Despite the slight changes in *G*, the exponential nature of algae growth amplifies even small variations in *G* into significant changes in TCHLA over time. For example, an 8% increase in *G* from the base-run value results in approximately a 30% rise in TCHLA. That is, as *G* increases from 0.039 1/day to 0.042 1/day, TCHLA rises from 34 to 44 mcg/L.

In the Flow scenario (Figure 5-8, panels a3, b3 and c3) μ is primarily influenced by limiting factors f(I) and f(P). f(I) decreases linearly at a rate of 0.027/λ[Flow] (R^2=0.997, p-value <0.01), indicating an inhibitory effect of light on μ as flow increases. This can be attributed to increasing total suspended solids as higher inflows lead to increased turbidity and subsequently, a higher light extinction coefficient in the water column. However, f(P) increases with inflow up to λ[Flow] = 1.5 due to the additional external load, then levels off towards its maximum value of 1.0. The combined influence of f(I) and f(P) results in μ increasing with an average rate of 0.013 (1/day/λ[Flow]) up to λ[Flow]=1.5, after which it decreases with a rate of 0.015 (1/day/λ[Flow]). As *res* remains almost constant, *g* follows the trend of μ.

Figure 5-8, panel c3 also shows that *hd* decreases with flow at an average rate of 0.024 1/day/λ[Flow]. The combined influence of *g* and *hd* leads to an almost constant *G* up to λ[Flow] = 0.75 followed by a decreasing trend thereafter. In particular, *G* is negative for λ[Flow]>2.3. The same pattern is reflected in Figure 5-7c, where TCHLA remains nearly constant at 60 mcg/L up to λ[Flow]=0.75, followed by a rapid decrease with an average rate of 55 mcg/L/λ[Flow]. This decrease is attributed to shorter RT which results in flushing out the algae and insufficient time for algae to grow. With further increases in flow (λ[Flow]>1.5), RT becomes so short that TCHLA approaches negligible levels, nearly zero at λ[Flow] = 2.5.

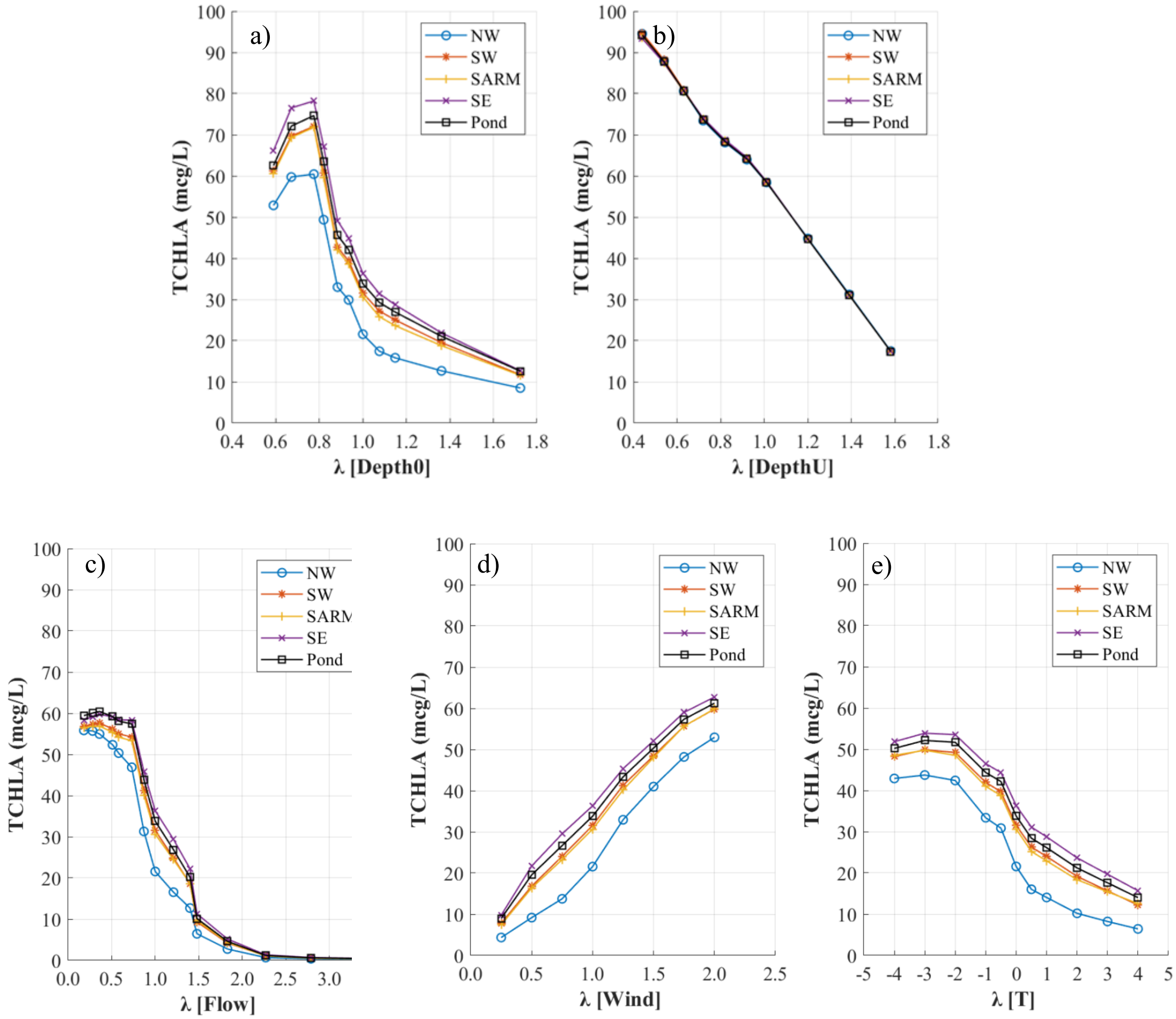

Figure 5-7: Variations of TCHLA (mcg/L) across the scenarios: a) Depth, b) Uniform Depth, c) Flow, d) Wind, and e) Temperature scenarios.

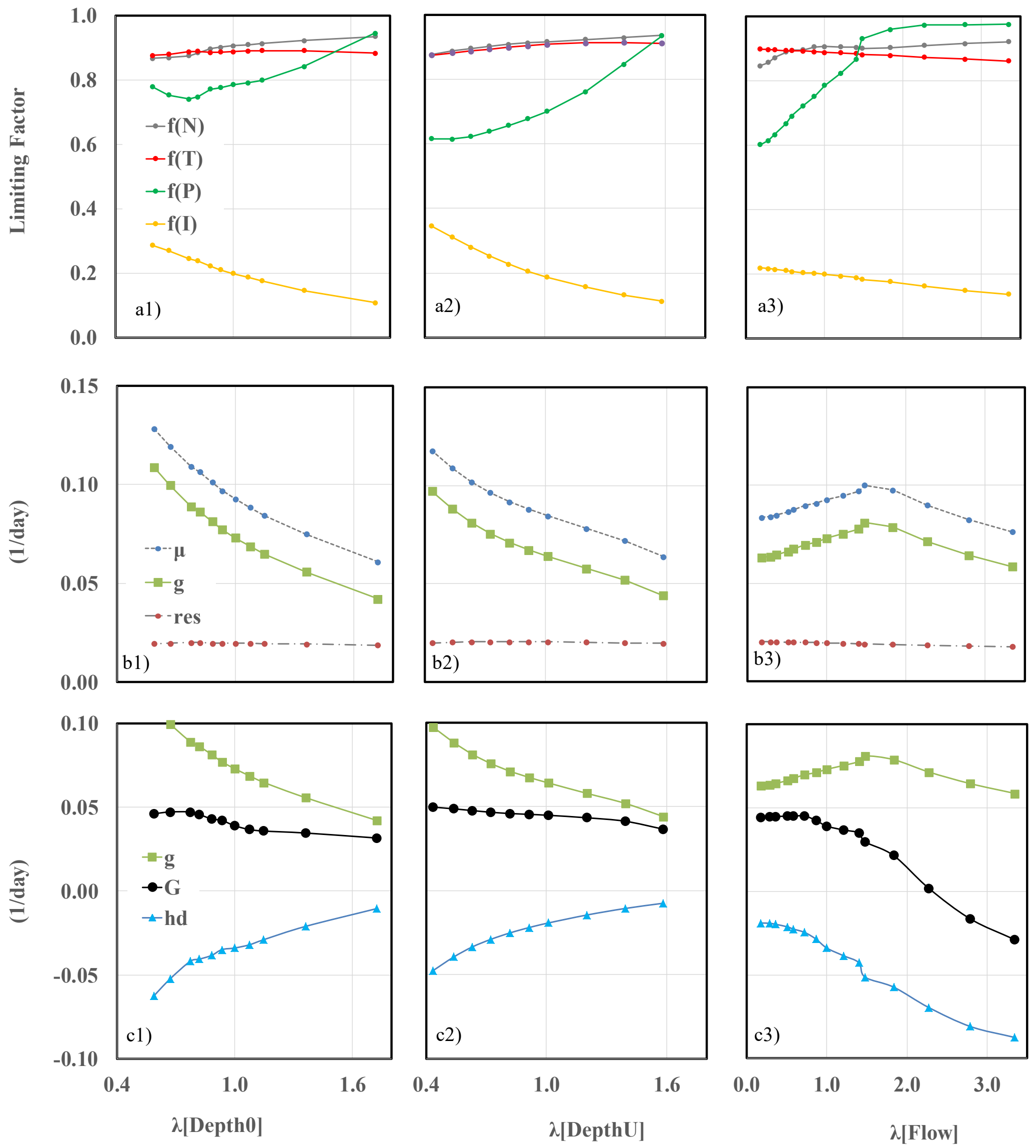

Figure 5-8: Key factors influencing TCHLA in; left column) Depth0, middle column) DepthU, and right column) Flow scenarios.

Figure 5-9 illustrates that *hd* increases monotonically with RT in the Depth0, DepthU, and Flow scenarios. Particularly, there is a similar RT-*hd* dependency in the Depth0 and Flow scenarios. It can be inferred that an increase in depth or a decrease in flow, that results in the same RT, corresponds to almost the same *hd*. However, this consistency does not extend to the RT-*g* relationship (Figure 5-10). While increased depth (leading to a longer RT) results in lower f(I), decreased flow (also resulting in longer RT) leads to higher f(I) as well as lower f(P) (Figure

5-8). Therefore, both depth scenarios show a monotonically decreasing RT-*g* relationship, while in the Flow scenario the relationship is non-monotonic. As a result, management practices to control algae biomass by reducing RT through modifications of flow or depth (e.g., Le'on et al. 2016; Olsson et al. 2022; Sutherland et al. 2014; Woodhouse et al. 2006; Zhao et al. 2023) may not work as intended.

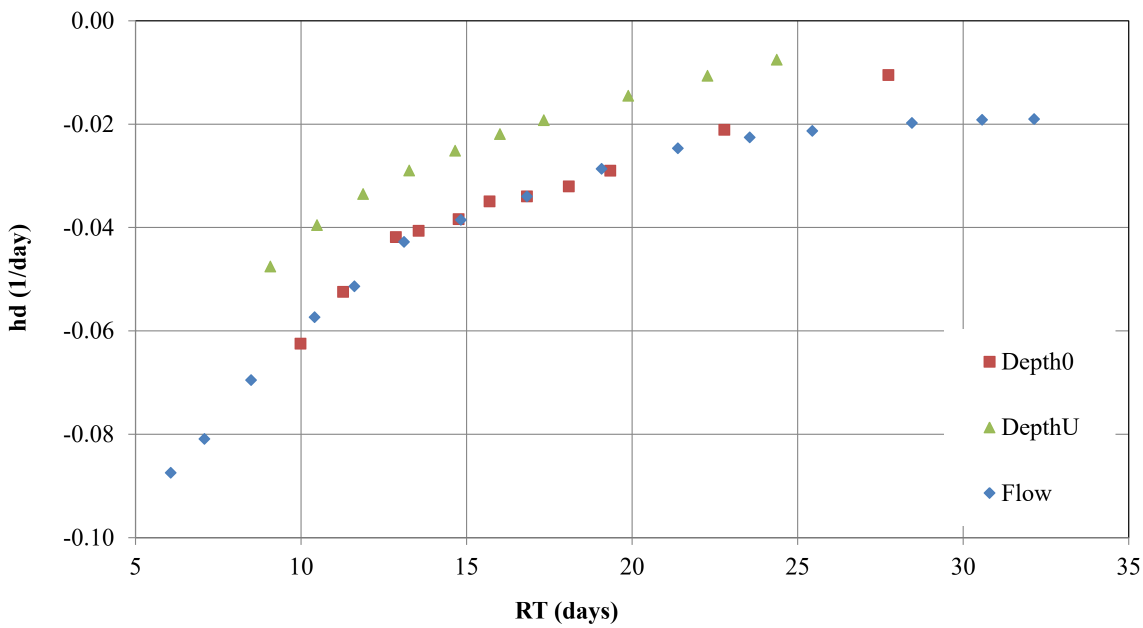

Figure 5-9: Physical transport rate (*hd*) versus retention time (RT) for Depth0, DepthU, and Flow scenarios

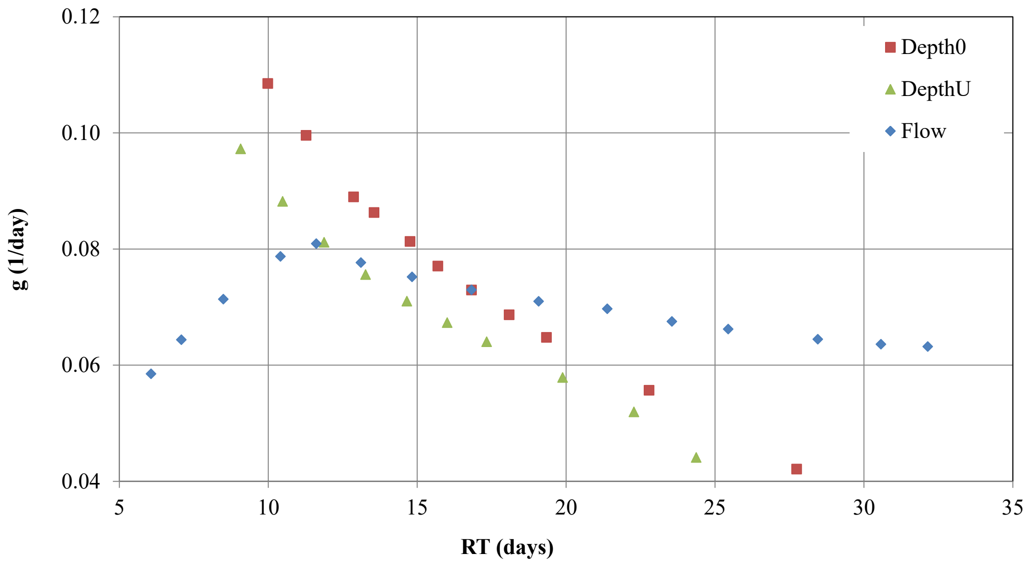

Figure 5-10: Net growth rate (*g*) versus retention time (RT) for Depth0, DepthU, and Flow scenarios

In the Wind scenario (Figure 5-7d), TCHLA and λ[Wind] have a linear relationship with a slope of 30 mcg/L/λ[Wind] (R^2=0.99, p-value <0.01). This means increasing wind speed by 50% results in increase of TCHLA by 49%. In Figure 5-11, panels a1 and b1 illustrate factors influencing μ, resulting in maximum μ at λ[Wind]=1.5. Although the *res* decreased with λ[Wind], due to decrease of temperatures (Appendix C, Figure C-9), *g*, similar to μ, reaches its maximum at λ[Wind]=1.5. However, as presented in Figure 5-11, panel c1, the non-monotonic variation of *hd* with λ[Wind], with a minimum at λ[Wind]=0.75, results in an increase in *G* and consequently TCHLA with an increase in λ[Wind].

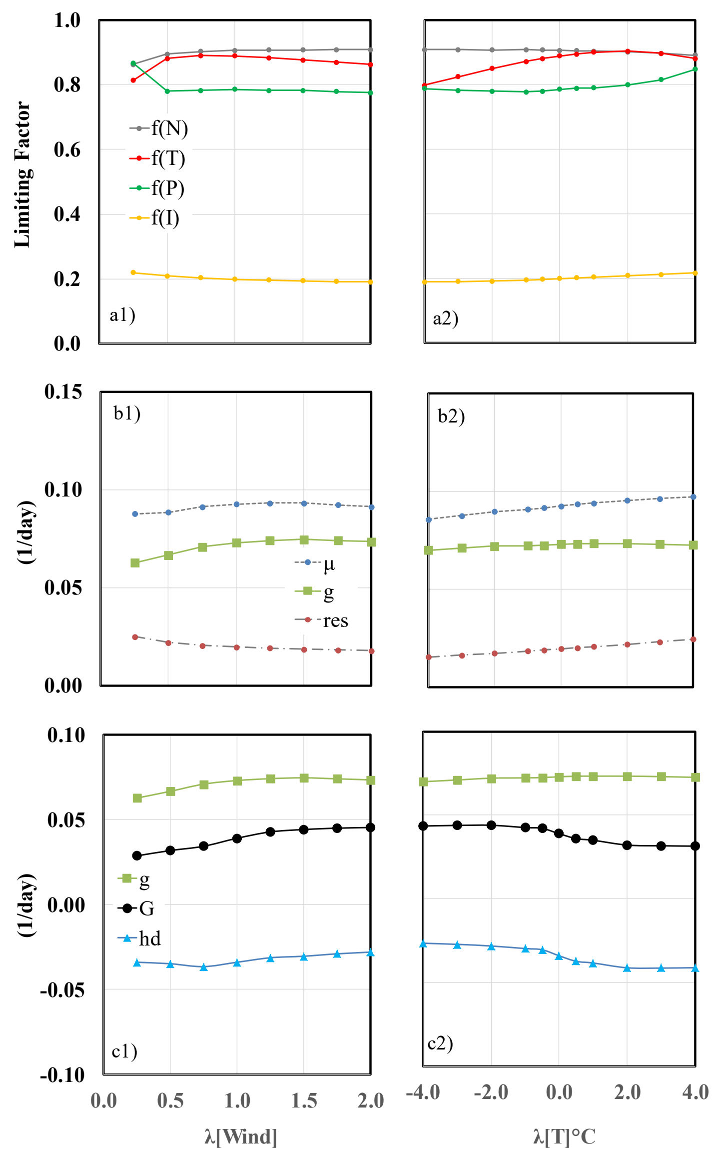

Figure 5-11: Key factors influencing TCHLA in; left column) Wind, and right column) Temperature scenarios.

Figure 5-7e shows that TCHLA is approximately 50 mcg/L for -4°C < λ[T] < -2°C, but for λ[T] > -2°C, TCHLA decreases rapidly in a nonlinear manner. The influencing factors on TCHLA in the temperature scenario are depicted in Figure 5-11, panels a1, b1 and c1. Although f(T) reaches its maximum at λ[T] = 2°C, the combined effects of other key factors results in *g* changing from 0.0700 1/day to 0.0733 1/day over the range of λ[T]. Yet, changes in *hd* versus λ[T] are more pronounced, decreasing from -0.0265 1/day to -0.0411 1/day, resulting in decreasing *G* and consequently TCHLA for λ[T] > -2°C.

Other studies have also reported a reduction in TCHLA in warmer scenarios. For example, Reilly (2003) reported a decrease in algae biomass in Lake Tanganyika, Africa, over the 80 years preceding their study, primarily due to a warmer climate. Additionally, Moss et al. (2003) reported that increasing temperature resulted in a decrease in the abundance of certain green algae species, such as Chlorophycota. However, Linden et al.(2015) and Trolle (2011) attributed the lower algae concentrations simulated in warmer scenarios to the limitations of the ELCOM-CAEDYM model, particularly in simulating biogeochemical rates.

In the Wind and Temperature scenarios, no clear relationship was found between *hd* and other state variables. In fact, RT remained relatively unchanged under these scenarios (e.g., varied less than 1.0 day in the temperature scenario). It is worth noting that *hd* could potentially be influenced by thermal and density stratification. While several studies have explored the impact of stratification and mixing on total algae biomass, they primarily attributed these changes to variations in biogeochemical factors like internal nutrient release and availability, which are not explanatory factors for *hd* (e.g., Lofton et al. 2022; Reilly et al. 2003; Ula´nczyk et al. 2021). Further research is required to understand how wind and temperature affect *hd*, especially in urban stormwater ponds.

It is important to note that the driving and state variables discussed above, including *g* and *hd*, represent pond-integrated values, which are values averaged over the pond and the simulation period. However, given the exponential growth/decay nature of algae, temporal variations of *g* and *hd* can also have a significant impact. For example, in the Temperature scenario, average *g* over the simulation period for λ[T]=3°C is higher than that of the base-run. As illustrated in Figure 5-12, water temperatures of the warmer run have exceeded the optimum range for algae growth in late June, early July, and early August, as reflected in the f(T) and *g* plots, thereby hindering algae growth. Although growth rates eventually recovered in the warmer run, algae growth was considerably inhibited, leading to a lower averaged TCHLA (17.6 mcg/L) compared to that of the base-run (33.8 mcg/L). In an exponential growth, earlier drops in algae biomass (e.g., due to flush-outs) or declines in growth rate (e.g., due to adverse biogeochemical conditions) can significantly hinder growth.

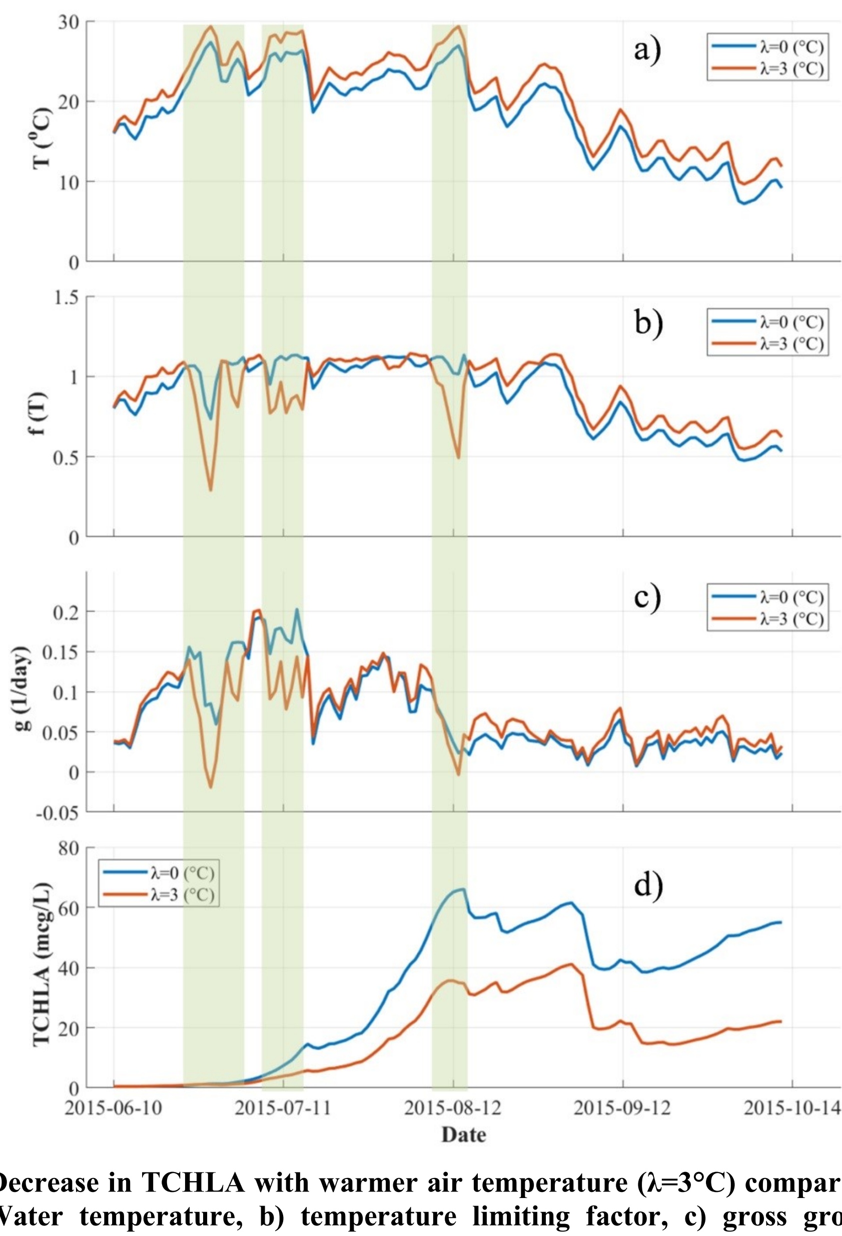

Figure 5-12: Decrease in TCHLA with warmer air temperature (λ=3°C) compared to the base-run (λ=0°C). a) Water temperature, b) temperature limiting factor, c) gross growth rate, and d) TCHLA concentration. Shaded areas indicate periods during which the warmer run has a lower gross growth rate.

5.3.6. **Impact of Different Scenarios on Dissolved Oxygen**

Figure 5-13 illustrates how dissolved oxygen (DO) responds to the defined scenarios. DO concentrations at the inlets are notably lower, due to the low-oxygen inflows imposed by boundary conditions. Additionally, Figure C-11 in Appendix C presents the same data, but with DO averaged at the surface, middle, and near-bed layers.

Over the ranges of λ[Depth0] and λ[DepthU], pond DO varies less than 0.6 and 0.3 mg/L, respectively (Figure 5-13a and b). A decreasing trend in DO is noticeable as λ[Flow] and λ[T] increase, with the maximum drop being 1.7 and 2.3 mg/L, respectively. In the Wind scenario, however, DO increases by more than 7.4 mg/L across the range of λ[Wind] (Figure 5-13d). Wind's influence on DO, surpassing the impacts of other scenarios, is noteworthy, given wind's milder effects on other state variables (panel d of Figure 5-4 to Figure 5-7). At very low wind speeds (λ[Wind]<0.5), pond DO drops below the NW levels that are due to the low-oxygen inflows.

In both Depth0 and DepthU scenarios, the more pronounced drop in near-bed DO (Figure C-11a and b) leads to a 2.1 mg/L top-bottom difference at the highest λ values. Similarly, though to a lesser degree, the top-bottom DO difference increases with respective λ values in the Wind and Temperature scenarios (Figure C-11d and e). The difference remains relatively constant at 1.0 mg/L in the Flow scenario (Figure C-11c).

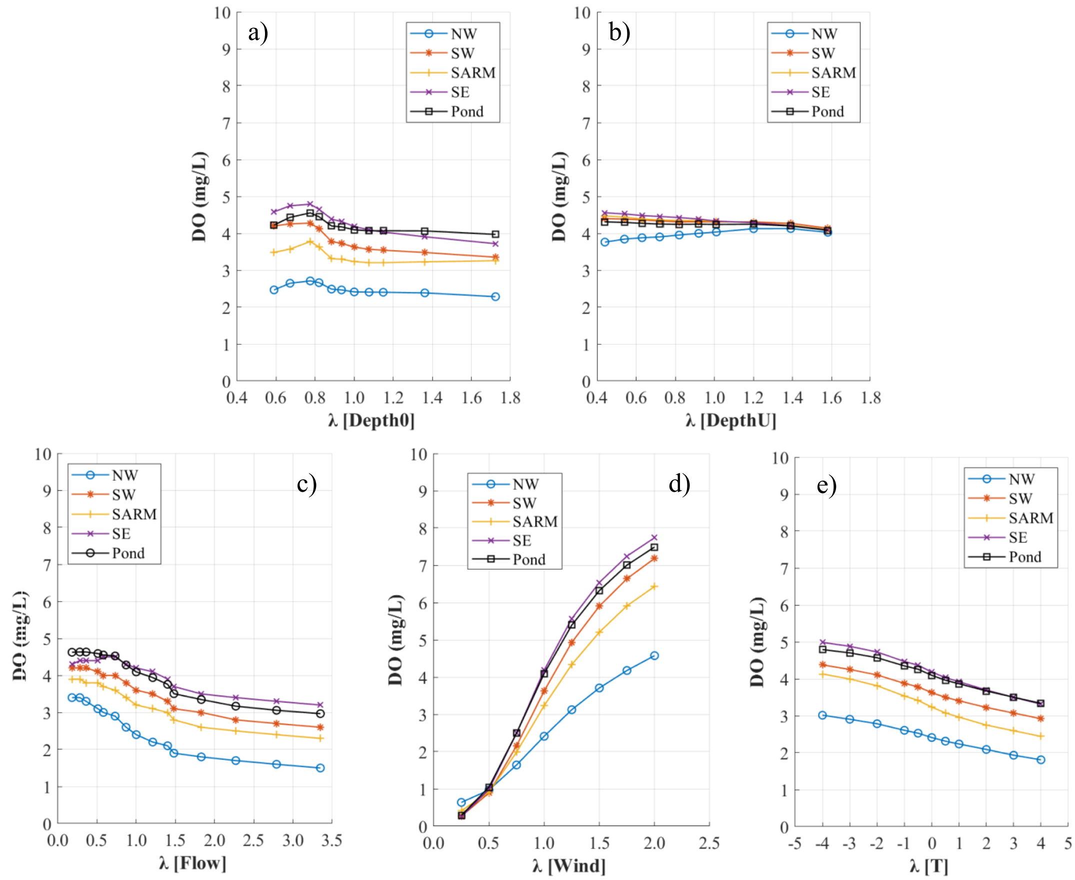

Figure 5-13: DO (mg/L) at sampling locations and the pond averaged during simulation period. a) Depth scenario, b) Uniform depth scenario, c) Flow scenario, d) Wind scenario, and e) Temperature scenario.

5.3.7. Interrelationship between DO and other variables

Dissolved oxygen (DO) is influenced by various factors, including water temperature, wind, stratification, and biogeochemical activities (Chen et al. 2019; Ji 2017). Figure 5-14 indicates that pond temperature is not a reliable explanatory variable for DO, as different scenarios display varying patterns: a linear decrease in the Wind and Temperature scenarios, a non-linear increase in the Flow scenario, and minimal change in the Depth0 and TP scenarios. Additionally, although Figure 5-15 implies that DO decreases with an increase in stratification, the relationship is not consistent across the scenarios. Therefore, thermal stratification strength (ΔT) cannot be the primary explanatory variable. Despite the presented DO-ΔT relationship being based on pond-averaged DO, similar relationship exists when average DO at the top, middle, and bottom layers are used (not presented here for brevity). This is because, as seen in Figure C-11, pond-averaged DO and average DO at the top, middle, and bottom layers have similar patterns across the scenarios.

Figure 5-16 illustrates the pond TCHLA-DO relationships across the scenarios including the TP scenario. Regression analysis confirms a statistically significant linear relationship between TCHLA and DO in each scenario. The relationship remains statistically significant when aggregating all scenarios except the Wind scenario (slope=0.021 mg DO/mcg TCHLA, R^2=0.83, p-value<0.01). This suggests that higher algae concentration (i.e. more photosynthesis) leads to higher DO. Notably, in Figure 5-16, the Wind scenario stands out with a slope of 0.15 mg DO/mcg TCHLA (R^2=0.98, p-value<0.01). This elevated slope is attributed to the oxygenation of water column by wind-induced mixing in addition to photosynthesis. This is expected and consistent with other studies (e.g., Chen et al. 2019). Therefore, it can be concluded that wind is the dominant driver of DO in the study pond.

Furthermore, it can be concluded that the increase in DO due to photosynthesis and wind-induced oxygenation outweighs other oxygen-depleting processes, such as algae degradation. This can be attributed to the pond's short RT, resulting in the flush-out of algae biomass before significant degradation can occur. This conclusion aligns with the findings of (Wium-Andersen et al. 2013).

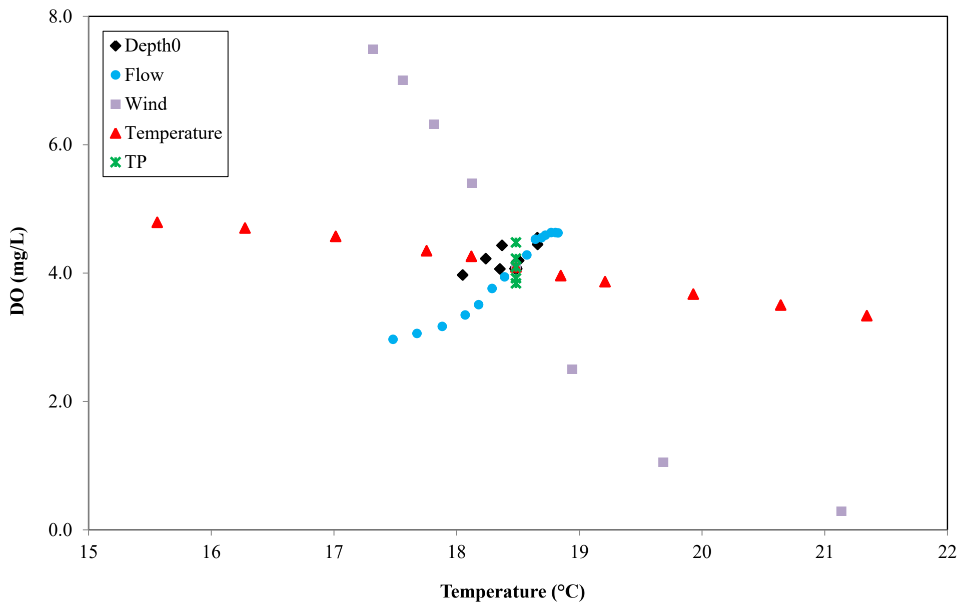

Figure 5-14: Pond DO and water temperature in Depth0, Flow, Wind, Temperature and Total Phosphorous scenarios.

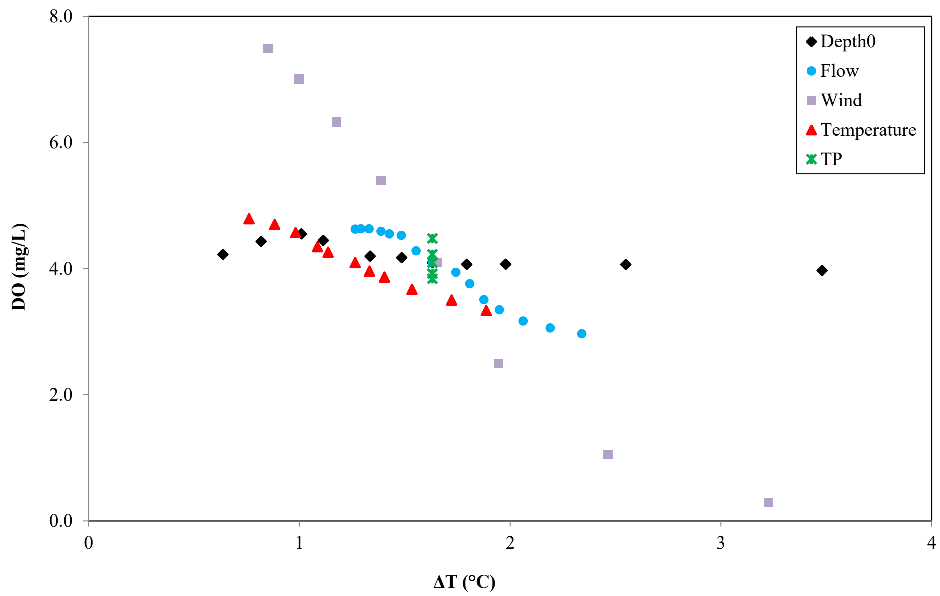

Figure 5-15: Pond DO and stratification strength ΔT in Depth0, Flow, Wind, and Temperature scenarios.

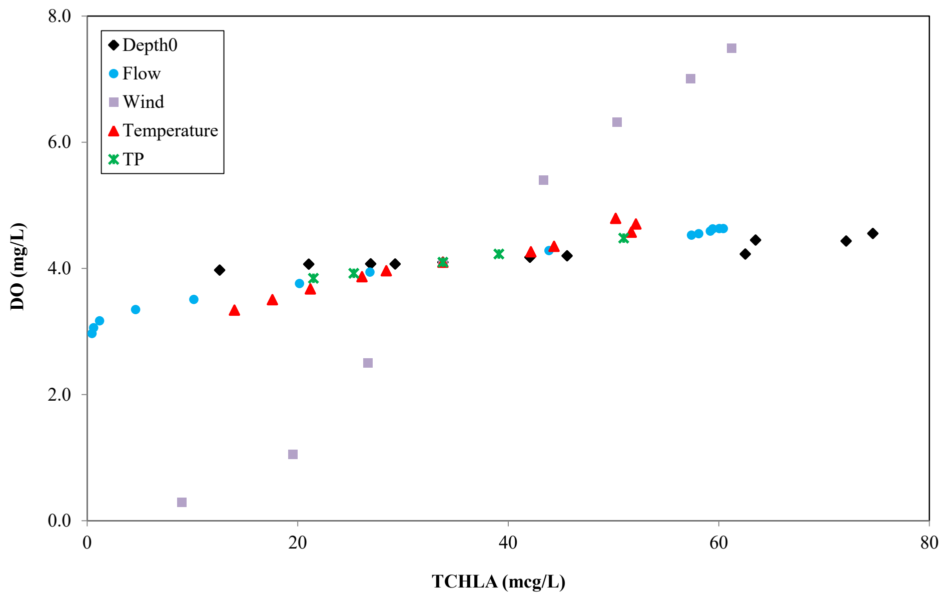

Figure 5-16: Pond DO and TCHLA in Depth0, Flow, Wind, Temperature and Total Phosphorous scenarios.

5.3.8. **Relationship between TCHLA and RT**

In Figure 5-17, time series of RT (panel a) and TCHLA (panel b) are plotted for the base-run for pond-averaged, as well as depth-averaged values at the sampling locations. A high degree of concordance between RT and TCHLA is evident, meaning increases in RT often correspond to increases in TCHLA, and vice versa. The Kendall τ test (details in Appendix C.2) confirms a strong and statistically significant RT-TCHLA association in the base-run (τ=0.67). The association remains statistically significant within all runs in all the scenarios, with a median τ of 0.65. Furthermore, a stronger association exists in the near-surface layer than in the near-bed layer (Figure 5-19a).

Figure 5-18 is a plot of base-run RT and TCHLA along a curtain passing through NW, NE, SARM and SE sampling locations (additional details in Appendix C.2 and Figure C-12). Depth-averaged RT and TCHLA, averaged over the simulation period, display a strong and statistically significant association (τ=0.75). The association remains statistically significant within all the runs of different scenarios, with a median τ of 0.72 (Figure 5-19b).

Despite the statistically significant association between RT and TCHLA within individual runs, attempting to predict TCHLA variations, even approximately, solely based on changes in RT and without considering the underlying drivers of that change, can be misleading. For example, Figure 5-20 illustrates that while a longer RT resulting from increased inflows (Flow Scenario) corresponds to an increase in TCHLA, a longer RT due to greater depths (Depth0 scenario) generally leads to a decrease in TCHLA. Additionally, it was previously shown in Figure 5-3 that an increase in total phosphorus (TP) is associated with higher TCHLA, while it does not have any impact on RT.

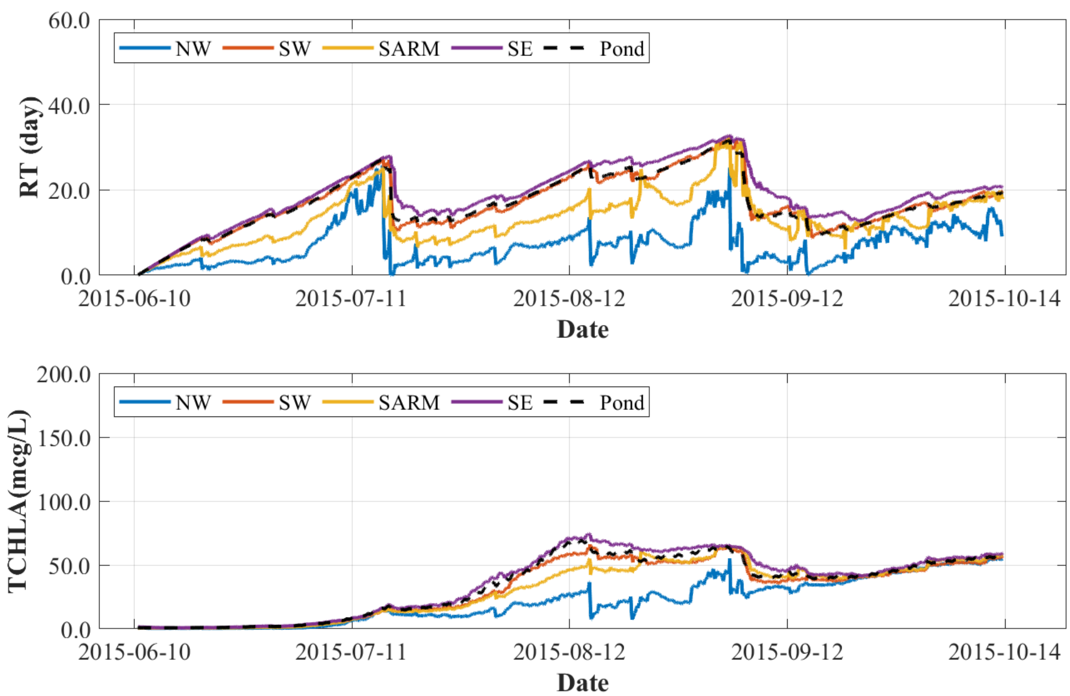

Figure 5-17: Time series of (top) RT and (bottom) TCHLA at the sampling locations (depth-averaged) and pond (pond-integrated) for the base-run.

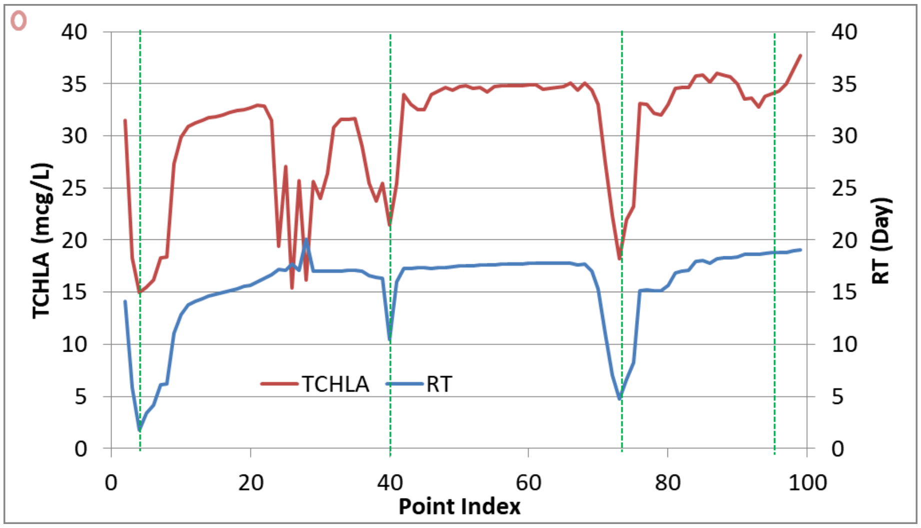

Figure 5-18: Depth-integrated TCHLA and RT along the selected axis. The index assigned to each point represents their sequential order along an axis extending from the NW inlet to the SE outlet. Vertical green lines indicate the positions of the inlets and outlet.

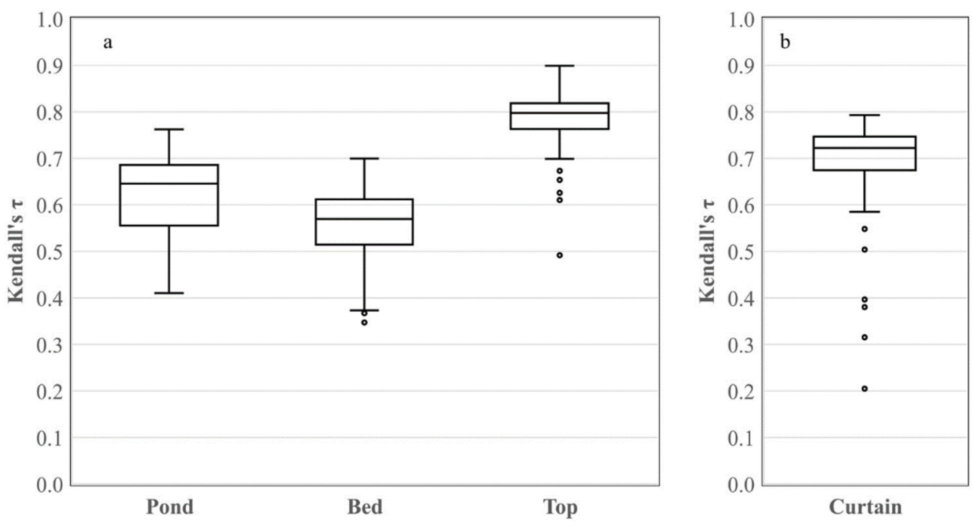

Figure 5-19: Kendall τ correlation coefficient between (a) time series of RT and TCHLA at pond, near-bed and near surface layers, and (b) time-averaged RT and TCHLA along a curtain connecting the sampling locations.

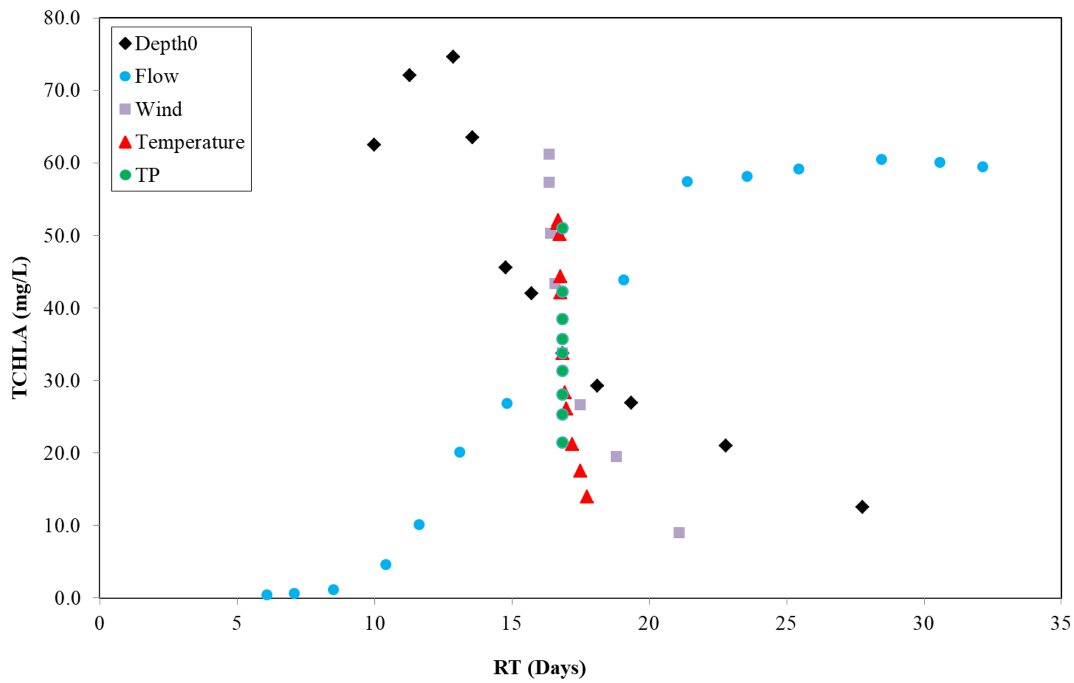

Figure 5-20: TCHLA-RT relationship for Depth0, Flow, Wind, Temperature and Total Phosphorous scenarios.

5.3.9. **Impact of the Scenarios on Pond's Trophic State**

Based on simulated TCHLA, the pond's trophic state was assessed under simulation scenarios. In Figure 5-21, time series of pond-integrated TCHLA for the base-run are plotted. The trophic state of the pond changed throughout the season, with eutrophic being the predominant state, occurring in 42% of the time, followed by hypereutrophic, occurring in 21% of the time (Table 5-5).

Moreover, from each scenario, the run that resulted in approximately a 40% decrease in average TCHLA from the base-run (34 mcg/L) was selected and presented in Figure 5-21. Thus, the average TCHLA for the selected runs is 20±2 mcg/L. As an example, in the TP scenario, the λ[TP] = 0.5 run is presented in the figure with an average TCHLA of 21.5 mcg/L. Both Figure 5-21 and Table 5-5 indicate that despite a 40% decrease in TCHLA, the prevalent trophic state of the pond remained eutrophic in all the runs, but the hypereutrophic state that was observed in the base-run did not occur. The figure also highlights the differences in the temporal variations of the tropic state between the scenarios. Additional examples of runs from different scenarios are presented in Appendix C, Figure C-13 to Figure C-18.

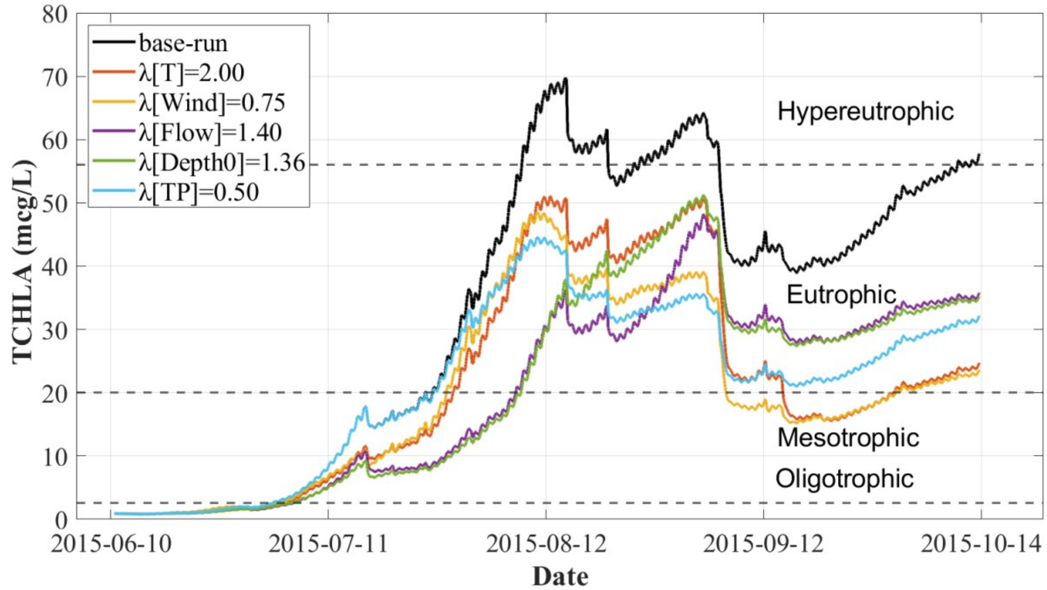

Figure 5-21: Variation of pond-averaged TCHLA in hourly time steps under selected runs of different scenarios in the study pond during the simulation period. Dashed lines represent the boundaries of trophic states.

Table 5-5: Percentage of each trophic state over the simulation period for the base-run and selected runs in each scenario.

Selected Runs	Oligotrophic	Mesotrophic	Eutrophic	Hypereutrophic
Base-run	18	18	42	21
λ[T] = 2°C	20	33	48	0
λ[Wind] = 0.75	19	39	42	0
λ[Flow] = 1.40	21	26	54	0
λ[Depth0] = 1.36	20	27	53	0
λ[TP] = 0.5	18	18	63	0

Finally, Table 5-6 outlines the required λ values in each scenario to achieve integrated TCHLA changes ranging from -50% to +50% from the base-run. These λ values were determined via interpolation (Appendix C, Figure C-18), as none of the predetermined λ values exactly resulted in, for example, a 25% change in TCHLA.

Table 5-6: TCHLA changes from the base-run and required λ values for Temperature, Wind, Flow, Depth0 and TP scenarios.

Change in TCHLA from the base-run (%)	TCHLA (mcg/L)	λ[T] °C	λ[Wind]	λ[Flow]	λ[Depth0]	λ[TP]
+50%	50.7	-1.7	1.53	0.81	0.83	1.97
+25%	42.3	-0.9	1.25	0.90	0.91	1.47
0% (base-run)	33.8	0.0	1.00	1.00	1.00	1.00
-25%	25.4	1.3	0.72	1.14	1.20	0.65
-50%	16.9	3.1	0.47	1.42	1.48	0.34

5.4. CONCLUSIONS

The ELCOM-CAEDYM model developed for the study pond was used to evaluate the impact of various scenarios on different variables whit the goal of determining those more influential on TCHLA. The model predicted that TCHLA concentrations were sensitive to geometry, temperature, wind, and inflows. Furthermore, the simulated TCHLA concentrations were sensitive to external nutrient loading, consistent with Nakhaei et al. (2021). However, within the perturbed range of external nutrient loading, this sensitivity was solely attributed to phosphorous (more specifically to its dissolved components, i.e., DOPL and PO4), not nitrogen components.

The presented results indicate a direct, albeit nonlinear, association between RT and TCHLA within individual runs of all scenarios. Despite the direct RT-TCHLA association, RT alone cannot reliably predict trends or approximately magnitudes of TCHLA given that algae biomass growth is controlled by both the net growth rate (*g*) and the physical transport rate (*hd*). Therefore, the impacts of management strategies focused on manipulation of nutrients (e.g., Huo et al. 2019; Linden et al. 2015) are more predictable as they only affect *g* and not *hd*. However, management strategies based on manipulating flow and depth, aiming to reduce *hd* by decreasing RT, can simultaneously influence *g*, thus not guaranteeing the anticipated impact on TCHLA.

A strong correlation was observed between air and water temperature in the study pond. However, warmer air temperatures, e.g., due to future climatic scenarios, could either increase or decrease TCHLA. In this study and for the simulation period, warmer scenarios resulted in lower TCHLA, as an increase in temperature negatively impacted the temperature limiting factor for the modelled algae group during the warmer periods and consequently inhibited algae growth. Increased wind speed reduced water temperatures and, consequently, increased TCHLA, while decreased wind speed had the opposite effect. It was observed that *hd* is impacted by both temperature and wind; however, no clear relationship between *hd* and RT was identified. The influence of temperature and wind on *hd* is possibly driven by other factors, such as circulation patterns and stratification, which needs further investigation in the future. Therefore, water quality modeling is recommended to more accurately evaluate the effectiveness of the proposed management strategies in the urban stormwater ponds.

Chapter 6. SUMMARY AND CONCLUSIONS

The role of urban stormwater ponds, originally designed to manage excess run off, has expanded over time to improve water quality before release downstream. However, these ponds may not always perform as expected, facing challenges such as excessive algae growth, unpleasant scenery, odors, and concerns about ice safety. This thesis is part of a comprehensive research project initiated in response to resident complaints regarding these issues in some residential areas of Edmonton, Canada. Since algae serves as a key indicator of water quality, investigating the factors impacting the algae dynamics in stormwater ponds became the motivation for the current study.

This study evaluated the performance of the ELCOM-CAEDYM model in representing the hydrodynamics and water quality of urban stormwater ponds. It also investigated the factors influencing algae dynamics. Furthermore, the calibrated model was used as a predictive tool to assess the impact of various climate and management scenarios on algae growth.

In this thesis, subsets of data acquired from a 2-year field monitoring program in three urban stormwater ponds in Edmonton, Canada, collected between October 2013 to October 2015, were used. The South Terwillegar2 (ST2) stormwater pond was selected as the main focus for investigating water quality. However, available information from two other ponds, Terwillegar Towne 2 (TT2) and Silverberry4 (SB4), was also utilized to provide the required data and enhance the study of ST2.

Visual inspection of field data measured at ST2 revealed spatial and temporal variations in water quality variables, including water temperature (T), dissolved oxygen (DO), nutrients, and total chlorophyll-a (TCHLA), which indicated the need for a three-dimensional (3D) model to represent hydrodynamics and water quality of the study pond. The ELCOM-CAEDYM model, which has been successfully applied in a wide range of water quality studies, was selected for the purpose of this study. The bathymetry and hypsometric relationships of the ponds were obtained through surveying the study area, and used to define the computational domain of the ELCOM-CAEDYM model. Collected data was further processed to define initial conditions, boundary conditions, as well as required datasets for calibration and validation of both hydrodynamics and water quality models.

Field surveying revealed several previously unknown challenges and inaccuracies, including differences between designed and as-built dimensions of the outlet structures. Therefore, the outlet structures of the three ponds were surveyed, and the stage-discharge curves were updated accordingly.

Direct measurement of inflow and outflow rates, that are very important boundary conditions for ELCOM-CAEDYM, was not feasible due to challenges associated with accessing the inlet and outlet pipes, concerns regarding the maintenance of flowmeters, and cost constraints. Therefore, time series of inflows into and outflows out of the ST2 pond were estimated. Outflows were determined based on the observed water levels and the updated stage-discharge relationship. Inflows were estimated using reverse level pool routing method. However, this back-routing approach significantly amplifies the noise in the measured water level time series, resulting in oscillatory inflows. These oscillations could potentially have had a significant impact in this study, since time series of estimated inflow may be corrupted with non-physical negative values, particularly during dry periods.

Through analytical and simulation analyses, the amplification factor, defined as the ratio of water level noise to inflow noise, was quantified. This factor is directly proportional to the area of the pond and inversely proportional to the numerical time step. To mitigate the issue of spurious oscillations and hence negative inflows, water levels were pre-processed with a Butterworth low-pass filter. While filtering with smaller cut-off frequency (fc) reduces the magnitude of the noise, it also more aggressively distorts the shape of the inflow hydrograph.

The optimal fc was determined based on limited inflow measurements available at the TT2 and SB4 ponds. Comparison between observed and back-routed inflows indicated that, for the sampling frequency (fs) of 6 hr^{-1} used for water level measurements in this study, pre-processing water levels with fc= 1/6 hr^{-1} minimized the RMSE of the calculated inflows while reasonably preserving the shape of the hydrographs. Given the similarity of all three ponds and the fact that the same measurement instruments were used for them, fc= 1/6 hr^{-1} was also used to filter the water level of ST2 prior to back-routing.

The ELCOM model was set up based on the defined computational domain and the required initial and boundary conditions. The model parameters were initially set at the values recommended by Nakhaei et.al (2018). ELCOM was further calibrated through adjustments of albedo and Secchi depth, while accounting for atmospheric instability for a calibration period between May 16th and October 3rd, 2014, reducing RMSE from 1.53 to 1.37 (°C). Albedo was identified as the most influential model parameter for water temperatures, and the calibrated value was determined to be 0.2. Subsequently, ELCOM was validated for the period between May 1st and October 14th, 2015.

ELCOM effectively represented the thermal structure of the pond, closely matching the observed patterns of mixed and stratified periods. The model accurately replicated the temporal and spatial variations of water temperature, capturing diurnal temperature variations and responses to the environmental forcing such as changes in air temperature and inflows. For example, ELCOM accurately simulated deepening of the thermocline during extended warm and dry periods. The spatial variability of the thermocline depth and thermal stratification was also accurately simulated. Shallower thermocline depths and more frequent stratification observed near inlets were also captured by the model. The depth of the thermocline generally increased from the inlet toward the outlet, and the pond became more mixed. Additionally, the model effectively captured the thermally mixed condition of the pond observed after high inflows (e.g., the rain event of late July 2014) and in response to cooler air temperatures (e.g., in September

2014). Overall, the pond had a warming effect of approximately 4°C as water passed through it. Error statistics for both the calibration and validation periods remained within or below the range of values reported in similar studies. In general both simulated and observed stratification occurrence decreased along the pond's major axis, with an increase at the SARM inlet. However, on average ELCOM underestimated the stratification occurrence by 15%.

The water quality model, CAEDYM, was configured to simulate the dynamics of phosphorus, nitrogen, dissolved oxygen (DO), and dominant algae groups, including chlorophytes, cyanobacteria, and cryptophytes in the ST2 stormwater pond. The required boundary conditions (e.g., nutrient components and DO) were defined based on direct field measurements or estimated based on other measurements. The static model was selected to simulate the diagenetic processes of water and sediment.

CAEDYM was configured initially with the same model parameters reported for stormwater ponds (Nakhaei et al. 2021), however results were not satisfactory in terms of simulated TCHLA. The model was further calibrated by tuning model parameters and the results effectively captured the temporal and spatial variations of TCHLA during calibration period. The RMSE of the calibrated model improved from 82.8 (mcg/L) in the initial run to 25.6 (mcg/L), however, the RMSE of DO, TN, and TP did not change significantly (between 1% and 8%). Dynamics of dissolved oxygen (DO) was also effectively simulated by CAEDYM, with some shortcomings in simulating diurnal variations. Total phosphorous (TP) was modelled with acceptable accuracy; however, CAEDYM was not successful in simulating total nitrogen (TN). The underperformance of the model in simulating nutrients is attributed to the assumptions made in assigning nutrient components in the boundary conditions. Nonetheless, visual assessments of the results and the RMSE values of DO, TN, and TP obtained in this study were comparable or in some cases better than those reported in similar studies (e.g., Nakhaei 2021).

The sensitivity of model variables to model parameters was quantified by defining a sensitivity index. The sensitivity analysis showed that TCHLA, with an average sensitivity index (SI) of 93%, was the most sensitive state variable to the model parameters, followed by DO with an SI of 16%. The high sensitivity of TCHLA can be explained by the fact that algae dynamics depend, directly or indirectly, on a wide range of parameters and variables. The SI for TN and TP was less than 10%. The lack of responsiveness of nutrients to changes in model parameters and the underperformance of the model in simulating nutrients suggest that in stormwater ponds, TP and TN are more influenced by the boundary conditions.

Additionally, the model parameters that had the most influence on TCHLA, DO, and TN were identified as maximum potential growth rate of phytoplankton (μ_{max}), respiration, mortality, and excretion coefficient (K_r), minimum internal phosphorous concentration (IP_{min}), and light half saturation constant for algae limitation (IK), in the order stated. Three of these parameters were also the influential parameters for TP which indicates the interdependencies of simulated variables. The discrepancy in the sensitivity of state variables and the influence of model parameters between the current research and findings reported for Lake Minnetonka (Missaghi et al. 2014) suggests that the sensitivity varies based on the specific application. Hence, for modeling water quality in bodies of water similar to the study stormwater pond, employing the parameters reported here rather than those obtained for much larger and deeper water bodies is expected to provide more accurate simulations.

This study also distinguishes itself by quantifying the impact of several climatological, hydrological, and nutrient scenarios on pond water quality. Simulations were conducted for scenarios in which the bathymetry, air temperature, wind speed, flow rate, external loadings of phosphorous and nitrogen components were altered and their respective impacts on model outputs, with an emphasis on TCHLA were investigated. These simulations showed that water temperature (T), stratification, residence time (RT), DO, and TCHLA were sensitive to the changes introduced by the defined scenarios. TCHLA was sensitive to both hydrodynamics, quantified by the physical transport rate (*hd*), and biogeochemical factors, quantified by the net growth rate (*g*). In addition, in nutrient scenarios, *g* and consequently TCHLA was found to be sensitive only to dissolved components of phosphorus, and not to nitrogen.

It was found that the impacts of strategies that only influence the net growth rate of algae (*g*) are rather intuitive. For example, decreasing nutrient load resulted in a decrease of algae in the pond. However, the outcomes of strategies that alter the physical transport rate (*hd*) are not as straightforward, since such strategies can simultaneously alter nutrient availability, light penetration, and water temperatures, thereby affecting the net growth rate (*g*) as well. For example, increasing flow can simultaneously increase the influx of nutrients while enhancing the flushing of algae and nutrients. Therefore, the interaction between *g* and *hd* in these scenarios is more complex, which underscores the importance of water quality modeling.

Results of the Temperature scenario showed, as expected, a strong correlation (R^2=0.99) between average air and water temperatures in the study pond. Scenarios with an average air temperature 2°C warmer than the base-run led to a decrease in TCHLA during the simulation period, as higher temperatures during warm days of summer reduced the temperature limiting factor and consequently inhibited algae growth. A decrease in wind speed resulted in a decrease in TCHLA, which may be attributed to the impact of wind on water temperature. This relationship is supported by the increase in simulated water temperature with decreasing wind speed (R^2=0.99). However, the influence of Temperature and Wind scenarios on *hd* was not as straightforward as the Depth and Flow scenarios where *hd* was found to be correlated with RT. In these scenarios, *hd* is likely driven by factors such as circulation patterns and stratification too, which need further investigation in future studies.

In this study, TCHLA was considered as the sum of different algae biomasses, aggregated for comparison with the observed TCHLA. Future studies could enhance the understanding of algae dynamics by modeling individual species separately. This requires calibrating the water quality model for individual algae groups alongside TCHLA. This approach may offer a better understanding of how different algae species respond to environmental changes and management strategies, thus refining predictive capabilities and enabling more targeted interventions for maintaining water quality in stormwater ponds. In addition, incorporating the effects of rooted aquatic plants (macrophytes) into the water quality model would enhance understanding of algae dynamics in stormwater ponds. Given the relatively small area of stormwater ponds, the littoral zone plays a more significant role in their ecological functioning, and macrophytes may compete with algae for nutrients and light. Consequently, modeling the interactions between macrophytes and algae may contribute to the development of effective management strategies for maintaining water quality in stormwater ponds.

Dissolved oxygen levels were mainly influenced by wind speed and total chlorophyll-a concentration (TCHLA). Wind speed affects oxygen transfer at the air-water interface, while TCHLA, representing phytoplankton biomass, influences oxygen through photosynthesis and respiration.

The results of the sensitivity analysis of the ELCOM-CAEDYM model can provide general guidelines for similar studies, reducing the number of calibration attempts. Sensitivity of the model to boundary conditions not only highlighted the importance of accurate field measurements, but also can be used to improve the design and management of urban stormwater ponds to meet water quality requirements for the current and future conditions.

Since ELCOM, with its default model parameters, can adequately simulate the thermal behavior of waterbodies, preliminary runs can be used during the design stage to predict the overall flow patterns and thermal structures of future stormwater ponds. Such preliminary simulations can be used to compare different pond layouts, as well as the locations of inlets and outlets. However, the major constraint lies in the available resources, particularly in terms of budget and modeling expertise.

In general, this study demonstrated that ELCOM-CAEDYM is able to simulate the water quality of small water bodies such as stormwater ponds with sufficient accuracy. For management scenarios aimed at retrofitting a pond design, changes may not always lead to the intended results. Therefore, depending on the scope and extent of a project, as well as available resources, modeling can be used along with or as an alternative to general design guidelines, to improve the design of these types of facilities.

Preliminary runs can also provide general guidelines for monitoring existing ponds. For example, simulated flow patterns and spatial and temporal variations in the degree of water column stratification can help identify sampling locations that are more representative of pond behavior for the calibration process. Additionally, these simulations can define sampling locations where measurements are representative of inflow boundary conditions. Due to the spatial and temporal variability of TCHLA and its sensitivity to model parameters, compared to nutrients, more frequent water sampling, at least for TCHLA, would improve model calibration and validation, and potentially increase the accuracy of the simulated results.

The results of this study indicated that increasing the depth of the pond by 0.5 m (i.e., λ[Depth0] = 1.36) could effectively prevent the occurrence of a hypereutrophic state during the peak of summer. This depth adjustment has a comparable impact to reducing the total phosphorous external load by 50%. Therefore, the construction of deeper stormwater ponds can be considered as a strategy for mitigation of algae blooms.

BIBLIOGRAPHY

Abtahi, S., Li, Y., and Asce, A. M. (2023). "Investigation of Corroded Bond-Slip Effects for Corroded RC Columns." *Journal of Structural Engineering*, 149(2), 1–16.

AEP. (1999). *STORMWATER MANAGEMENT GUIDELINES for the Province of Alberta*.

Ahmed, S. S., Loewen, M. R., Zhang, W., Ghobrial, T. R., Zhu, D. Z., Mahmood, K., and Duin, B. Van. (2022). "Field observations of stratification in stormwater wet ponds." *Journal of Environmental Management*, Elsevier Ltd, 322(September), 115988.

Ahmed, S. S., Zhang, W., Loewen, M. R., Zhu, D. Z., Ghobrial, T. R., Mahmood, K., and Duin, B. Van. (2023). "Stratification and its consequences in two constructed urban stormwater wetlands." *Science of the Total Environment*, Elsevier B.V., 872(January), 162179.

Alberta Government. (2013). "Evaporation and Evapotranspiration in Alberta." (April), 1–283.

Aldama, A., and Aguilar, E. (2007). "Flow Rate Estimation via Inverse Flood Routing and Spectral Error Control." *AGU Spring Meeting Abstracts*, H41A-03A.

Badfar, M., Barati, R., Ph, D., Dogan, E., and Tayfur, G. (2021). "Reverse Flood Routing in Rivers Using Linear and Nonlinear Muskingum Models." 26(6), 1–12.

Beeton, A. M. (1958). "Relationship between Secchi Disc Readings and Light Penetration in Lake Huron." *Transactions of the American Fisheries Society*, 87(1), 73–79.

Bentzen, T. R., Larsen, T., and Rasmussen, M. R. (2008). "Wind effects on retention time in highway ponds." *Water science and technology : a journal of the International Association on Water Pollution Research*, 57(11), 1713–20.

Boegman, L., Loewen, M. R., Culver, D. A., Hamblin, P. F., and Charlton, M. N. (2008). "Spatial-Dynamic Modeling of Algal Biomass in Lake Erie : Relative Impacts of Dreissenid Mussels and Nutrient Loads." 134(6), 456–468.

Bolkhari, H. (2014). "Modelling the Impacts of Climate Change on the Hydrodynamics and Biogeochemistry of Lake Simcoe, Hamilton Harbour and the Bay of Quinte." Queen's University.

Bruce, L. C., Hamilton, D., Imberger, J., Gal, G., Gophen, M., Zohary, T., and Hambright, K. D. (2006). "A numerical simulation of the role of zooplankton in C, N and P cycling in Lake Kinneret, Israel." *Ecological Modelling*, 193(3–4), 412–436.

Bruce, L. C., and Imberger, J. (2009). "The role of zooplankton in the ecological succession of plankton and benthic algae across a salinity gradient in the Shark Bay solar salt ponds." *Hydrobiologia*, 626(1), 111–128.

Bruen, M., and Dooge, J. C. I. (2007). "Harmonic analysis of the stability of reverse routing in channels." *Hydrology and Earth System Sciences*, 11(1), 559–568.

Butterworth, S. (1930). "On the theory of filter amplifiers." *Experimental Wireless and the Wireless Engineer*, 7, 536–541.

Carlson, R. E. (1977). "A trophic state index for lakes." *Limnology and Oceanography*, 22(2), 361–369.

Carraro, E., Guyennon, N., Hamilton, D., Valsecchi, L., Manfredi, E. C., Viviano, G., Salerno, F., Tartari, G., and Copetti, D. (2012). "Coupling high-resolution measurements to a three-dimensional lake model to assess the spatial and temporal dynamics of the cyanobacterium Planktothrix rubescens in a medium-sized lake." *Hydrobiologia*, 698(1), 77–95.

Chan, T. U., Hamilton, D. P., Robson, B. J., Hodges, B. R., and Dallimore, C. (2002). "Impacts of Hydrological Changes on Phytoplankton Succession in the Swan River , Western Australia." *Estuaries*, 25(6), 1406–1415.

Chen, L., Aoust, P. M. D., Rennie, C. D., Poulain, A., Pick, F., Wang, R., and Delatolla, R.

(2019). “Numerical investigation on the impact of wind-induced hydraulics on dissolved oxygen characteristics in a shallow stormwater pond.” 309–325.

Chow, V. T., Maidment, D. R., and Mays, L. W. (1988). *Applied Hydrology*. McGraw-Hill, New York.

Chow, V. Te. (1959). *Open-Channel Hydraulics*. McGraw-Hill, New York.

Chowdhary, H. (2009). “Copula-Based Multivariate Hydrologic Frequency Analysis.” Louisiana State University and Agricultural and Mechanical College.

Conn, R. M., and Fiedler, F. R. (2006). “Increasing Hydraulic Residence Time in Constructed Stormwater Treatment Wetlands with Designed Bottom Topography.” *Water Environment Research*, 78(13), 2514–2523.

Cui, Y., Zhu, G., Li, H., Luo, L., Cheng, X., Jin, Y., and Trolle, D. (2016). “Modeling the response of phytoplankton to reduced external nutrient load in a subtropical Chinese reservoir using DYRESM-CAEDYM.” *Lake and Reservoir Management*, Taylor & Francis, 32(2), 146–157.

Cuthbertson, A., Lynn, E., Anderson, M., and Redmond, K. (2014). *Estimating Historical California Precipitation Phase Trends Using Gridded Precipitation , Precipitation Phase , and Elevation Data*.

D’Oria, M., Mignosa, P., and Tanda, M. G. (2012). “Reverse level pool routing: Comparison between a deterministic and a stochastic approach.” *Journal of Hydrology*, Elsevier B.V., 470–471, 28–35.

D’Oria, M., and Tanda, M. G. (2012). “Reverse flow routing in open channels: A Bayesian Geostatistical Approach.” *Journal of Hydrology*, Elsevier B.V., 460, 130–135.

Deng, C., Liu, P., Guo, S., Wang, H., and Wang, D. (2015). “Estimation of nonfluctuating reservoir inflow from water level observations using methods based on flow continuity." *Journal of Hydrology*, Elsevier B.V., 529, 1198–1210.

Dipper, F. (2022). "The seawater environment and ecological adaptations." *Elements of Marine Ecology*, Elsevier, 37–151.

Dooge, J., and Bruen, M. (2005). "Problems in reverse routing." *Acta Geophysica Polonica*, 53(4), 357–371.

Elliott, J. A. (2011). "Is the future blue-green? A review of the current model predictions of how climate change could affect pelagic freshwater cyanobacteria." *Water Research*, Elsevier Ltd, 46(5), 1364–1371.

Elliott, J. A., Jones, I. D., and Thackeray, S. J. (2006). "Testing the sensitivity of phytoplankton communities to changes in water temperature and nutrient load, in a temperate lake." *Hydrobiologia*, 559, 401–411.

Fenton, J. D. (1992). "Reservoir routing." *Hydrological Sciences*, 37(3), 233–246.

Fisher, M. M., Reddy, K. R., and James, R. T. (2005). "Internal Nutrient Loads from Sediments in a Shallow, Subtropical Lake." *Lake and Reservoir Management*, 21(3), 338–349.

Gal, G., Hipsey, M. R., Parparov, A., Wagner, U., Makler, V., and Zohary, T. (2009). "Implementation of ecological modeling as an effective management and investigation tool: Lake Kinneret as a case study." *Ecological Modelling*, 220(13–14), 1697–1718.

Gal, G., Parparov, A., Wagner, U., and Rozenberg, T. (2004). "Testing the impact of management scenarios on water quality using an ecosystem model." *In Complexity and Integrated Resources Management.Transactions of the Second Biennial Meeting of the International Environmental Modelling and Software Society. Citeseer*.

German, J., Svensson, G., Gustafsson, L. G., and Vikström, M. (2003). "Modelling of temperature effects on removal efficiency and dissolved oxygen concentrations in stormwater ponds.” *Water science and technology : a journal of the International Association on Water Pollution Research*, 48(9), 145–54.

Gilboa, Y., Friedler, E., Talhami, F., and Gal, G. (2022). “A novel approach for accurate quantification of lake residence time — Lake Kinneret as a case study.” *Water Research X*, Elsevier Ltd, 16(July), 100149.

Hamilton, D. P., and Schladow, S. G. (1997). “Prediction of water quality in lakes and reservoirs. Part I - Model description.” *Ecological Modelling*, 96(1–3), 91–110.

Hamrick, J. M. (1992). *A Three-Dimensional Environmental Fluid Dynamics Computer Code: Theoretical and Computational Aspect*.

Hannoun, I., John, E., Kavanagh, K. B., Chiang, W. L., Ding, L., Preston, A., Rackley, I., and Karafa, D. (2006). “Use of ELCOM and CAEDYM for Water Quality Simulation in Boulder Basin.” *Proceedings of the Water Environment Federation 2006*, 3943–3970.

He, J., Valeo, C., and Chu, A. (2015). “Variation in Water Quality of a Stormwater Pond from Diurnal Thermal Stratification.” *Journal of Water Resource and Hydraulic Engineering*, 4(1–2), 189–198.

Henley, B. J., Thyer, M. A., Kuczera, G., and Franks, S. W. (2011). “Climate-informed stochastic hydrological modeling: Incorporating decadal-scale variability using paleo data.” *Water Resources Research*, 47(11), 1–14.

Hipsey, M. R. (2013). *Computational Aquatic Ecosystem Dynamics Model : CAEDYM v3.3 User Guide*. Centre for Water Research University of Western Australia.

Hipsey, M. R., Antenucci, J. P., and Hamilton, D. (2013). *Computational Aquatic Ecosystem Dynamics Model: CAEDYM v3.2 Science Manual*.

Hipsey, M. R., Gal, G., Antenucci, J. P., Zohary, T., Makler, V., and Imberger, J. (2006). "Lake Kinneret Water Quality Management System." *Seventh International Conference on Hydroscience and Engineering, Philadelphia, PA, September*.

Hodges, B. (2000). "Numerical Techniques in CWR-ELCOM (code release v.1)." *Centre for Water Research, Univ. Western Australia*.

Hodges, B., and Dallimore, C. (2013a). "Estuary , Lake and Coastal Ocean Model : ELCOM v2 . 2 Science Manual."

Hodges, B., and Dallimore, C. (2013b). "Estuary , Lake and Coastal Ocean Model : ELCOM v2 . 2 User Manual."

Hodges, B., and Dallimore, C. (2016). *HydroNumerics-Aquatic Ecosystem Model: AEM3D- v1.0 User Manual*.

Hodges, B. R., Imberger, J., Saggio, A., and Winters, K. B. (2000). "Modeling basin-scale internal waves in a stratified lake." *Limnology and Oceanography*, 45(7), 1603–1620.

Huang, A., Rao, Y. R., Lu, Y., and Zhao, J. (2010). "Hydrodynamic modeling of Lake Ontario : An intercomparison of three models." 115(March), 1–16.

Huo, S., He, Z., Ma, C., Zhang, H., Xi, B., Xia, X., and Xu, Y. (2019). "Stricter nutrient criteria are required to mitigate the impact of climate change on harmful cyanobacterial blooms." *Journal of Hydrology*, Elsevier, 569(8), 698–704.

Ji, Z.-G., Hu, G., Shen, J., and Wan, Y. (2007). "Three-dimensional modeling of hydrodynamic processes in the St. Lucie Estuary." *Estuarine, Coastal and Shelf Science*, 73(1–2), 188–200.

Ji, Z.-G., and Jin, K.-R. (2016). "An integrated environmental model for a surface flow constructed wetland: Water quality processes." *Ecological Engineering*, 86, 247–261.

Ji, Z. G. (2017). *Hydrodynamics and water quality : modeling rivers, lakes, and estuaries*. JohnWiley & Sons Inc, New York.

Jin, K.-R., Ji, Z.-G., and James, R. T. (2007). "Three-dimensional Water Quality and SAV Modeling of a Large Shallow Lake." *Journal of Great Lakes Research*, International Association for Great Lakes Research, 33(1), 28–45.

Katopodis, C. (1987). *Introduction to Fishway Design*. Freshwater Institute, Department of Fisheries and Oceans, Winnipeg, Manitoba, Canada.

Koussis, A. D., and Mazi, K. (2015). "Reverse flood and pollution routing with the lag-and-route model." *Hydrological Sciences Journal*, 61(10), 1952–1966.

Koussis, A. D., Mazi, K., Lykoudis, S., and Argiriou, A. A. (2012). "Reverse flood routing with the inverted Muskingum storage routing scheme." *Natural Hazards and Earth System Sciences*, 12, 217–227.

Kristensen, P., Sondergaard, M., and Jeppesen, E. (1992). "Resuspension in a Shallow Eutrophic Lake." *Hydrobiologia*, 228(1), 101–109.

Le'on, G., Beamud, S. G., Temporetti, P., Adri'an Gonzalo Atencio, Diaz, M. M. D., and Pedrozo, F. L. P. (2016). "Stratification and residence time as factors controlling the seasonal variation and the vertical distribution of chlorophyll- a in a subtropical irrigation reservoir." *International Review of Hydrobiology*, (101), 36–47.

Lee, H., Chung, S., Ryu, I., and Choi, J. (2013). "Three-dimensional modeling of thermal stratification of a deep and dendritic reservoir using ELCOM model." *Journal of Hydro-Environment Research*, Elsevier B.V, 7(2), 124–133.

León, L. F., Imberger, J., Smith, R. E. H., Hecky, R. E., Lam, D. C. L., and Schertzer, W. M. (2005). "Modeling as a Tool for Nutrient Management in Lake Erie : a Hydrodynamics

Study." *Journal of Great Lakes Research*, Elsevier, 31(1995), 309–318.

Leon, L. F., Smith, R. E. H., Hipsey, M. R., Bocaniov, S. a., Higgins, S. N., Hecky, R. E., Antenucci, J. P., Imberger, J. a., and Guildford, S. J. (2011). "Application of a 3D hydrodynamic–biological model for seasonal and spatial dynamics of water quality and phytoplankton in Lake Erie." *Journal of Great Lakes Research*, International Association for Great Lakes Research, 37(1), 41–53.

Leonhardt, G., D'Oria, M., Kleidorfer, M., and Rauch, W. (2014). "Estimating inflow to a combined sewer overflow structure with storage tank in real time: Evaluation of different approaches." *Water Science and Technology*, 70(7), 1143–1151.

Lewis, D. M., Brookes, J. D., and Lambert, M. F. (2004). "Numerical models for management of Anabaena circinalis." *Journal of Applied Phycology*, 16(6), 457–468.

Linden, L. Van Der, Daly, R. I., and Burch, M. D. (2015). "Suitability of a Coupled Hydrodynamic Water Quality Model to Predict Changes in Water Quality from Altered Meteorological Boundary Conditions." *Water*, 7(1), 348–361.

Lofton, M. E., Howard, D. W., Mcclure, R. P., Wander, H. L., Woelmer, W. M., Hounshell, A. G., Lewis, A. S. L., and Carey, C. C. (2022). "Experimental thermocline deepening alters vertical distribution and community structure of phytoplankton in a 4- - year whole- - reservoir manipulation." (April), 1903–1924.

Machado, D. a, and Imberger, J. (2012). "Managing wastewater effluent to enhance aquatic receiving ecosystem productivity: a coastal lagoon in Western Australia." *Journal of environmental management*, Elsevier Ltd, 99, 52–60.

Marsalek, J. (2003). "Road salts in urban stormwater: an emerging issue in stormwater management in cold climates." *Water science and technology : a journal of the*

International Association on Water Pollution Research, 48(9), 61–70.

Marsalek, J., Rochfort, Q., Grapentine, L., and Brownlee, B. (2002). "Assessment of stormwater impacts on an urban stream with a detention pond." *Water Science and Technology*, 45(3), 255–263.

Marsalek, J., Watt, W. E., and Henry, D. (1992). "Retrofitting stormwater ponds for water quality control." *Water Poll. Res. J. Canada*, 27(2), 403–422.

Marsalek, P. M., Watt, W. E., Marsalek, J., and Anderson, B. C. (2000). "Winter flow dynamics of an on-stream stormwater management pond." *Water Quality Research Journal of Canada*, 35(3), 505–523.

MathWorks. (2023). "MATLAB and Statistics Toolbox Release." Natick, Massachusetts, United States.

Mcdonald, D., and Muricken, D. (2009). *North Saskatchewan River Water Quality Model: Alberta Environment Technical Report*.

Missaghi, S., and Hondzo, M. (2010). "Evaluation and application of a three-dimensional water quality model in a shallow lake with complex morphometry | Miki Hondzo - Academia.edu." *Ecological Modelling*, 221, 1512–1525.

Missaghi, S., and Hondzo, M. (2011). "3D water quality modeling of a morphologically complex lake , sensitivity and uncertainty analyses , and examples of model applications." (December), 12–16.

Missaghi, S., Hondzo, M., and Melching, C. (2014). "Three-Dimensional Lake Water Quality Modeling: Sensitivity and Uncertainty Analyses." *Journal of Environment Quality*, 42(6), 1684.

Mooij, W. M., Janse, J. H., De Senerpont Domis, L. N., Hu¨lsmann, S., and Ibelings, B. W.

(2007a). “Predicting the effect of climate change on temperate shallow lakes with the ecosystem model PCLake Predicting the effect of climate change on temperate shallow lakes with the ecosystem model PCLake.” *Hydrobiologia (2007)*, (June), 584:443–454.

Mooij, W. M., Janse, J. H., De Senerpont Domis, L. N., Hülsmann, S., and Ibelings, B. W. (2007b). “Predicting the effect of climate change on temperate shallow lakes with the ecosystem model PCLake.” 2100, 443–454.

Mooij, W. M., Trolle, D., Jeppesen, E., Arhonditsis, G., Belolipetsky, P. V., Chitamwebwa, D. B. R., Degermendzhy, A. G., DeAngelis, D. L., Senerpont Domis, L. N., Downing, A. S., Elliott, J. A., Fragoso, C. R., Gaedke, U., Genova, S. N., Gulati, R. D., Håkanson, L., Hamilton, D. P., Hipsey, M. R., ‘t Hoen, J., Hülsmann, S., Los, F. H., Makler-Pick, V., Petzoldt, T., Prokopkin, I. G., Rinke, K., Schep, S. a., Tominaga, K., Dam, A. a., Nes, E. H., Wells, S. a., and Janse, J. H. (2010). “Challenges and opportunities for integrating lake ecosystem modelling approaches.” *Aquatic Ecology*, 44(3), 633–667.

Mortimer, C. H. (1941). “The Exchange of Dissolved Substances Between Mud and Water in Lakes.” *Journal of Ecology*, 29(2), 280–329.

Moss, B., Mckee, D., Atkinson, D., Collings, S. E., Eaton, J. W., Gill, A. B., Harvey, I., Hatton, K., Heyes, T., and Wilson, D. (2003). “How important is climate? Effects of warming, nutrient addition and fish on phytoplankton in shallow lake.” *Journal of Applied Ecology*, 40, 782–792.

Nakhaei, N. (2017). “Computational and Empirical Water Quality Modeling.” Queen’s University.

Nakhaei, N., Boegman, L., Mehdizadeh, M., and Loewen, M. (2018). “Hydrodynamic modeling of Edmonton storm-water ponds.” *Environmental Fluid Mechanics*, Springer Netherlands, 19(2), 305–327.

Nakhaei, N., Boegman, L., Mehdizadeh, M., and Loewen, M. (2021). "Three-dimensional biogeochemical modeling of eutrophication in Edmonton stormwater ponds." *Ecological Modelling*, Elsevier B.V., 456(July).

Oberts, G. L. (2003). "Cold climate BMPs: solving the management puzzle." *Water Science and Technology*, 48(9), 21–32.

Oberts, Marsalek, J., and Viklander, M. (2000). "Review of Water Quality Impacts of Winter Operation of Urban Drainage." *Water Quality Research Journal of Canada*, 35(4), 781–808.

Olding, D. D. (2000). "Algal Communities as a Biological Indicator of Stormwater Management Pond Performance and Function." *Water Quality Research Journal of Canada*, 35(3), 489–503.

Olding, D. D., Hellebust, J. A., Douglas, M. S. V, and Hill, R. (2000). "Phytoplankton community composition in relation to water quality and water-body morphometry in urban lakes, reservoirs, and ponds." *Canadian Journal of Fisheries and Aquatic Sciences*, 57(10), 2163–2174.

Olsson, F., Mackay, E. B., Moore, T., Barker, P., Davies, S., Hall, R., Spears, B., Wilkinson, J., and Jones, I. D. (2022). "Annual water residence time effects on thermal structure: A potential lake restoration measure?" *Journal of Environmental Management*, Elsevier Ltd, 314(April), 115082.

Orihel, D. M., Baulch, H. M., Casson, N. J., North, R. L., Parsons, C. T., Seckar, D. C. M., and Venkiteswaran, J. J. (2017). "Internal phosphorus loading in Canadian fresh waters : a critical review and data analysis." *Canadian Journal of Fisheries and Aquatic Sciences*

Aquatic Sciences, 2029(September), 2005–2029.

Owens, E. M., Effler, S. W., and Matthews, D. A. (2014). "Modeling the Fate and Transport of Plunging Inlfows to Onondaga Lake." *Journal of the American Water Resources Association*, 50(1), 205–218.

Özkundakci, D., Hamilton, D., and Trolle, D. (2011). "Modelling the response of a highly eutrophic lake to reductions in external and internal nutrient loading." *New Zealand Journal of Marine and Freshwater Research*, 45(2), 165–185.

Özkundakci, D., McBride, C. G., and Hamilton, D. . (2012). "Parameterisation of sediment geochemistry for simulating water quality responses to long-term catchment and climate changes in polymictic, eutrophic Lake Rotorua, New Zealand." *Water Pollution XI. WIT Transactions on Ecology and the Environment*, 164, 171–182.

Pagendam, D. E., and Percival, D. B. (2015). "Estimating freshwater flows from tidally affected hydrographic data." *Journal of the American Water Resources Association*, 51, 1619–1634.

Paturi, S., Boegman, L., and Rao, Y. R. (2012). "Hydrodynamics of eastern Lake Ontario and the upper St. Lawrence River." *Journal of Great Lakes Research*, 38, 194–204.

Perumal, M., Moramarco, T., Sahoo, B., and Barbetta, S. (2010). "On the practical applicability of the VPMS routing method for rating curve development at ungauged river sites." *Water Resources Research*, 46(3), 1–22.

Ponce, V. M. (1989). *Engineering hydrology : principles and practices*. Prentice Hall, Englewood Cliffs, NJ.

Potter, M., Wiggert, D., and Bassem, R. (2011). *Mechanics of Fluids*. Cengage Learning.

Qin, Q. Q., and Shen, J. (2017). "The contribution of local and transport processes to phytoplankton biomass variability over different timescales in the Upper James River , Virginia." 196, 123–133.

Reed, R. K. (1977). "On Estimating Insolation over the Ocean." *Journal of Physical Oceanography*, 7(3), 482–485.

Reilly, C. M. O., Alin, S. R., and Plisnier, P. (2003). "Climate change decreases aquatic ecosystem productivity of Lake Tanganyika , Africa." *Nature*, 424(August), 5–7.

Riley, J. P., and Skirrow, G. (1975). *Chemical Oceanography*. Chemical Oceanography, Academic Press.

Romero, J. R., Antenucci, J. P., and Imberger, J. (2004). "One- and three-dimensional biogeochemical simulations of two differing reservoirs." *Ecological Modelling*, 174(1–2), 143–160.

Roseen, R. M., Ballestero, T. P., Houle, J. J., Avelleneda, P., Wildey, R., and Briggs, J. (2006). "An Examination of Cold Climate Performance of Low Impact Development Stormwater BMPs in a Northern Climate." *Current Practices in Cold Regions Engineering*, American Society of Civil Engineers, Reston, VA, 1–13.

Rosten, H. I., and Spalding, D. B. (1987). *The Phoenics reference manual: CHAM TR/200*. CHAM.

Sabouri, F., Gharabaghi, B., Mcbean, E., and Tu, C. (2016). "Thermal Investigation of Stormwater Management Ponds." *Journal of Water Management Modeling*, 24(2016), 1–8.

Sallenave, R. (2011). *Managing Filamentous Algae in Ponds*. *Guide W-103. New Mexico State University Cooperative Extension Service. College of Agricultural, Consumer and Environmental Sciences.*

Semadeni-Davies, A. (2006). "Winter performance of an urban stormwater pond in southern Sweden." *Hydrological Processes*, 20(1), 165–182.

Shaw, J. K. . ., Watt, W. F., Marsalek, J., Anderson, B. ., and Crowder, A. A. (1997). "Flow Pattern Characterization in an Urban Stormwater Detention Pond and Implications for Water Quality." 32(1), 53–71.

She, Y., Kemp, J., Richards, L., and Loewen, M. (2016). "Investigation into freezing point depression in stormwater ponds caused by road salt." *Cold Regions Science and Technology*, Elsevier B.V., 131, 53–64.

Siegel, a, Cotti-Rausch, B., Greenfield, D., and Pinckney, J. (2011). "Nutrient controls of planktonic cyanobacteria biomass in coastal stormwater detention ponds." *Marine Ecology Progress Series*, 434(Nosengo 2003), 15–27.

Silva, C. P., Marti, C. L., and Imberger, J. (2014). "Physical and biological controls of algal blooms in the Río de la Plata." *Environmental Fluid Mechanics*, 14(5), 1199–1228.

Søndergaard, M., Jensen, P. J., and Jeppesen, E. (2001). "Retention and Internal Loading of Phosphorus in Shallow, Eutrophic Lakes." *Hydrobiologia*, 506–509, 135–145.

Song, K., Xenopoulos, M. A., Marsalek, J., and Frost, P. C. (2015). "The fingerprints of urban nutrients: dynamics of phosphorus speciation in water flowing through developed landscapes." *Biogeochemistry*, Springer International Publishing, 125(1), 1–10.

Sun, X. Y., Newham, L. T. H., Croke, B. F. W., Norton, J. P., and Carlo, M. (2012). "Environmental Modelling & Software Three complementary methods for sensitivity analysis of a water quality model." *Environmental Modelling and Software*, Elsevier Ltd, 37, 19–29.

Sutherland, D. L., Turnbull, M. H., and Craggs, R. J. (2014). "ScienceDirect Increased pond depth improves algal productivity and nutrient removal in wastewater treatment high rate algal ponds." *Water Research*, Elsevier Ltd, 53, 271–281.

Szymkiewicz, R. (1993). "Solution of the inverse problem for the St Venant equations." *Journal of Hydrology*, 147, 105–120.

Tayfur, G., and Moramarco, T. (2022). "Kinematic reverse flood routing in natural rivers using stage data." *Applied Water Science*, Springer International Publishing, 12(8), 1–16.

Thomann, R. V., and Mueller, J. A. (1987). *Principles of surface water quality modeling and control*. Harper & Row, New York.

Todaro, V., D'Oria, M., Tanda, M. G., and Gómez-Hernández, J. J. (2019). "Ensemble smoother with multiple data assimilation for reverse flow routing." *Computers and Geosciences*, 131(May), 32–40.

Torres, J. ., Soler, A., SAEZ, J., and ORTUNO, J. . (1997). "Hydraulic performance of a deep wastewater stabilization pond." *Water Research*, 31(4), 679–688.

Trolle, D., Hamilton, D. P., Hipsey, M. R., Bolding, K., Bruggeman, J., Mooij, W. M., Janse, J. H., Nielsen, A., Jeppesen, E., Elliott, J. A., Makler-Pick, V., Petzoldt, T., Rinke, K., Flindt, M. R., Arhonditsis, G. B., Gal, G., Bjerring, R., Tominaga, K., Hoen, J., Downing, A. S., Marques, D. M., Fragoso, C. R., S??ndergaard, M., and Hanson, P. C. (2012). "A community-based framework for aquatic ecosystem models." *Hydrobiologia*, 683(1), 25–34.

Trolle, D., Hamilton, D. P., Pilditch, C. A., Duggan, I. C., and Jeppesen, E. (2011). "Predicting the effects of climate change on trophic status of three morphologically varying lakes: Implications for lake restoration and management." *Environmental Modelling and Software*, Elsevier Ltd, 26(4), 354–370.

Trolle, D., Jørgensen, T. B., and Jeppesen, E. (2008a). "Predicting the effects of reduced external nitrogen loading on the nitrogen dynamics and ecological state of deep Lake Ravn, Denmark, using the DYRESM-CAEDYM model." *Limnologica*, 38(3–4), 220–232.

Trolle, D., Skovgaard, H., and Jeppesen, E. (2008b). "The Water Framework Directive: Setting the phosphorus loading target for a deep lake in Denmark using the 1D lake ecosystem model DYRESM-CAEDYM." *Ecological Modelling*, 219(1–2), 138–152.

Ula´nczyk, R., Kli´s, C., Łozowski, B., Babczy´nska, A., Wo´znica, A., Długosz, J., and Wilk-Wo´zniak, E. (2021). "Phytoplankton production in relation to simulated hydro- and thermodynamics during a hydrological wet year – Gocza ł kowice reservoir (Poland) case study." *Ecological Indicators*, 121, 106991.

Wakelin, S. C., Elefsiniotis, P., and Wareham, D. G. (2003). "Assessment of Stormwater Retention Basin Water Quality in Winnipeg , Canada." *Water Quality Research Journal of Canada*, 38(3), 433–450.

Walker, D. J. (1998). "Modelling residence time in stormwater ponds." *Ecological Engineering*, 10(February), 247–262.

Wang, Y., Shenglian, G., Chen, H., and Zhou, Y. (2014). "Comparative study of monthly inflow prediction methods for the Three Gorges Reservoir." *Stochastic Environmental Research and Risk Assessment*, 28, 555–570.

Wanninkhof, R. H. (1992). "Relationship between wind speed and gas exchange." *Journal of Geophysical Research*, 97(C5), 7373–7382.

Water Measurement Manual: A Guide to Effective Water Measurement Practices for Better Water Management. (2001). Department of the Interior, Bureau of Reclamation, Washington, DC.

Watt, W. E., Marsalek, J., and Anderson, B. C. (2004). "The Kingston Pond: A Case Study of Stormwater Pond Upgrading." *Enhancing Urban Environment by Environmental*

Upgrading and Restoration Nato Science Series: IV: Earth and Environmental Sciences, 43, 23–32.

Wen, Z., Wang, H., Shan, H., Cao, Y., Tan, L., Zhu, T., Cai, Q., Ni, L., Zhang, X., Chou, Q., and Cao, T. (2023). "Water depth modulates the species richness – biomass relationship in submerged macrophytes." *Frontiers in Environmental Science*, 11(May), 1–9.

Wium-Andersen, T., Nielsen, A. H., Hvitved-Jacobsen, T., Brix, H., Arias, C. A., and Vollertsen, J. (2013). "Modeling the eutrophication of two mature planted stormwater ponds for runoff control." *Ecological Engineering*, Elsevier B.V., 61, 601–613.

Woodhouse, C. A., Gray, S. T., and Meko, D. M. (2006). "Updated streamflow reconstructions for the Upper Colorado River Basin." *Water Resources Research*, 42(5), 1–16.

Yajima, H., and Choi, J. (2013). "Changes in phytoplankton biomass due to diversion of an inflow into the Urayama Reservoir." *Ecological Engineering*, Elsevier B.V., 58, 180–191.

Yevdjevich, V. M. (1959). "Analytical Integration of the Differential Equation for Water Storage." *Journal of Research of the National Bureau of Standards - B. Mathematics and Mathematical Physics*, 63(1), 43–52.

Zhao, Q., Mao, J., Cai, H., and Dai, H. (2023). "Local flushing time and its relationship to reservoir eutrophication in Xiangxi Bay, China." *Lake and Reservoir Management*, Taylor & Francis, 39(1), 72–87.

Zhen-Gang, J. (2017). *Hydrodynamics and Water Quality Modeling Rivers, Lakes, and Estuaries*. John Wiley & Sons Inc.

Zoppou, C. (1999). "Reverse Routing of Flood Hydrographs Using Level Pool Routing." *Journal of Hydrologic Engineering*, American Society of Civil Engineers, 4(2), 184–188.

Appendix A. FIELD MEASUREMENTS AND PROCESSING

A.1. HYPSOMETRIC CURVES OF THE STUDY PONDS

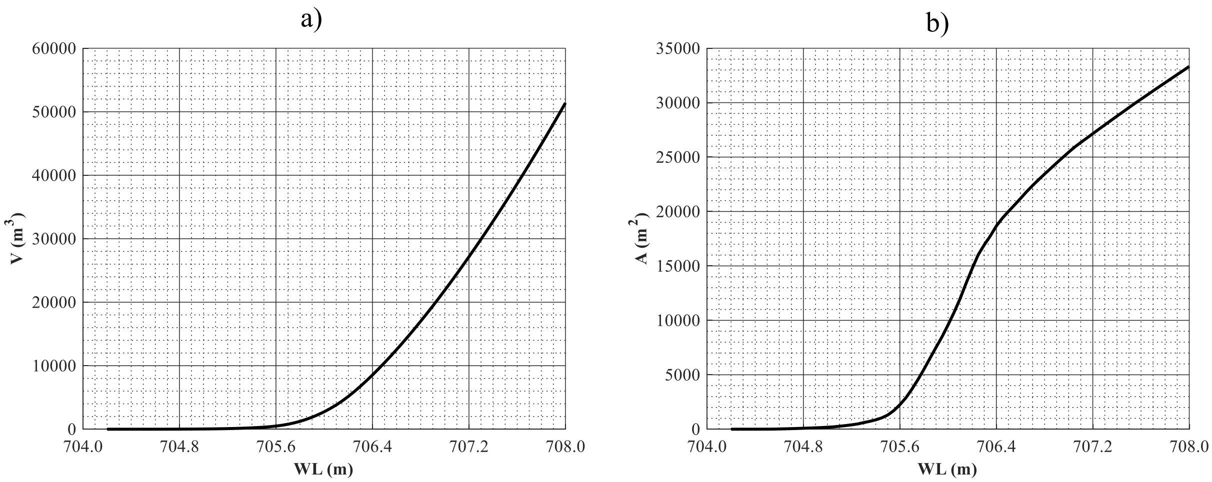

Figure A-1: SB4 hypsometric curves: a) level-volume and b) level-area relationship.

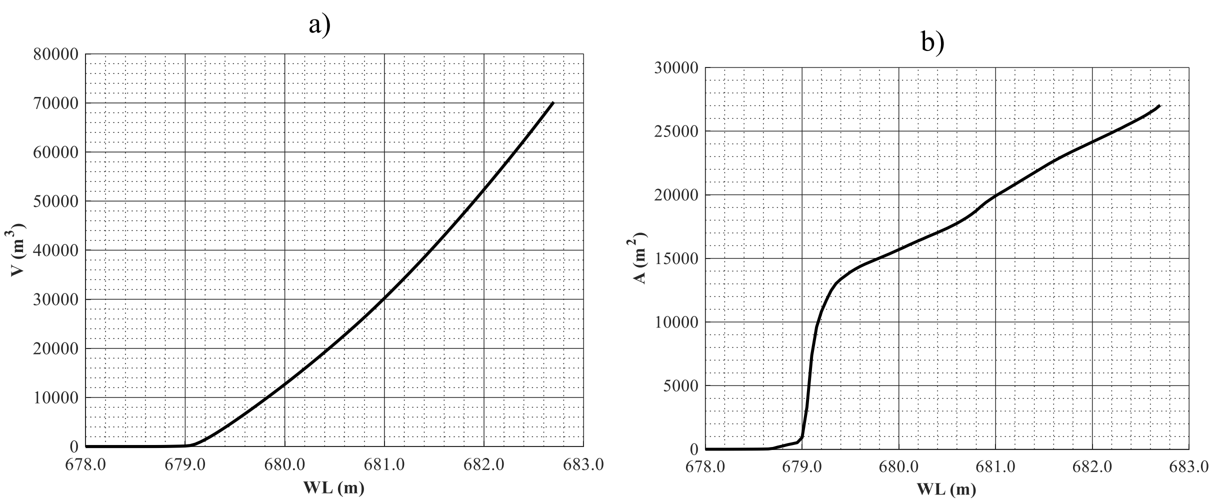

Figure A-2: TT2 Hypsometric curves: a) level-volume and b) level-area relationship.

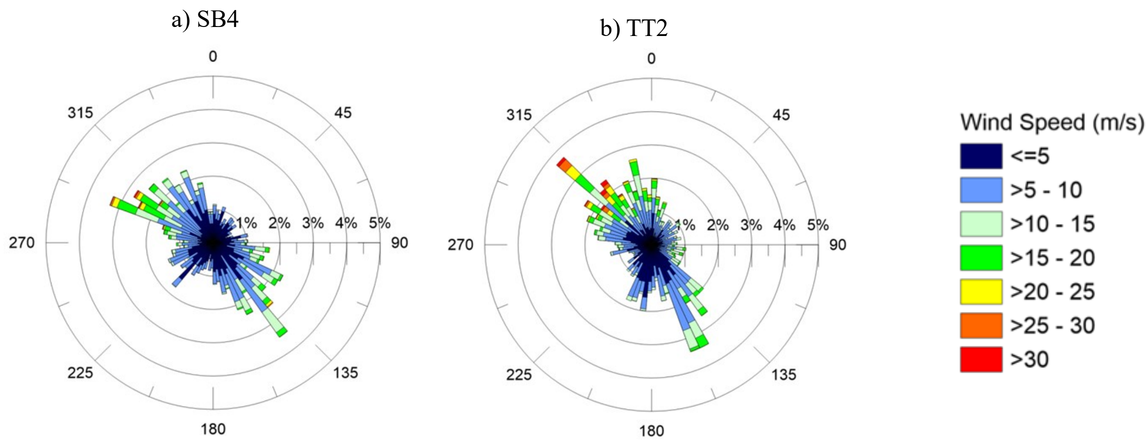

Figure A-3: Wind speed and direction illustrated as a windrose measured at (a) SB4 and (b) TT2 from October 2013 to October 2015.

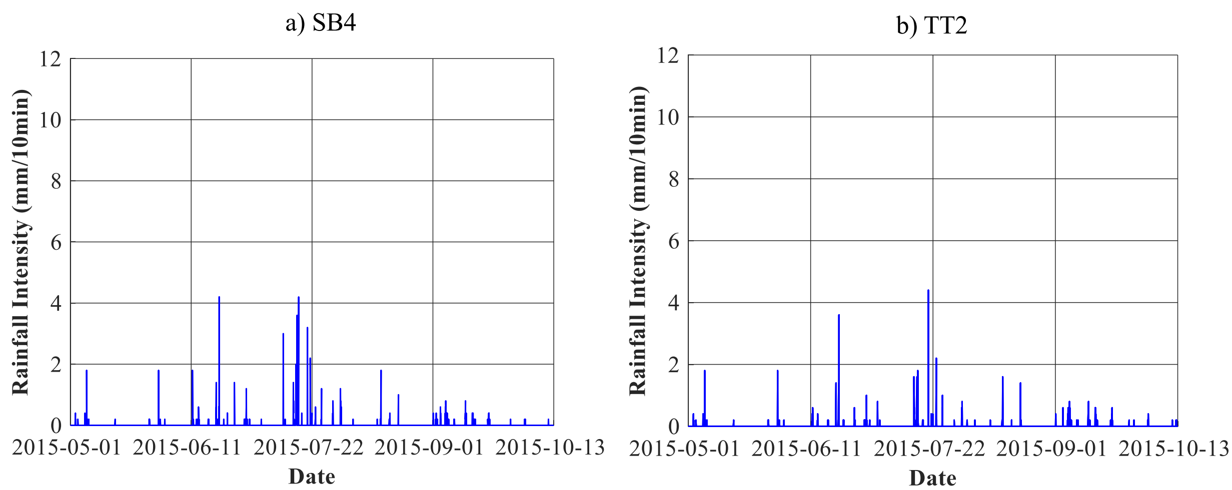

Figure A-4: Rainfall intensity in open-water season of 2015: a) SB4 and b) TT2.

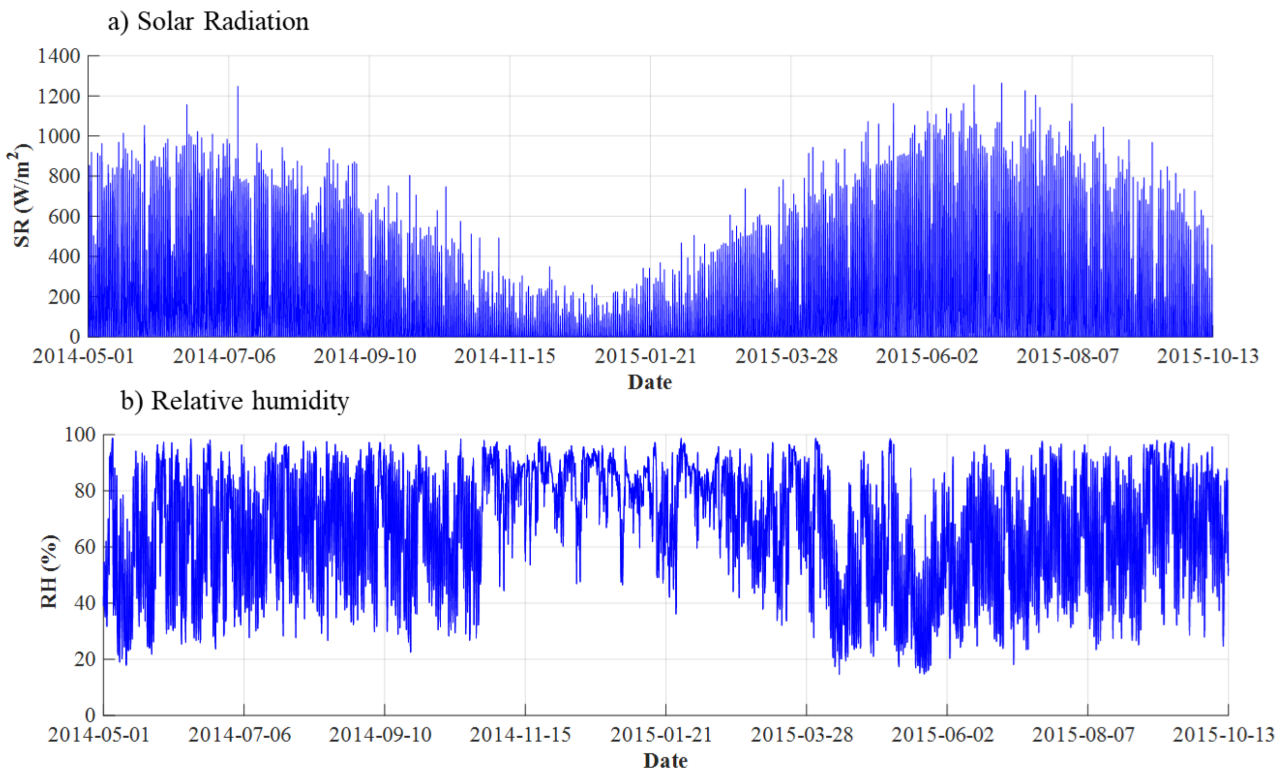

Figure A-5: Meteorological data measured at 10-minute intervals from the weather station installed at ST2: a) solar radiation (SR), and b) relative humidity (RH).

A.2. In-Pond Instrumentation

Table A-1: Details of in-pond instruments at SB4.

Installation Date	Removal Date	Location	Instrument Type	Distance From Bed
25-Oct-13	22-Apr-14	SE	SWS_TD	
25-Oct-13	22-Apr-14	NE	HOBO_Tidbit	0.28
25-Oct-13	22-Apr-14	NE	HOBO_Tidbit	0.47
25-Oct-13	22-Apr-14	NE	SWS_CTD	0.67
25-Oct-13	22-Apr-14	NE	SWS_TD	0.98
25-Oct-13	22-Apr-14	NW	RBR_Duo	0.29
25-Oct-13	22-Apr-14	NW	SWS_CTD	0.65
25-Oct-13	22-Apr-14	NW	RBR_Duo	0.90
22-May-14	02-Jun-14	NE	HOBO_Tidbit	0.26
22-May-14	02-Jun-14	NE	SWS_TD	0.90
22-May-14	02-Jun-14	NE	HOBO_Tidbit	1.32
22-May-14	02-Oct-14	SE	SWS_TD	
22-May-14	02-Oct-14	NE	HOBO_Tidbit	0.49
22-May-14	02-Oct-14	NE	HOBO_Tidbit	0.68
22-May-14	02-Oct-14	NE	HOBO_Tidbit	1.08
22-May-14	02-Oct-14	ESE	HOBO_Tidbit	0.040*
22-May-14	02-Oct-14	ESE	HOBO_Tidbit	0.36*
22-May-14	02-Oct-14	SE	HOBO_Tidbit	0.33*
22-May-14	02-Oct-14	SE	HOBO_Tidbit	0.04
22-May-14	02-Oct-14	SSE	HOBO_Tidbit	0.02*
22-May-14	02-Oct-14	SSE	HOBO_Tidbit	0.30*
02-Jun-14	24-Jul-14	NW	RBR_Duo	0.25
02-Jun-14	24-Jul-14	NW	HOBO_Tidbit	0.56
02-Jun-14	24-Jul-14	NW	SWS_TD	0.74
02-Jun-14	24-Jul-14	NW	HOBO_Tidbit	0.98
02-Jun-14	24-Jul-14	NW	RBR_Duo	1.33
02-Jun-14	02-Oct-14	NE	SWS_CTD	0.28
02-Jun-14	02-Oct-14	NE	HOBO_Tidbit	0.83
02-Jun-14	02-Oct-14	NE	SWS_CTD	1.29
19-Jun-14	02-Oct-14	NNW	HOBO_Tidbit	0.71*
19-Jun-14	02-Oct-14	NNW	HOBO_Tidbit	0.48*
19-Jun-14	02-Oct-14	NNW	HOBO_Tidbit	0.20*
30-Jul-14	02-Oct-14	NW	RBR_Duo	0.30
30-Jul-14	02-Oct-14	NW	SWS_TD	0.75
30-Jul-14	02-Oct-14	NW	HOBO_Tidbit	0.94
30-Jul-14	02-Oct-14	NW	HOBO_Tidbit	1.20
11-Oct-14	21-Apr-15	SE	SWS_CTD	
11-Oct-14	21-Apr-15	NE	RBR_Duo	0.30

11-Oct-14	21-Apr-15	NE	HOBO_Tidbit	0.45
11-Oct-14	21-Apr-15	NE	RBR_Duo	0.62
11-Oct-14	21-Apr-15	NE	SWS_CTD	0.85
11-Oct-14	21-Apr-15	NE	HOBO_Tidbit	1.22
11-Oct-14	21-Apr-15	NE	HOBO_Tidbit	0.67
11-Oct-14	21-Apr-15	NE	HOBO_Tidbit	0.87
11-Oct-14	21-Apr-15	NE	HOBO_Tidbit	1.28
11-Oct-14	21-Apr-15	NE	EXO2	0.33
11-Oct-14	21-Apr-15	NW	HOBO_Tidbit	0.22
11-Oct-14	21-Apr-15	NW	HOBO_Tidbit	0.37
11-Oct-14	21-Apr-15	NW	SWS_TD	0.56
11-Oct-14	21-Apr-15	NW	HOBO_Tidbit	0.75
11-Oct-14	21-Apr-15	NW	HOBO_Tidbit	0.97
11-Oct-14	21-Apr-15	NW	HOBO_Tidbit	1.36
24-Apr-15	22-Jun-15	NE	EXO2	1.07
24-Apr-15	22-Jun-15	NW	HOBO_Tidbit	0.20
24-Apr-15	22-Jun-15	NW	HOBO_Tidbit	0.50
24-Apr-15	22-Jun-15	NW	SWS_TD	0.84
24-Apr-15	22-Jun-15	NW	HOBO_Tidbit	1.08
24-Apr-15	22-Jun-15	NW	HOBO_Tidbit	1.28
24-Apr-15	22-Jun-15	NW	HOBO_Tidbit	1.60
24-Apr-15	22-Jun-15	SE	SWS_CTD	
24-Apr-15	22-Jun-15	NE	RBR_Duo	0.29
24-Apr-15	22-Jun-15	NE	SWS_TD	0.67
24-Apr-15	22-Jun-15	NE	HOBO_Tidbit	0.80
24-Apr-15	22-Jun-15	NE	RBR_Duo	0.93
24-Apr-15	22-Jun-15	NE	HOBO_Tidbit	1.30
24-Apr-15	22-Jun-15	NE	HOBO_Tidbit	1.60
22-Jun-15	12-Aug-15	SE	SWS_TD	
25-Jun-15	12-Aug-15	NE	RBR_Duo	0.29
25-Jun-15	12-Aug-15	NE	SWS_TD	0.60
25-Jun-15	12-Aug-15	NE	HOBO_Tidbit	1.15
25-Jun-15	12-Aug-15	NE	RBR_Duo	0.85
25-Jun-15	12-Aug-15	NE	HOBO_Tidbit	1.60
25-Jun-15	12-Aug-15	NE	EXO2	1.09
14-Aug-15	15-Oct-15	NE	RBR_Duo	0.27
14-Aug-15	15-Oct-15	NE	SWS_TD	0.63
14-Aug-15	15-Oct-15	NE	RBR_Duo	0.87
14-Aug-15	15-Oct-15	NE	HOBO_Tidbit	1.13
14-Aug-15	15-Oct-15	NE	HOBO_Tidbit	1.54
14-Aug-15	15-Oct-15	NE	EXO2	0.30

*Distance is referenced to water surface.

Table A-2: Details of in-pond instruments at TT2.

Installation Date	Removal Date	Location	Instrument Type	Distance From Bed
22-Oct-13	30-Apr-14	NW	RBR_Duo	0.34
22-Oct-13	30-Apr-14	NW	HOBO_Tidbit	0.54
22-Oct-13	30-Apr-14	NW	HOBO_Tidbit	0.76
22-Oct-13	30-Apr-14	NW	SWS_CTD	1.05
22-Oct-13	30-Apr-14	NW	HOBO_Tidbit	1.27
22-Oct-13	30-Apr-14	NW	RBR_Duo	1.60
22-Oct-13	30-Apr-14	SE	HOBO_Tidbit	0.34
22-Oct-13	30-Apr-14	SE	HOBO_Tidbit	0.57
22-Oct-13	30-Apr-14	SE	HOBO_Tidbit	0.78
22-Oct-13	30-Apr-14	SE	SWS_CTD	1.05
22-Oct-13	30-Apr-14	SE	HOBO_Tidbit	1.30
22-Oct-13	30-Apr-14	SE	SWS_TD	1.62
22-Oct-13	30-Apr-14	NE	HOBO_Tidbit	0.31
22-Oct-13	30-Apr-14	NE	HOBO_Tidbit	0.58
22-Oct-13	30-Apr-14	NE	HOBO_Tidbit	0.76
22-Oct-13	30-Apr-14	NE	SWS_TD	1.04
22-Oct-13	30-Apr-14	NE	HOBO_Tidbit	1.32
22-Oct-13	30-Apr-14	NE	HOBO_Tidbit	1.52
22-Oct-13	30-Apr-14	NE	HOBO_Tidbit	1.74
16-May-14	24-Jul-14	NW	RBR_Duo	0.37
16-May-14	24-Jul-14	NW	HOBO_Tidbit	0.76
16-May-14	24-Jul-14	NW	HOBO_Tidbit	1.30
16-May-14	24-Jul-14	NW	SWS_TD	1.50
16-May-14	24-Jul-14	NW	HOBO_Tidbit	1.71
16-May-14	24-Jul-14	NW	RBR_Duo	2.17
16-May-14	02-Oct-14	NE	HOBO_Tidbit	0.40
16-May-14	02-Oct-14	NE	SWS_CTD	0.73
16-May-14	02-Oct-14	NE	HOBO_Tidbit	1.11
16-May-14	02-Oct-14	NE	HOBO_Tidbit	1.51
16-May-14	02-Oct-14	NE	HOBO_Tidbit	1.91
16-May-14	02-Oct-14	NE	HOBO_Tidbit	2.32
16-May-14	02-Oct-14	NE	SWS_CTD	2.55
16-May-14	02-Oct-14	SE	HOBO_Tidbit	0.30
16-May-14	02-Oct-14	SE	HOBO_Tidbit	0.90
16-May-14	02-Oct-14	SE	SWS_TD	1.39
16-May-14	02-Oct-14	SE	HOBO_Tidbit	1.80
16-May-14	02-Oct-14	SE	HOBO_Tidbit	2.24
29-Jul-14	02-Oct-14	NW	RBR_Duo	0.36
29-Jul-14	02-Oct-14	NW	HOBO_Tidbit	0.79
29-Jul-14	02-Oct-14	NW	HOBO_Tidbit	1.35
29-Jul-14	02-Oct-14	NW	SWS_TD	1.55
29-Jul-14	02-Oct-14	NW	RBR_Duo	1.84
29-Jul-14	02-Oct-14	NW	HOBO_Tidbit	2.11
10-Oct-14	21-Apr-15	NE	RBR_Duo	0.26
10-Oct-14	21-Apr-15	NE	HOBO_Tidbit	0.86
10-Oct-14	21-Apr-15	NE	HOBO_Tidbit	1.30
10-Oct-14	21-Apr-15	NE	HOBO_Tidbit	1.74

10-Oct-14	21-Apr-15	NE	RBR_Duo	2.14
10-Oct-14	21-Apr-15	NE	SWS_CTD	2.42
10-Oct-14	21-Apr-15	NE	HOBO_Tidbit	2.82
10-Oct-14	21-Apr-15	NE	SWS_CTD	0.28
10-Oct-14	21-Apr-15	NE	EXO2	1.14
10-Oct-14	21-Apr-15	NW	HOBO_Tidbit	0.32
10-Oct-14	21-Apr-15	NW	HOBO_Tidbit	0.56
10-Oct-14	21-Apr-15	NW	HOBO_Tidbit	0.79
10-Oct-14	21-Apr-15	NW	SWS_TD	1.14
10-Oct-14	21-Apr-15	NW	HOBO_Tidbit	1.40
10-Oct-14	21-Apr-15	NW	HOBO_Tidbit	1.77
10-Oct-14	21-Apr-15	SE	HOBO_Tidbit	0.31
10-Oct-14	21-Apr-15	SE	HOBO_Tidbit	0.74
10-Oct-14	21-Apr-15	SE	HOBO_Tidbit	1.01
10-Oct-14	21-Apr-15	SE	SWS_TD	1.19
10-Oct-14	21-Apr-15	SE	HOBO_Tidbit	1.36
10-Oct-14	21-Apr-15	SE	HOBO_Tidbit	1.68
10-Oct-14	21-Apr-15	SE	HOBO_Tidbit	2.12
29-Oct-14	21-Apr-15	Centre	HOBO_Tidbit	0.19
29-Oct-14	21-Apr-15	Centre	HOBO_DO	0.35
29-Oct-14	21-Apr-15	Centre	HOBO_Tidbit	0.51
29-Oct-14	21-Apr-15	Centre	HOBO_DO	0.70
29-Oct-14	21-Apr-15	Centre	SWS_TD	0.95
29-Oct-14	21-Apr-15	Centre	HOBO_DO	1.17
29-Oct-14	21-Apr-15	Centre	HOBO_DO	1.43
29-Oct-14	21-Apr-15	Centre	HOBO_Tidbit	1.75
24-Apr-15	23-Jun-15	NE	RBR_Duo	0.30
24-Apr-15	23-Jun-15	NE	SWS_CTD	0.60
24-Apr-15	23-Jun-15	NE	HOBO_Tidbit	1.33
24-Apr-15	23-Jun-15	NE	SWS_CTD	1.83
24-Apr-15	23-Jun-15	NE	HOBO_Tidbit	2.32
24-Apr-15	23-Jun-15	NE	RBR_Duo	2.68
24-Apr-15	23-Jun-15	NE	HOBO_Tidbit	3.45
24-Apr-15	23-Jun-15	SE	HOBO_Tidbit	0.30
24-Apr-15	23-Jun-15	SE	HOBO_Tidbit	0.70
24-Apr-15	23-Jun-15	SE	HOBO_Tidbit	1.26
24-Apr-15	23-Jun-15	SE	SWS_TD	1.78
24-Apr-15	23-Jun-15	SE	HOBO_Tidbit	2.27
24-Apr-15	23-Jun-15	SE	HOBO_Tidbit	2.75
24-Apr-15	23-Jun-15	NW	HOBO_Tidbit	0.35
24-Apr-15	23-Jun-15	NW	SWS_TD	0.83
24-Apr-15	23-Jun-15	NW	HOBO_Tidbit	1.31
24-Apr-15	23-Jun-15	NW	HOBO_Tidbit	1.87
24-Apr-15	23-Jun-15	NW	HOBO_Tidbit	2.25
24-Apr-15	23-Jun-15	NE	EXO2	3.00
29-Apr-15	23-Jun-15	Centre	HOBO_DO	0.34
29-Apr-15	23-Jun-15	Centre	HOBO_DO	0.83
29-Apr-15	23-Jun-15	Centre	SWS_TD	1.12
29-Apr-15	23-Jun-15	Centre	HOBO_DO	1.36
29-Apr-15	23-Jun-15	Centre	HOBO_DO	1.83
25-Jun-15	12-Aug-15	NE	RBR_Duo	0.24

25-Jun-15	12-Aug-15	NE	SWS_TD	0.59
25-Jun-15	12-Aug-15	NE	HOBO_Tidbit	0.96
25-Jun-15	12-Aug-15	NE	HOBO_Tidbit	1.31
25-Jun-15	12-Aug-15	NE	HOBO_Tidbit	1.63
25-Jun-15	12-Aug-15	NE	HOBO_Tidbit	1.97
25-Jun-15	12-Aug-15	NE	RBR_Duo	2.26
25-Jun-15	12-Aug-15	NE	HOBO_Tidbit	2.60
25-Jun-15	12-Aug-15	NE	HOBO_Tidbit	2.98
25-Jun-15	12-Aug-15	Centre	HOBO_DO	0.33
25-Jun-15	12-Aug-15	Centre	HOBO_DO	0.80
25-Jun-15	12-Aug-15	Centre	SWS_TD	1.08
25-Jun-15	12-Aug-15	Centre	HOBO_DO	1.33
25-Jun-15	12-Aug-15	Centre	HOBO_DO	1.84
25-Jun-15	12-Aug-15	NE	EXO2	2.67
14-Aug-15	15-Oct-15	NE	RBR_Duo	0.29
14-Aug-15	15-Oct-15	NE	SWS_TD	0.64
14-Aug-15	15-Oct-15	NE	HOBO_Tidbit	0.94
14-Aug-15	15-Oct-15	NE	HOBO_Tidbit	1.31
14-Aug-15	15-Oct-15	NE	HOBO_Tidbit	1.59
14-Aug-15	15-Oct-15	NE	HOBO_Tidbit	1.93
14-Aug-15	15-Oct-15	NE	RBR_Duo	2.20
14-Aug-15	15-Oct-15	NE	HOBO_Tidbit	2.57
14-Aug-15	15-Oct-15	NE	HOBO_Tidbit	2.96
14-Aug-15	15-Oct-15	NE	EXO2	2.68
14-Aug-15	15-Oct-15	Centre	HOBO_DO	0.35
14-Aug-15	15-Oct-15	Centre	HOBO_DO	0.83
14-Aug-15	15-Oct-15	Centre	SWS_TD	1.13
14-Aug-15	15-Oct-15	Centre	HOBO_DO	1.35
14-Aug-15	15-Oct-15	Centre	HOBO_DO	1.86

Table A-3: Details of in-pond instruments at ST2.

Installation Date	Removal Date	Location	Instrument Type	Distance From Bed
24-Oct-13	30-Apr-14	SW	HOBO_Tidbit	0.33
24-Oct-13	30-Apr-14	SW	HOBO_Tidbit	0.56
24-Oct-13	30-Apr-14	SW	SWS_TD	0.82
24-Oct-13	30-Apr-14	NW	HOBO_Tidbit	0.28
24-Oct-13	30-Apr-14	NW	SWS_TD	0.56
24-Oct-13	30-Apr-14	NW	HOBO_Tidbit	0.80
24-Oct-13	30-Apr-14	NW	SWS_CTD	1.08
24-Oct-13	30-Apr-14	SE	RBR_Duo	0.40
24-Oct-13	30-Apr-14	SE	SWS_CTD	0.76
24-Oct-13	30-Apr-14	SE	RBR_Duo	1.04
16-May-14	24-Jul-14	SE	RBR_Duo	0.23
16-May-14	24-Jul-14	SE	HOBO_Tidbit	0.55
16-May-14	24-Jul-14	SE	SWS_TD	0.81
16-May-14	24-Jul-14	SE	HOBO_Tidbit	1.05
16-May-14	24-Jul-14	SE	RBR_Duo	1.45
16-May-14	02-Oct-14	SW	SWS_CTD	0.36
16-May-14	02-Oct-14	SW	HOBO_Tidbit	0.74
16-May-14	02-Oct-14	SW	HOBO_Tidbit	0.97
16-May-14	02-Oct-14	SW	HOBO_Tidbit	1.21
16-May-14	02-Oct-14	SW	SWS_CTD	1.53
16-May-14	02-Oct-14	NW	HOBO_Tidbit	0.32
16-May-14	02-Oct-14	NW	HOBO_Tidbit	0.80
16-May-14	02-Oct-14	NW	SWS_TD	1.27
16-May-14	02-Oct-14	NW	HOBO_Tidbit	1.49
16-May-14	02-Oct-14	NW	HOBO_Tidbit	1.82
29-Jul-14	02-Oct-14	SE	RBR_Duo	0.30
29-Jul-14	02-Oct-14	SE	HOBO_Tidbit	0.59
29-Jul-14	02-Oct-14	SE	SWS_TD	0.81
29-Jul-14	02-Oct-14	SE	RBR_Duo	1.17
29-Jul-14	02-Oct-14	SE	HOBO_Tidbit	1.46
10-Oct-14	21-Apr-15	NW	SWS_CTD	0.41
10-Oct-14	21-Apr-15	NW	EXO2	0.74
10-Oct-14	21-Apr-15	NW	RBR_Duo	0.32
10-Oct-14	21-Apr-15	NW	HOBO_Tidbit	0.75
10-Oct-14	21-Apr-15	NW	HOBO_Tidbit	0.99
10-Oct-14	21-Apr-15	NW	RBR_Duo	1.20
10-Oct-14	21-Apr-15	NW	SWS_CTD	1.47
10-Oct-14	21-Apr-15	NW	HOBO_Tidbit	1.86
10-Oct-14	21-Apr-15	SW	HOBO_Tidbit	0.28
10-Oct-14	21-Apr-15	SW	HOBO_Tidbit	0.56
10-Oct-14	21-Apr-15	SW	SWS_TD	0.73
10-Oct-14	21-Apr-15	SW	HOBO_Tidbit	0.89
10-Oct-14	21-Apr-15	SW	HOBO_Tidbit	1.30

10-Oct-14	21-Apr-15	SARM	HOBO_Tidbit	0.28
10-Oct-14	21-Apr-15	SARM	HOBO_Tidbit	0.51
10-Oct-14	21-Apr-15	SARM	SWS_TD	0.80
10-Oct-14	21-Apr-15	SARM	HOBO_Tidbit	1.03
10-Oct-14	21-Apr-15	SARM	HOBO_Tidbit	1.44
24-Apr-15	15-Oct-15	SW	HOBO_Tidbit	0.30
24-Apr-15	15-Oct-15	SW	HOBO_Tidbit	0.65
24-Apr-15	15-Oct-15	SW	SWS_TD	0.91
24-Apr-15	15-Oct-15	SW	HOBO_Tidbit	1.23
24-Apr-15	15-Oct-15	SW	HOBO_Tidbit	1.47
24-Apr-15	15-Oct-15	SW	HOBO_Tidbit	1.92
24-Apr-15	22-Jun-15	NW	EXO2	1.95
24-Apr-15	15-Oct-15	SARM	HOBO_Tidbit	0.31
24-Apr-15	15-Oct-15	SARM	HOBO_Tidbit	0.71
24-Apr-15	15-Oct-15	SARM	SWS_TD	1.05
24-Apr-15	15-Oct-15	SARM	HOBO_Tidbit	1.41
24-Apr-15	15-Oct-15	SARM	HOBO_Tidbit	1.88
24-Apr-15	22-Jun-15	NW	RBR_Duo	0.36
24-Apr-15	22-Jun-15	NW	SWS_CTD	0.82
24-Apr-15	22-Jun-15	NW	HOBO_Tidbit	1.11
24-Apr-15	22-Jun-15	NW	SWS_CTD	1.36
24-Apr-15	22-Jun-15	NW	RBR_Duo	1.71
24-Apr-15	22-Jun-15	NW	HOBO_Tidbit	2.04
24-Apr-15	22-Jun-15	NW	HOBO_Tidbit	2.35
25-Jun-15	12-Aug-15	NW	RBR_Duo	0.41
25-Jun-15	12-Aug-15	NW	SWS_TD	0.78
25-Jun-15	12-Aug-15	NW	HOBO_Tidbit	1.02
25-Jun-15	12-Aug-15	NW	HOBO_Tidbit	1.30
25-Jun-15	12-Aug-15	NW	HOBO_Tidbit	1.54
25-Jun-15	12-Aug-15	NW	RBR_Duo	1.74
25-Jun-15	12-Aug-15	NW	HOBO_Tidbit	2.06
25-Jun-15	12-Aug-15	NW	HOBO_Tidbit	2.52
25-Jun-15	12-Aug-15	NW	EXO2	1.99
14-Aug-15	15-Oct-15	NW	RBR_Duo	0.41
14-Aug-15	15-Oct-15	NW	SWS_TD	0.75
14-Aug-15	15-Oct-15	NW	HOBO_Tidbit	1.06
14-Aug-15	15-Oct-15	NW	HOBO_Tidbit	1.32
14-Aug-15	15-Oct-15	NW	HOBO_Tidbit	1.55
14-Aug-15	15-Oct-15	NW	RBR_Duo	1.76
14-Aug-15	15-Oct-15	NW	HOBO_Tidbit	2.08
14-Aug-15	15-Oct-15	NW	HOBO_Tidbit	2.50
14-Aug-15	15-Oct-15	NW	EXO2	1.16

A.3. DIRECT FLOWS MEASUREMENT

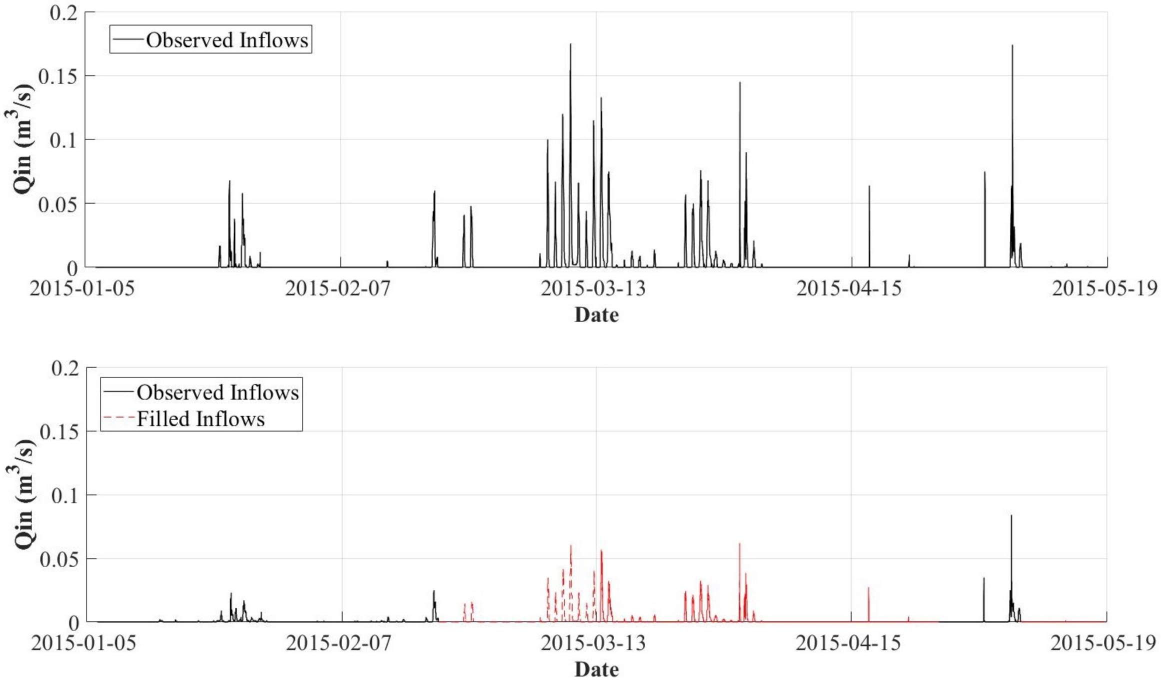

Figure A-6: Measured inflows (Qin) at the NE inlet (top panel) and the SE inlet (bottom panel) of TT2. The data gap at SE inlet, filled using the ratio method, is shown in red dashed line.

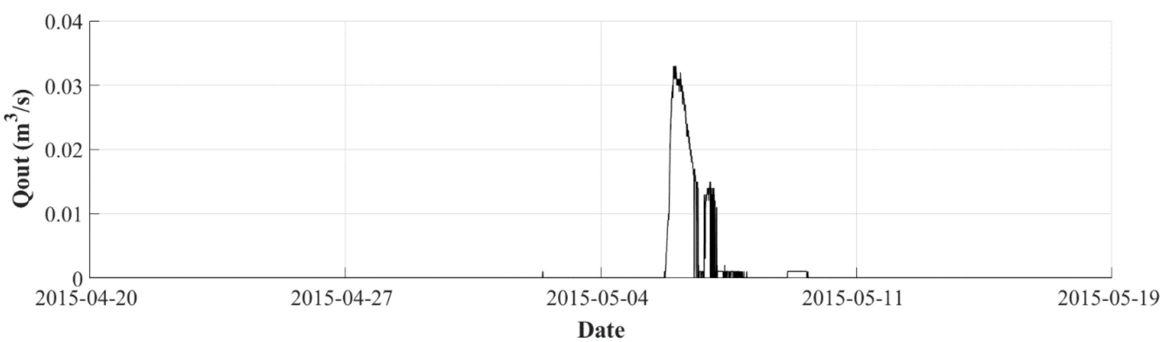

Figure A-7: Measured outflows (Qout) at TT2.

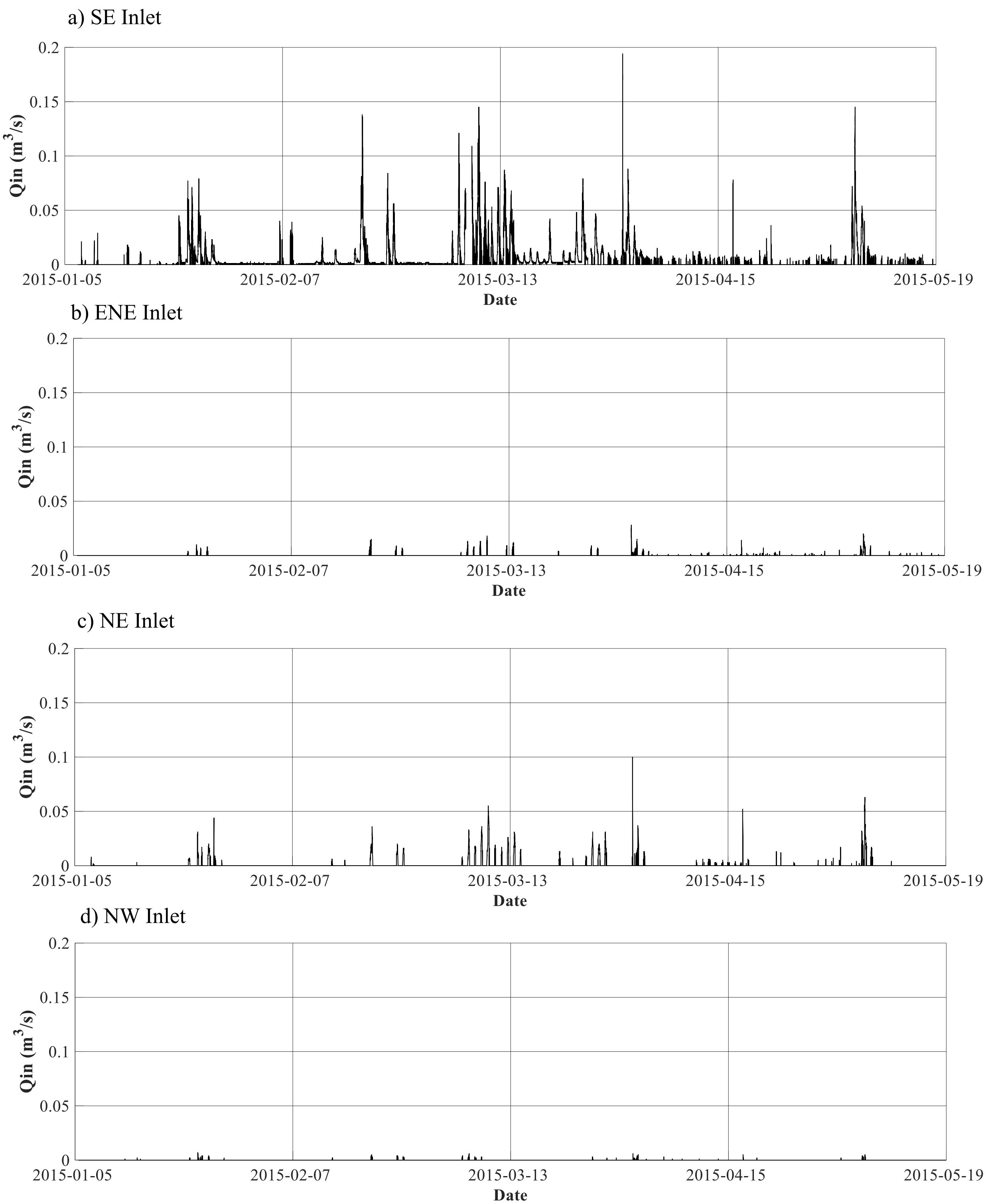

Figure A-8: Measured inflows (Qin) at different SB4 inlets.

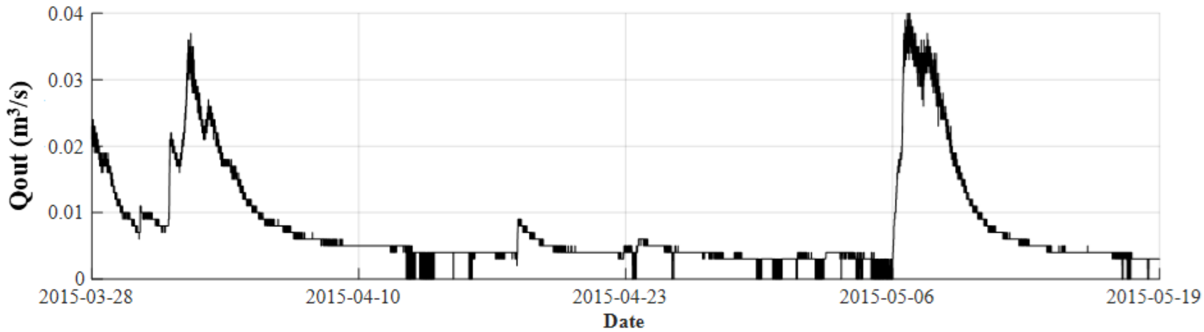

Figure A-9: Measured outflows (Qout) at SB4.

A.4. UPDATING RATING CURVES

The relationship between outflow and the water level can be presented as a rating curve. The rating curve of each pond was documented in the design reports provided by the City of Edmonton. However, the outlet structures had been modified from the initial design, and the rating curves had to be updated to reflect the observed as-built configuration information to develop the as-built rating curves of study ponds. Rating curves of study ponds were updated based on the equations governing the outflows from outlet structures. The equations and assumptions for developing as-built rating curves are presented here.

When the water levels at TT2 are above the NWL, the flow passes over the contracted weir and reaches the second chamber on the downstream side of the weir. The water exits the second chamber via a circular orifice and enters a 600 mm diameter pipe. It was assumed that when the water levels in the second chamber are lower than levels in the first chamber, the outflow is controlled only by the contracted weir. Figure A-10 shows a schematic view of a contracted weir functions under free conditions (i.e., the downstream water levels are below NWL) and the outflows are estimated as follows:

$$Qout = C_d \cdot \frac{2}{3} \cdot (b - 0.2H) \cdot H^{1.5} \cdot \sqrt{2g} \tag{A-1}$$

where $Qout$ (m³/s) is the discharge, C_d is the dimensionless weir coefficient, g (m/s²) is the acceleration due to gravity, b (m) is the width of the crest, and H (m) is the head of water above NWL. The contraction effect, velocity of approach, viscosity, and surface tension are accounted for by C_d. The discharge coefficient varies as a function of H and is given by:

$$C_d = C_{d^*} + 0.08\frac{H}{y} \tag{A-2}$$

where C_{d^*} (dimensionless) was assumed to be 0.61 for a contracted weir, and y (m) is the sill height (Potter et al. 2011).

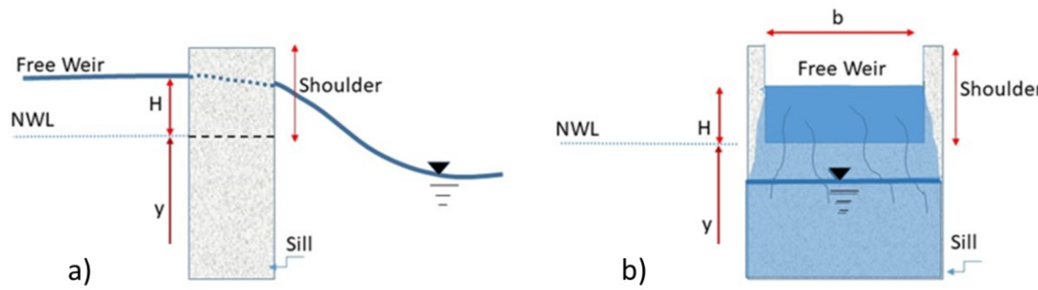

Figure A-10: Schematic view of rectangular orifice: a) Side view and b) Front view.

When the levels at two chambers of TT2 are the same, the flow is controlled by the circular orifice which is fully submerged under these conditions. Figure A-11 depicts a schematic view of a submerged circular orifice. The outflow through this orifice is calculated as follows:

$$Qout = C_o \cdot \frac{\pi}{4} D^2 \cdot \sqrt{2gh_o} \tag{A-3}$$

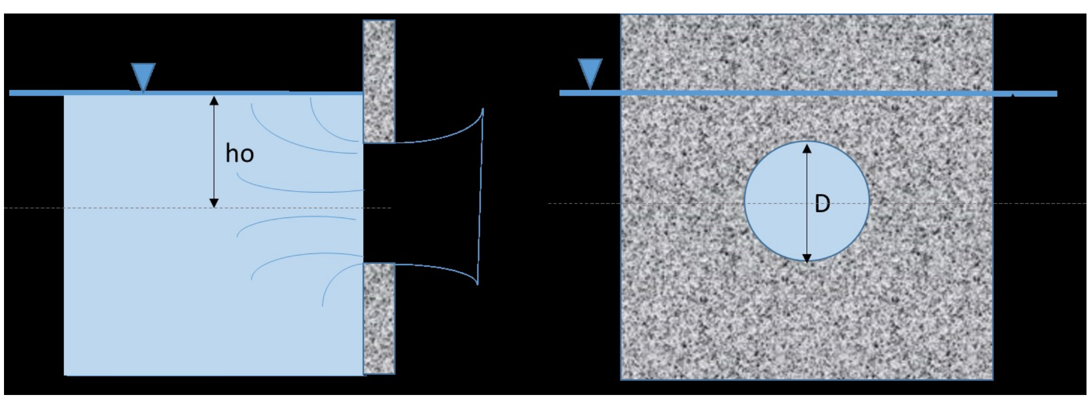

Figure A-11: Schematic view of a submerged circular orifice. a) Side view, b) Front view.

Outflows at SB4 are controlled by the rectangular orifice. However, for the levels between the top and bottom of the opening, the orifice functions as a contracted rectangular weir. Figure A-12 shows a rectangular orifice which is not fully submerged and functions as a weir. However, when the water levels are above the top of the orifice opening, the outflows are calculated as follows:

$$Qout = C_g \cdot b \cdot G\sqrt{2g(H - 0.5G)} \tag{A-4}$$

where G (m) is the orifice opening, and C_g is the dimensionless orifice coefficient that was assumed to be 0.61 for the sharp-edged orifice (*Water Measurement Manual: A Guide to Effective Water Measurement Practices for Better Water Management* 2001). In this pond, high flow is controlled by a rectangular weir. However, the water level did not reached to the weir during the period of this study.

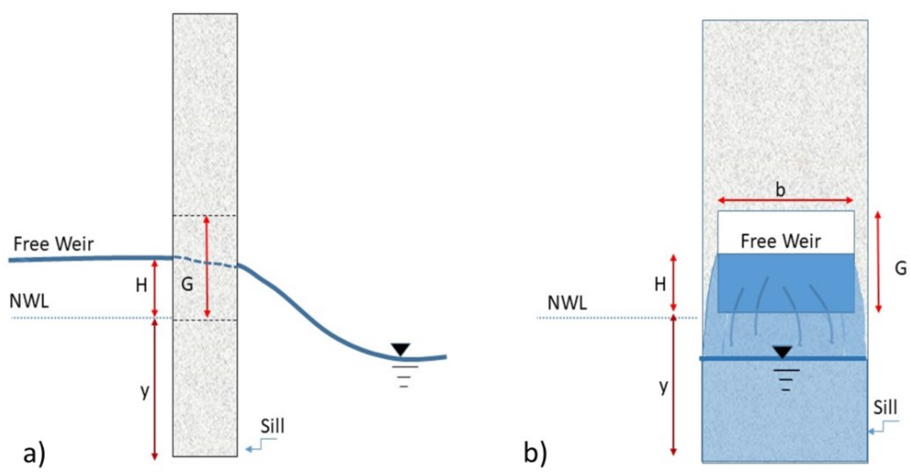

Figure A-12: Schematic view of rectangular orifice which functions as weir. a) Side view, b) Front view.

A.5. WATER LEVEL ELEVATIONS

Water level time series at each pond were calculated from the Diver data and manual water level measurements. The Divers measure the total pressure (H_{Total}) above their sensors. In order to calculate the head only due to the water column (H_w), the barometric pressure at the water surface (H_{ws}) was subtracted from the total pressure as follows:

$$H_w = H_{Total} - H_{ws} \tag{A-5}$$

where all pressures are expressed as meters of water. The barometric pressure (H_{air}) was measured at the weather station which is Δh_p meters above the water surface. Therefore, the barometric pressure at the water surface is derived by:

$$H_{ws} = H_{air} + \frac{\Delta h_p \times \rho_{air}}{\rho_{water}} \tag{A-6}$$

where ρ_{water} and ρ_{air} are the density of water and air, respectively. Knowing the deployed elevation of each sensor, H_{inst} (m), the water level for each sensor is calculated as:

$$WL = H_{ws} + H_{inst} \tag{A-7}$$

where WL (m) is the water level elevation above the sea level. Finally, The water level time series for each pond was calculated by averaging the water levels acquired from all the divers installed within that pond.

A.6. WATER QUALITY SAMPLING

Table A-4: Detection limit, and 95% confidence interval of parameters analysed at the Biogeochemical Analytical Service Laboratory (BASL).

Analyte	Detection Limit	Concentration Range	Expanded Uncertainty (95% confidence interval)
Alkalinity	2mg/L	5-50mg/L	5.7%
Alkalinity	2mg/L	50-500mg/L	5.1%
Chloride	0.03mg/L	0.3-5mg/L	8.5%
Chloride	0.03mg/L	5-20mg/L	5.7%
Conductivity	0.3uS	3-200uS	1.8%
Conductivity	0.3uS	200-4000uS	0.3%
DOC	0.1mg/L	1-5mg/L	16.7%
DOC	0.1mg/L	5-50mg/L	8.6%
Ammonium	2ug/L	20-200ug/L	9.4%
Ammonium	2ug/L	200-2000ug/L	5.3%
Nitrate/Nitrite	1ug/L	10-200ug/L	6.6%
Nitrate/Nitrite	1ug/L	200-2000ug/L	5.7%
Sulfate	0.05mg/L	0.5-5mg/L	12.4%
Sulfate	0.05mg/L	5-80mg/L	7.3%
SRP/TPP	1ug/L	10-200ug/L	5.9%
SRP/TPP	1ug/L	200-2000ug/L	4.6%
TN/TDN	7ug/L	50-2000ug/L	10.9%
TN/TDN	7ug/L	2000-6000ug/L	9.3%
TP/TDP	1ug/L	10-200ug/L	7.7%
TP/TDP	1ug/L	200-2000ug/L	9.0%
DIC	0.1mg/L	1-50mg/L	10.0%

Table A-5 and Table A-6 present the results of water quality samples from ST2, analysed at the Biogeochemical Analytical Service Laboratory (BASL).

Table A-5: Water quality sampling results for ST2 (Part I).

Sample Date	Sampling Location	Depth (m)	Secchi Disk (cm)	NH3 (N mcg/L) #2	NO2+NO3(N mcg/L) #1	TN (N mcg/L) #10	TDN (N mcg/L) #10	TKN (N mcg/L) #10
12-May-14	NW	0.5	-	5	3	1590	-	1587
12-May-14	SW	0.5	-	<MDL	<MDL	1300	-	1300
12-May-14	SARM	0.5	-	<MDL	3	1280	-	1277
12-May-14	SE	0.5	-	3	3	1280	-	1277
28-May-14	NW	0.5	-	332	533	1780	-	1247
28-May-14	SW	0.5	-	203	215	1400	-	1185
28-May-14	SE	0.5	-	95	96	1060	-	964
28-May-14	SARM	1	-	102	139	1080	-	941
12-Jun-14	NW	0.5	-	49	1130	1920	-	790
12-Jun-14	SW	0.5	-	17	192	942	-	750
12-Jun-14	SARM	1	-	6	514	1060	-	546

12-Jun-14	SE	0.5	-	6	18	564	-	546
26-Jun-14	SE	0.5	-	9	<MDL	738	-	738
26-Jun-14	SARM	1	-	53	31	985	-	954
26-Jun-14	SW	0.5	-	49	<MDL	863	-	863
26-Jun-14	NW	0.5	-	139	1200	2100	-	900
16-Jul-14	NW	0.5	-	86	1,350	2380	-	1030
16-Jul-14	SW	0.5	-	3	<MDL	677	-	677
16-Jul-14	SARM	1	-	6	155	961	-	806
16-Jul-14	SE	0.5	-	6	<MDL	670	-	670
07-Aug-14	SE	0.5	145	<MDL	<MDL	727	-	727
07-Aug-14	NW	0.5	132	5	<MDL	1350	-	1350
18-Aug-14	SARM	1	75	90	19	1090	-	1071
18-Aug-14	NW	0.5	60	31	163	1340	-	1177
03-Sep-14	SARM	1	54	27	<MDL	1100	-	1100
03-Sep-14	NW	0.5	38	120	99	1500	-	1401
17-Sep-14	SARM	1	50	<MDL	41	1300	-	1259
17-Sep-14	NW	0.5	90	47	216	1620	-	1404
01-Oct-14	SARM	1	89-90	73	<MDL	1560	-	1560
01-Oct-14	NW	0.5	90	79	93	1600	-	1507
15-Oct-14	SARM	0.5	45	<MDL	<MDL	1490	-	1490
15-Oct-14	NW	1	45-52	5	22	1700	-	1678
29-Oct-14	SARM	0.5	49	<MDL	<MDL	1480	-	1480
29-Oct-14	NW	1	44	55	201	1530	-	1329
07-May-15	S	-	-	178	793	1040	728	<MDL
07-May-15	NW	-	-	136	1,030	1020	732	<MDL
14-May-15	SARM	0.5	61	<MDL	<MDL	703	1048	1048
14-May-15	SE	0.5	50	3	<MDL	1070	2240	2240
14-May-15	SW	0.5	55	<MDL	<MDL	783	1008	1008
14-May-15	SW	1.5	55	<MDL	<MDL	728	1392	1392
14-May-15	NW	0.5	59	10	170	1010	1440	1270
14-May-15	NW	1.5	59	<MDL	2,680	4220	4640	1960
27-May-15	SARM	0.5	193*	30	<MDL	764	832	832
27-May-15	SE	0.5	173*	4	<MDL	743	800	800
27-May-15	SW	0.5	194*	18	<MDL	761	800	800
27-May-15	NW	0.5	78	40	6	791	1192	1186
27-May-15	NW	1.5	78	<MDL	2,340	2970	4160	1820
28-May-15	SARM	-	-	586	912	2030	2872	1960
28-May-15	NW	-	-	36	1,480	2070	2244	764
10-Jun-15	SARM	0.5	151*	<MDL	<MDL	930	1060	1060
10-Jun-15	SE	0.5	168*	44	<MDL	950	924	924
10-Jun-15	SW	0.5	194*	<MDL	<MDL	828	896	896
10-Jun-15	NW	0.5	156	224	66	1370	1480	1414
10-Jun-15	NW	2	156	657	1,520	3810	4200	2680
22-Jun-15	SARM	0.5	150	7	<MDL	839	1044	1044
22-Jun-15	SE	0.5	168	30	<MDL	834	980	980
22-Jun-15	SW	0.5	148	<MDL	<MDL	788	1012	1012
22-Jun-15	NW	0.5	59	119	<MDL	778	1068	1068
22-Jun-15	NW	2	59	258	2,020	2720	2908	888
07-Jul-15	SARM	0.5	126	16	<MDL	802	636	636
07-Jul-15	SARM	0.5	126	21	<MDL	829	1072	1072

07-Jul-15	SARM	0.5	126	23	<MDL	842	992	992
07-Jul-15	SE	0.5	132	3	<MDL	774	848	848
07-Jul-15	SW	0.5	101	<MDL	<MDL	702	1032	1032
07-Jul-15	NW	0.5	121	97	4	797	1028	1024
07-Jul-15	NW	1.5	121	76	1,970	3300	4160	2190
21-Jul-15	SARM	0.5	77	25	176	764	968	792
21-Jul-15	SE	0.5	110	8	9	594	872	863
21-Jul-15	SW	0.5	80	19	207	725	996	789
21-Jul-15	NW	0.5	42	<MDL	1,410	1730	2336	926
21-Jul-15	NW	2	42	133	2,075	4380	4360	2285
04-Aug-15	SARM	0.5	32	72	3	622	1700	1697
04-Aug-15	SE	0.5	-	76	2	911	1528	1526
04-Aug-15	SW	0.5	33	27	3	864	1712	1709
04-Aug-15	NW	0.1	25	13	10	821	3724	3714
04-Aug-15	NW	0.1	25	10	9	706	3780	3771
04-Aug-15	NW	0.1	25	8	9	901	3864	3855
04-Aug-15	NW	2	25	230	1,390	2200	2784	1394
18-Aug-15	SARM	0.5	25	3	3	805	2132	2129
18-Aug-15	SE	0.5	25	4	3	982	2084	2081
18-Aug-15	SW	0.5	24	<MDL	<MDL	743	1772	1772
18-Aug-15	NW	0.5	26	28	21	1080	1872	1851
18-Aug-15	NW	2	26	136	1,020	1740	2088	1068
01-Sep-15	SARM	0.5	15	<MDL	<MDL	1010	2236	2236
01-Sep-15	SE	0.5	19	<MDL	<MDL	998	2288	2288
01-Sep-15	Bend	0.5	19	<MDL	<MDL	879	2032	2032
01-Sep-15	NW	0.5	21	10	17	1250	2556	2539
01-Sep-15	NW	2	21	241	152	1630	2608	2456
16-Sep-15	SE	0.5	30	101	166	1230	1768	1602
16-Sep-15	SW	0.5	28	71	344	1230	1724	1380
16-Sep-15	NW	0.5	22	190	749	1250	2088	1339
16-Sep-15	NW	2	22	103	3,610	4310	4640	1030
30-Sep-15	SARM	0.5	40	21	250	1140	1536	1286
30-Sep-15	SE	0.5	38	17	225	1120	1536	1311
30-Sep-15	SW	0.5	30	26	213	1650	2052	1839
30-Sep-15	SW	1.5	30	104	276	1150	1752	1476
30-Sep-15	NW	0.5	36	21	434	1210	1672	1238
30-Sep-15	NW	1.5	36	295	867	2540	2776	1909
13-Oct-15	SE	0.5	35	316	143	1280	1748	1605
13-Oct-15	SW	0.5	33	298	198	1330	1840	1642

Method Detection Limit (MDL)

Table A-6 Water quality sampling results for ST2 (Part II).

Sample Date	Sampling Location	Depth (m)	SRP (P mcg/L) #1	TP (P mcg/L) #3	TDP (P mcg/L) #4	TPP (P mcg/L)	DOC (C mg/L) #0.1	DIC (C mg/L) #0.5	TCHLA (mcg/L) #0.2
12-May-14	NW	0.5	3	124	22	98	10.9	22.3	74.51
12-May-14	SW	0.5	2	108	21	83	10.7	21.1	56.82
12-May-14	SARM	0.5	2	95	20	70	10.1	20.9	57.01
12-May-14	SE	0.5	3	91	20	68	11	20.6	60.76
28-May-14	NW	0.5	7	103	28	22	9.6	22	13.59
28-May-14	SW	0.5	3	84	35	47	9.8	24.9	12.22
28-May-14	SE	0.5	3	67	31	24	10.3	25.9	8.1
28-May-14	SARM	1	3	62	26	28	10	25.6	10.22
12-Jun-14	NW	0.5	11	167	18	35	45.3	23	1.52
12-Jun-14	SW	0.5	6	29	18	12	11	15.4	1.41
12-Jun-14	SARM	1	4	23	15	10	10.5	13.9	4.67
12-Jun-14	SE	0.5	3	22	16	10	10.6	14	1.87
26-Jun-14	SE	0.5	10	45	35	10	11.1	15.1	1.32
26-Jun-14	SARM	1	11	62	48	10	11.3	16.8	<MDL
26-Jun-14	SW	0.5	16	56	51	11	11.7	17.5	<MDL
26-Jun-14	NW	0.5	3	37	21	11	14.9	34	<MDL
16-Jul-14	NW	0.5	5	80	47	14	11.7	32.8	38.62
16-Jul-14	SW	0.5	12	51	34	21	9.8	12.7	8.54
16-Jul-14	SARM	1	10	50	32	21	10.1	16.2	7.62
16-Jul-14	SE	0.5	4	40	25	18	10.3	10.5	3.85
07-Aug-14	SE	0.5	5	981	-	17	9.5	14.4	4.1
07-Aug-14	NW	0.5	3	149	-	85	9.7	11.4	271.08
18-Aug-14	SARM	1	47	121	-	43	11.1	21.3	12.31
18-Aug-14	NW	0.5	9	81	-	59	13.3	30.5	42.8
03-Sep-14	SARM	1	24	127	-	68.6	12.6	26.5	19.43
03-Sep-14	NW	0.5	10	143	-	63	15.4	30.5	31.82
17-Sep-14	SARM	1	17	152	-	107.7	12.9	31.5	45.96
17-Sep-14	NW	0.5	10	114	-	91.7	13	33.6	71.96
01-Oct-14	SARM	1	18	152	-	63.7	12.7	36.3	47.61
01-Oct-14	NW	0.5	10	125	-	57.7	12.6	36.9	52.85
15-Oct-14	SARM	0.5	14	160	-	69	13.8	38.3	80.05
15-Oct-14	NW	1	17	156	-	73	13.9	42.2	108.93
29-Oct-14	SARM	0.5	13	120	-	80	13.1	42.4	40.43
29-Oct-14	NW	1	5	103	-	74	12.1	42.7	27.99
07-May-15	S	-	61	101	70	31.6	4.8	7.8	-
07-May-15	NW	-	62	111	74	43.1	7.5	14.8	-
14-May-15	SARM	0.5	3	112	25	72.1	8.4	16.4	39.7
14-May-15	SE	0.5	2	170	63	93.2	9	17.4	66.49
14-May-15	SW	0.5	1	108	31	77.5	9	15.5	42.47
14-May-15	SW	1.5	5	198	33	137.5	8.7	16.3	172.58
14-May-15	NW	0.5	4	100	30	72.3	9.2	16.2	39.49
14-May-15	NW	1.5	7	95	35	62.5	7.9	61.9	58.99
27-May-15	SARM	0.5	3	93	43	24.3	12	13.7	0.49
27-May-15	SE	0.5	2	45	28	17.9	12.5	13.5	0.59

27-May-15	SW	0.5	2	42	31	19.4	13.6	13.9	0.11
27-May-15	NW	0.5	4	80	56	19.2	13.1	19.1	15.87
27-May-15	NW	1.5	17	164	29	147.5	14.3	61.9	139.29
28-May-15	SARM	-	23	303	28	279.6	10.4	25.7	-
28-May-15	NW	-	34	60	28	36.6	22.5	78.3	-
10-Jun-15	SARM	0.5	36	99	84	30.4	17	25.5	0.48
10-Jun-15	SE	0.5	48	121	95	33.6	17.7	24.9	1.69
10-Jun-15	SW	0.5	42	102	81	30.6	17.7	27	0.95
10-Jun-15	NW	0.5	60	143	120	30.6	20.9	40.4	0.44
10-Jun-15	NW	2	532	643	598	52.9	14.7	71.3	1.6
22-Jun-15	SARM	0.5	7	56	44	24.1	15.6	17.6	9.76
22-Jun-15	SE	0.5	9	64	49	45.5	15.6	17.7	5.41
22-Jun-15	SW	0.5	9	81	48	26.2	15.6	20.9	18.8
22-Jun-15	NW	0.5	20	92	39	54.8	13.3	21.4	15.01
22-Jun-15	NW	2	45	91	54	43	10.6	39.5	4.34
07-Jul-15	SARM	0.5	21	77	56	33.7	14.7	16.7	3.52
07-Jul-15	SARM	0.5	24	90	57	28.4	14.8	16.2	3.92
07-Jul-15	SARM	0.5	24	96	56	24.5	14.7	16.4	3.68
07-Jul-15	SE	0.5	24	81	54	37.1	15	16.3	5.89
07-Jul-15	SW	0.5	34	101	64	50.1	15.3	20.7	7.27
07-Jul-15	NW	0.5	5	66	31	32.2	16.4	22.3	4.49
07-Jul-15	NW	1.5	23	168	44	148.7	14.3	56.1	71.32
21-Jul-15	SARM	0.5	27	96	56	50.9	10.7	18	14.15
21-Jul-15	SE	0.5	24	77	51	74.5	11.5	17.9	8.92
21-Jul-15	SW	0.5	3	114	52	91.2	9.7	16.4	12.52
21-Jul-15	NW	0.5	43	138	36	139.7	8.1	16.5	56.78
21-Jul-15	NW	2	3	103	54	62.4	9.2	29.8	3.86
04-Aug-15	SARM	0.5	30	188	71	154.3	9.8	23.8	53.92
04-Aug-15	SE	0.5	38	188	89	142.2	10	23.2	58.8
04-Aug-15	SW	0.5	13	161	55	148.9	9.9	24.9	40.96
04-Aug-15	NW	0.1	14	369	44	445.2	11.6	29	127.58
04-Aug-15	NW	2	6	99	25	110	11.3	48.8	21.12
18-Aug-15	SARM	0.5	4	311	45	334.6	10.8	31.9	85.28
18-Aug-15	SE	0.5	4	300	50	306.4	10.6	31.7	84.85
18-Aug-15	SW	0.5	5	264	28	304.6	10.6	31.4	90.72
18-Aug-15	NW	0.5	<MDL	210	40	234.2	11.2	31	125.88
18-Aug-15	NW	2	8	98	33	112.3	12.6	39.5	22.19
01-Sep-15	SARM	0.5	7	271	54	185.6	11.9	34.1	89.63
01-Sep-15	SE	0.5	7	264	44	230	12.7	33.3	94.3
01-Sep-15	Bend	0.5	6	283	27	294.6	12.1	35	81.9
01-Sep-15	NW	0.5	8	309	63	233.6	11.9	37.2	97.65
01-Sep-15	NW	2	11	292	109	174.7	11.3	39.9	72.45
16-Sep-15	SE	0.5	7	138	42	88.6	7.7	27.3	71.29
16-Sep-15	SW	0.5	9	153	35	126.9	6.6	23.8	71.66
16-Sep-15	NW	0.5	8	172	31	124.4	6.1	22.3	30.46
16-Sep-15	NW	2	31	139	26	97.4	8.3	47.2	5.67
30-Sep-15	SARM	0.5	10	117	17	100.3	8.1	33.3	54.01
30-Sep-15	SE	0.5	14	119	14	99.8	7.8	30.8	62.35
30-Sep-15	SW	0.5	12	169	60	88.8	8.3	31.4	91.77
30-Sep-15	SW	1.5	10	142	17	110.3	8.1	34.5	56.41

30-Sep-15	NW	0.5	13	120	15	101.6	8.3	33.2	60.36
30-Sep-15	NW	1.5	20	98	47	75.9	8.6	48.4	25.92
13-Oct-15	SE	0.5	7	116	24	103.1	8	37.9	28.27
13-Oct-15	SW	0.5	8	128	30	107.1	8.2	18.3	31.8

Method Detection Limit (MDL)

The following figures depict the measured dissolved oxygen (DO) and temperature (T) at ST2 used in this study. The data were obtained through measurements conducted either by in-pond instruments or profiling.

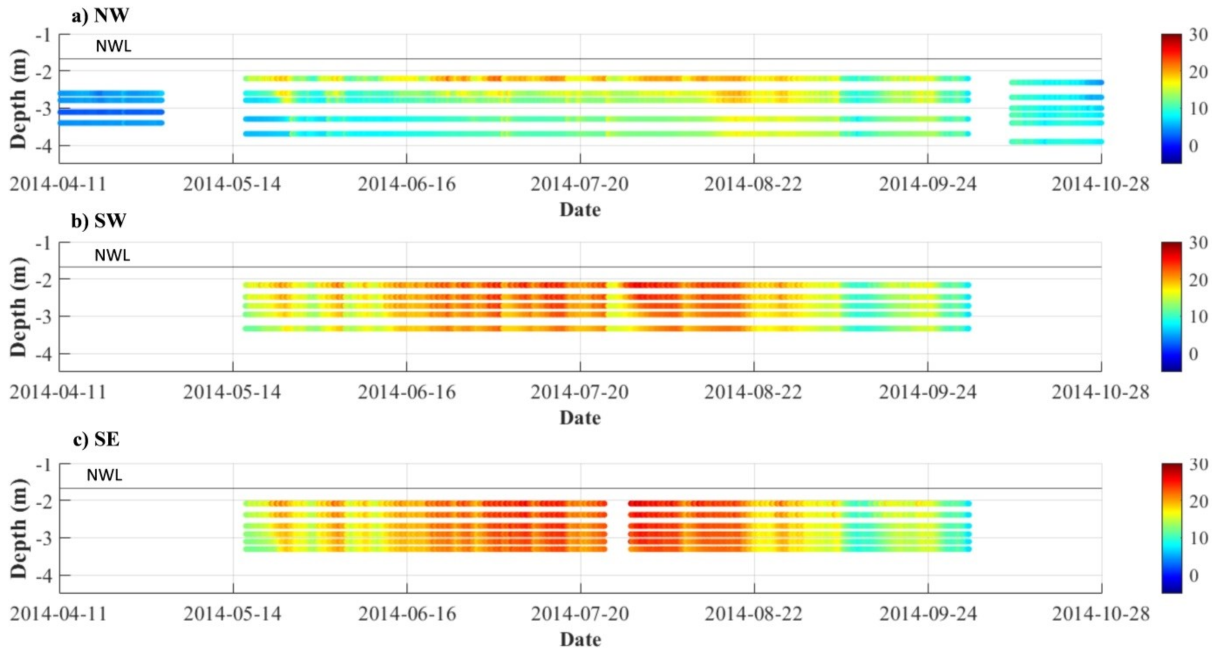

Figure A-13: Measured temperature (°C) at sampling locations within ST2 in 2014.

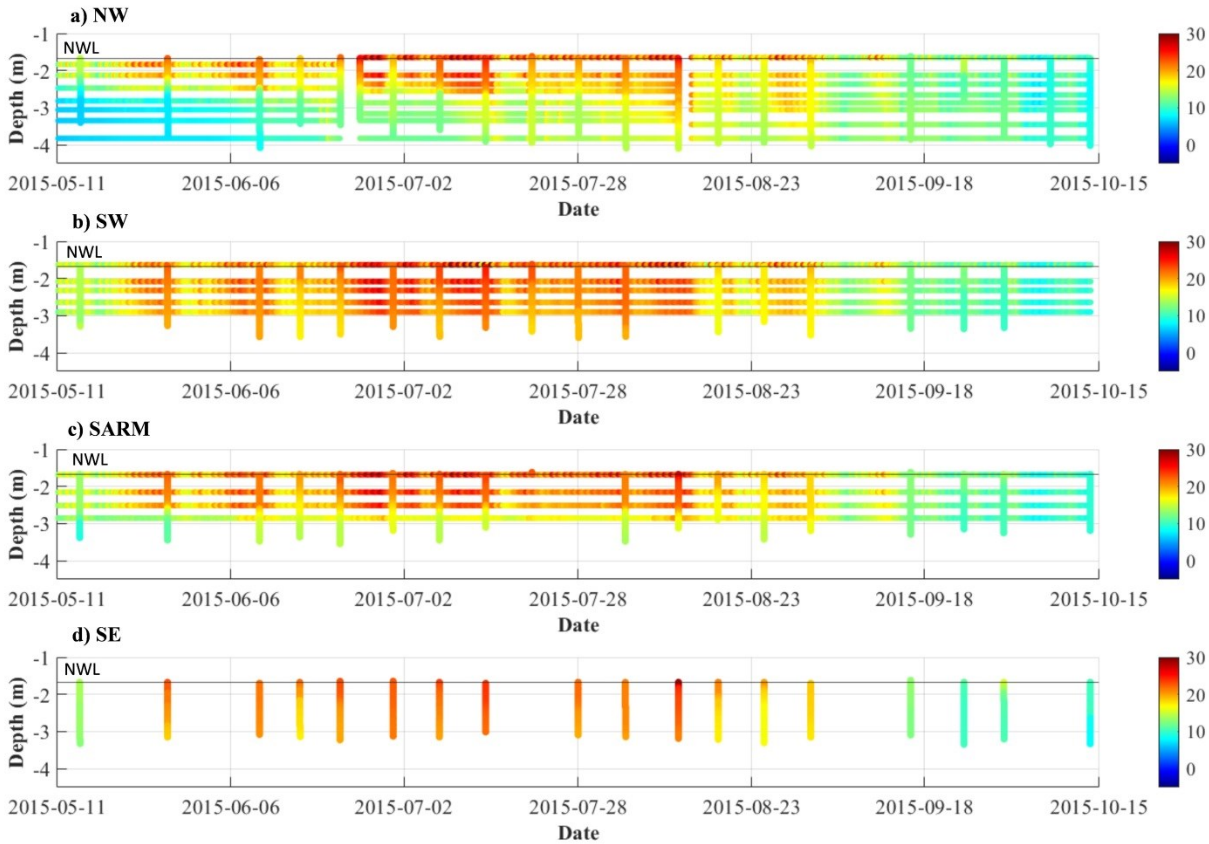

Figure A-14: Measured temperature (°C) at sampling locations within ST2 in 2015.

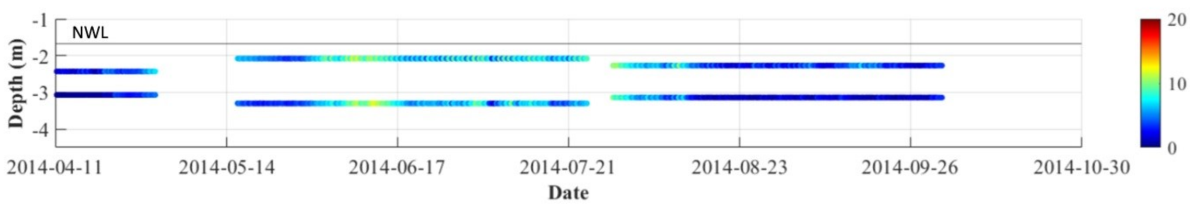

Figure A-15: Measured dissolved oxygen (mg/L) at SE sampling location of ST2 in 2014.

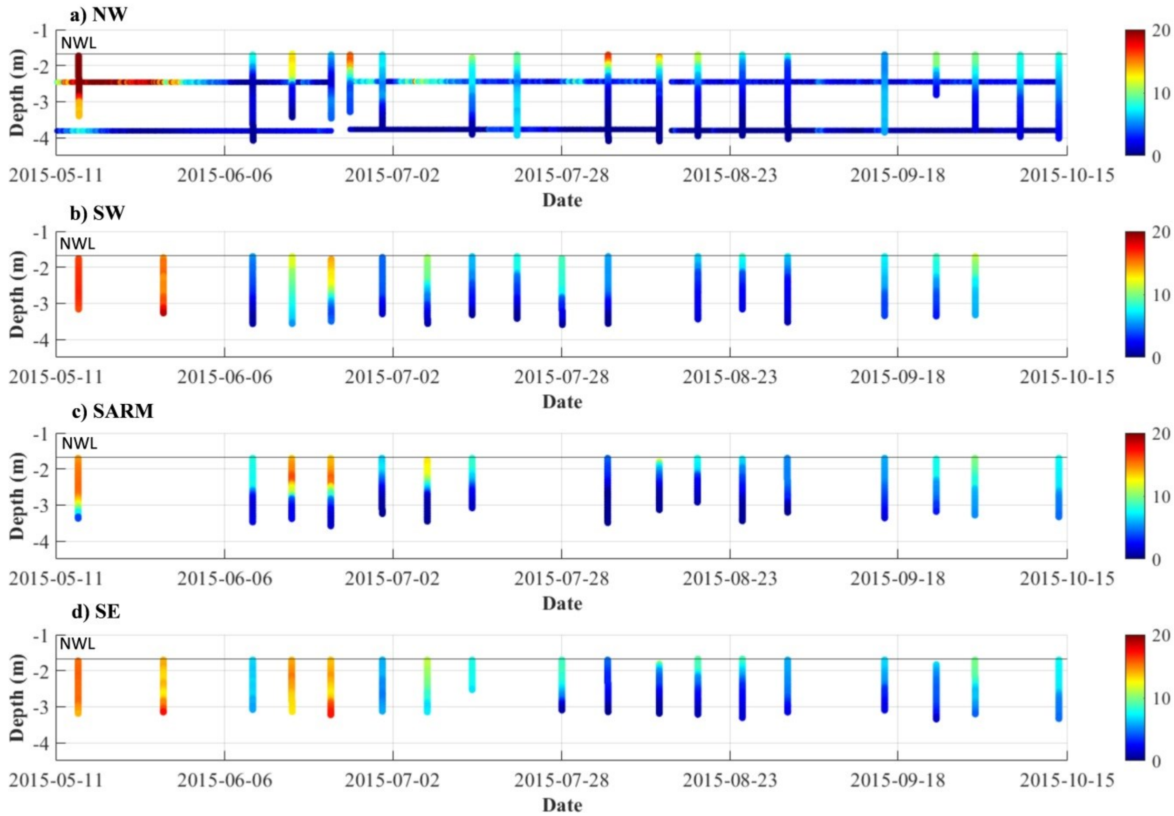

Figure A-16: Measured dissolved oxygen (mg/L) at measuring locations of ST2 in 2015.

In 2014, TCHLA was measured only through water sampling. In 2015, an EXO2 was deployed in the NE location to measure TCHLA every 5 minutes. Depth profiles of TCHLA were measured at all sampling locations in 2015.

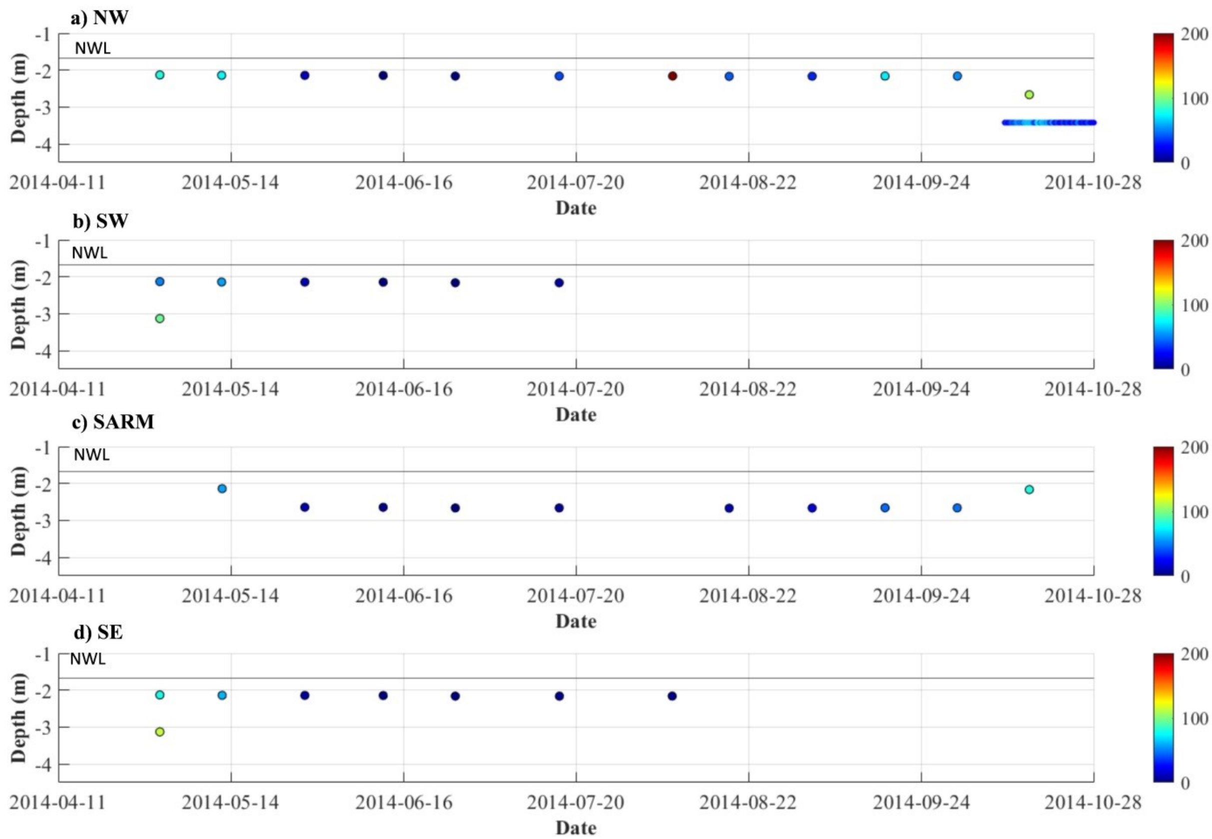

Figure A-17: Measured TCHLA (mcg/L) at measuring locations of ST2 in 2014.

The following figures depict the measured total nitrogen (TN), and total phosphorous (TP) used in the current study. Data were measured by analysing the water quality samples in the BASL

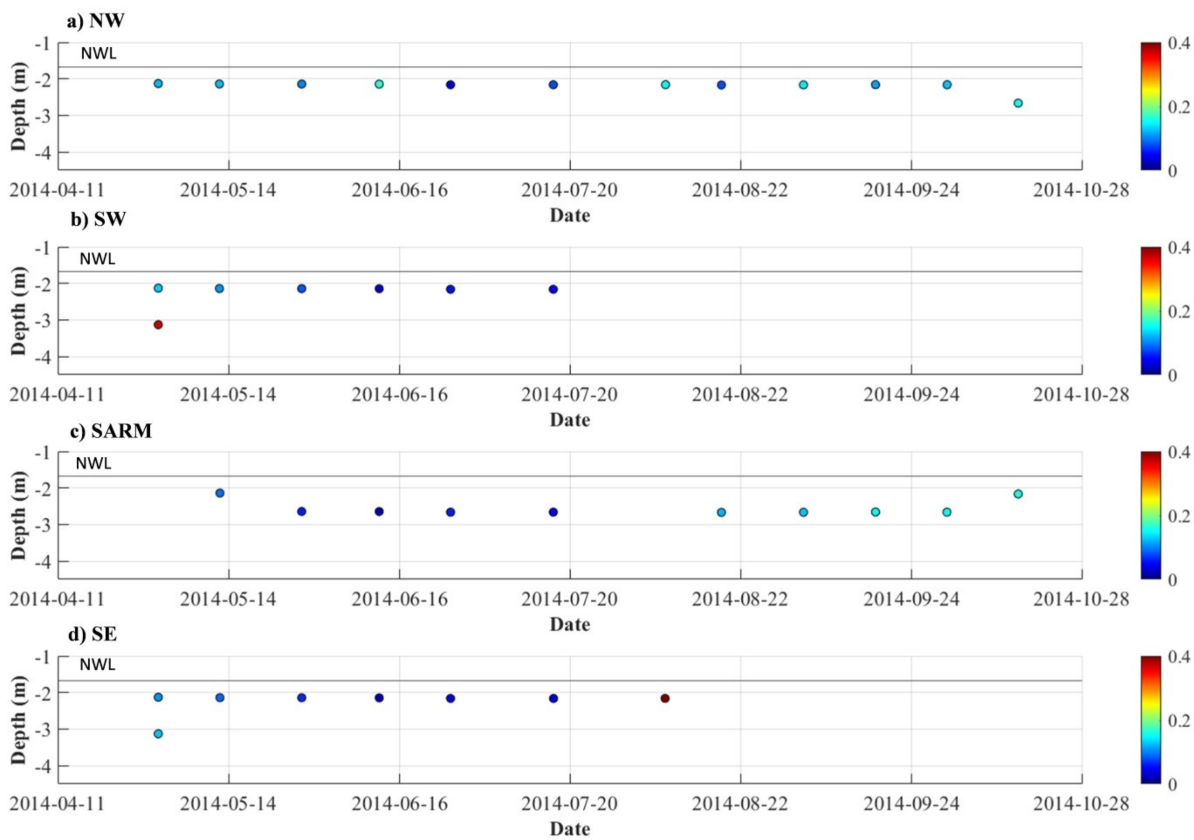

Figure A-18: Measured TP (mg/L) at different locations in ST2 in 2014.

Figure A-19: Measured TP (mg/L) at different locations in ST2 in 2015.

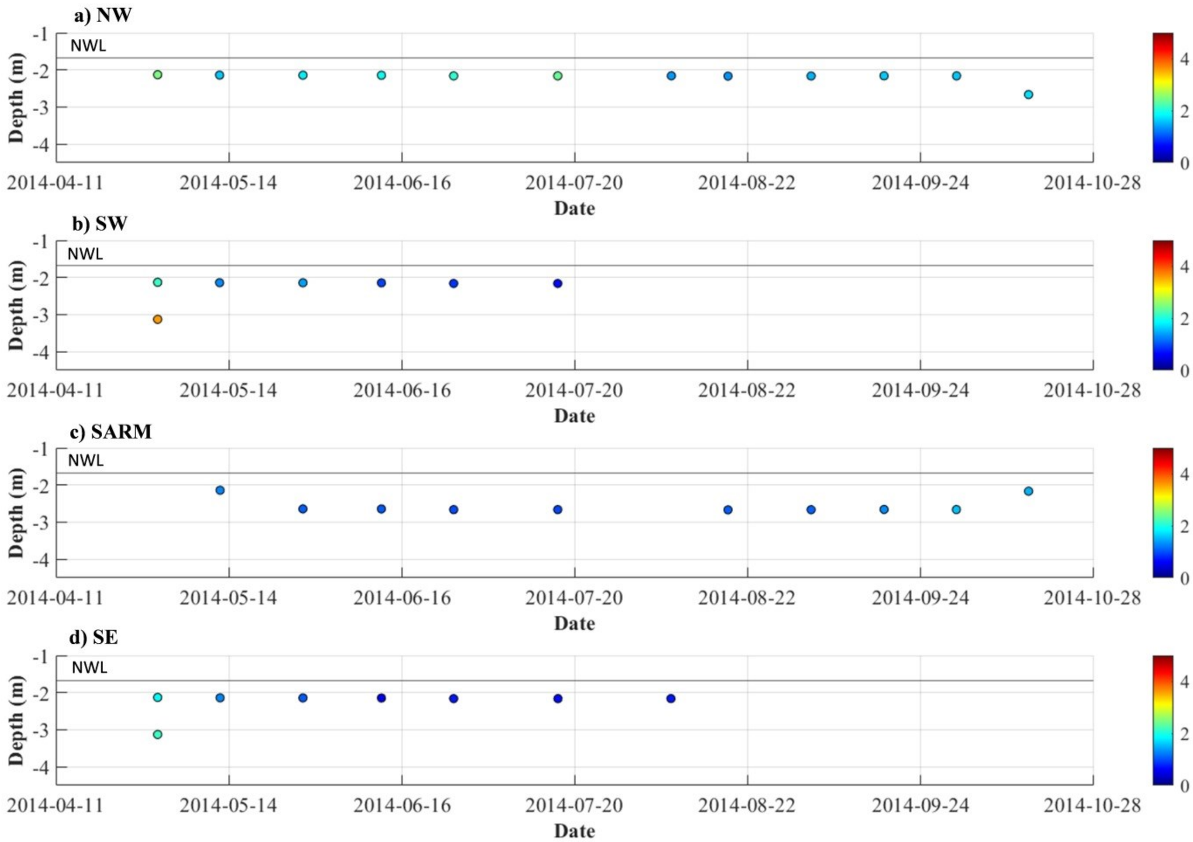

Figure A-20: Measured TN (mg/L) at different locations in ST2 in 2014.

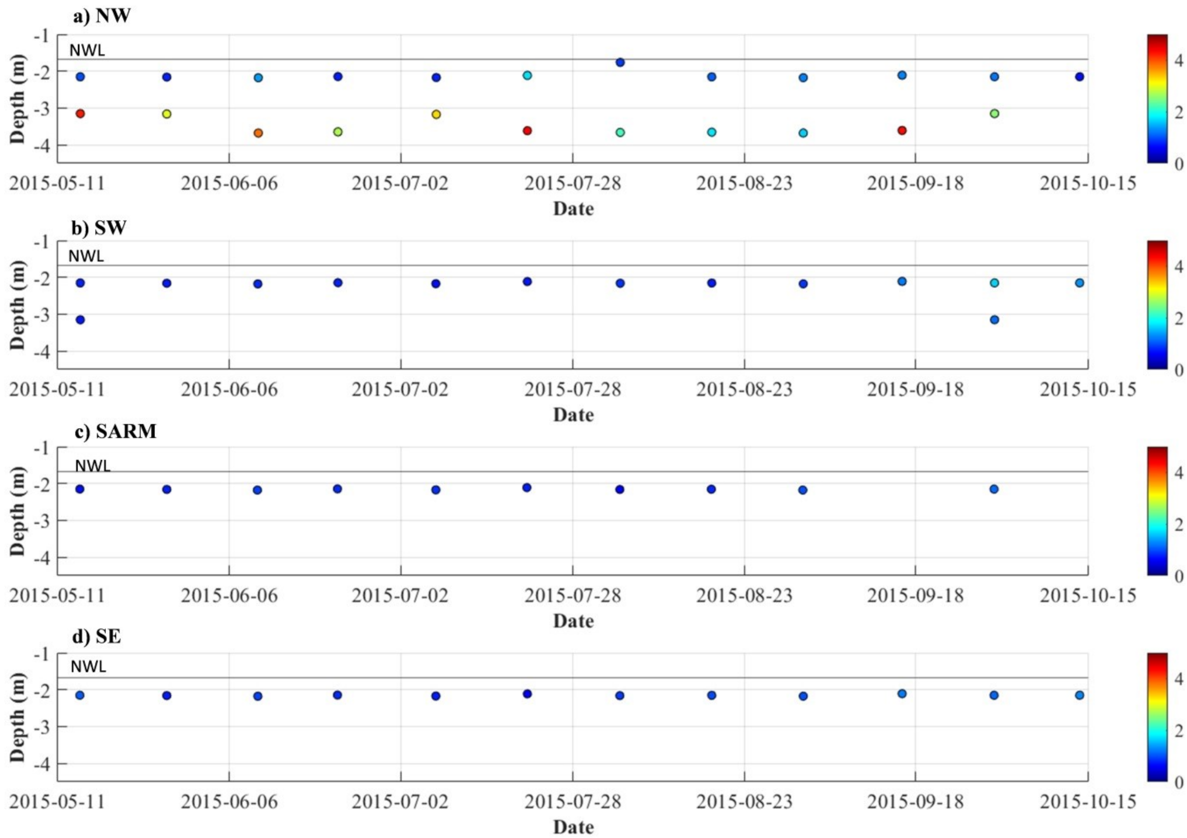

Figure A-21: Measured TN (mg/L) at different locations in ST2 in 2015.

Table A-7: Phylum, Class and Family of algae samples along with the average percentage of each Class in ST2 during sampling periods of 2014 and 2015.

Algae Phylum	Algae Class	Algae Family	ST2 Average Percentage of Algae Class
Chlorophyta	Ulvophyceae	Cladophoraceae	**4.8**
	Chlorophyceae	Chlorosarcinaceae, Characiaceae, Scenedesmaceae, Selenastraceae, Volvocaceae, Neochloridaceae, Hydrodictyaceae,	**28.4**
	Trebouxiophyceae	Chlorellaceae, Oocystaceae	**8.7**
Charophyta	Conjugatophyceae	Desmidiaceae, Closteriaceae, Zygnema	**7.2**
Cyanobacteria	Cyanophyceae	Microcystaceae, Nostocaceae, Rivulari	**22.7**
Euglenozoa	Euglenophyceae	Euglenophyceae	**25.8**
Cryptophyta	Cryptophyceae	Chroomonadaceae	**1.0**
Dinoflagellata	Dinophyceae	Gymnodiniaceae, Gymnodiniaceae	**0.0**
Diatom	Bacillariophyceae	Bacillariophyceae spp	**1.5**

Appendix B. ELCOM-CAEDYM; CALIBRATION, VALIDATION, AND SENSITIVITY ANALYSIS

B.1. EQUATIONS USED IN CAEDYM, ADOPTED FROM BRUCE AND IMBERGER 2009, GAL ET AL. 2009, HIPSEY ET AL. 2013, ROMERO ET AL. 2004.

B.4.1. Generic Parameterization of Processes

The index j denotes the generic variable identifier.

a) Oxygen Dependencies

• $f_j^{DO1}(DO) = \dfrac{DO}{(DO + K_{DO_j})}$

• $f_j^{DO2}(DO) = \dfrac{K_{DO_j}}{(DO + K_{DO_j})}$

$DO =$ Dissolved Oxygen (mg/L)

$K_{DO_j} =$ Half saturation constant of DO for nutrient sediment flux (mg O/L)

b) Temperature dependency

• $f_j^{T_1}(T) = \vartheta_j^{T-20} + \vartheta_j^{c_j(T-a_j)} + b_j$

$\vartheta_j =$ Temperature multiplier

$a_j =$ Constant, $f(\vartheta_j, T_{std}, T_{\max}, c)$,

$b_j =$ Constant, $f(\vartheta_j, T_{std}, a_j, c)$

$c_j =$ Constant, $f(a_j, b_j)$

a_j, b_j, and c_j, solved numiricaly to satisfy following conditions:

$f_j^{T_1}(T) = 1 \quad if\ T = T_{std} = 20$

$f_j^{T_1}(T) = 0 \quad if\ T = T_{\max}$

$\dfrac{\partial f_j^{T_1}(T)}{\partial T} = 0 \quad if\ T = T_{opt}$

• $f_j^{T_2}(T) = \vartheta_j^{T-20}$

c) Dissolved Sediment Flux

$\bullet f_j^{DSF}(T, DO) = \dfrac{S_j}{\Delta z_{bot}} f_S^{T_2}(T) f_j^{DO_1}(DO)$

$S_j =$ Static sediment exchange rate of j from sediment (g m^2/day)

$\Delta z_{bot} =$ Thickness of computational layer adjacent to sedmiment (m)

d) Atmospheric Gas Exchanges

$\bullet f_j^{ATM}(j) = \dfrac{k_j}{\Delta z_{surf}}(j_{ATM} - j_{surf})$

$k_j =$ Transfer coefficient (m/day)

$j_{ATM} =$ Equivalent j concenteration in the air (air-water interface) (mg/L)

$j_{surf} = j$ concenteration in the surface layer (mg/L)

$\Delta z_{surf} =$ Vertical thickness of compoutational surface layer (m)

e) Settling

$\bullet f_j^{SET}(j) = \dfrac{V_{s_j} j}{\Delta z}$

$V_{s_j} =$ Settling Velocity of j (m/day)

$\Delta z =$ Vertical thickness of compoutational layer (m)

f) Mineralization

$\bullet f_j^{DEC}(T, DO, j) = R_{DEC_j} f_j^{T1}(T)\ (f_j^{DO1}) j$

$R_{DEC_j} =$ Mineralization rate of j (1/day)

B.4.2. Nutrient Uptake Functions

- $U_{CO_2}(A_i) = \mu_{\max_i} f_{A_i}^{T_1}(T) \min[(f(I), f(P), f(N)] A_i Y_{C:Chla}$
- $U_{SRP}(A_i) = UP_{\max_i} f_{A_i}^{T_1}(T) \left[\frac{IP_{\max_i} - AIP_i}{IP_{\max_i} - IP_{\min_i}} \frac{SRP}{SRP + K_{P_a}} \right] A_i$
- $U_{NH_4}(A_i) = P_{N_i} UN_{\max_i} f_{A_i}^{T_1}(T) \left[\frac{IN_{\max_i} - AIN_i}{IN_{\max_i} - IN_{\min_i}} \frac{NH_4 + NO_3}{NH_4 + NO_3 + K_{N_a}} \right] A_i$
- $U_{NO_3}(A_i) = (1 - P_{N_i}) UN_{\max_i} f_{A_i}^{T_1}(T) \left[\frac{IN_{\max_i} - AIN_i}{IN_{\max_i} - IN_{\min_i}} \frac{NH_4 + NO_3}{NH_4 + NO_3 + K_{N_a}} \right] A_i$

Where

- $f(I) = 1 - \exp(-\frac{1}{I_{ka}})$
- $f(N) = \frac{IN_{\max_i}}{IN_{\max_i} - IN_{\min_i}} \left[1 - \frac{IN_{\min_i}}{AIN_i} \right]$
- $f(P) = \frac{IP_{\max_i}}{IP_{\max_i} - IP_{\min_i}} \left[1 - \frac{IP_{\min_i}}{AIP_i} \right]$
- $P_{N_i} = \left[\frac{NH_4\, NO_3}{(NH_4 + K_{N_a})(NO_3 + K_{N_a})} \right] \left[\frac{NH_4\, K_{N_a}}{(NH_4 + NO_3)(NO_3 + K_{N_a})} \right]$

A_i = Algae concenteration $\left(\text{mg Chla}/\text{m}^3\right)$
i = Index of algae group (in this study, i=1 to 3)
U_{CO_2} = Algae CO_2 uptake function
U_{SRP} = Algae SRP uptake function
U_{NH_4} = Algae NH_4 uptake function
U_{NO_3} = Algae NO_3 uptake function
$\mu_{\max_i}$ = Maximum growth rates of algae (1/day)
$UP_{\max_i}$ = Maximum phosphorus uptake rate $\left(\text{mg P}/\left(\text{mg Chla}\right)/\text{day}\right)$
$IP_{\max_i}$ = Maximum internal phosphorus concentration $\left(\text{mg P}/\left(\text{mg Chla}\right)\right)$
AIP_i = Internal phosphorus concentration $\left(\text{mg P}/\left(\text{mg Chla}\right)\right)$
$IP_{\min_i}$ = Minimum internal phosphorus concentration $\left(\text{mg P}/\left(\text{mg Chla}\right)\right)$
K_{P_a} = Half saturation constant for phosphorus uptake $\left(\text{mg}/\text{L}\right)$
$UN_{\max_i}$ = Maximum nitrogen uptake rate $\left(\text{mg P}/\left(\text{mg Chla}\right)/\text{day}\right)$
$IN_{\max_i}$ = Maximum internal nitrogen concentration $\left(\text{mg P}/\left(\text{mg Chla}\right)\right)$
AIN_i = Internal nitrogen concentration $\left(\text{mg P}/\left(\text{mg Chla}\right)\right)$
$IN_{\min_i}$ = Minimum internal nitrogen concentration $\left(\text{mg P}/\left(\text{mg Chla}\right)\right)$
K_{N_a} = Half saturation constant for nitrogen uptake $\left(\text{mg}/\text{L}\right)$

B.4.3. Respiration, Mortality, and Excretion

$R_{CO_2}(A_i) = f_{res_i}\, k_{r_i}\, f_{A_i}^{T_2}(T)\, A_i - k_{pr}\, U_{CO_2}(A_i)$

$\bullet E_{DOC}(A_i) = f_{DOM_i}\, k_{r_i}\left[(1 - f_{res_i})\, f_{A_i}^{T_2}(T)\right] A_i$

$\bullet E_{POC}(A_i) = (1 - f_{DOM_i})\, k_{r_i}\left[(1 - f_{res_i})\, f_{A_i}^{T_2}(T)\right] A_i$

$\bullet E_{DOP}(A_i) = f_{DOM_i}\, k_{r_i}\left[\, f_{A_i}^{T_2}(T)\right] AIP_i$

$\bullet E_{POC}(A_i) = (1 - f_{DOM_i})\, k_{r_i}\left[\, f_{A_i}^{T_2}(T)\right] AIP_i$

$\bullet E_{DOP}(A_i) = f_{DOM_i}\, k_{r_i}\left[\, f_{A_i}^{T_2}(T)\right] AIN_i$

$\bullet E_{POC}(A_i) = (1 - f_{DOM_i})\, k_{r_i}\left[\, f_{A_i}^{T_2}(T)\right] AIN_i$

f_{res_i} = Fraction of respiration of algae relative to total metabolic loss

k_{r_i} = Metabolic loss rate coefficient (1/day)

$k_{pr} = 0.14$

f_{DOM_i} = Fraction of metabolic loss that goes to DOM

B.2. Differential Equations for Mass Balance of Dissolved Oxygen, Phosphorous, and Nitrogen

It should be noted that all concentrations are subjected to hydrodynamics.

a) Dissolved Oxygen

$$\bullet\ \frac{\partial DO}{\partial t} = \underbrace{f_{DO}^{ATM}}_{\text{Atmospheric Flux}} - \underbrace{S_{SOD} f_{SOD}^{DO_1}(DO)\, f_{SED}^{T_2}(T)}_{\text{Sediment Oxygen Demand}} - \underbrace{\cdots}_{\text{Nitrification}}$$

$$- \underbrace{\cdots}_{\text{mineralization}} + \underbrace{\sum^{N_A} \left[\mu_i (1 - k_p) - k_{ri} f_A^{T_2}(T) \right] Y_{O:C} Y_{C:Chla} A_i}_{\text{Algae consumption/production}}$$

S_{SOD} = Static DO consumption by sediment (g/m^2/day)

k_{nit} = Maximum nitrification rate under oxygen saturationat at 20 °C (1/day)

$Y_{O:N}$ =Stiochiometric ratio of DO to N during nitrification (g DO/ (g N))

$Y_{O:C}$ =Stiochiometric ratio of DO to C (g DO/ (g C))

$Y_{C:Chla}$ =Stiochiometric ratio of C to Chla (g C/ (g Chla))

$R_{DEC_{DOC}}$ = Mineralization rate for DOC (1/day)

μ_i = Algae growth (1/day)

k_p = Rate of photorespiration (1/day)

k_{ri} =Algal loss ratee due to respiration, mortality, and excretion (1/day)

A_i = Concentration of the i^{th} algal group (g/m^3)

b) Phosphorous

$$\bullet\ \frac{\partial SRP}{\partial t} = \underbrace{\cdots}_{\text{mineralization (bact-P)}} - \underbrace{\sum^{N_A} U_{SRP}(A_i)}_{\text{Algae Uptake}} + \underbrace{\cdots}_{\text{Sediment Flux}} \underbrace{\cdots}_{\text{Adsorption and Desorption}}$$

$$\bullet\ \frac{\partial DOP}{\partial t} = \underbrace{\cdots}_{\text{Decomposition}} \underbrace{\cdots}_{\text{mineralization (bact-P)}} \underbrace{\cdots}_{\text{Sediment Flux}} \underbrace{\sum^{N_A} E_{DOP}(A_i)}_{\text{Biological Mortality and Excretion}}$$

$$\bullet\ \frac{\partial POP}{\partial t} = -\underbrace{\cdots}_{\text{Decomposition}} \underbrace{\cdots}_{\text{Settling}} \underbrace{\sum^{N_A} E_{POP}(A_i)}_{\text{Biological Mortality and Excretion}}$$

$$\bullet\ \frac{\partial PIP}{\partial t} = -\underbrace{\cdots}_{\text{Adsorption and Desorption}} \underbrace{\cdots}_{\text{Settling}}$$

c) Nitrogen

$$\bullet \frac{\partial NH_4}{\partial t} = \ldots \sum^{N_A} U_{NH}(A_i) + \ldots$$

$$\ldots - \ldots$$

where ko_{NH_4} = Nitrification rate (1/day)

$$\bullet \frac{\partial NO_3}{\partial t} = \ldots \sum^{N_A} U_{NO}(A_i) - \ldots$$

where ko_{NH_4} = Denitrification rate (1/day)

$$\bullet \frac{\partial DON}{\partial t} = \ldots$$

$$\sum^{N_A} E_{DON}(A_i)$$

Biological Mortality and Excretion

$$\bullet \frac{\partial PON}{\partial t} = - \ldots \sum^{N_A} E_{PON}(A_i)$$

Biological Mortality and Excretion

$$\bullet \frac{\partial PIN}{\partial t} = - \ldots$$

B.3. Estimation of State variables

Table B-1: Estimated mandatory state variables used in CAEDYM.

CAEDYM State Variable	Estimated value based on measured data
DOPL	$TDP - PO_4$
POPL	$(0.6-0.8)\times(TPP)-AIP$
PIP	$TPP-POPL$
AIP	$C:Chla\ 50:1;\ C:P\ (41000-77000)$
DONL	$\frac{2}{3}\times(TKN-NH4-PIN)$
PONL	$\frac{1}{3}\times(TKN-NH4-PIN)$
Algae group	Measured percentage × Chla

Adopted from (Nakhaei 2017)

B.4. ELCOM-CAEDYM, MODEL SETUP AND RESULTS

B.4.1. Computational Domain

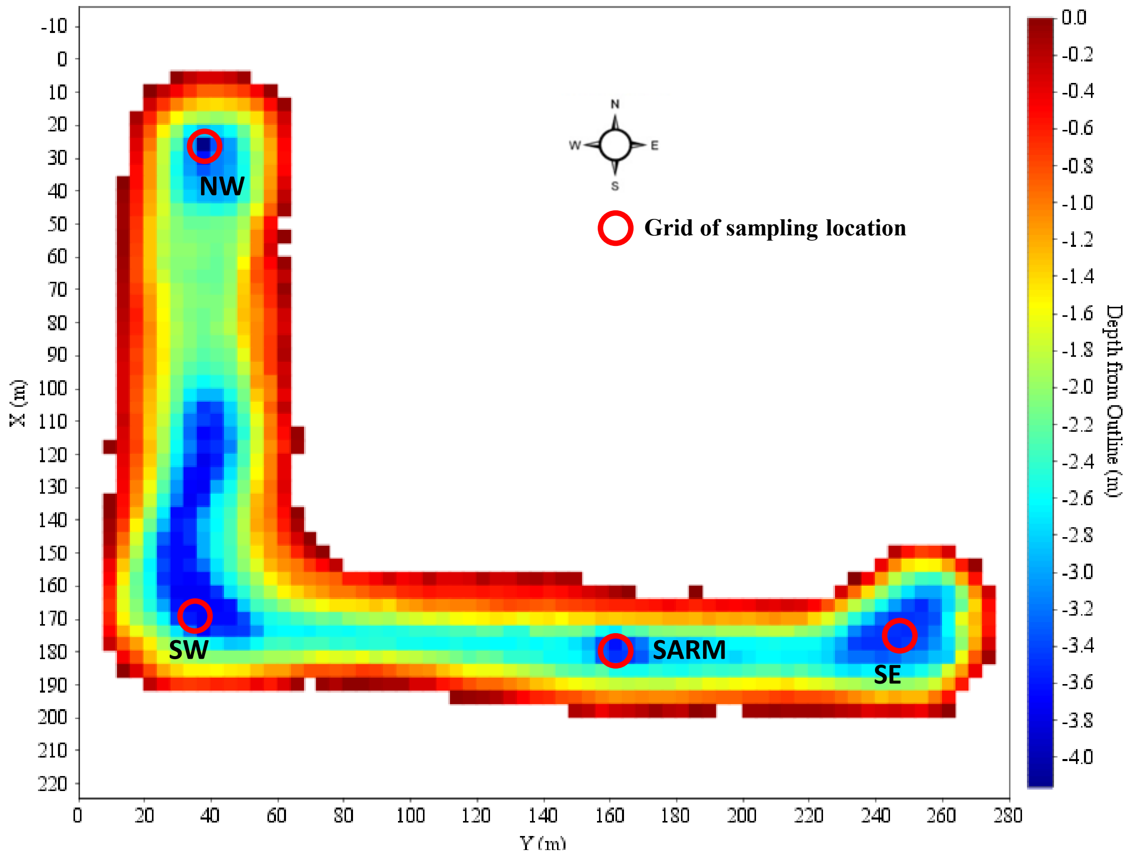

Figure B-1: Computational domain of ST2 used in ELCOM-CAEDYM

B.4.2. **ELCOM Sensitivity**

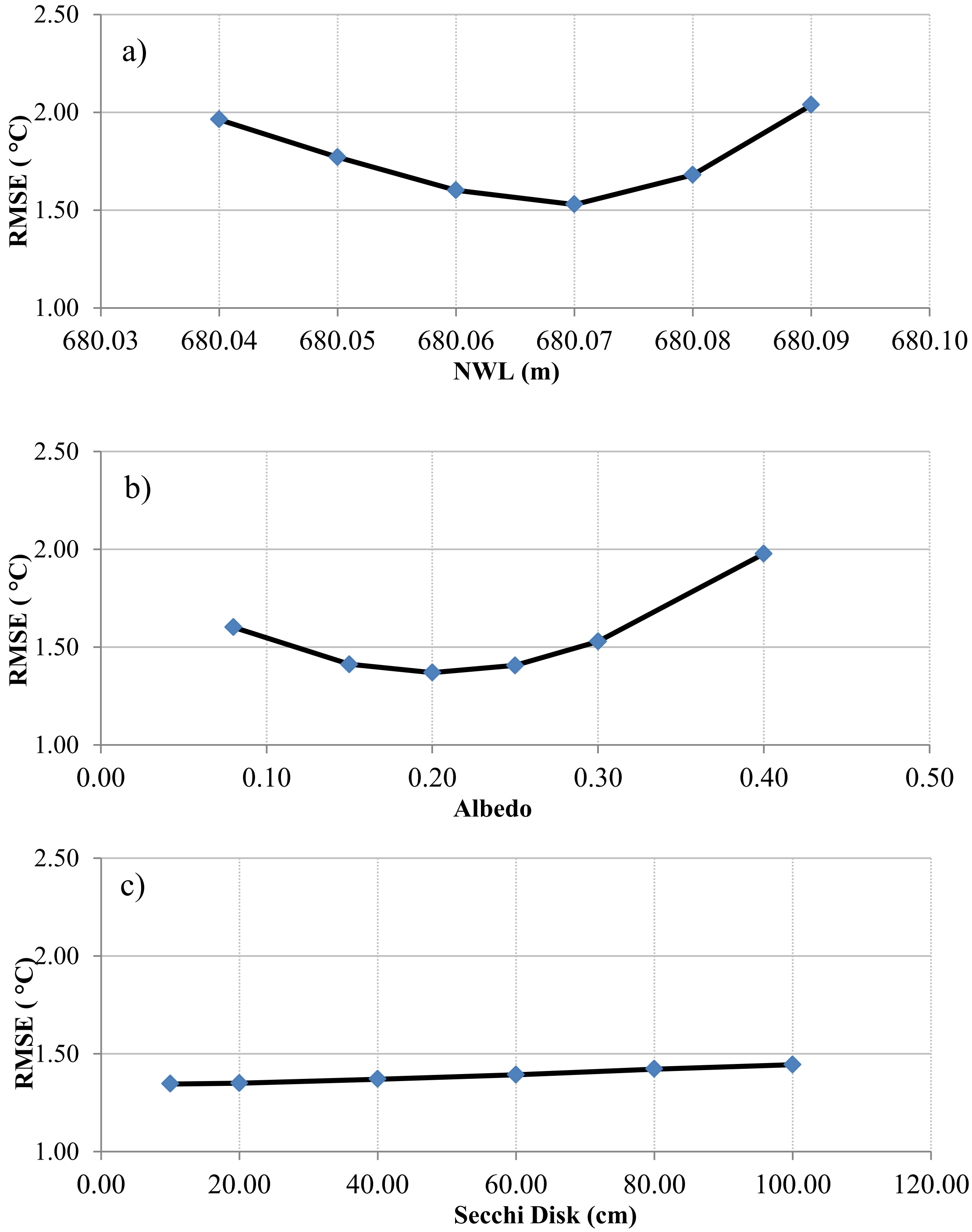

Figure B-2: Variation of RMSE (°C) of modelled temperature by ELCOM during calibration period with: a) NWL (m), when albedo=0.30 and Secchi disk=40 cm, b) albedo, when NWL=680.07 m and Secchi disk=40 cm, and c) Secchi disk, when albedo=0.20 and NWL=680.07 m.

B.4.3. Visual Assessment of ELCOM Performance

Here the modelled temperature for calibration and validation runs are presented for selected locations and the results are compared with those measured. For calibration and validation runs, the visual assessment was conducted by comparing the modeled temperature versus all measurements acquired by both deployed sensors and profiling.

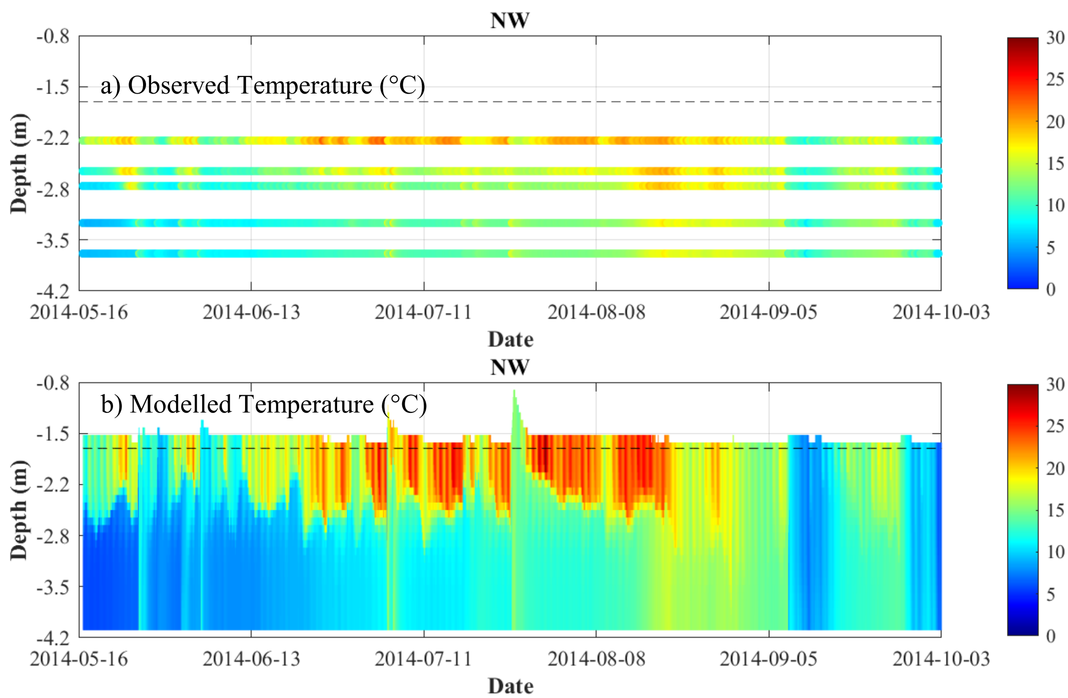

Figure B-3: Visual comparison of a) observed, and b) modelled temperature (°C) at NW sampling location of ST2 during calibration period (2014).

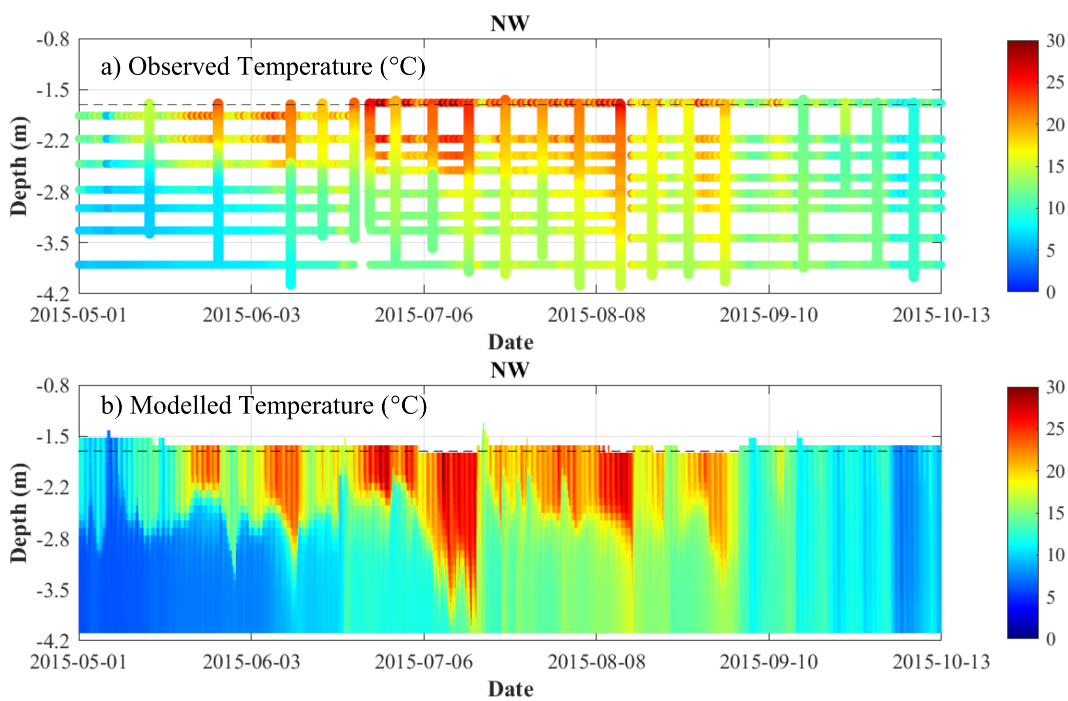

Figure B-4: Visual comparison of: a) observed, and b) modelled temperature (°C) at NW sampling location of ST2 during validation period (2015).

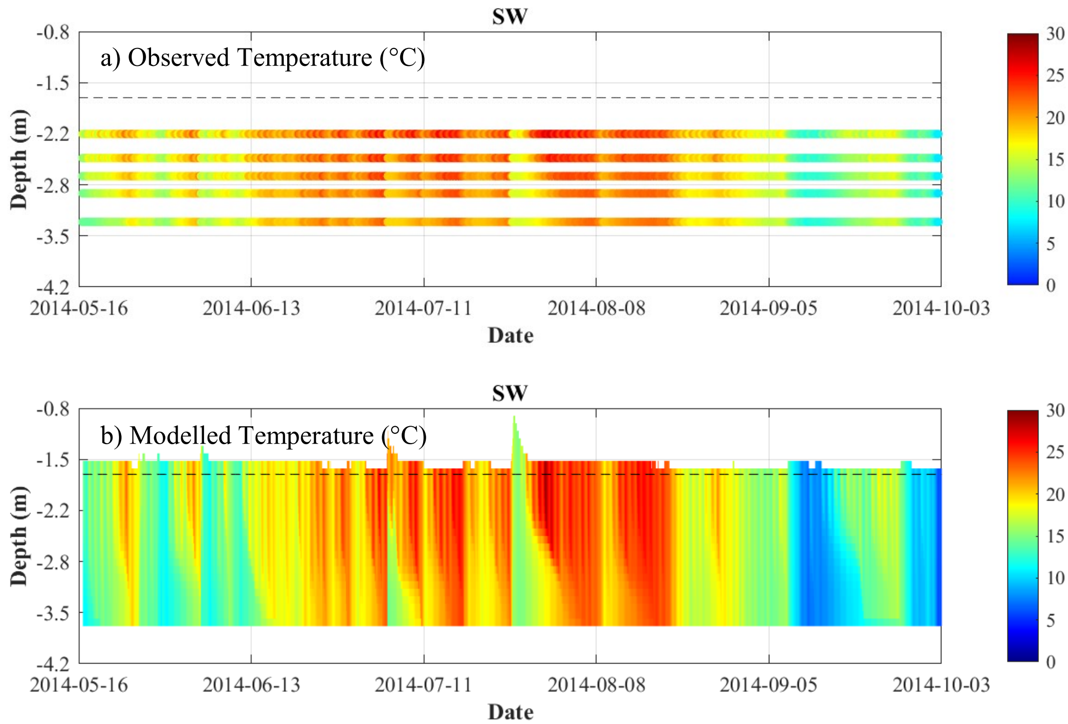

Figure B-5: Visual comparison of a) observed, and b) modelled temperature (°C) at NW sampling location of ST2 during calibration period (2014).

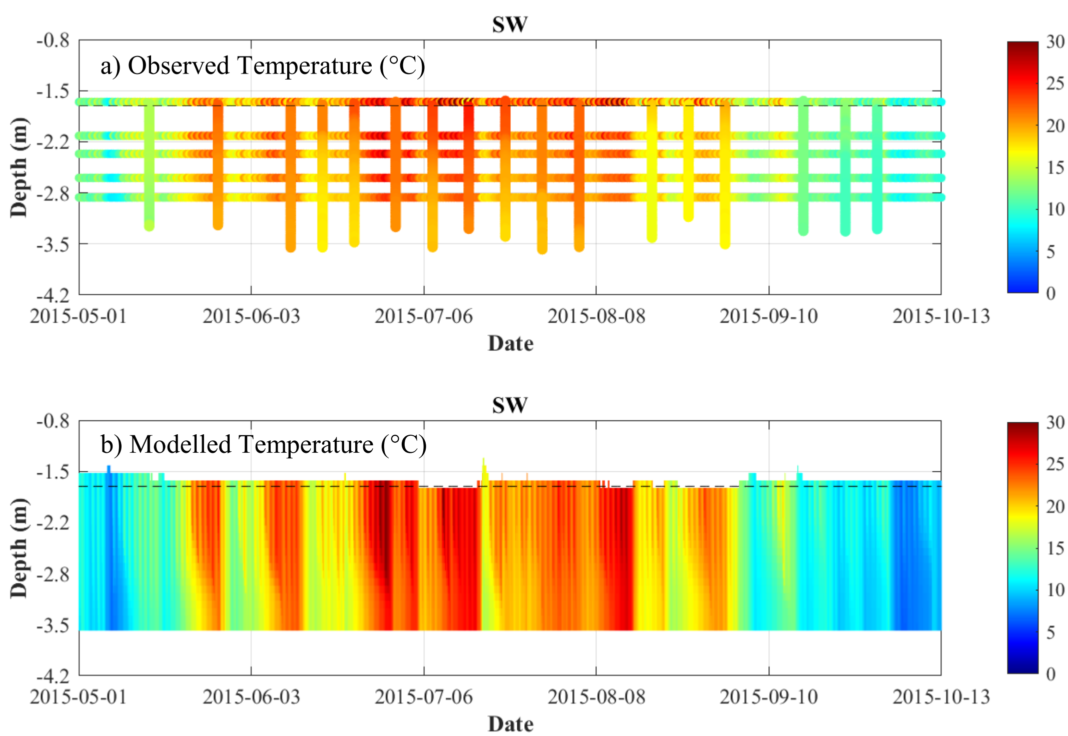

Figure B-6: Visual comparison of: a) observed, and b) modelled temperature (°C) at SW sampling location of ST2 during validation period (2015).

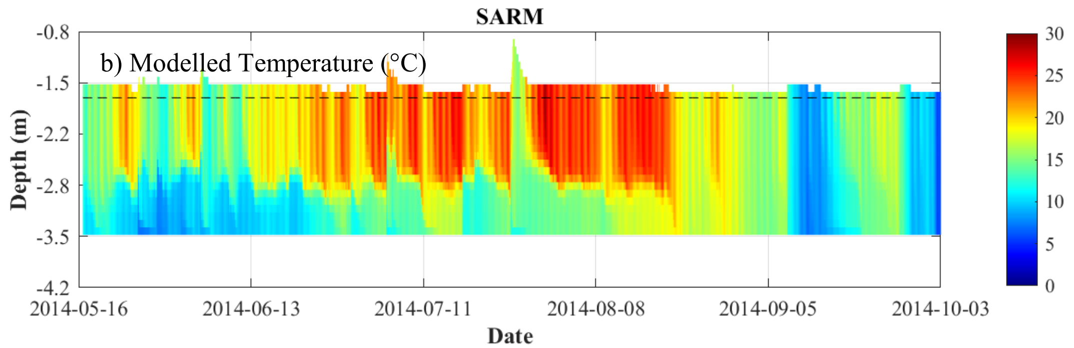

Figure B-7: Visual assessment of modelled temperature at SW sampling station of ST2 during calibration period (2014). No measurement at this location during calibration period.

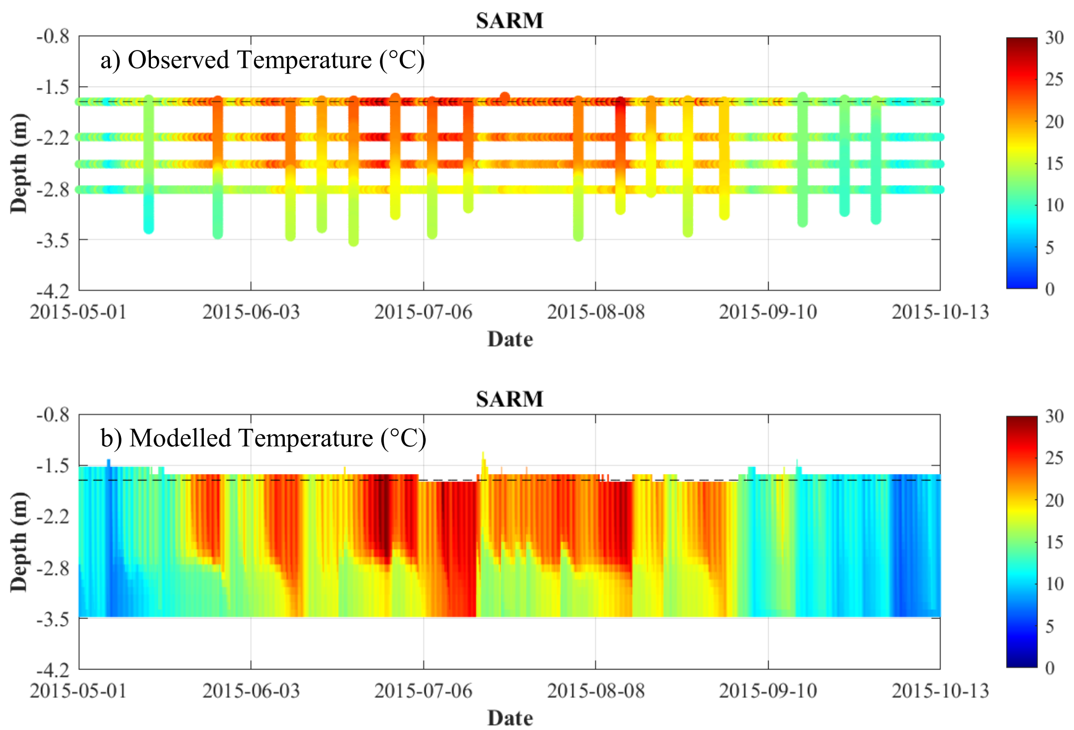

Figure B-8: Visual comparison of: a) observed, and b) modelled temperature (°C) at SARM sampling location of ST2 during validation period (2015).

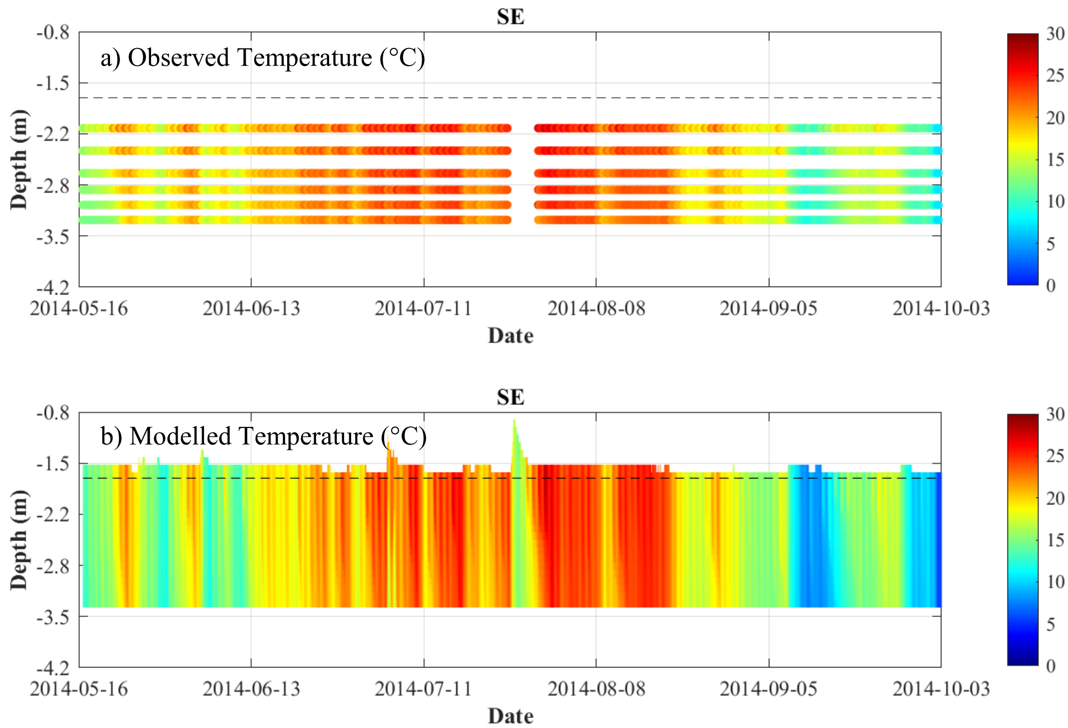

Figure B-9: Visual comparison of a) observed, and b) modelled temperature (°C) at SE sampling location of ST2 during calibration period (2014).

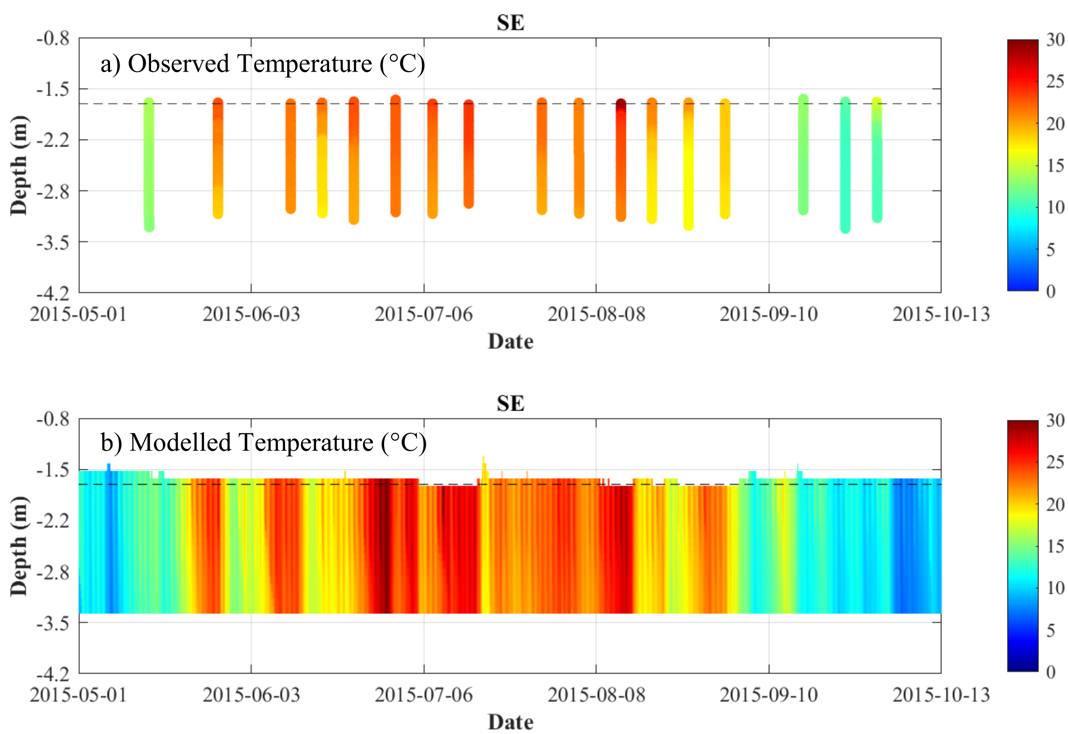

Figure B-10: Visual comparison of a) observed, and b) modelled temperature (°C) at SE sampling location of ST2 during calibration period (2014).

B.4.4. **Assessment of CAEDYM Performance**

3.2.2.1 Total Nitrogen

Figure B-11 and Figure B-12 display scatter plots of measured and simulated TN during the calibration period. The overlaid continuous time series are the simulated TN at the average measurement depths. During calibration period, the average RMSE at NW, 1.22 mg/L, was lower than at other sampling locations (Table 4-6). The model performed well near the bed with an RMSE of 0.49 mg/L, compared to 1.65 mg/L near the surface. The improved agreement near the bed is mainly due to the influence of boundary conditions assigned based on the near-bed measurements

Figure B-13 shows that during the validation period, CAEDYM's performance significantly improved at all sampling locations, with an average RMSE of 0.47 mg/L compared to 1.42 mg/L in the calibration period (Table 4-6). It should be noted that the inconsistency of boundary condition assignment also has affected the simulation results and the statistics.

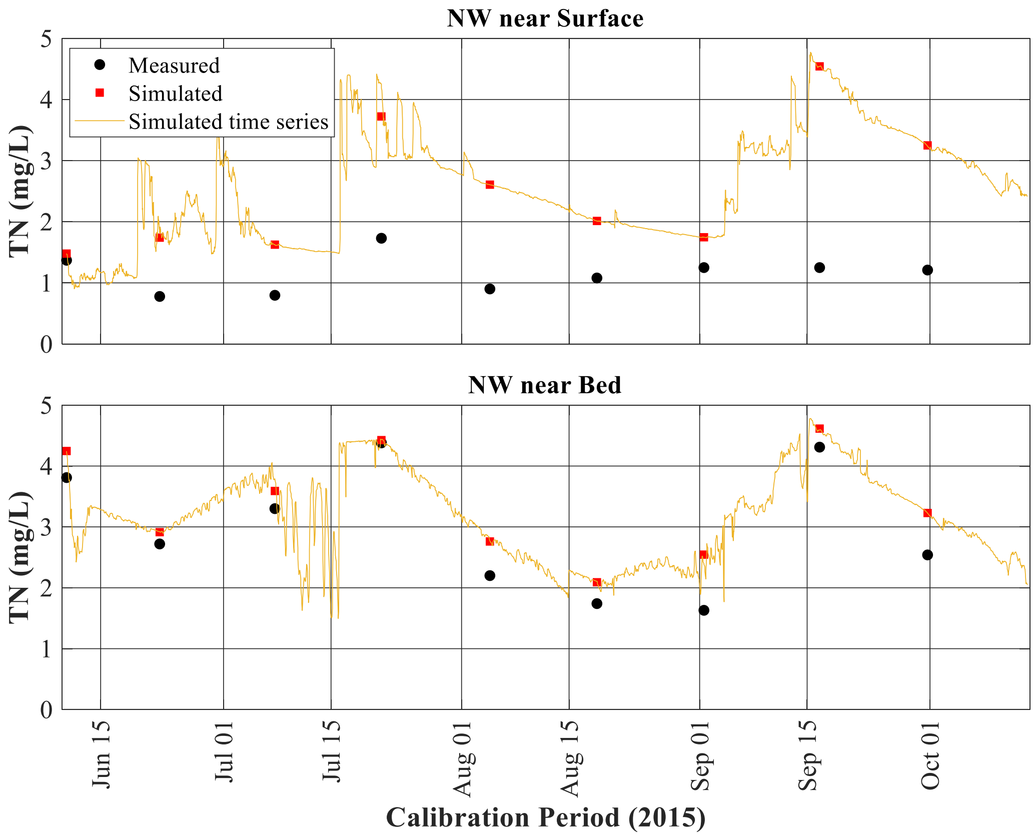

Figure B-11: Measured and simulated TN at NW near surface (top) and near bed (bottom) during calibration period.

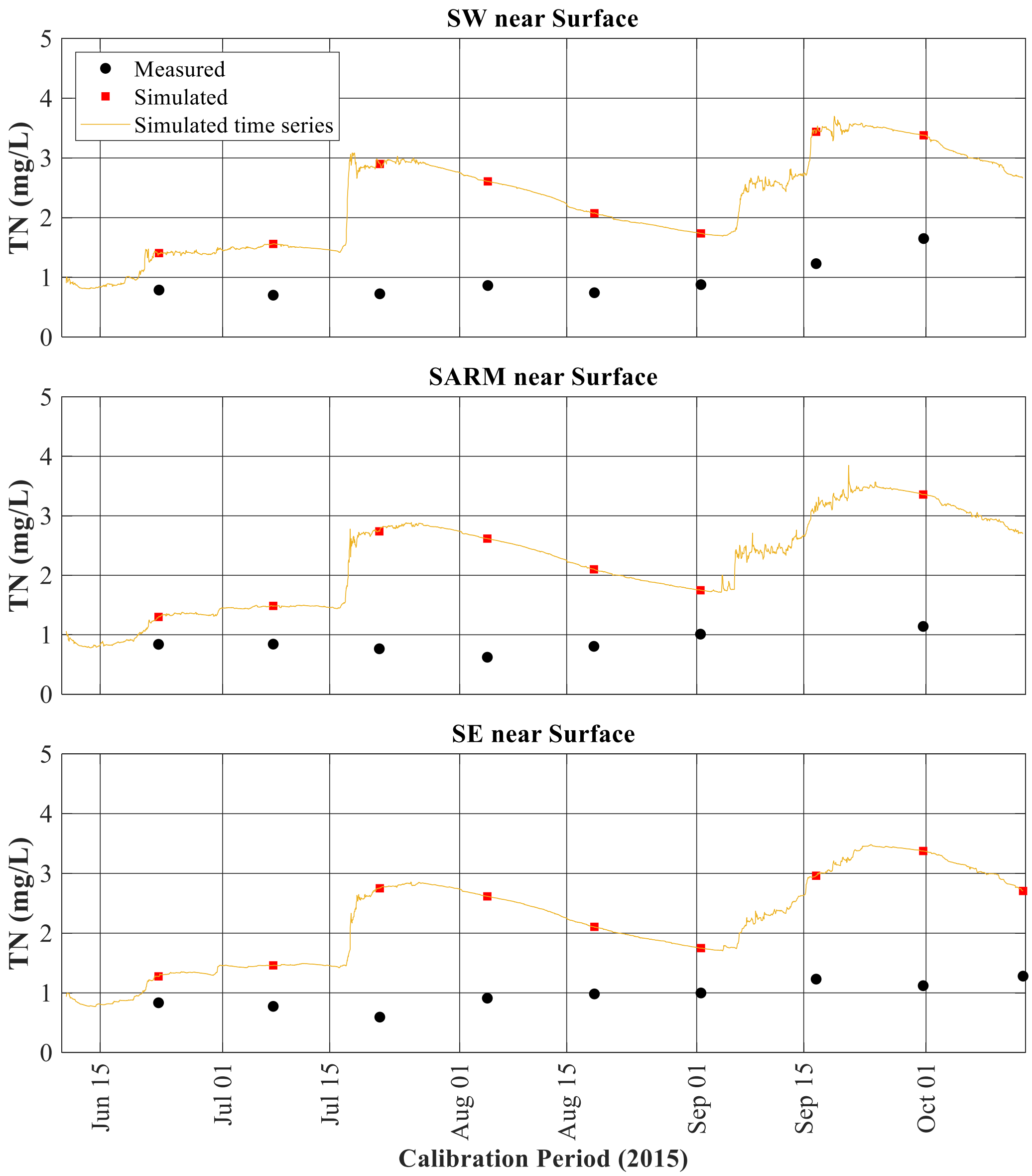

Figure B-12: Measured and simulated TN at near surface of SW (top) SARM (middle), and SE (bottom) during calibration period.

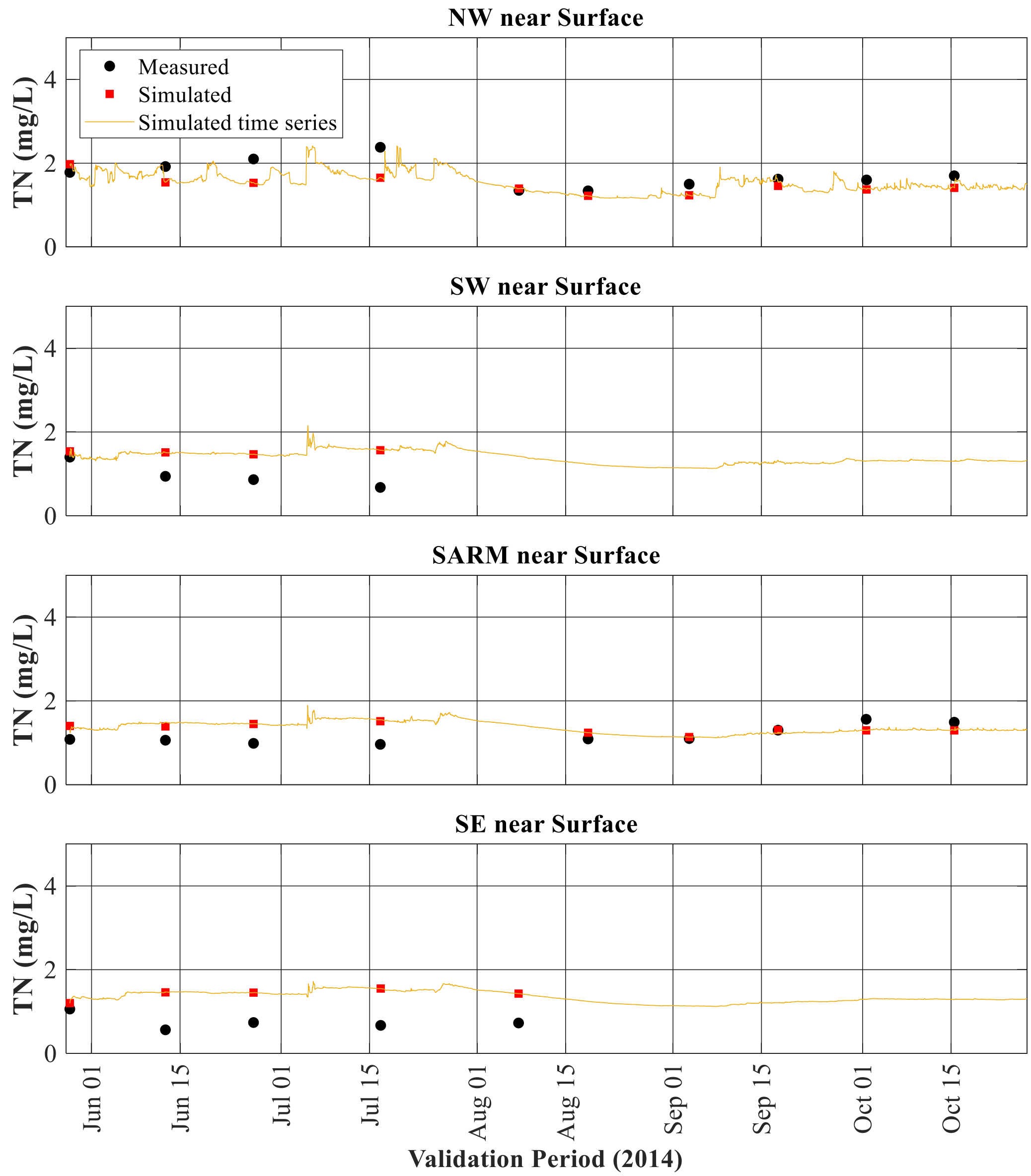

Figure B-13: Measured and simulated TN during calibration period at sampling location.

3.2.2.1 Total Phosphorous

As discussed in Chapter 4 During calibration period, especially from early August to early September 2015, CAEDYM underestimated near surface TP across all the sampling locations. Here the measured and simulated TP at SW, SARM, and SE sampling locations are presented

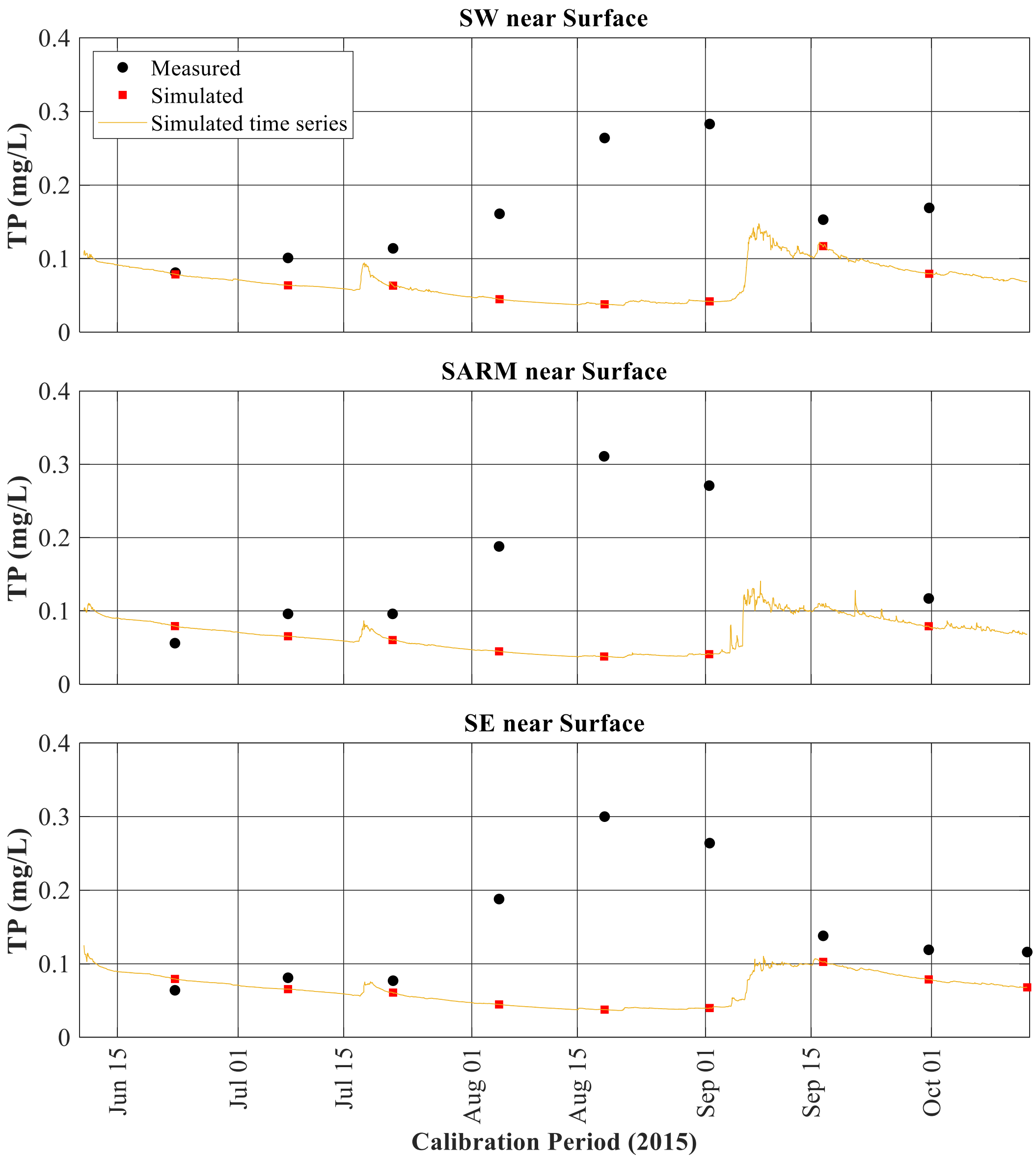

Figure B-14: Comparison of observed and simulated TP at SW (top), SARM (middle), and SE (bottom) during calibration period.

The simulated TP during validation period at sampling locations is presented in Figure B-15

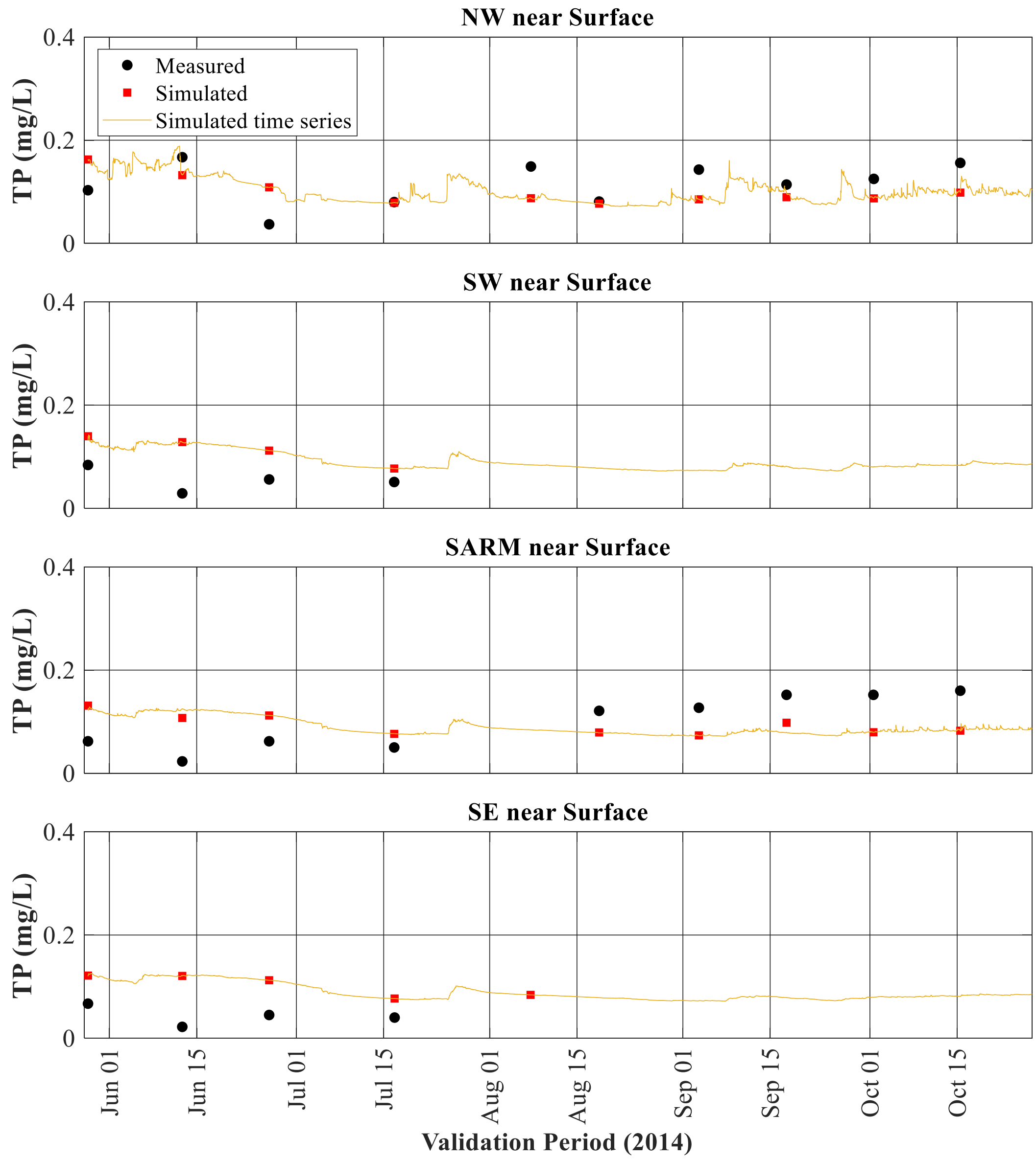

Figure B-15: Comparison of observed and simulated TP at sampling locations during validation period.

3.2.2.1 Dissolved Oxygen

Figure B-16 to Figure B-19 compare measured and simulated dissolved oxygen (DO) at all sampling locations during the calibration period, illustrating differences between the two datasets. DO measurements by deployed instruments were more reliable as the instruments were consistently calibrated before deployment. Furthermore, the measured DO was within a reasonable range (less than 15 mg/L). Therefore, only deployed measurements were used for quantitative assessment (Table 4-6). However, for visual assessment, when available, both datasets were considered (Figure B-16 to Figure B-19), indicating that CAEDYM captured DO variation with depth in all the sampling locations. Higher DO near the surface and lower DO near the bed were well represented by CAEDYM, particularly at the NW sampling location, where more stratification was presented.

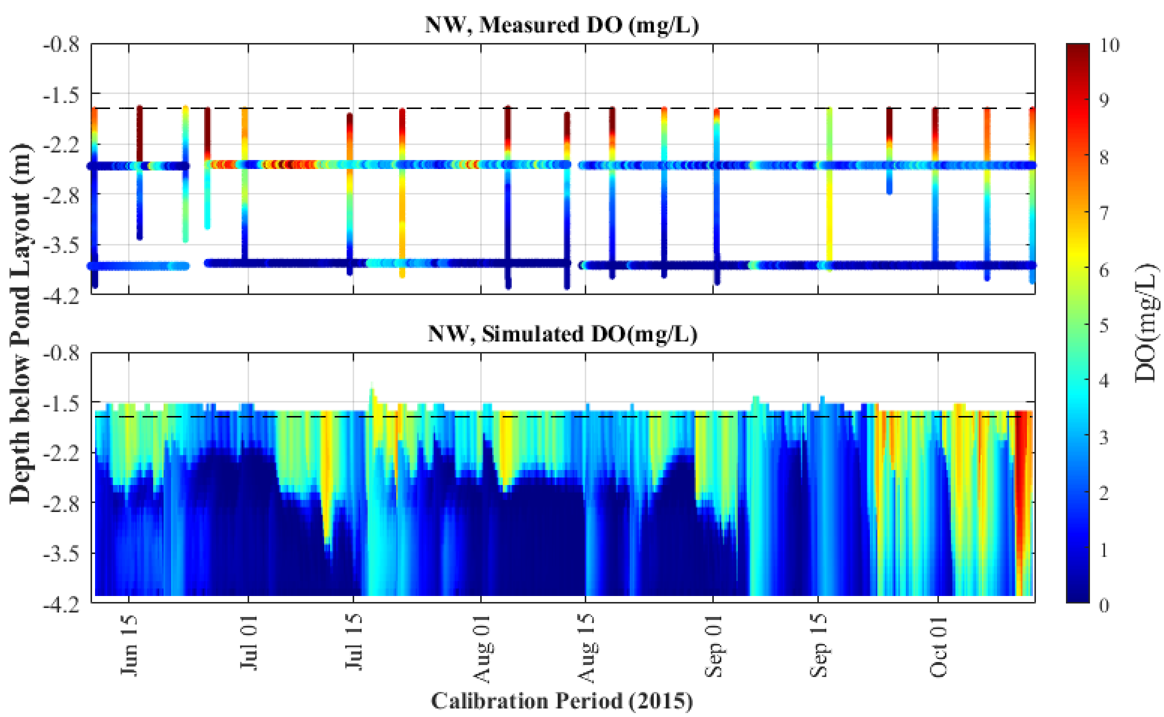

Figure B-16: Measured and simulated DO at NW sampling location during calibration period (2015).

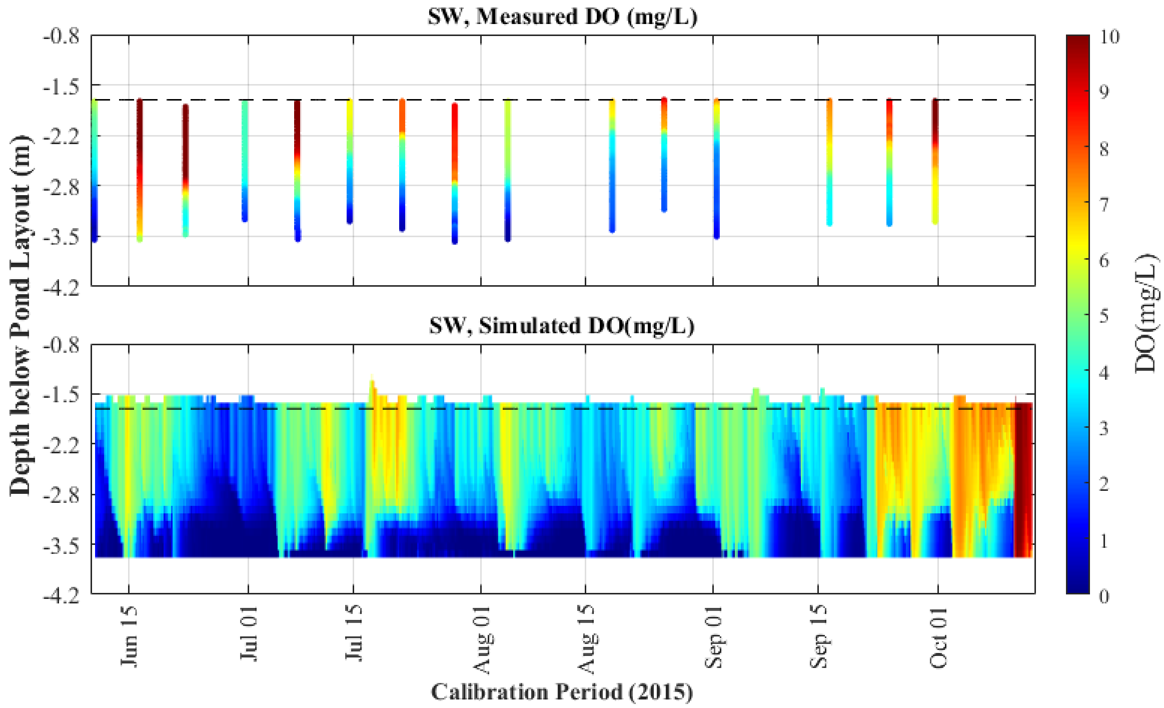

Figure B-17: Measured and simulated DO at SW sampling location during calibration period (2015).

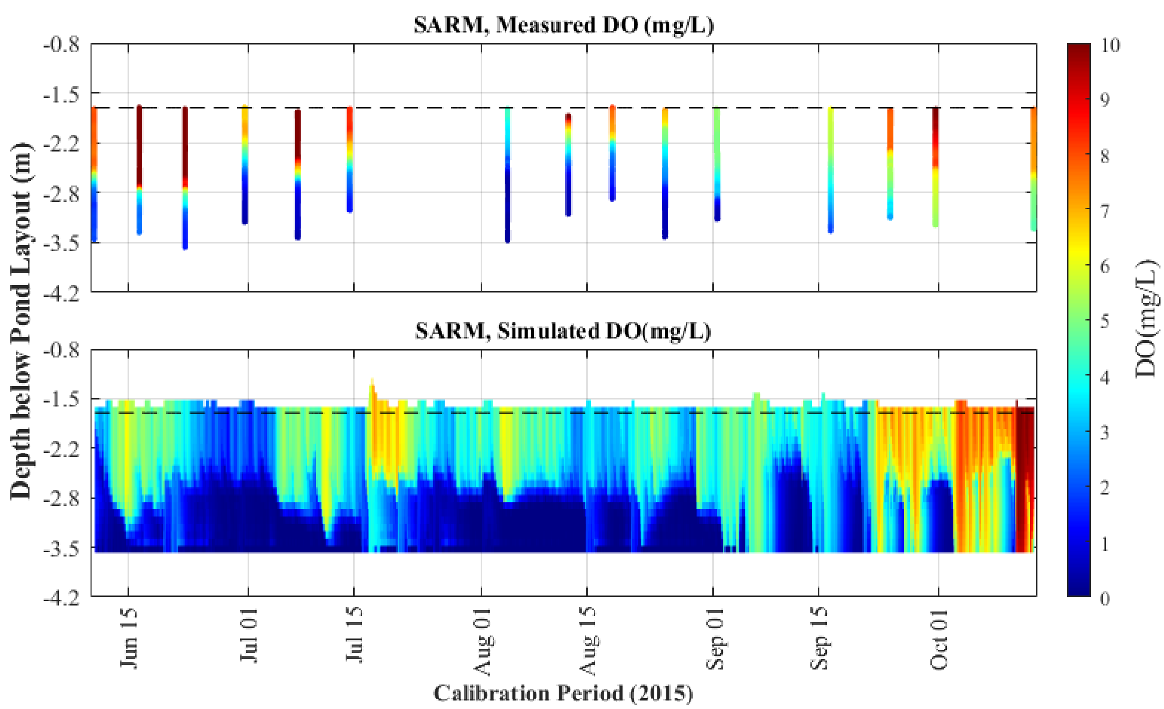

Figure B-18: Measured and simulated DO at SARM sampling location during calibration period (2015).

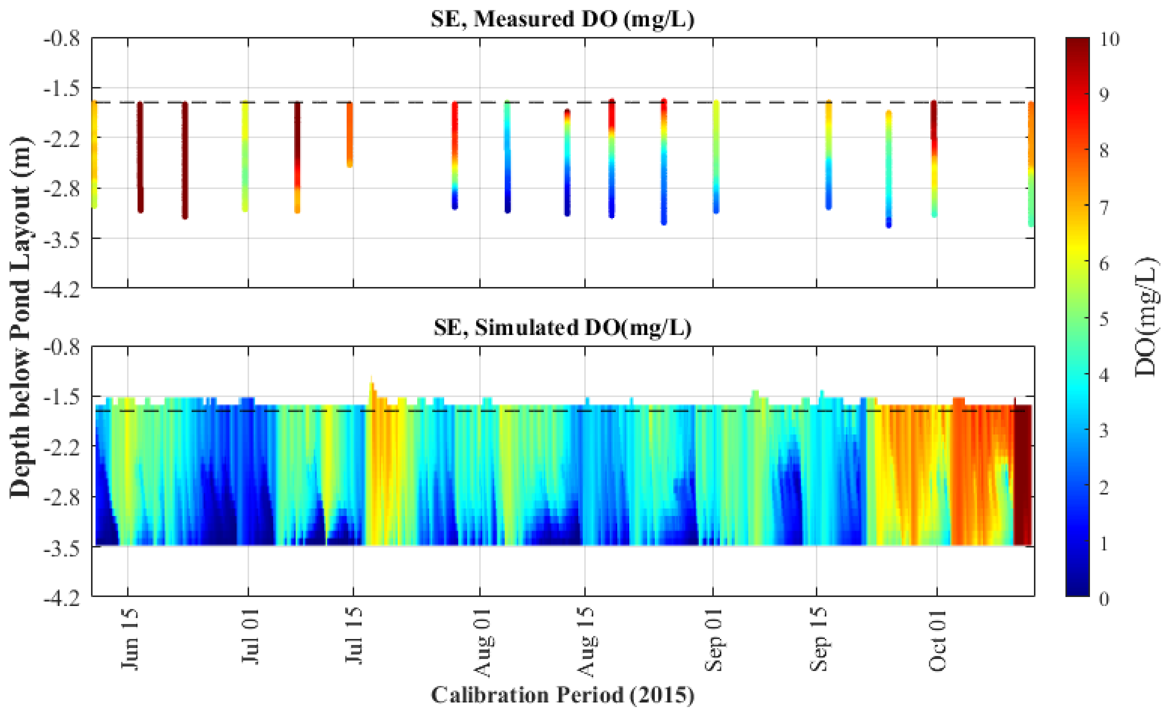

Figure B-19: Measured and simulated DO at SE sampling location during calibration period (2015).

Figure B-20 compares the measured and simulated DO at the SE sampling location during the validation period.

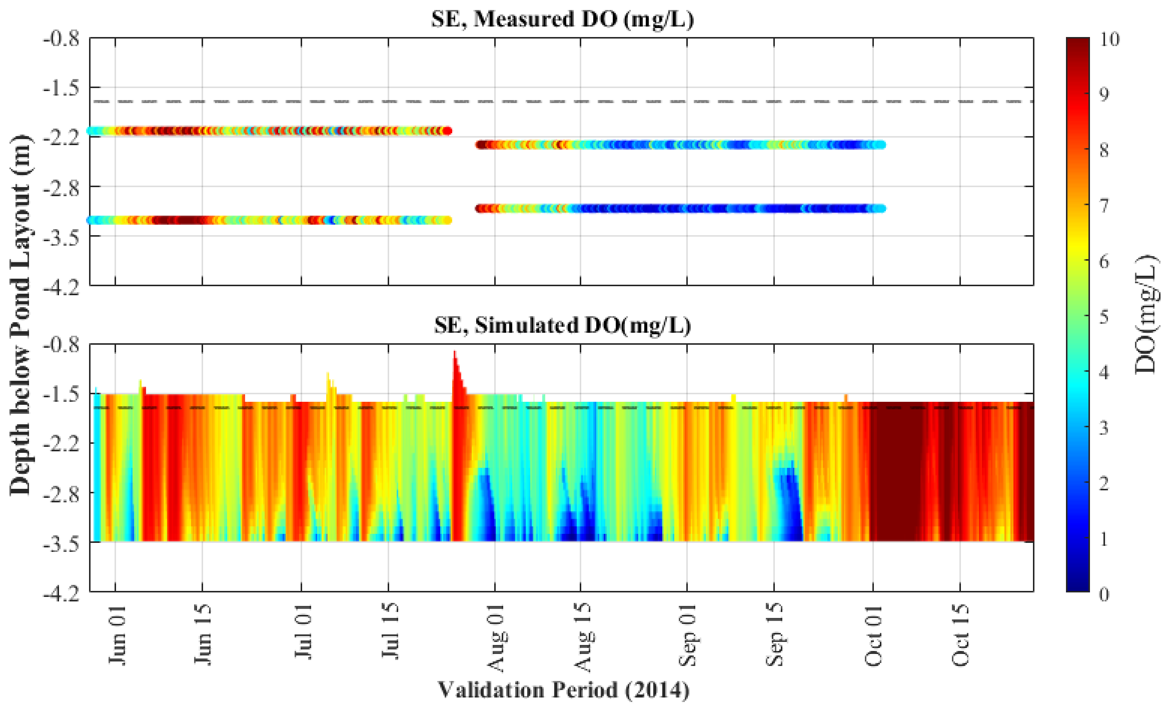

Figure B-20: Measured and simulated DO at SE sampling location during validation period (2014).

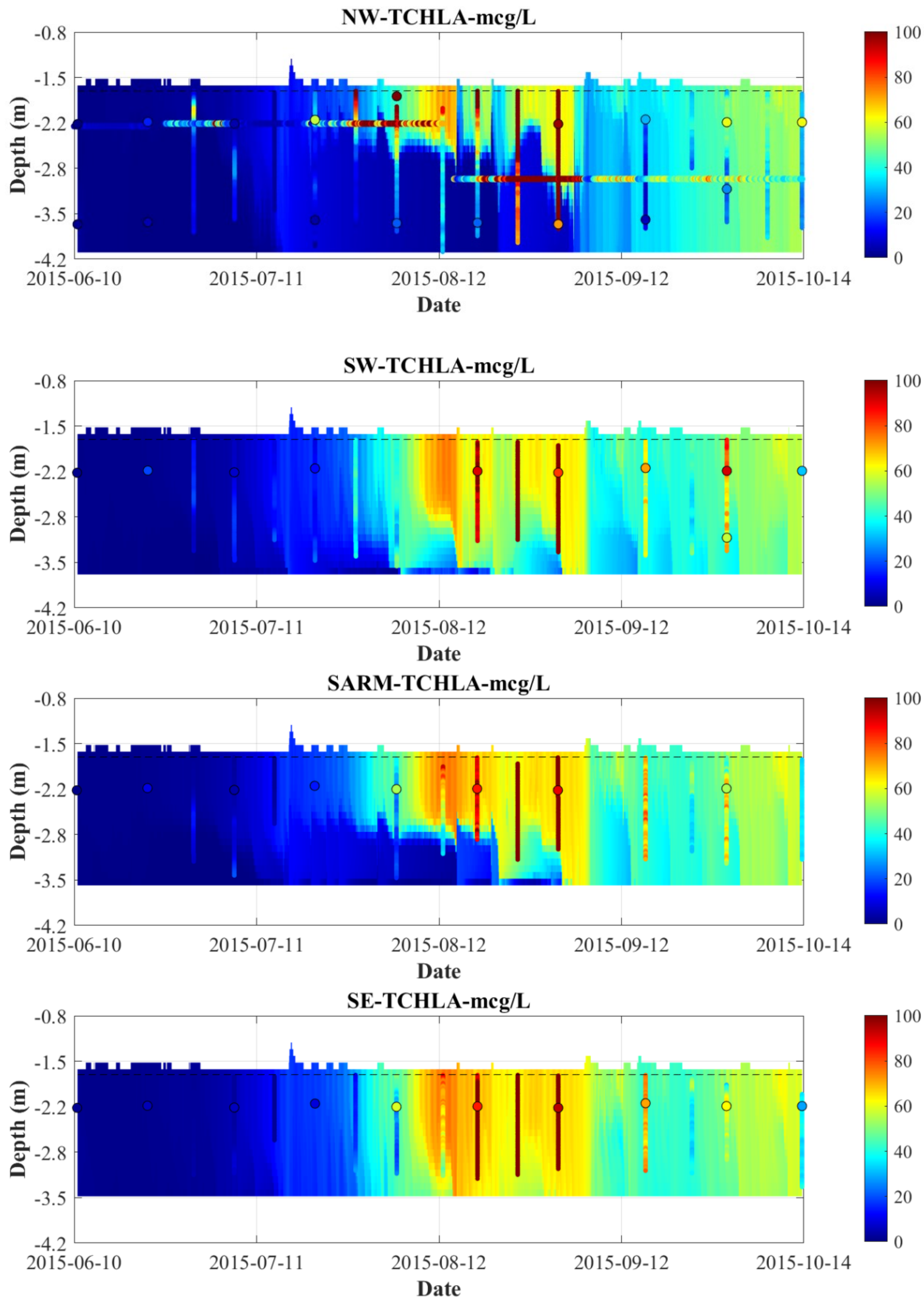

Figure B-21: Modelled and observed TCHLA at different locations of ST2 during the calibration period. Individual points, vertical and horizontal points represent the data measured by water quality sampling, EXO2 profiling, and deployed EXO2.

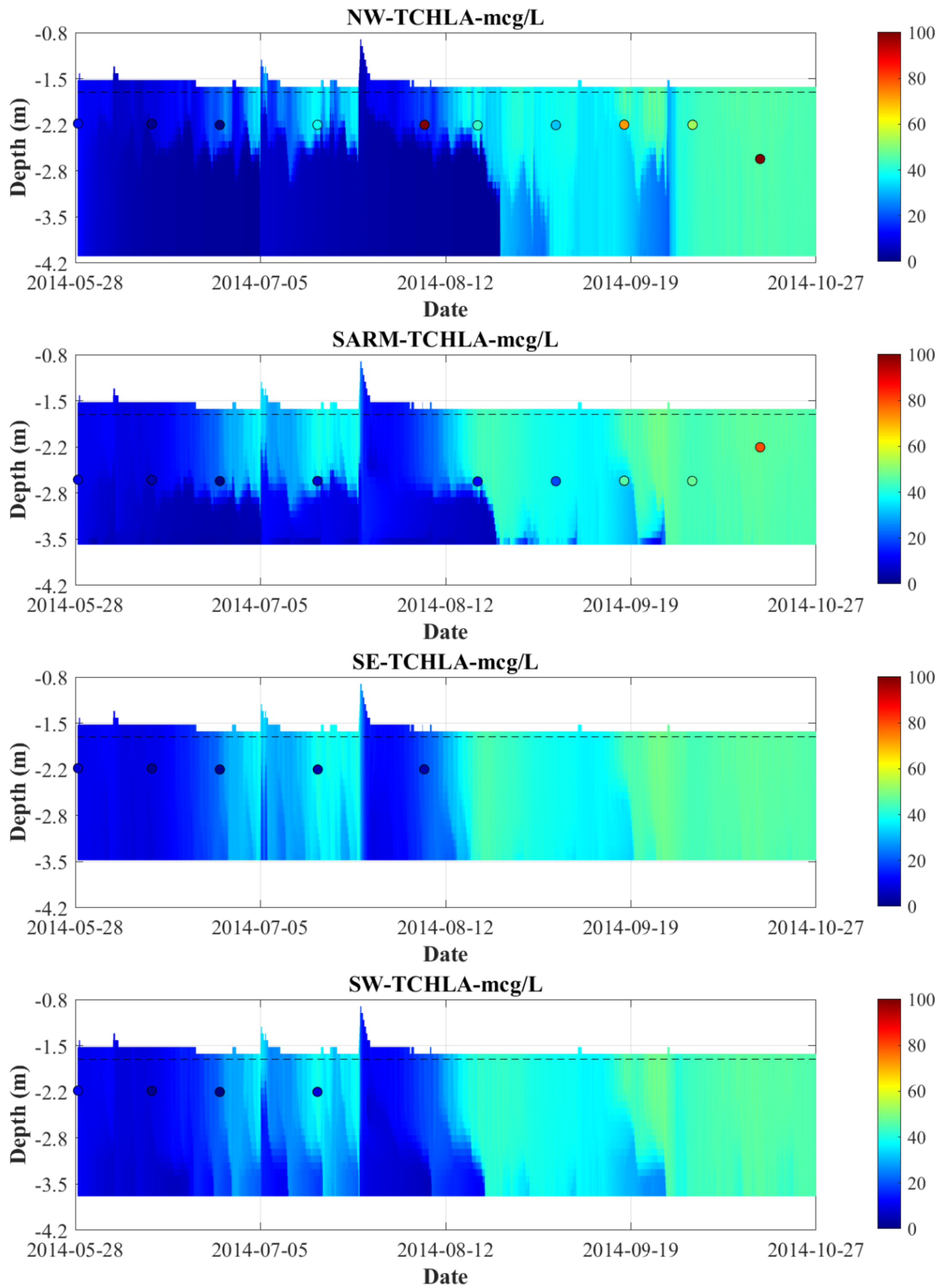

Figure B-22: Modelled and observed TCHLA at different locations of ST2 during the validation period.

Appendix C.

C.1. Additional Figures

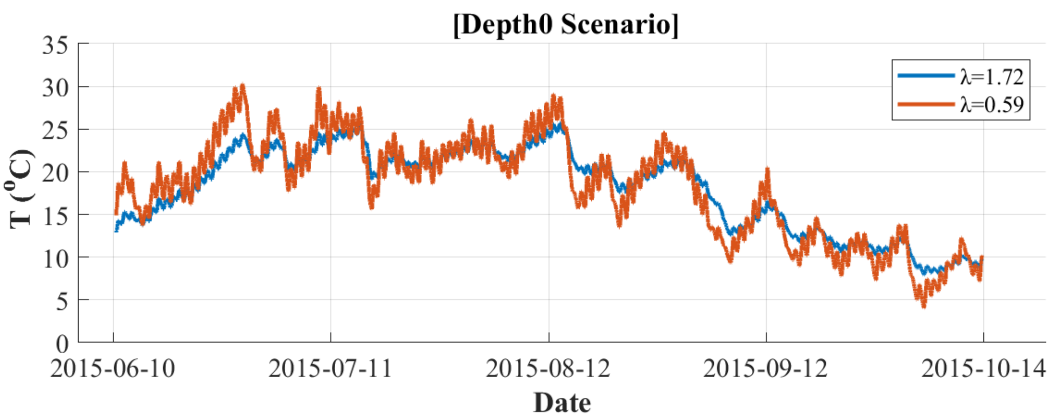

Figure C-1: Comparison of pond daily averaged temperature (T) for the largest and smallest values of λ[Depth0] during the simulation period, highlighting greater temperature variability at lower λ, i.e., the shallower pond.

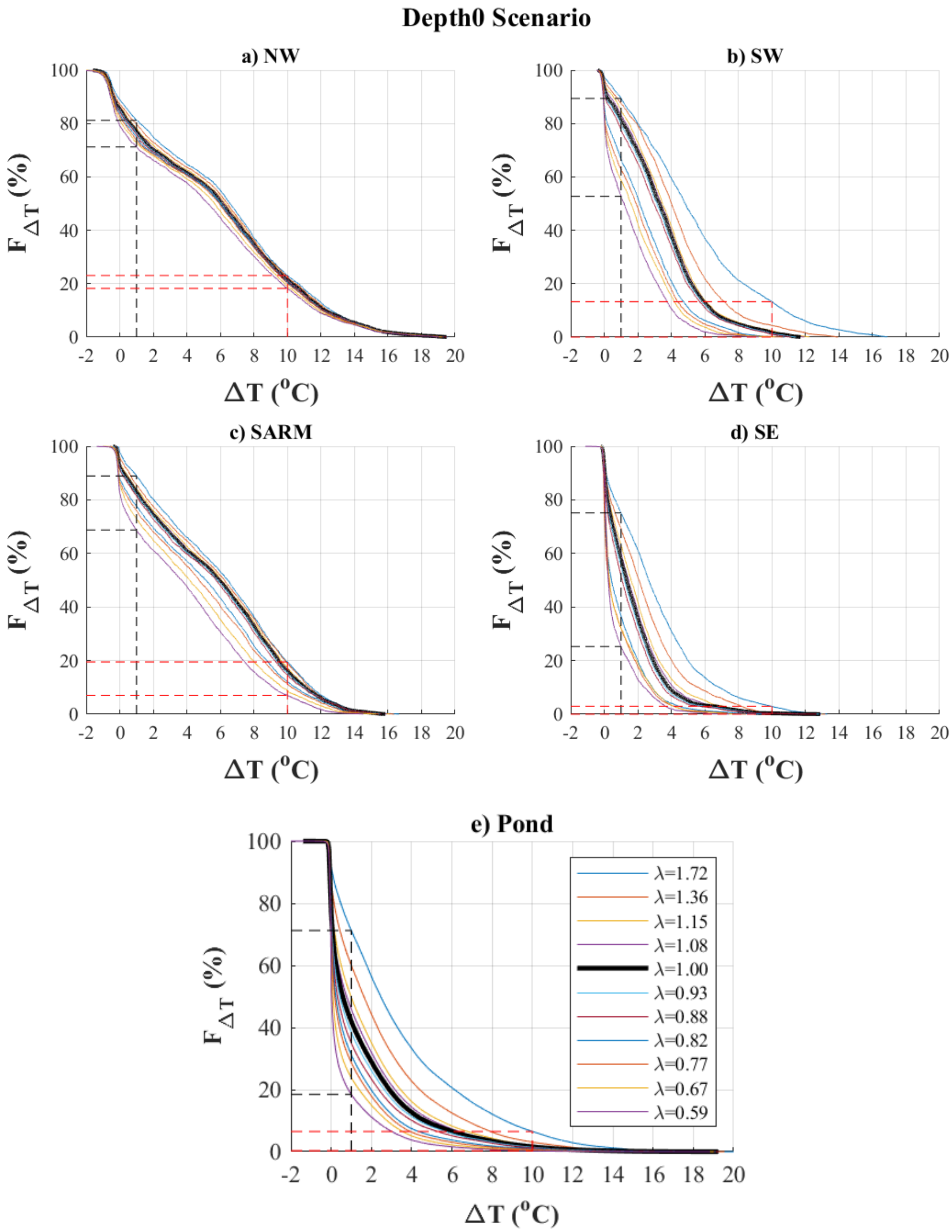

Figure C-2: Percentage of time ($F_{\Delta T}$) the stratification strength (ΔT) is greater than a given value at sampling locations and pond, averaged over the simulation period for different λ[Depth0].

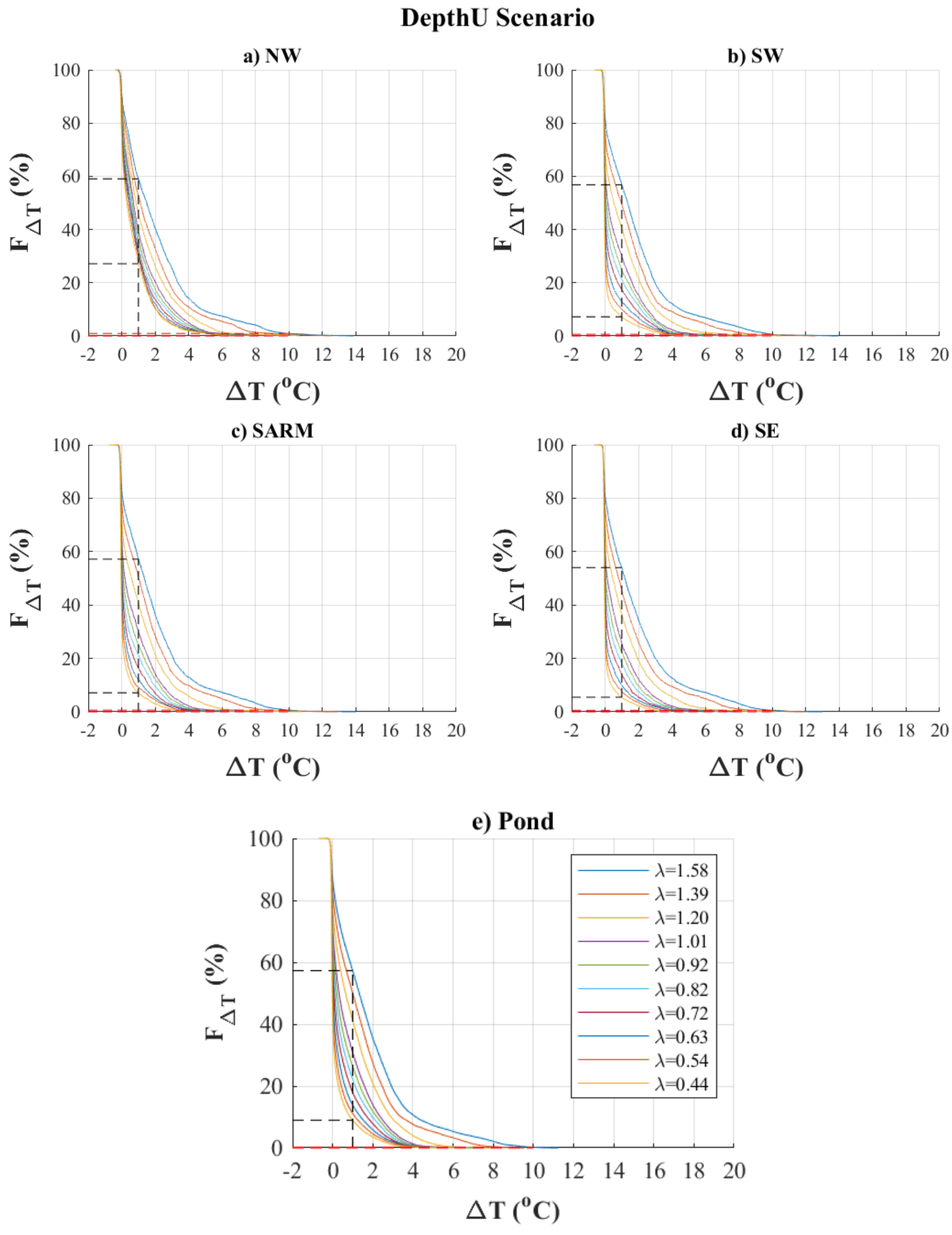

Figure C-3: Percentage of time (FΔT) the stratification strength (ΔT) is greater than a given value at sampling locations and pond, averaged over the simulation period for different λ[DepthU].

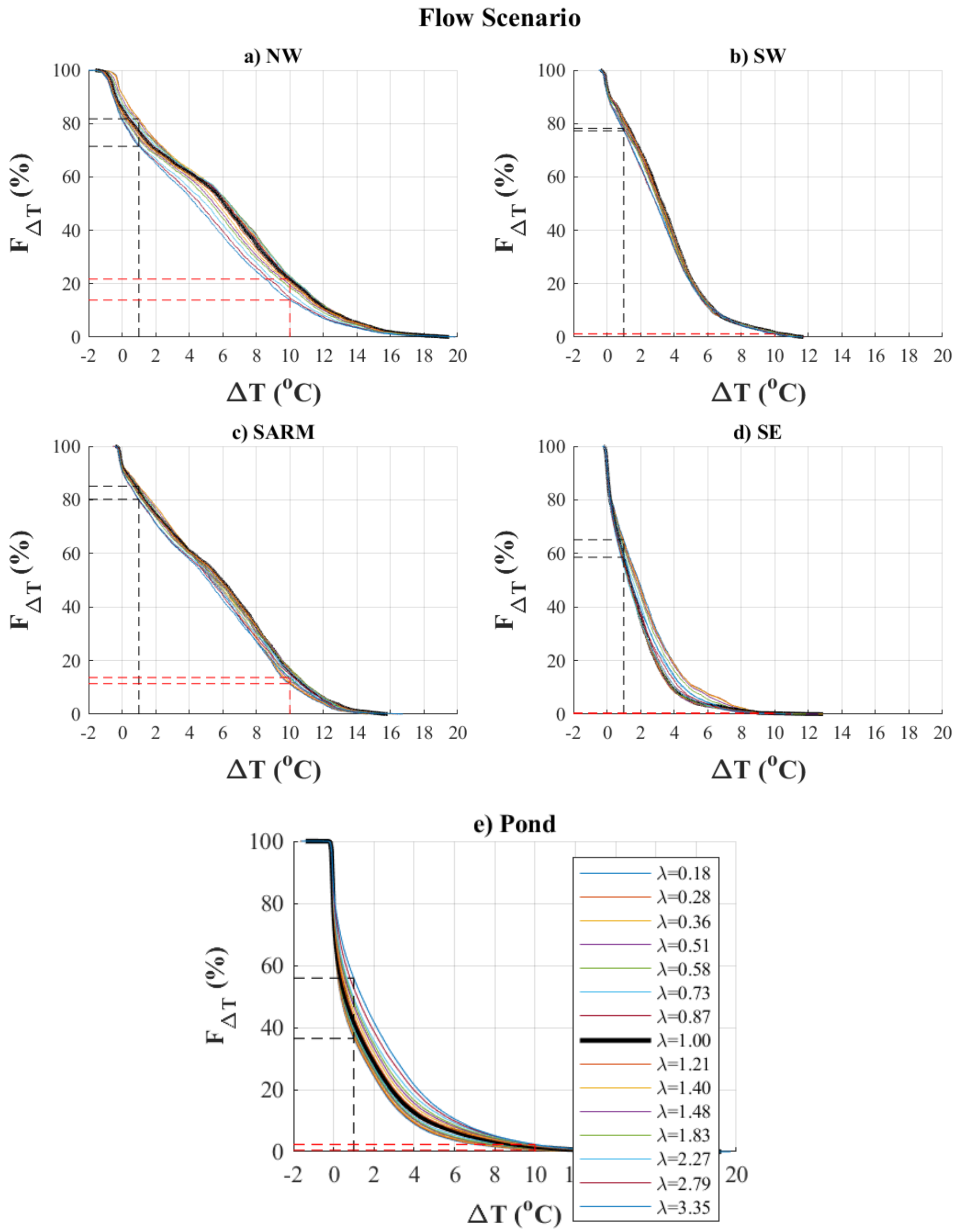

Figure C-4: Percentage of time ($F_{\Delta T}$) the stratification strength (ΔT) is greater than a given value at sampling locations and pond, averaged over the simulation period for different λ[Flow].

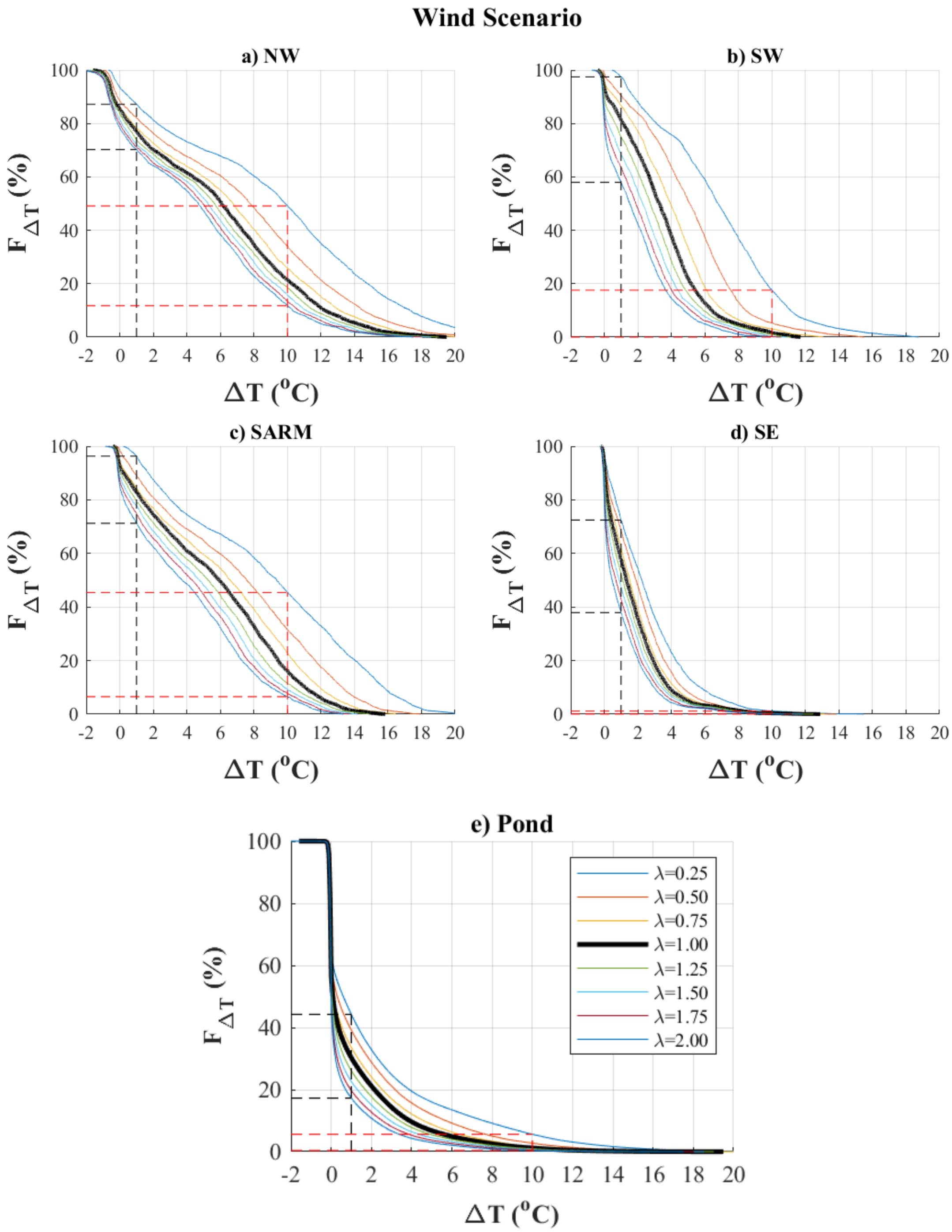

Figure C-5: Percentage of time ($F_{\Delta T}$) the stratification strength (ΔT) is greater than a given value at sampling locations and pond, averaged over the simulation period for different λ[Wind].

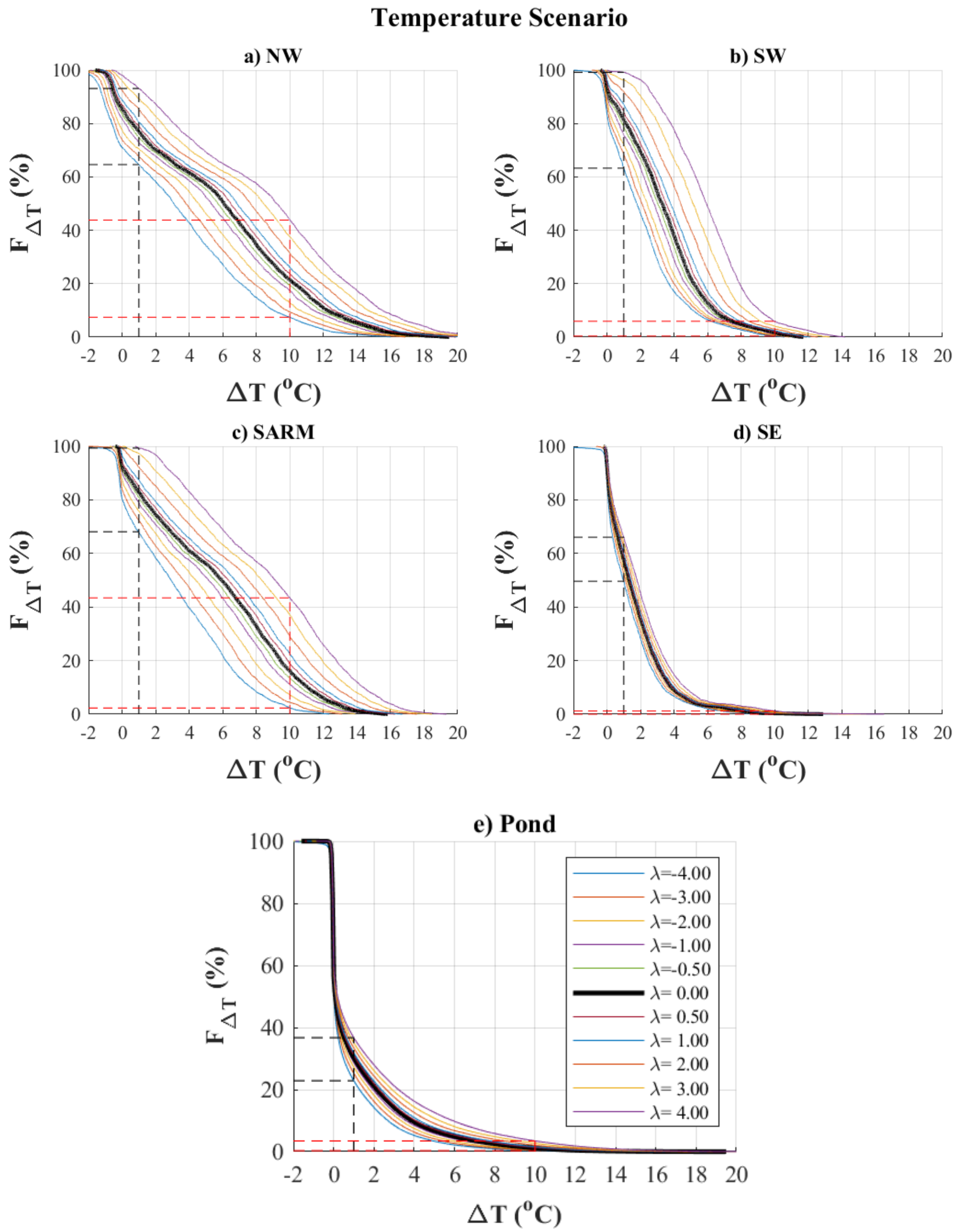

Figure C-6: Percentage of time ($F_{\Delta T}$) the stratification strength (ΔT) is greater than a given value at sampling locations and pond, averaged over the simulation period for different λ[Temperature].

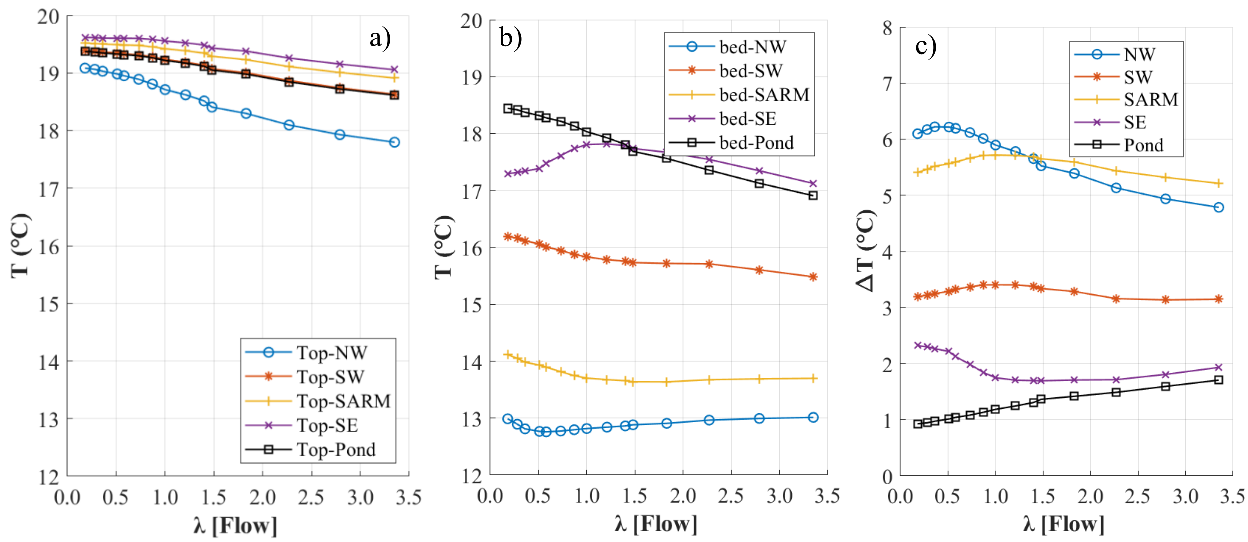

Figure C-7: a) Integrated surface temperature (top), b) integrated near-bed temperature (bed), and c) integrated Temperature difference between the surface and bed at sampling locations and the pond. All temperatures are averaged over the simulation period.

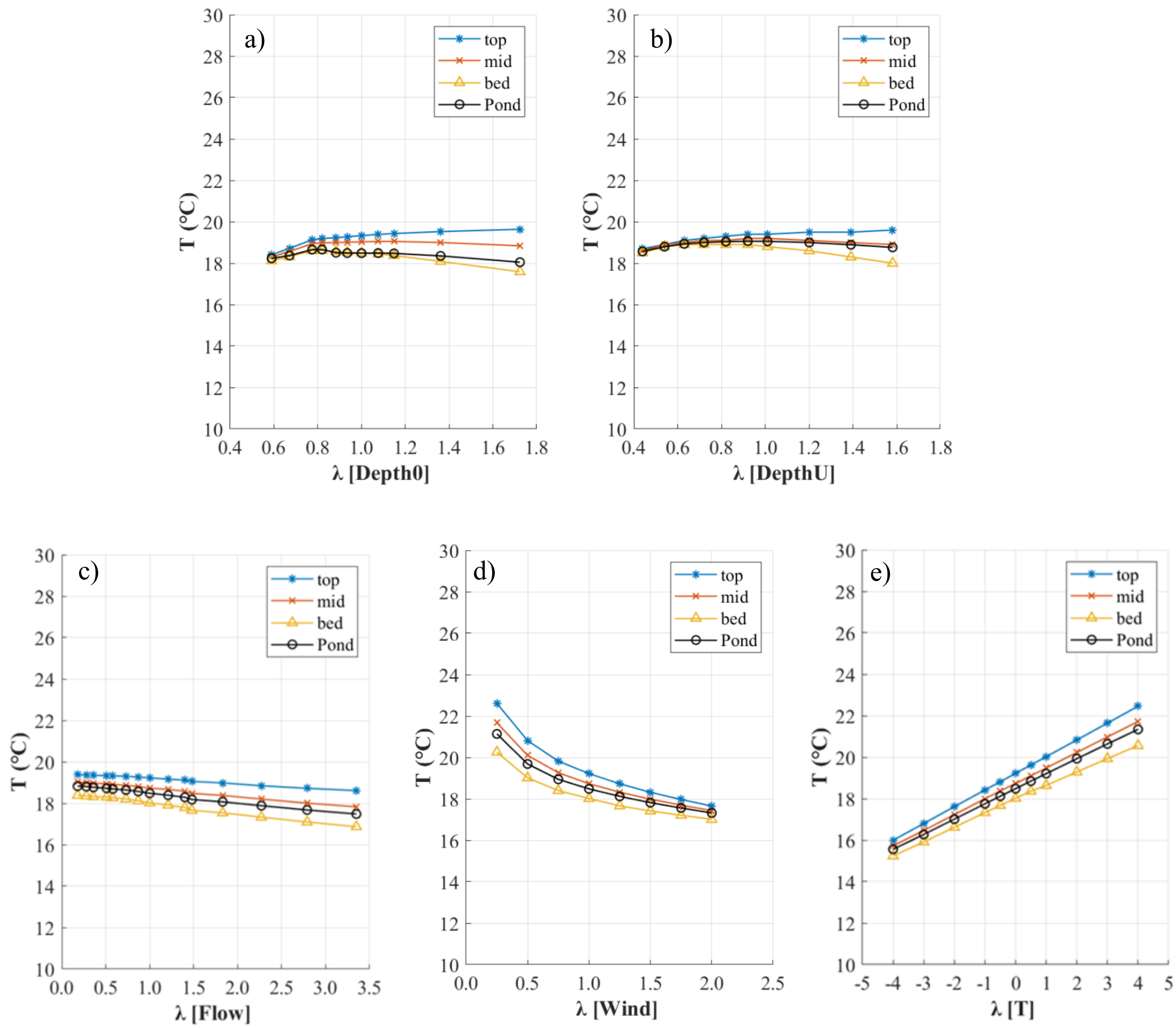

Figure C-8: Integratedt temperature (T) at the surface (top), middle (mid), and near-bed (bed) layers, and pond-integrated (Pond), during the simulation period for different scenarios. The results indicate that the average pond temperature is higher than the bed layer, but lower than the middle layer.

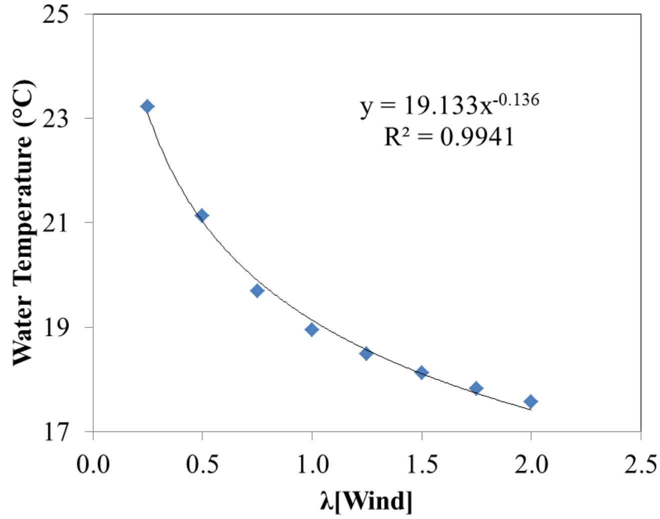

Figure C-9: Average of pond's water temperature versus λ[Wind] during simulation period.

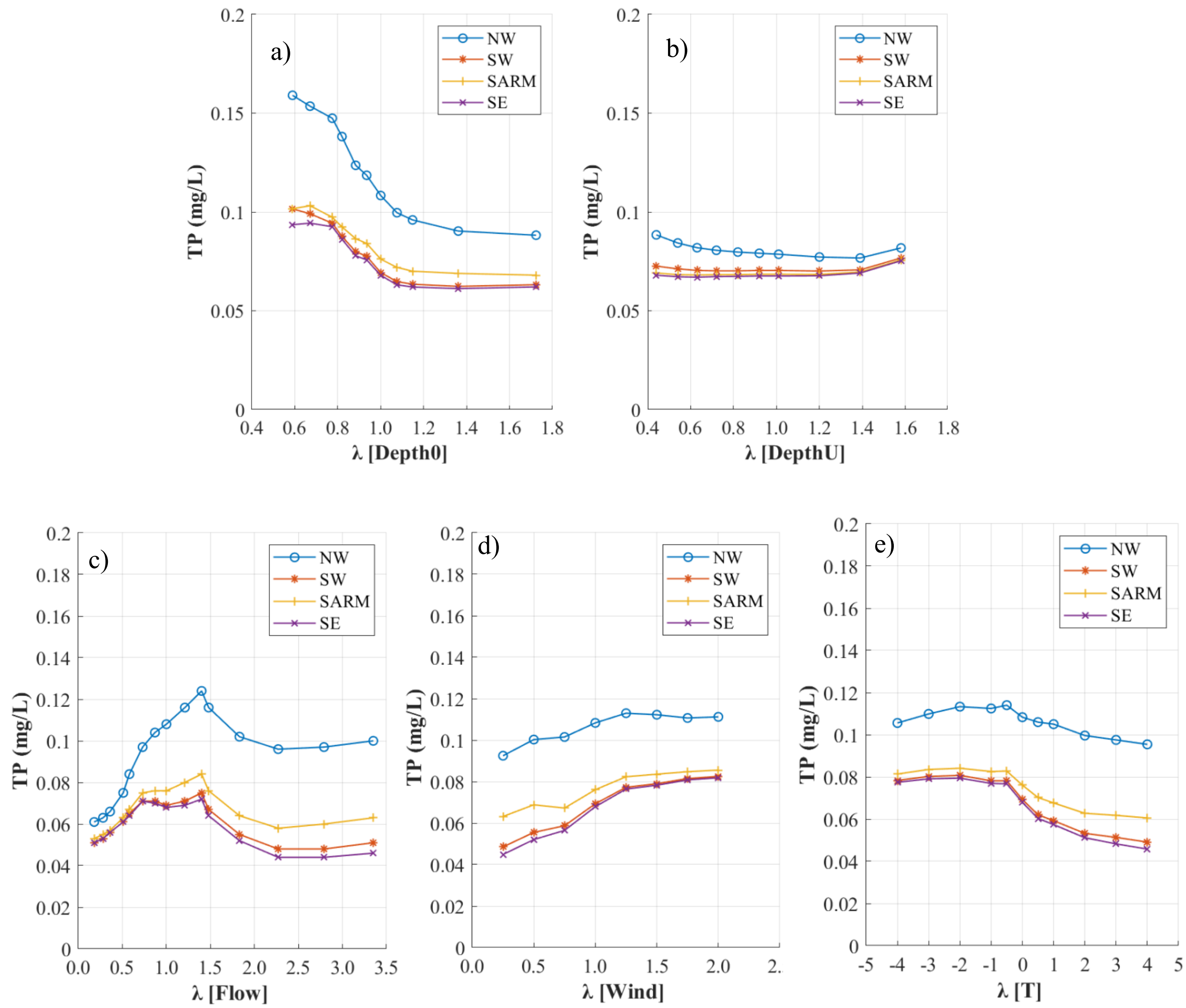

Figure C-10: Total Phosphorous, TP (mg/L), at sampling locations during simulation period with λ corresponded to each scenario: a) Depth, b) Uniform depth, c) Flow, d) Wind, and e) Temperature scenarios.

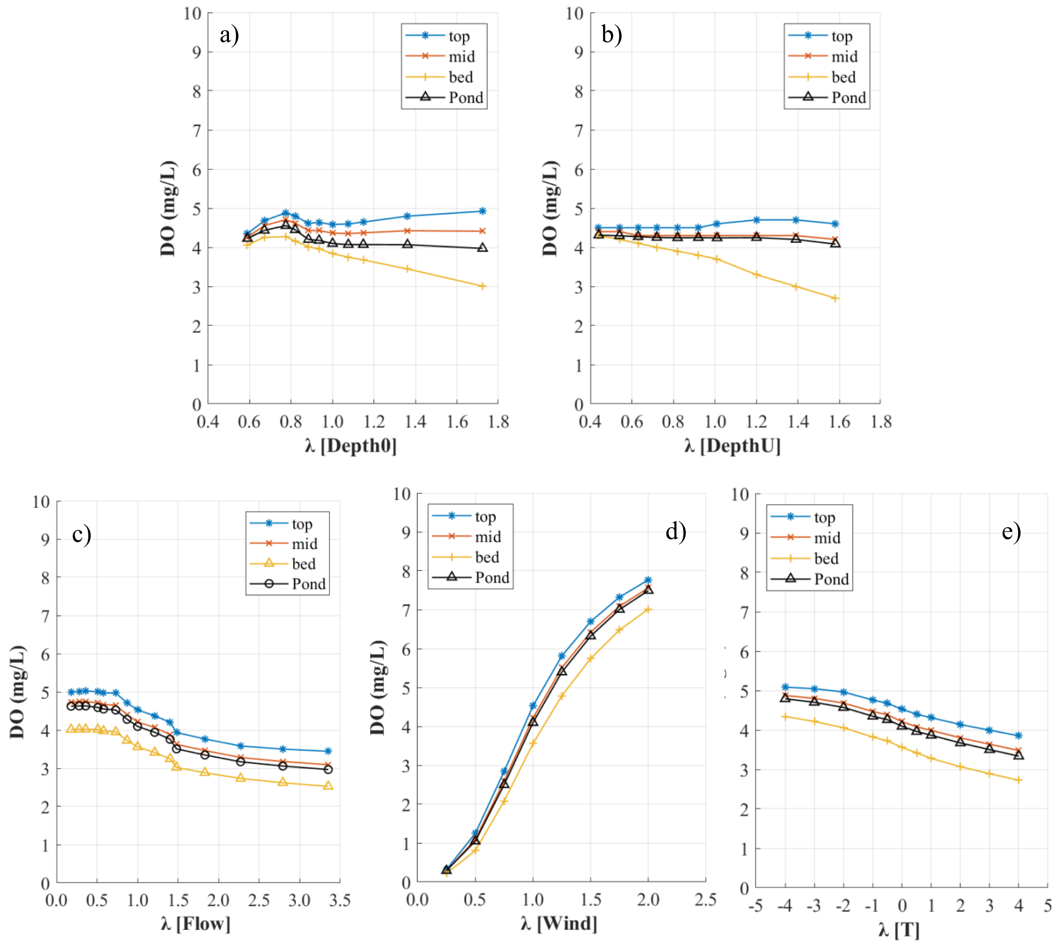

Figure C-11: Dissolved oxygen, DO (mg/L), at surface, middle and near-bed layers and pond averaged during simulation period. a) Depth, b) Uniform depth, c) Flow, d) Wind, and e) Temperature scenarios.

C.2. RT-TCHLA Association Using the Non-Parametric Kendall Test

The non-parametric Kendall's correlation coefficient (τ) (Kendall, 1938) was used to quantify the strength of the association between RT and TCHLA. Kendall's τ quantifies the association between two variables by measuring the proportion of concordant pairs. Similar to Pearson's linear correlation coefficient, a perfect association between the two variables results in a correlation coefficient of ±1, while a value of 0 indicates no association. The interpretation of τ values could be subjective; however, it is commonly suggested that $|\tau|>0.3$ indicate a strong correlation, $0.1<|\tau|<0.3$ indicate a moderate correlation, and $|\tau|<0.1$ indicate a weak to no correlation (Chowdhary 2009; Cuthbertson et al. 2014). To test the significance of the association, the Kendall τ independence test was used under the null hypothesis of $\tau=0$. The MATLAB correlation function (MathWorks. 2023) computed the strength of the association (τ) and the level of statistical significance (p-value).

First, the Kendall test was conducted to assess the association between RT and TCHLA time series in each run (42 total runs) for the Depth0, Flow, Wind and Temperature scenarios. In each run, pond-integrated, as well as top and bottom layers averages of RT and TCHLA time series were used. All associations were found to be strong and statistically significant(p-value<0.01) (Figure 5-19a).

Next, to assess the association between TCHLA and RT across different locations within the study pond, depth-averaged values of these variables were obtained at 99 points along a curtain that connects the NW inlet, SW inlet, SARM inlet, and SE outlet (Figure C-12). These variables were then averaged over the simulation period. For example, Figure 5-18 depicts average RT and TCHLA along this axis for the base-run, highlighting their direct association. Similar to the temporal analysis, for each run, the Kendall test was performed using MATLAB. All the tests were statistically significant, and with the exception of one run in the Flow scenario, all associations were strong (Figure 5-19b).

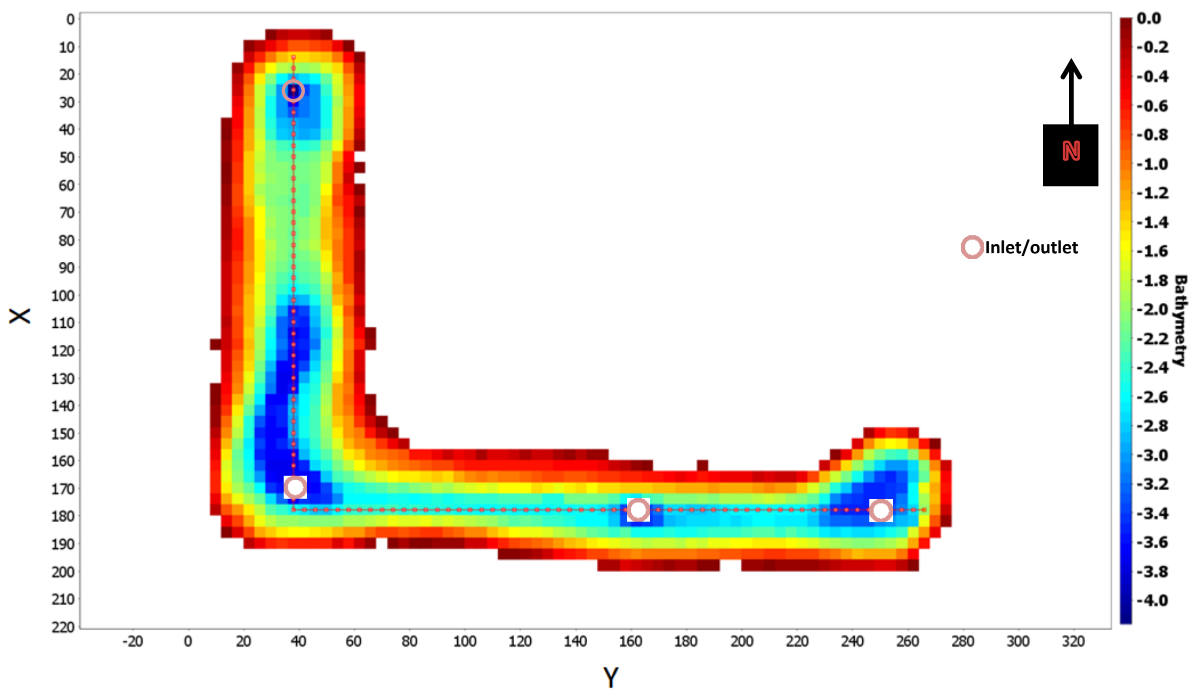

Figure C-12: Small red dots representing locations of water columns for analysis of RT-TCHLA association.

C.3. MORE RESULTS OF ASSOCIATION OF SCENARIOS AND TCHLA

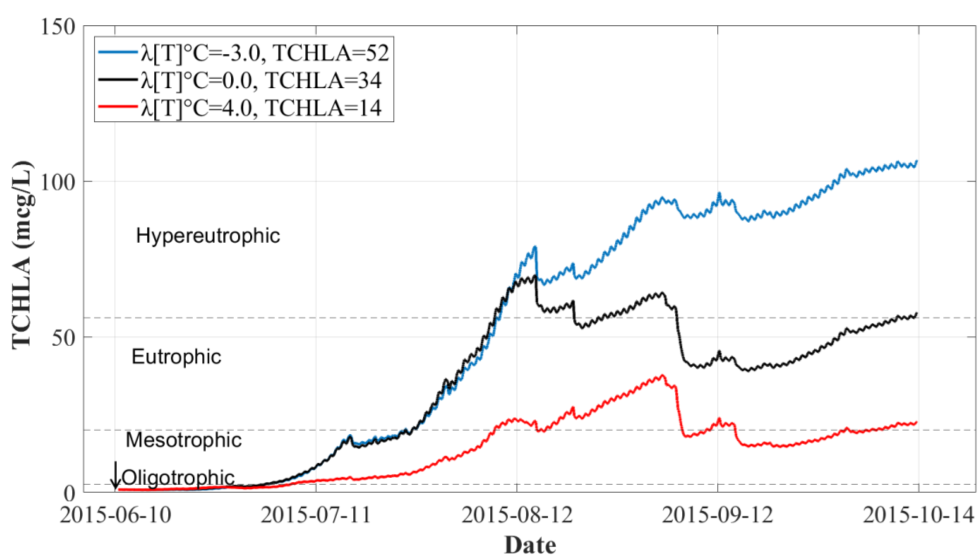

Figure C-13: Variation of pond- averaged TCHLA (mcg/L) in hourly time steps under selected runs of Temperature scenario in the study pond during the simulation period. Dashed lines represent the boundaries of trophic states.

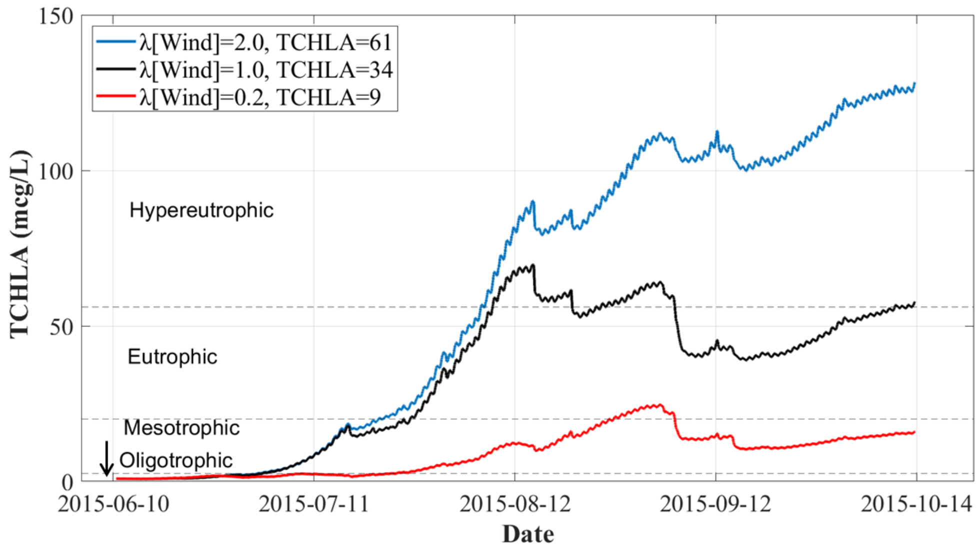

Figure C-14: Variation of pond- averaged TCHLA (mcg/L) in hourly time steps under selected runs of Wind scenario in the study pond during the simulation period. Dashed lines represent the boundaries of trophic states.

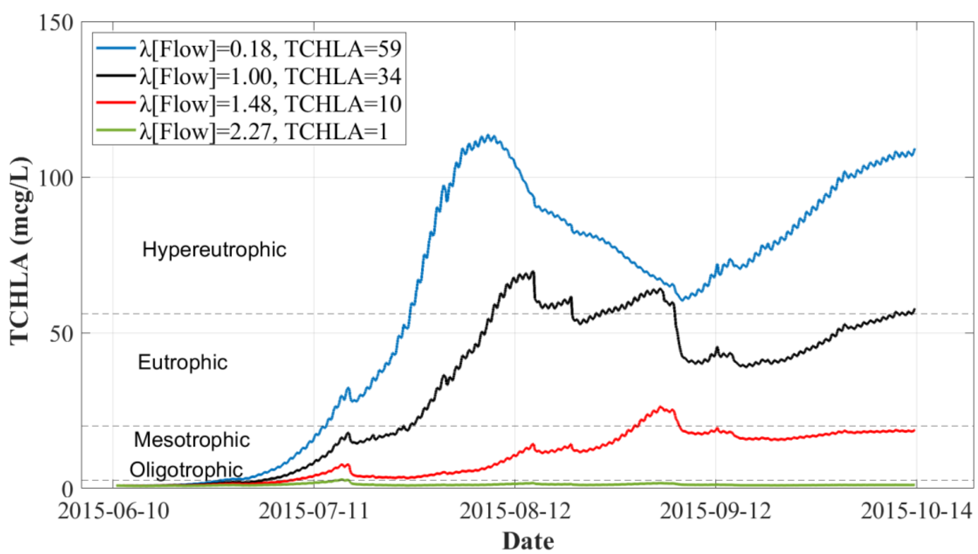

Figure C-15: Variation of pond- averaged TCHLA (mcg/L) in hourly time steps under selected runs of Wind scenario in the study pond during the simulation period. Dashed lines represent the boundaries of trophic states.

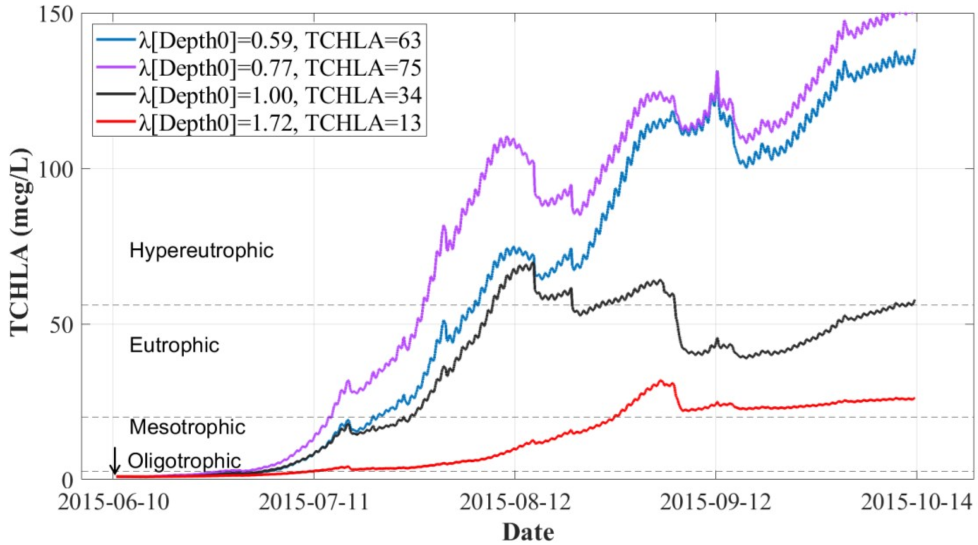

Figure C-16: Variation of pond- averaged TCHLA (mcg/L) in hourly time steps under selected runs of Depth0 scenario in the study pond during the simulation period. Dashed lines represent the boundaries of trophic states.

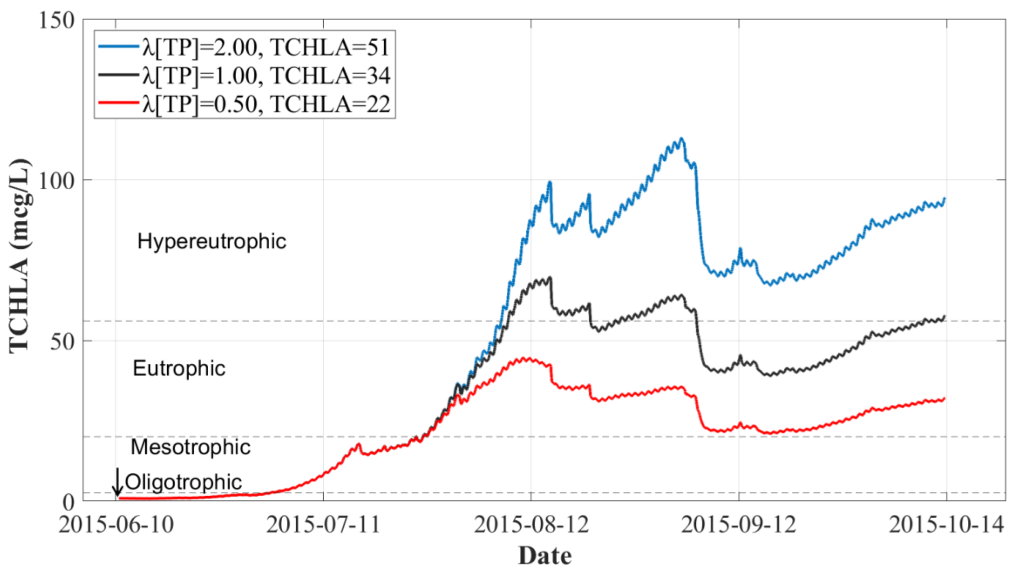

Figure C-17: Variation of pond- averaged TCHLA (mcg/L) in hourly time steps under selected runs of TP scenario in the study pond during the simulation period. Dashed lines represent the boundaries of trophic states.

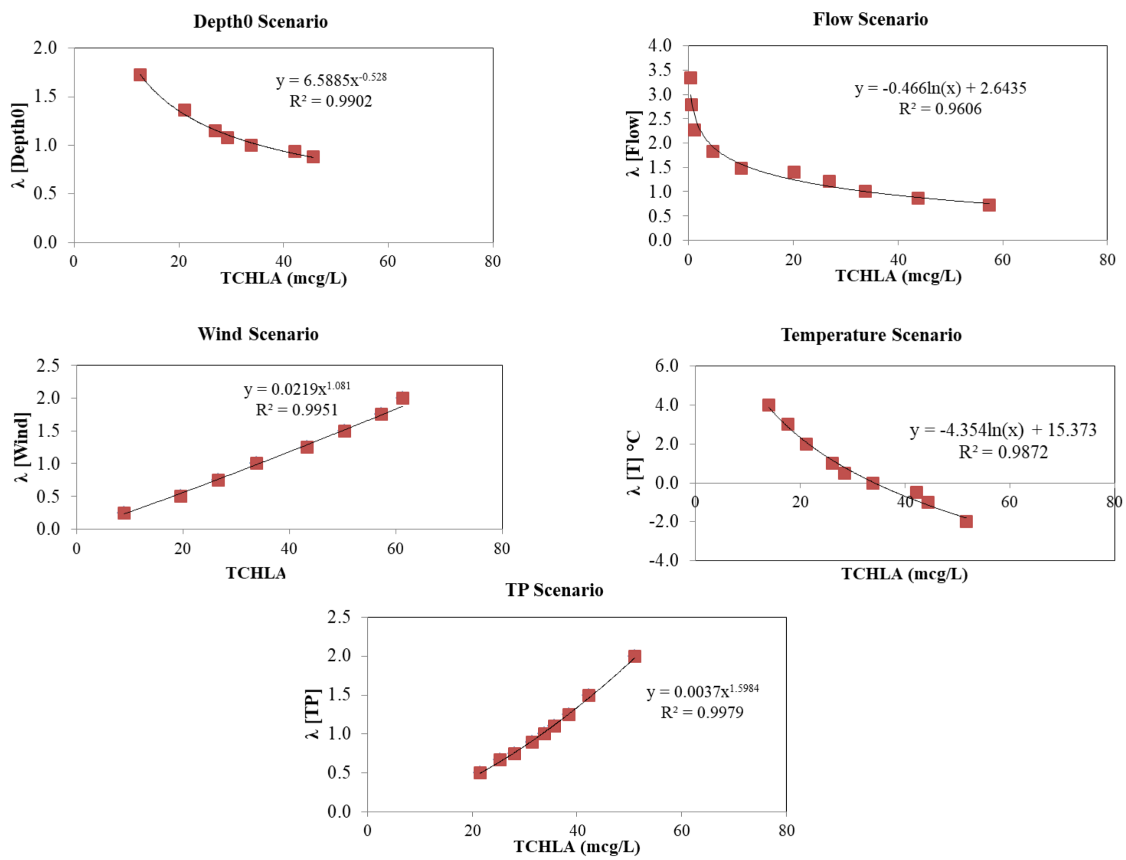

Figure C-18: Relationship between the average of pond-integrated TCHLA during simulation period and λ in different scenarios.